A Real-time Management of Distribution Voltage Fluctuations due to High Solar Photovoltaic (PV) Penetrations

Shibani Ghosh

Dissertation submitted to the faculty of the Virginia Polytechnic Institute and State University in partial fulfillment of the requirements for the degree of

DOCTOR OF PHILOSOPHY

in

Electrical Engineering

Saifur Rahman

Manisa Pipattanasomporn

Virgilio A. Centeno

Alireza Haghighat

Guoqiang Yu

December 9, 2016

Arlington, Virginia

Keywords: Solar photovoltaic (PV) system, High PV penetration, Distribution voltage regulation, Solar generation forecasting, Active power curtailment

A Real-time Management of Distribution Voltage Fluctuations due to High Solar Photovoltaic (PV) Penetrations

Shibani Ghosh

Abstract

Due to the rapid growth of grid-tied solar photovoltaic (PV) systems in the generation mix, the distribution grid will face complex operational challenges. High PV penetration can create overvoltages and voltage fluctuations in the network, which are major concerns for the grid operator. Traditional voltage control devices like switched capacitor banks or line voltage regulators can alleviate slow-moving fluctuations, but these devices need to operate more frequently than usual when PV generation fluctuates due to fast cloud movements. Such frequent operations will impact the life expectancy of these voltage control devices.

Advanced PV inverter functionalities enable solar PV systems to provide reliable grid support through controlled real injection and/or reactive power compensation. This dissertation proposes a voltage regulation technique to mitigate probable impacts of high PV penetrations on the distribution voltage profile using smart inverter functionalities. A droop-based reactive power compensation method with active power curtailment is proposed, which uses the local voltage regulation at the inverter end. This technique is further augmented with very short-term PV generation forecasts. A hybrid forecasting algorithm is proposed here which is based on measurement-dependent dynamic modeling of PV systems using the Kalman Filter theory. Physical modeling of the PV system is utilized by this forecasting algorithm. Because of the rise in distributed PV systems, modeling of geographic dispersion is also addressed under PV system modeling.

The proposed voltage regulation method is coordinated with existing voltage regulator operations to reduce required number of tap-change operations. Control settings of the voltage regulators are adjusted to achieve minimal number of tap-change operations within a predefined time window. Finally, integration of energy storage is studied to highlight the value of the proposed voltage regulation technique vis-à-vis increased solar energy use.

A Real-time Management of Distribution Voltage Fluctuations due to High Solar Photovoltaic (PV) Penetrations

Shibani Ghosh

General Audience Abstract

Rapid growth of grid-tied solar photovoltaic (PV) systems poses both opportunities and technical challenges for the electric distribution grid. Significant among them are overvoltage and voltage fluctuations in the network, which may lead to overheating of electrical devices and equipment malfunction. Due to the variable nature of solar irradiance, existing voltage control devices often need to operate more frequently than usual which can cause recurring maintenance needs for these devices.

To make solar PV more grid-friendly, changes are taking place in grid codes which encourage developing advanced PV inverter functions. With these functions, a smart inverter, which possesses bidirectional communication capability, can be integrated into a smart grid environment. This work discusses how these inverters can provide active power curtailment and reactive power compensation to maintain voltages at their points of interconnection.

The inherent variability and uncertainty in solar energy production can be addressed with solar forecasting. Application of PV generation forecasting as a tool to aid distribution voltage control is proposed in this dissertation. Using solar forecasting, smart inverters can contribute in relieving the stress on other voltage control devices due to PV-induced fluctuations. Integrating storage elements can also aid this voltage regulation method, as they can consume surplus PV generation when needed.

This dissertation is designed to provide a systematic approach to manage the overvoltage and voltage fluctuations on a real-time basis for a high PV penetration scenario. Proposed methodology combines smart inverter functionalities with solar forecasting and develops an application which can be realized to ensure seamless PV integration in a growing landscape of renewables.

Acknowledgments

First and foremost, I would like to express my sincerest gratitude to my advisor Prof. Saifur Rahman for his unwavering support and guidance over the last five years. He always encouraged me and trained me to be an independent researcher. He is an outstanding mentor and working with him has been a remarkable experience. I truly admire his discipline, dedication and passion towards his research work. He provided me plethora of resources to learn from and continues to do so for my future as a professional. I am forever thankful to him for all his wise words and inspiring thoughts.

I would like to thank Dr. Manisa Pipattanasomporn for her contributions in my PhD research. She was always there to help me whenever I struggled to find my ways forward. I am grateful to her for being very kind and patient with me. I found her warm and friendly smile to be very comforting, all the times. She taught me how to shine through adverse situations and keep working hard.

I would like to extend my special thanks to my advisory committee members- Dr. Alireza Haghighat, Dr. Virgilio Centeno and Dr. Guoqiang Yu. Their comments and feedback helped me scrutinize my work from different perspectives and made this dissertation more comprehensive.

I also want to thank all faculties, staff and my fellow graduate students at Advanced Research Institute (ARI). I learnt a great deal working with Dr. Mallikarjuna Vallem back in 2013 and I highly appreciate his support. I also want to thank Yonael for his help regarding solar data collection and other project works at ARI. I earnestly thank my friends at ARI- Hamideh, Desong, Moshiur bhai, Sneha, for making my four years at ARI lively. I would also like to thank my friends from other institutes- Prachi, Srivats, Mahesh, Taha, Avik and others from NVC and Blacksburg campuses, for their companionship.

I want to take this opportunity to thank my parents, Alo Das and Sudhir Chandra Ghosh, from the bottom of my heart for everything that they have done and continue to do for me. Even though I have been thousands of miles away from them, their love and unconditional support always gave me the strength to get going. They never lost their faith in me and sacrificed a great lot in their lives to help me come this far. I also want to thank my brother, Suash, for being a constant source of motivation.

This acknowledgement would not be complete without mentioning my husband, Avijit Saha. He is my core support system and words cannot articulate my admiration for him. I feel fortunate to have a best friend and partner in him. No matter how difficult the challenges of graduate life seemed, his positive energy boosted my confidence to confront them. His family has also been very supportive throughout these years and I deeply appreciate their cooperation.

I would like to extend my heartfelt thanks to my dear friends- Hridoy, Arun, Himadri, Nuva and Omee. All our fun get-togethers revitalized me. Their friendship made me feel at home, at all times. I also want to thank the local Bangladeshi student communities for making me a part of various activities.

Lastly, I want to thank two of my special friends- tea and music, for keeping me up and running through thick and thin!

To my wonderful family and loving friends…

Table of Contents

List of Figures

List of Tables

Abbreviations

ANN	Artificial Neural Network
APC	Active Power Curtailment
APCf	Active Power Curtailment using solar generation Forecasts
AT	Atmospheric Transmittance
CVR	Conservation Voltage Reduction
DER	Distributed Energy Resources
DG	Distributed Generation
EPS	Electric Power System
KF	Kalman Filter
kWp	Kilo Watts Peak
LDC	Line Drop Compensation
LV	Low Voltage
MAPE	Mean Absolute Percentage Error
MPPT	Maximum Power Point Tracking
NREL	National Renewable Energy Laboratory
nRMSE	Normalized Root Mean Square Error
NWP	Numerical Weather Prediction
OLTC	On-Load Tap Changer
OPF	Optimal Power Flow
pf	Power Factor
POI	Point of Interconnection
PV	Photovoltaic
RMS	Root Mean Square
RPC	Reactive Power Compensation
SCB	Switched Capacitor Bank
SVC	Static VAr Compensator
UQ	University of Queensland
VR	(Line/step) Voltage Regulator
VT-ARI	Virginia Tech- Advanced Research Institute

1. Introduction

1.1 Background

Solar photovoltaic (PV) energy deployment is accelerating at a rapid pace throughout the world. On a global scale, more PV capacity was added into the generation mix between 2010 and 2014 than in the previous four decades [1].

The global growth in cumulative PV capacity is shown in Fig. 1-1 for the years 2000-2015 [2]. As seen in Fig. 1-1, the global PV capacity passed the 100 GW mark in 2012. Within the next three years this figure had more than doubled to 229.3 GW. By the end of 2015, Europe stood as the world's leading region in terms of cumulative PV capacity (97 GW), being closely followed by Asia-Pacific countries including China (96 GW). In 2015, 50.6 GW of PV had been installed globally, of which the largest share belonged to China (46%). The U.S. market scored third in annual addition with 7.3 GW PV following Japanese market which installed 11 GW in 2015. Because of competitive cost structure, utility-scale PV systems are leading the growth of PV industry. However, the residential/commercial PV applications are also showing major growth. For example, in the U.S. solar market, the residential PV is one of the fastest growing sectors which has shown more than 50% of annual growth every year since 2012. In 2015, residential PV capacity grew by 66% from 2014, adding over 2 GW's of new installations (Fig. 1-2). By the end of 2015, this sector accounted for about 29% of the U.S. solar market [3].

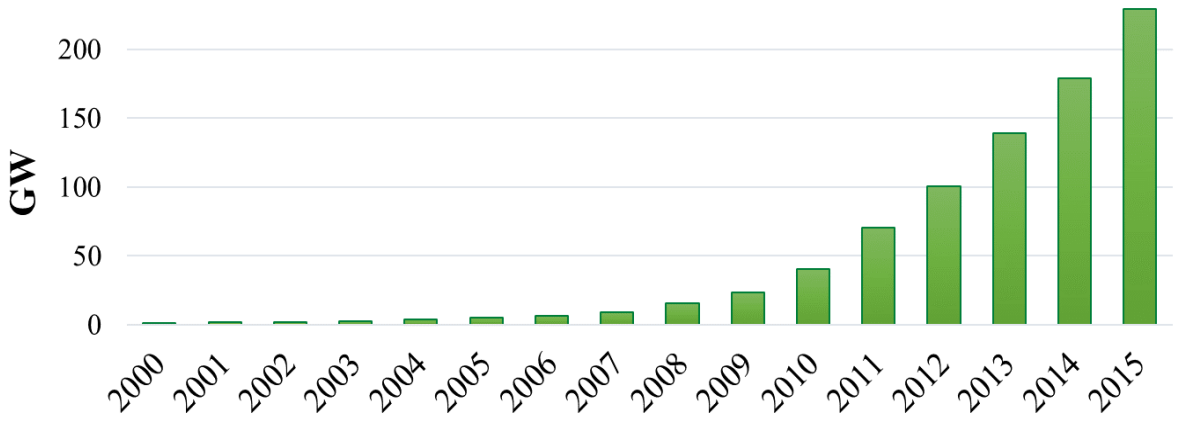

Fig. 1-1 Global PV cumulative installed capacity (2000-2015)

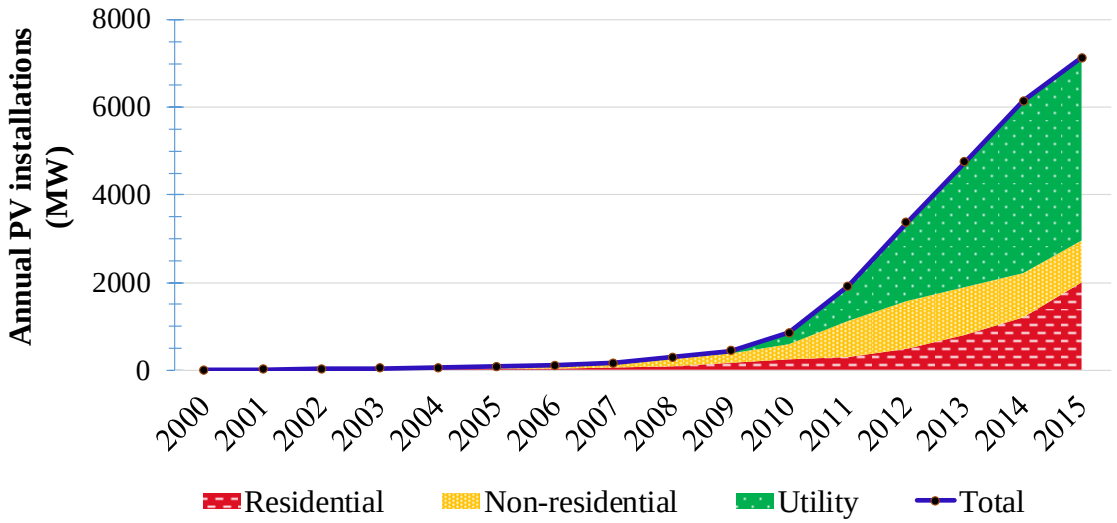

Fig. 1-2 Annual solar PV installations in the U.S.: residential, non-residential and utility sectors (2000-2015)

While the large-scale PV plants are being connected to the grid through existing or newly commissioned transmission lines, the residential and commercial PV sectors are hooked up at sub-transmission level or mostly in the distribution network. Consequently, as the number of PV systems integrated into the distribution grid grows, the evolving grid faces several opportunities as well as challenges. An array of challenges regarding network operation arises from the inherent variability in solar irradiance due to cloud transients and diurnal effects. While the shorter-timescale fluctuations are vital to distribution grid operators and load following markets [4, 5], the variability in the long-term is of interest for transmission planning work. Output intermittency in case of high penetration of PV translates into potential concerns for the traditional distribution networks. Some of these issues are briefly mentioned below which were highlighted in a 2011 article published in IEEE power & energy magazine [6].

- *Reverse power flow*:

When PV generation is high, the power flow direction through lines might get reversed as it can offset some of the total feeder load, and feed power to neighboring feeders or to transmission network at daytime. This situation will create operational hazards for equipments which are especially designed to handle unidirectional flow. For example, in traditional distribution network, many of the overcurrent protection devices and line voltage regulators belong to this category.

Hence, to accommodate high PV penetration, such unidirectional devices have to be replaced by their bidirectional counterparts.

- *Overvoltage and voltage fluctuations:*

The PV generation reduces the feeder load and in return increases bus voltages. But at times of cloud transients, significant voltage fluctuations can be observed throughout the system. Both of these situations become more problematic as the PV penetration grows. The extent of voltage fluctuations is not only a function of the PV generation but also dependent on the PV plant location and the network configuration. Much work has been reported with realistic case study simulations and/or experimental results analyzing these two phenomena.

- *Effects on voltage control devices:*

In a traditional distribution network, the voltage rise due to PV generation directly impacts the operation of voltage control devices like On-load tap changer (OLTC), Switched capacitor banks (SCB) and line voltage regulators (VR). All of these devices inherit operational delays due to their control techniques, typically around 30-90s. When voltage fluctuations happen in such timescales, these control devices can detect them and take necessary actions to make adjustments. However, due to the higher frequency of PV-induced voltage fluctuations, these devices will have to operate more frequently than usual to keep the network voltage within prescribed limits.

Frequent operations of VR's often lessen their expected life. The tap change in a VR is usually implemented by a quick-break, slow-make switching mechanism. This switching mechanism in a standard VR is implemented with a gear-driven switch with a motor and power supply. Longevity of the VR thus depends on the life of its switch. Also, the tap-changer contacts and insulating fluid can deteriorate with use. Manufacturers define a certain number of operations for this switch to signify the 'maintenance-free usage'. In a case study performed by National Renewable Energy Laboratory (NREL) it was seen that for the Colorado State University Foothills campus project, maintaining a tight voltage bandwidth (1V bandwidth on a 120V base) had created a situation where the regulators operated hundreds of thousands of times over a one-year period [7]. Two of those regulators were found non-operational later and had to be replaced by the electric utility (Xcel Energy). However, advanced tap changing controllers are emerging as innovative technologies which are equipped with features like adjustable bandcenter and bandwidth, flexible

intertap time delay and reverse flow operation [8, 9]. These devices are expected to provide better grid support even under high penetration of intermittent renewables. Coordinating these devices with PV inverters will be even more effective to grid operators, once such devices are widely deployed in a smart grid environment.

Faster switching of SCB's also has similar maintenance concerns as in with VR's. Switching SCB's generally do not cause serious transient problem for utility equipment [10]. But these transients are likely to get magnified at the customer end causing nuisance tripping of adjustable speed-drives [11].

- *Impact on losses*:

With increasing PV penetration serving parts of the load in the distribution network, the power flow into the feeder line decreases. This results in lower than normal current flow in the feeder causing losses in the distribution network to decrease. However, at high penetration levels the power flow reverses and line currents can be higher than normal flow without PV. This will result in higher losses.

Among these various technical challenges raised by high PV penetrations, this dissertation focuses on the issues of voltage rise and fluctuations and resulting effects on existing voltage control devices, namely VR's. A review of the recent literature suggests that, efficient voltage regulation algorithms can be realized locally with smart PV inverters. Extensions of these algorithms can also include the operation of existing voltage control devices. Further flexibility can be added to voltage control when the variability and uncertainty in solar generation is managed properly, i.e., the system has some form of integrated forecasting methodology. Along with keeping the voltage profile within the prescribed limit, the proposed technique also helps to minimize tap-changing operations for the VR's. In other words, based on short-term generation forecasts, solar PV units can help the grid operator to reduce the wear and tear of the existing devices, along with managing the network voltage profile.

1.2 Scope and objectives of the dissertation

The objective of this research is to mitigate the impact of high PV penetrations on distribution grids by developing a coordinated algorithm to implement distribution voltage control. Such voltage control is expected to ensure seamless integration of large-scale PV integration in a

distribution feeder mostly serving residential and commercial loads. The proposed coordinated voltage control algorithm utilizes the variable real and reactive power injection capability of a PV inverter, together with existing voltage control devices like the VR's. Reactive power compensation and active power curtailment methods successfully provide local voltage control at the inverter point of interconnection (POI). Such control realized at the inverter POI can prevent local distribution overvoltage, which is a major concern for high PV penetration in distribution grids. Besides, it helps reduce excessive tap changing operations of the VR's when the solar irradiance is highly fluctuating. VR's usually operate in local or autonomous control mode where the tap position is changed according to the voltage sensed at its terminals or determined through the predefined line drop compensation properties. In this coordinated scheme, the VR's are controlled in a supervisory fashion where the voltage regulation center and/or regulation bandwidth are adjusted according to the PV generation or variable real/reactive power input from the inverter. This way, a PV inverter perform voltage control along with the existing VR's, thus reducing the stress on these devices due to PV-induced fluctuations.

On top of the coordinated voltage regulation scheme, solar generation forecasts are used to enhance the algorithm(s) further. PV generation forecasts aid the algorithm(s) to determine appropriate control parameters for the operation of VR's so that it can help minimize their tap-changing operations for the given duration. Because this forecasting is performed on a short-term basis, it gives the algorithm(s) more granularity to adjust VR control settings throughout the day, rather than scheduling these settings for day-ahead scenario. Very-short term PV output forecasts (≤1-minute resolution) are generated based on a hybrid technique, which incorporates both physical (empirically based on regression analysis of past data clustered according to weather type/seasonal classification) and statistical models (based on Kalman Filter (KF) theory). High resolution (15-second interval) data for relevant weather parameters (like irradiance, ambient temperature, wind velocity etc.) and PV generation data are available from the rooftop PV system placed on Virginia Tech Advanced Research Institute (VT-ARI) building in Arlington, Virginia. The KF technique is implemented to dynamically model (and thus forecast) the output of the PV system, based on these data. The real power forecasts are integrated in the algorithm to aid the real/reactive power injection technique for local voltage regulation. Short-term forecasts (1-6 hours ahead) can be deployed to help with the supervisory control of the VR's.

As this dissertation focuses on a high PV penetration scenario within its scope, modeling distributed PV is also discussed here. Geographic dispersion affects the aggregate PV power in a sense that the variability is reduced as compared to a single PV system. This spatial variability along with the location of PV system(s) is of importance, since irradiance fluctuations result in comparatively larger voltage transients when the PV plant/fleet is placed towards the end of a radial feeder. Also, the further it is from the VR's (in electrical distance), the less the cloud and resultant voltage transients would impact the daily VR operation. VR operation is coordinated in this proposed methodology with local voltage regulation by PV inverters to minimize tap change counts. Storage integration is also addressed here which can further reduce voltage fluctuations induced by variability in PV power.

Overall, for this dissertation, these aforementioned analyses are presented under the following tasks:

- ***Developing a short-term PV generation estimation model using regression analysis*:** For this task, regression analysis is performed on measured data and a physical PV performance model (for the VT-ARI PV system) is developed. This model takes into account weather types in different seasons. Irradiance and ambient temperature are the inputs into the model. Instead of ambient temperature, module temperature is used for this regression analysis, as direct measurements are available. Dependence of PV generation on wind speed is also a part of this study. Geographic smoothing effect is also studied here that can be utilized in modeling distributed PV integration.

- ***Developing and validating a Kalman Filter (KF) based forecasting model:*** The aforementioned model needs weather data (irradiance and ambient temperature) to forecast PV power generation. By integrating KF technique with this physical model, very short-term (≤1-minute resolution) PV power forecasts are delivered. This method adaptively tunes the model for a given day according to incoming measurements, to reduce the prediction error. After the forecasting model is prepared, its performance is assessed offline and compared with that of a naïve prediction model.

- ***Employing local voltage regulation from the inverter based on PV forecasts*:** Local voltage control is investigated numerically (on realistic case studies) where control decisions are taken based on forecasts and realized only at inverter point of interconnection. In this approach, other devices, namely, voltage regulators work independently but the PV inverter is able to control

the higher frequency voltage fluctuations. The local control is intended to regulate the voltage with reactive power compensation (RPC) or variable power factor (pf) mode and would only rely on real or active power curtailment (APC) when reactive power compensation alone cannot provide the desired regulation. Power factor criteria are also maintained by this method.

- ***Implementing a coordinated voltage regulation scheme*:** Coordinating VR operation with locally controlled inverters can reduce tap change operations. The proposed coordinated regulation scheme makes direct control decisions for the inverter (real and reactive power set-points for PV inverters), but provides supervisory control for the VR's, i.e. the controller instructs the target VR to change its bandwidth or voltage reference rather than communicating the exact tap positions. Both inverters and VR's thus retain their local/autonomous modes of regulation, but the coordination (based on PV output forecasts) ensures that their actions are not counterproductive. Also, storage integration is analyzed with PV inverter operations.

1.3 Contributions

This section briefly describes contributions from this dissertation:

- *Very short-term PV generation forecasting*

This dissertation discusses the development of a forecasting model that can provide very short-term PV generation forecasts (≤1-minute resolution) based on a hybrid technique. The hybrid technique considers the physical modeling of PV output as a function of weather parameters (irradiance, temperature and wind velocity). For developing this model, dynamics of these input variables are studied on a very short timescale. Besides, geographic dispersion is also considered for simulating aggregate power from a PV fleet.

- *Application of KF technique for very short-term PV generation forecasting*

KF theory has been rarely applied in the solar generation forecasting area. This technique is used here to yield very short-term solar generation forecasts which is again used as a tool to aid the proposed voltage regulation scheme. KF technique utilizes measurement based dynamic modeling and estimation method, and thus is particularly useful for such a case where the forecasting time horizon is very small. Also, for the application purpose, the forecasting is required in different timescales (very short-term for fast operating inverters, and short-term forecasts for comparatively slower devices like VR's), which can be implemented with KF technique.

- *Forecasting based voltage regulation technique*

A local voltage regulation technique is developed here that adaptively changes real/reactive injection/absorption from the PV inverter based on PV generation forecasts to prevent distribution overvoltage, in case of high PV penetrations. Using PV forecasts, an imminent overvoltage scenario is predicted, while the proposed method combines a droop-based reactive power estimation method along with active power curtailment technique to prevent such overvoltage issues. The proposed technique determines a virtual curtailment threshold margin even when overvoltage is not likely to occur according to the generation forecast. In this way the performance of this method does not get hampered by instantaneous forecasting errors in case the PV forecast is much lower than the generated PV power.

- *Coordinated operation of voltage regulators with PV inverter and storage integration*

The proposed technique coordinates the operation of the smart inverter and existing VR's to reduce tap-changing operations of the VR's. For this, the VR's are controlled in a supervisory fashion where their control settings (regulation voltage and bandwidth) are adjusted while they are operating in an autonomous mode. Appropriate control settings for VR's are employed along with the forecasting based local voltage regulation technique. This way, the voltages at the inverter terminals can be maintained within predefined bounds by the inverters and the number of VR tap-changing count in a given period of time can also be minimized. Storage integration is also studied to further reduce voltage fluctuations.

2. Literature review

This chapter thoroughly looks into the past research work that has been done in the areas related to the overall methodology proposed and developed in this dissertation. The literature search is divided in two broad sections. The first section (section 2.1) highlights the research work about mitigating the impacts on distribution voltage profiles due to the growing presence of PV in the grid. The second part, section 2.2, summarizes the findings in the literature about solar PV generation forecasting, as the proposed work considers using PV power forecasts as an aid to minimize impacts of PV on the distribution voltage profile. Section 2.3 sums up the knowledge gap identified from the literature review.

2.1 Voltage regulation in presence of PV

Historically, inverters were designed and sold with real power or kW rating rather than its apparent power or kVA rating. This unity power factor operation was mandated by interconnection standards. But the rapid growth of renewables led to the need of reactive regulation from their end [12]. Subsequently, existing standards (IEEE 1547) have been revised to include the reactive power requirements applicable for distributed energy resources (DER). The voltage regulation requirement has been updated in the first amendment of IEEE Standard for Interconnecting Distributed Resources with Electric Power Systems, published in May, 2014. Under its general requirements, the voltage regulation modification is stated as- coordination with and approval of the area electric power system (EPS) and DER operators, shall be required for the DER to actively participate to regulate the voltage by changes of real and reactive power [13].

The advent of smart inverter functionalities has enabled the inverter based DER's, such as solar PV and battery storage systems, to provide reliable grid support. Some common, standard-based functions have been proposed by EPRI as a result of its collaborative effort with U.S. Department of Energy (DOE), Sandia National Laboratories, and the Solar Electric Power Association [14]. Some of these functions are:

- Remote ON/OFF
- Power factor control
- Volt /VAR support

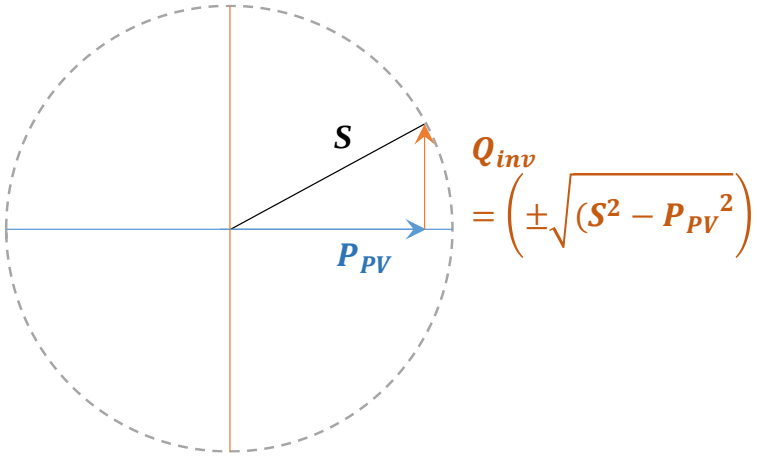

Fig. 2-1 Inverter reactive power capability model

- Volt /Watt function
- Frequency/Watt function
- Low/ High voltage and frequency ride through
- Power curtailment

Such functions allow PV or other inverter based DER's to participate in supporting the grid. As a result, similar functionalities are being set as general interconnection requirements for smart inverters. For example, California Public Utilities Commission (CPUC) has put forth some requirements termed as 'Electric Rule No. 21' for utilities. Under this rule, protective functions like over/under voltage trip functions, and preventing unintended islanding are defined. In the category of 'prevention of interference' functions, dynamic Volt/VAR operations, fixed power factor, low/high voltage ride-through etc. have been specified. Such as, for Pacific Gas and Electric Company (PG&E), a smart inverter is required to operate dynamically within a power factor range of ± 0.85 for larger (>15 kW) systems, and ± 0.9 for smaller systems (≤15 kW), down to 20% of rated power, based on available reactive power. Also, the inverter should be able to consume/produce reactive power to increase/decrease line voltage [15]. These requirements were expected to be effective from July 2016. Apart from reactive compensation, real power curtailment has also find its way in revised grid codes. For example, Germany revised its Renewable Energy Sources Act in 2012 to oblige new PV installations (> 30 kW) to allow remote curtailment [1].

Inverters are capable of operating as a four-quadrant converter, as explained by Fig. 2-1. PV inverters can supply reactive power according to its instantaneous real power output (P_{PV}) and

rated capacity. The inverter can dispatch reactive power (Q_{inv}) as long as the real power generation does not reach the apparent power rating (S). This concept is described in the Fig. 2-1 with a phasor diagram [16]. So, when the PV generation is at its peak (near mid-day), there will not be enough reactive power to be dispatched from the inverter, unless the injected real power is less than the maximum available power or active power curtailment takes place.

Distribution voltage regulation in presence of PV has therefore been a well-researched topic for the past decades. Several authors talk particularly about overvoltage problems due to PV's [17-21]; while others reported how the voltage related issues can be solved when Distributed Generation (DG) units proliferate in the network, in general [22-24]. Some papers like [24, 25] focus on inverter-based DG's for voltage control, which could be applied to solar PV systems. Along with controlling real/reactive injection to the grid at the inverter POI, external devices like energy storage [26-28] or supercapacitors [29] have also been considered in the literature for voltage control purposes.

Voltage regulation methods realized via PV inverter with/without other voltage control devices are discussed in the following section with respect to the design approaches, i.e. centralized or decentralized or their hybrid variants.

2.1.1 Centralized regulation schemes

Centralized control schemes, as found in the literature, take into account the whole network in question and optimizes the overall performance of the network by fulfilling specific objective functions. In [30], the authors talk about three inverter control strategies- optimal reactive power control with rated capacity, optimal reactive power control with increased inverter capacity, and optimal reactive power control and active power curtailment with increased inverter capacity. A centralized feeder controller in their system takes in all the collected data and based on the network status it decides upon what kind of control option (among the aforementioned three) to realize, and the optimal set-points for the individual inverter is passed along. Underlying assumption for this study is that, wide-spread two-way communication infrastructure is available and accessible for the inverters.

Similar network-wide optimization is conducted in [31] where the authors modeled rooftop PV units into a LV feeder and optimized their real and reactive power injections. They proposed a

systematic and unified optimal inverter dispatch problem which is formulated with a cost function consisting power losses, active power curtailment from PV, and voltage deviation from average. Like it was mentioned in [30], this paper also assumes that the calculated real and reactive power set-points (from the Optimal power flow (OPF) results) would be conveyed to the inverters via communication link. In their case study, the number of feasible options increase exponentially as the number of houses or PV systems increases, making the original nonconvex problem burdensome for real-time optimization. So the authors derived a computationally affordable, convex reformulation and made it efficiently solvable within the order of sub-second. Such semidefinite relaxation techniques were also applied in [32] for an unbalanced three-phase distribution network to perform OPF based energy management problems. Formulating the network voltage control as an OPF problem is also presented in [33]. The objective function in this work not only minimizes line and inverter losses, it also minimizes energy consumption by including Conservation Voltage Reduction (CVR) technique. CVR works on the principle that, an acceptable voltage band can be operated in the lower half of the band without causing any harm to consumer appliances and producing considerable energy savings [34]. But CVR highly depends on network topology and nature of load and suits best for constant impedance loads (like incandescent lighting loads) since their energy consumption is directly proportional to the terminal voltage [35]. The authors in [33] modeled one of Southern California Edison's (SCE) distribution feeder which had a large 5 MW PV system installed far from the substation. This analysis suggests that there exists a tradeoff between line loss and CVR, as a higher voltage level would reduce line loss but increase energy consumption for the CVR part. An optimal tradeoff was found by the solar output, total load and voltage constraints.

Unlike [30-31], T. Senjyu et al. implemented a centralized control scheme in [36] with other voltage control devices like load ratio control transformer, step voltage regulator, shunt capacitor, shunt reactor, and static VAR compensator. The operation of each device is determined with an objective function given by weighted sum of voltage deviation in all nodes and total losses. They use genetic algorithm (GA) to optimize the voltage profile as it is described to be a fast-paced technique to achieve approximate solution. Tabu search (TS) was combined with GA in another similar work [37] which is an extended local search algorithm. This [36] is an early work discussing optimal distribution voltage control which does not consider DG unit as a participant of the scheme. Their case study on a residential distribution circuit with line capacity of 2500 kVA

provides that, when all the devices are considered, a large voltage margin can be taken on. This work too assumes that communication infrastructure is widespread, so that the decision parameters (on-off status for shunt capacitor and reactor, capacity of static VAR compensator and tap location of step voltage regulator) can be sent to the devices. Later, this approach was illustrated further in [38] with the application of PV inverters as a source to provide reactive power support along with tap changing transformers. This work pitches two control strategies against the conventional method of tap change operation (line drop compensation). The first strategy operates with fixed reactive power from inverter and optimizes the tap position to keep the voltage deviations in all nodes at minimum; while the second one is a coordinated method which treats both tap positions and reactive output from PV as variables. Along with reducing the voltage fluctuations, these methods also reduced the required number of tap change operations; the latter method providing the better results between the two.

The optimization methods to employ real-time centralized voltage control schemes are often computationally burdensome. So, deriving optimal schedule ahead of time also provides a lucrative option to utilize the untapped reactive power capacity of the inverters. For scheduling the optimal control references, predicted values of demand and PV generation or solar irradiance are used by researchers [39-41]. In [40], voltage references of the PV inverters and the tap position of the transformers are optimized according to the day-ahead forecasts given by a Fuzzy theory based prediction method. But on the day of operation a re-optimization is also conducted so that the forecasting errors could be corrected. Such re-planning method to utilize updated values of solar generation forecasts was not considered in the earlier version of this work as reported in [41]. On the other hand, authors in [39] assumed that the forecasting errors are random vectors and follow a Gaussian distribution. These works mostly discuss about the optimization techniques which use PV forecasts but do not delve into the details about how the forecasting techniques can be integrated directly with the voltage control methods if shorter timescale is to be considered.

2.1.2 Distributed or decentralized techniques

In decentralized or distributed control approaches no central decision making method is applied. Thus, such control methods can operate with little or no data exchange among its components. Reference [42] discusses about a decentralized method where the ultimate objective is to achieve optimal solution by taking local information into account. A database is created by iteratively

calculating optimal voltage control references for randomized load/generation scenarios. After that, the correlations of the available local information (like terminal voltage or phase angle) and corresponding optimal reference are analyzed. Weighing factors are derived from this analysis and then optimal references are derived using the weighted sum of local information or measured data. This concept of decentralized optimization based on local measurements is also expanded in [43]. Objective of the optimization problem here is to minimize voltage deviations by controlling reactive injections from DG. While the discussion in [43] mostly revolved around DG in one location, [44] focuses on multiple DG's which are connected through a communication channel, but do not talk to any common 'center'. Thus the active and reactive injection by each DG and their node voltages are known to all DG's. Among them, the one with highest network impedance (as seen from the DG node) is chosen to increase/decrease its reactive injection or curtail real power injection in order to keep the voltage within limit.

In [45], the authors mention identifying a decentralized control algorithm that minimizes line losses and voltage deviations by optimally dispatching the reactive power of PV inverters. Again, like [42], correlation between optimal reactive injection and locally observable voltage measurements (for distributed PV sites) is utilized to employ the optimization technique without any dedicated communication infrastructure. For the sample case study, the derived local control law performed within close vicinity of the central optimal solution. Reference [46] also examines a form of distributed Volt/VAR control with distributed rooftop PV inverters, which can be considered as similar control operation realized at capacitor banks located along the feeder and transformer tap changers. A piecewise linear droop characteristic between the reactive power injection and the voltage magnitude at the PV inverter terminals is assumed here [46].

2.1.3 Coordinated regulation strategies

For coordinated regulation schemes, exchange of measurements and device status data need not always be real-time; hence the presence of two-way communication infrastructure is not mandatory. These coordination schemes, as suggested by the literature review, consider the operational aspects of other voltage control devices and chalk out the set-points of the DG units accordingly, and coordinate with them in an offline fashion. Other types of schemes which assume the presence of the communication layer, update their decision parameters (like P/Q/pf set-points of inverter(s) or tap positions of VR's) and coordinate with the intended devices on real-time basis

or in a periodic manner. Coordination can also be performed with the assumption of one or more control element running in their respective autonomous operation modes. Some of the works are cited in the following table (Table 2-1) about coordinated strategies for voltage control when PV or other DG units are present.

Table 2-1 Literature search on coordinated voltage control strategies

Brief summary	***Case study, Devices and PV/DG specs***	***Technique***	***Comm. Network***
This work considers coordinating the operation of OLTC's and static VAr compensator (SVC's) while PV units are present in the unbalanced system. Here the coordination is formulated as an optimization problem to minimize the energy losses. A two-stage optimization is done here- first stage requires day-ahead forecasts for load and generation which reduces the search space for the following stage; and in second stage a local optimization is conducted with present load and generation values (either measured or forecast). As their study focused on unbalanced system, they analyzed uniform (same setting in all phases) and non-uniform operation for OLTC's and SVC's. The authors also discussed how the method would perform when cloud transients happen. For the case study discussed they found out that their proposed method could solve the optimization problem with very short term forecasts and provide tap-change commands (might require very fast steps of switching to account for the voltage transient) to OLTC.	Modified IEEE 123 bus system is used here. The authors considered different load profiles- residential, industrial and commercial. OLTC and SVC; no control was performed on PV- neither any reactive injection from PV, nor any real power curtailment. A PV unit is installed at every node with a constant power load (capacity of 50% of peak load at that node) for simulating high penetration scenario. PV's are modeled as negative loads.	Optimization performed in two-stages with mixed-integer nonlinear programming (MINLP) formulation. [47]	Needed

The authors proposed a coordination method in this paper which is based on the combination of the concepts of line drop compensation, control zones and selecting operational set-points for voltage regulators (reference voltage, dead band, time delay). This method aims to provide reasonable recovery time for system voltage and also minimize the required number of operations for the active control devices. While designing the controller for the DG it is assumed that the DG can inject variable amounts of real and/or reactive power to the grid. The time delay parameter for the DG controller is set in such a way so that OLTC operation has more priority than DG and DG would only come into action when the OLTC cannot compensate for the voltage error (for the boundary bus between the control zones of OLTC and DG) fully.	The case study looks into a part of a distribution network of Aurora Energy, which is a distribution utility in Tasmania. The main feeder is 48 km long, has 1.0136-MVA load and 69 load buses. The example of coordination between OLTC and DG is discussed. Generic schedulable DG's (like diesel or gas) are talked about here only but might be applicable for PV with smart-inverter functionalities.	The voltage regulation issue is not formulated as an optimization problem, rather control zones are defined for OLTC and DG in a way so that both have equal priorities. Unnecessary waiting time is reduced as the OLTC and DG controller blocks are designed separately. [48]	Not needed
This work uses voltage sensitivity as an index to coordinate the relation between reactive power and corresponding feed-in power of a PV system in a radial grid. In the active power dependent method, the required reactive power injection is taken as a function of the local active power of a PV system. The authors define a threshold value for active power above which the PV system starts to consume reactive power linearly to regulate the voltage. Voltage sensitivity matrix is employed to coordinate the slope of this linear relationship and active power threshold among PV	As a case study, a utility grid located in Northern Jutland, Denmark, is used. This grid consists of 8 feeders and 35 buses. High penetration of PV is assumed where 24 PV systems with four different nameplate powers are unevenly distributed throughout the feeder. The PV	The technique used here relies on the reactive compensation from inverter which is expressed as a linear function of real generation. Parameters which characterize this linear relationship are	Not needed

systems to regulate either the target bus voltage or the overall voltage profile. Prior analyses are needed to build the sensitivity matrices from running load flow under extreme conditions. The parameters for each PV units were determined from these sensitivity matrix entries. In the study, non-identical active power threshold values were used which proved to improve the inverter loading problem but at the expense of more reactive consumption.	systems are of 15, 20, 25 and 30 kW of size. Voltage regulation was only done by means of PV units, no other device was considered here for voltage regulation purpose.	the slope factor and threshold values; which are calculated based on the voltage sensitivity of the PV bus. [49]	
This work proposes a coordinated control algorithm which tries to maintain an optimal voltage profile before and after PV systems are connected to the grid. From the problem formulation perspective, it's a centralized algorithm providing optimal set-points to all the control devices including PV. The PV controllers adjust the power factors in this case through an iterative process to reduce the voltage deviations from the desired value. These desired value of node voltages are calculated by disconnecting the PV's from the network and controlling the voltage only with other automated devices. The work includes varying levels of PV penetration to evaluate their proposed technique. For the given case study, the proposed method was able to mitigate the voltage rise caused by PV penetration. Losses were found to decrease for 10% and 20% penetration, but was on the gain when the penetration level reached 30%. The steps taken by	The circuit model used as a case study is derived from actual data for a circuit in Michigan. It serves 2751 residential customer and 111 industrial customers. Voltage control is achieved with two sets of voltage regulators and switched shunt capacitors. 1000 kW PV generators are considered here with three penetration scenarios: 10%, 20% and 30%.	Overall coordinated algorithm first calculates the optimal operating schedule without PV. Afterwards the controllable PV's are coordinated to adjust their pf's to minimize the deviation from the optimal schedule in terms of losses and steps taken by the automated devices. [50]	Needed

voltage regulators would steadily increase as the penetration level goes up, but the proposed method reduced the switching steps significantly.			
This piece of work was published when active management of DG's was still a new concept. It discusses about a distribution system management coordinated controller employing OLTC regulation with optimal reactive injection from DG's. Before proposing the actual controller, the impacts of increasing DG penetration on passive network voltage regulation were visited. Their control structure works with two blocks- distribution state estimator and coordinated controller. The controller takes voltage range and estimated voltages as inputs. OLTC tap commutation command is determined from these inputs as necessary, while keeping the reactive power exchanges with DG to an optimum. DG power factor control then aims at the loss minimization.	Realistic radial distribution network with two feeders is used as a sample network here. One feeder has low DG penetration (7.80 MW of DG compared to 15.50 MW of load); and the other one with high penetration (30.15 MW of DG with 12.70 MW load). OLTC control is discussed here along with controlled real and reactive injection from DG.	Coordinated controller decides on tap change variable for OLTC and reference phase angle for DG's. On the DG end, reactive power injection is controlled locally based on its active generation. [51]	Needed
This paper features DG management integration to a decentralized, adaptive zone-based Volt/VAR control based on other controllable devices like OLTCs/voltage regulators (VRs), shunt capacitor banks and distribution static synchronous compensators (DSTATCOMs). The control schemes included in the proposed method follow predefined control hierarchy like a centralized controller. In that hierarchy,	Modified IEEE 34 node test feeder is divided in couple of zones to apply the proposed adaptive zoning method. DG's are added in different locations to illustrate how the critical node voltage is improved with the coordinated	Coordinated control proposed here follow a hierarchy that, DG operation is prioritized if it is located in the same distance as other voltage	Needed

the closest DG (from the critical node where voltage limit violation occurs) should regulate first to minimize reactive power flows. Adaptive zoning is applied to keep the control actions as local as possible and only combines as many adjacent zones as needed to resolve the voltage deviation. Although this design is modular, the method requires extensive control and communication technology throughout the whole network.	control. The case study includes OLTC, VR's, capacitor banks and distribution static synchronous compensators (DSTATCOM's). DG units are characterized with controllability in real and reactive injection.	control devices. Otherwise, the closer the control device to the critical node, the higher the priority for its operation. [52]	
Detailed impact of PV on VR's and OLTC is discussed in this work. To minimize these negative impacts, an optimal reactive power coordination strategy is proposed in this paper. This optimization is based on the assumption that, the one day ahead forecasts for load and PV generation are known with sufficient accuracy. The objective of the optimization function is to keep the operation of VR's and OLTC at minimal, along with preventing VR runaway situation. VR runaway situation arises when it fails to control the voltage at the target bus even after reaching the lowest/highest tap limit. The VR operation is kept autonomous while the PV and OLTC are updated through the communication links with the set-points to account for the daily variations in irradiance and load. Another variants of the work are described in [53, 54], where the VR operation is controlled to accommodate for PV output variation.	Case study presented in this paper is based on the UK Generic distribution system which has 95 buses (11 kV). The illustrations reveal that the net load is about 2.1 MW while there are two PV plants each having 1 MW capacity. Operation of OLTC and VR's are considered in this work with controllable PV.	The objective of the optimization problem is to minimize the total number of tap operations over the 24 h period. The authors consider constraints about current balance, voltage limits, branch flow/transform er capacity, and inverter ratings. Primal-dual interior point technique is employed here to solve	Needed

Likewise, the work presented in [53] changes the VR tap positions according to its estimation of PV output with the insolation sensor. Instead of operating the VR's in line drop compensation mode, [54] assumes that any voltage violation is communicated to the VR controller for actuating the motor to change its tap position.		the optimization problem. [55]	
This paper talks about the use of droop-based active power curtailment techniques for overvoltage prevention in radial overhead residential suburban LV feeder for roof-top PV units. These droop parameters need not be updated dynamically. Two types of designs were considered here- one with same droop parameters for all houses/inverters, other one with different droop parameters (based on voltage sensitivity of the system obtained running a Newton–Raphson load flow for the backbone of the LV feeder) so that the curtailed power can be shared equally among inverters. Such sharing allows all the houses to collectively control the feeder voltage [20]. In that case the houses closer to the transformer were able to export full PV power available even at maximum net power generation scenario.	The sample system has an LV feeder with total 12 houses connected to a 75 kVA transformer. Each house has a building integrated photovoltaic thermal (BIPV/T) rooftop system, capable of generating 22 kW of thermal energy and 8.4 kW of electrical energy. No other voltage control devices are considered for this study.	Droop based control assumes a linear function between the active power to be curtailed (from maximum available PV output) and voltage correction to be achieved. The slope or droop parameter for this relationship is derived from first order voltage sensitivity analysis. [19]	Not needed

2.2 Solar forecasting

2.2.1 Approaches or techniques used

PV generation is highly dependent on weather conditions, namely insolation and ambient temperature. Wind velocity and wind direction also influence PV output to some extent [56]. PV forecasting method can be broadly divided into two categories- physical or statistical. Physical approach is the one where a 'performance model' of the particular PV system is used deterministically, whereas in statistical approach historic dataset are used to train the 'forecasting model' with little or no reliance on PV models [57].

The physical forecasting method uses a model similar to Fig. 2-2 with the exception of using weather 'forecast' data to provide PV generation 'forecast'. For the statistical method, a past set of measurements are used as training dataset and numerical analyses are performed on it to develop a 'forecast model' (example: autoregressive (AR)/artificial neural network (ANN) model) which can predict future PV generation based on numerical weather prediction (NWP) data [58]. Hybrid forecasting methods are developed utilizing both physical and statistical forecasting approaches.

Among the statistical methods, machine learning and time-series methods have been in vogue among researchers, in recent years. The forecasting accuracy for machine learning methods increase as the size of the training dataset grows. Statistical approaches follow the well-known time series methods that are based on the assumption that the data have an intrinsic periodic structure (daily/seasonal) [59].

Machine learning based forecasting models are discussed in literature regarding irradiance and consequent PV power forecasting for short to mid-term scenarios. In depth literature study reveals that the Neural Network (NN or ANN) based techniques are mostly focused on in the recent works. ANN is an information processing paradigm inspired by the way human nervous systems processes

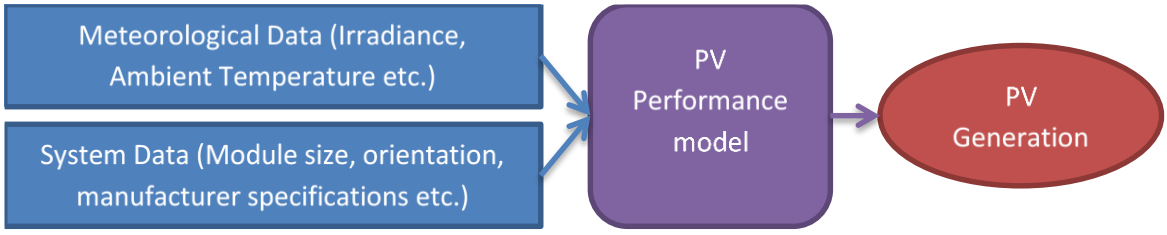

Fig. 2-2 Schematic of a physical PV model [57]

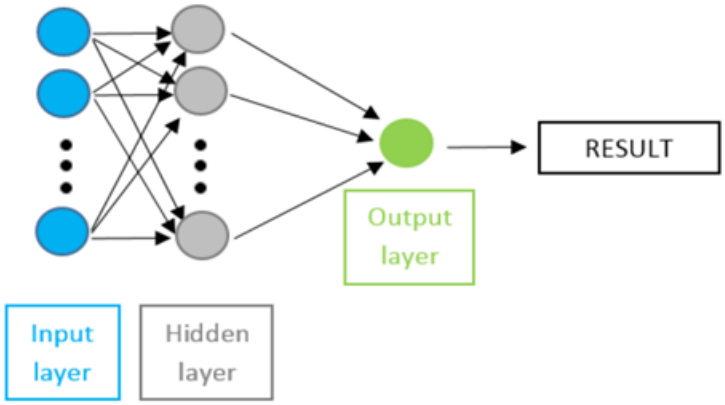

Fig. 2-3 General approach for ANN [61]

information. A large number of highly interconnected processing elements (Neurons) working in unison to solve specific problems construct the uniqueness of this network. ANN can learn from the examples and hence it is configured for a specific application, such as pattern recognition, through a machine learning process. ANN applications are developed by many researchers to successfully model solar radiation and other weather data and thus these can improve typical statistical approaches [60]. Fig. 2-3 shows the general morphology of an ANN, which pretty much resembles the way a biological brain accomplishes a particular task or deals with a function of interest [61]. Brief explanation about the types of ANN's and other methods used in solar forecasting are stated in section 2.2.2.

Variety of machine learning techniques are applied in [62] on historical National Weather Service (NWS) weather forecasts and these are correlated to generation data from solar panels. The models discussed in this paper are developed using linear least square regression as well as support vector machines (SVM). They conclude that models derived with SVM's with Radial Basis Function (RBF) kernels make a promising way of increasing accuracy in solar power prediction. Six weather metrics (temperature, dew point, wind velocity, sky cover, precipitation, humidity) are used to provide short-term forecasts (3 hours in the future) in this work. In [63], authors also show that RBF based ANN models provide superior performances compared to AR and local linear regression (LLR) models. Irradiation, temperature, and wind velocity are utilized as the input information to a NN proposed in [64] to estimate the maximum power generation from PV module. In [65], four NN techniques were discussed for 24 hour ahead solar forecasting for a 20 kW system. Another SVM model is presented in [66] which takes into account weather condition based classification (cloudy, foggy, sunny, and rainy). Here, based on the one-day ahead weather

forecast, the weather type and condition are selected, after which the related SVM forecasting model is chosen to forecast the one-day ahead power output in 15-minute resolution. Weather clustering is also emphasized in [67] where the authors show that for their case study concerning a wavelet based NN method, the root mean square error (RMSE) is 9.49% higher if no such clustering is done. Unlike most of the papers, [68] uses the input of irradiance and day of the year to solve a problem of one day-ahead forecasting of solar energy production. Their training window is 15 days. The width of this window warns the network about the temporal context or presence of a specific season. ANN based solar forecasting can also be integrated to home energy management systems (HEMS) as well, as depicted in [69].

Time series based forecasting models which deal with stochastic properties of the generation/irradiance data had also been investigated by other researchers, besides machine learning methods. Based on historical data; pattern identification, parameter estimation, and model checking are utilized to make a mathematical model of the forecasting problem [70]. Examples of such models are autoregressive model (AR); moving average model (MA), autoregressive moving average model (ARMA), auto regressive integrated moving average model (ARIMA). In [71] the authors mention that an ARMA model is preferable over Persistence model for short and medium-term prediction on a micro-grid level. A seasonal ARIMA (SARIMA) model that may incorporate short-term solar radiation forecasts derived from NWP models is discussed in [72] along with two ANN models with multiple inputs for the day-ahead and intra-day forecasting of grid-connected PV power plants (in Greek power systems). A modified AR model where NWP are used as exogenous inputs besides lagged observations is evaluated in [73]. This work concludes that ARX outperforms naive solar predictors like Persistence, Diurnal persistence, Diurnal mean model.

Hybrid models combine two or more separate forecasting methods to improve the prediction accuracy. [74] describes a hybrid method where ten very widely used regression techniques are tried on local datasets for ensemble generation. The hybrid algorithm presented in [75] uses a combination of a data filtering technique based on wavelet transform (WT) and a soft computing model based on fuzzy adaptive resonance theory mapping (FA) network, which is optimized using an optimization technique based on firefly (FF) algorithm. The authors state that their model provides superior performance compared to other individual and hybrid ANN based techniques. An alternative approach combining a self-organizing map (SOM), a learning vector quantization (LVQ) network, the support vector regression (SVR) method, and the fuzzy inference approach to

make 1-day ahead hourly forecasting of PV power generation is presented in [76]. In the forecasting stage, the authors use six SVR submodels regarding the weather type for the day.

The weather dependence of solar power can be empirically modeled by following a physical approach, if not deterministically. Physical modeling helps to understand which weather information is pertinent in solar power calculation. Mostly the irradiance and module temperature are used to output solar power in statistical analyses. Another necessary parameter is the cloud cover which can be superimposed on a clear-sky model to generate better forecasts. A clear sky radiation model is used in [77] based on Hottel's [78] atmospheric transmittance relations. This work uses the clear-sky radiation data and weather data obtained from public website to train the Nonlinear Autoregressive model with Exogenous inputs (NARX) based forecasting model. Huang et al. considers both the performance model of a PV cell and the position of the Sun [79]. The defining parameters of a physical model are site-specific and can be determined from historical data. Correlation coefficients of PV output power and other weather parameters are reported in [80] for a PV park, located in Southern Italy (University of Salento campus).

Measurement based dynamic prediction methods like Kalman Filter (KF) approach has also been discussed by some researchers, besides statistical methods and physical models. KF refers to an algorithm that uses a series of measurements observed over time, containing noise (random variations) and other inaccuracies, and produces estimates of unknown variables that tend to be more precise than those based on a single measurement alone. Fig. 2-4 briefly presents the concept of recursive process of KF as an algorithm [81].

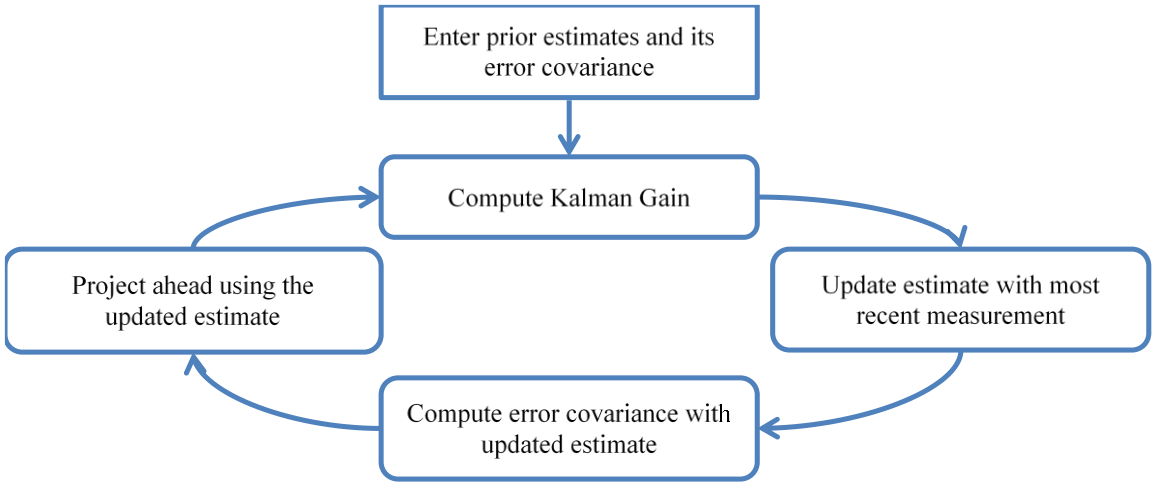

Fig. 2-4 . Basic schematic of a Kalman Filter loop [81]

Here, the Kalman gain changes in every time step and is calculated by processing discrete measurements in an optimal fashion, so that the estimation error can be minimized.

Hassanzadeh et al. uses KF approach to predict the irradiance for a plant at a utility company [82] for different sampling periods. KF technique was also adopted by Chaabene et al. in [83] to propose a methodology for dynamic forecasting of meteorological parameters. A similar model was discussed in [84] which predicts a solar generation on medium and short-term bases as a function of solar irradiance and ambient temperature (for a 1 kWp PV panel established in Northern Tunisia) considering their values during the day before. For this work, climatic parameters models are adjusted every five minutes on the basis of their acquired values and of the last prediction errors calculated, in order to perform a next prediction. The author here used an ARMA model linked to KF. This work reported that, due to the instability of weather, the error rate increases in the cold season compared to the hot season. In [85] the authors use KF based predictor for 1-minute interval data from two solar power installations with identical equipment (in Fayetteville, AR), each rated at 13 kW and featuring remote internet monitoring of output power, for 15-minute ahead forecasting. This multiple rate KF based predictor used historical data correlated with daily and seasonal variations. The authors evaluated two designs for this predictor. Statistical mean values were weighed more than the measured ones in one design and vice versa for the other. Reasonably, the latter design provided more accurate forecast when sudden changes were observed, such as for a partly cloudy day.

Short-term irradiance variation occurs mostly due to cloud movement. Tracing the cloud movement thus can prove to be of great aid to solar forecasting tools. Projecting the future location of moving clouds and integrating it to forecasting model is at its nascent stage for short-term solar generation forecasting scenarios. Hemispherical sky imager based forecasting was implemented in an experiment conducted in the microgrid of 42 MWp located in University of California, San Diego [86]. The authors concluded that the accuracy of the method was limited by the shortcomings of the sky imager used. However, they also deduced that short deterministic forecast horizons were feasible with the method, which were practically impossible with satellites or NWP's. Satellite-derived images were used in [87] for 1-6 hours ahead irradiance forecasting. The authors relied on pixel-specific cloud motion determination for several locations spread throughout the US. One corollary of this study was that, the accuracy of satellite models might not be improved dramatically by increased image resolution for short-term forecasting. Even though the concept of

cloud motion detection seems lucrative to better the accuracy of minutes ahead forecast, the pre-processing of large dataset might make it difficult to implement. For moderate temporal (few minutes ahead) and spatial scales (few kilometers), accurate prediction of the extent and motion of deforming clouds is a complex task for solar forecasting applications [88].

2.2.2 Forecasting time horizons

Researchers have looked into the solar generation forecasting problem for varying timescales, because, applications of solar forecasting as a tool also differ with the forecasting time horizon. While short to medium-term solar generation forecasts can address the concerns for the network operation, long-term forecasts can aid unit commitment and scheduling [89]. Commonly used terms, i.e. short, medium, or long-term, describing the forecasting horizon do not have any global definition. Nevertheless, as identified in [90], most of the researchers broadly consider few hours ahead forecasts to fall in the short-term category; whereas minutes timescale falls within very short-term category [63, 91- 92]. Table 2-2 summarizes some of the notable works found in literature featuring short-term solar generation forecasts. Along with the system and respective dataset information, the techniques used by the authors are mentioned in this table with brief definitions. Most of the works reported in this table use offline dataset training. This training process involves only fixed historical records whereas; the online training makes direct forecasts using both past measurements and NWP data through online meteorological services [93]. For online applications, training or modeling time is a crucial performance index but for these offline methods forecasting errors are more suitable to evaluate the performances of these techniques. Most of the researchers rely on the following types of errors as the performance evaluation criteria:

- *Simple mean based*:
    - Mean absolute percentage error (MAPE):

$$MAPE\ (\%) = 100 * \frac{\sum_{n=1}^{N} \left[\left| \frac{P_{true}(n) - P_{forecast}(n)}{P_{true}(n)} \right| \right]}{N} \quad \ldots \quad \text{Eqn. (2-1)}$$

Here,

$N = total\ number\ of\ samples$

$P_{true}(n) = True\ or\ measured\ value\ of\ solar\ generation\ at\ nth\ instance$

$P_{forecast}(n) = Solar\ generation\ forecast\ at\ nth\ instance$

- Normalized mean absolute error (nMAE):

$$nMAE\ (\%) = 100 * \frac{\sum_{n=1}^{N}\left[\left|\frac{P_{true}(n) - P_{forecast}(n)}{P_{norm}}\right|\right]}{N} \quad \ldots \quad \text{Eqn. (2-2)}$$

All the parameters here are same as in case of MAPE except that the errors are normalized with a fixed parameter,

$P_{norm} = Fixed\ value\ with\ which\ the\ errors\ are\ normalized$

This fixed value can be a local or the global maximum of the defined period or the installed capacity of the system or the range of variation.

- *Root mean square (RMS) based:*

  - Root mean square error (RMSE):

$$RMSE = \sqrt{\frac{\sum_{n=1}^{N}\left(P_{true}(n) - P_{forecast}(n)\right)^2}{N}} \quad \ldots \quad \text{Eqn. (2-3)}$$

  - Normalized root mean square error (nRMSE):

$$nRMSE\ (\%) = 100 * \frac{RMSE}{P_{norm}} \quad \ldots \quad \text{Eqn. (2-4)}$$

The normalization value here is similar to the parameter mentioned in the preceding discussion of nMAE.

- *Correlation coefficient:*

This coefficient is a measure of how strongly the predicted values correlate (linearly) with the measured values. If the prediction technique yielded perfect results, the predicted vs measured values would provide a straight line of slope 1, graphically.

Correlation coefficient is defined by:

$$\rho_{P_{true},P_{forecast}} = \frac{cov(P_{true}, P_{forecast})}{var(P_{true})\ var(P_{forecast})} \quad \ldots \quad \text{Eqn. (2-5)}$$

Where cov(.) is the covariance operator and var(.) expresses the variance operator. Simple rearranging of the formula states that:

$$\rho_{P_{true},P_{forecast}} = \frac{N\sum\left(P_{true} * P_{forecast}\right) - \left(\sum P_{true}\right)\left(\sum P_{forecast}\right)}{\sqrt{\left\{N\sum\left({P_{true}}^2\right) - \left(\sum P_{true}\right)^2\right\}\left\{N\sum\left({P_{forecast}}^2\right) - \left(\sum P_{forecast}\right)^2\right\}}} \quad \ldots \quad \text{Eqn. (2-6)}$$

Numerical value of correlation coefficient lies between -1 and 1. For solar generation forecasting scenario, expected value of $\rho_{P_{true},P_{forecast}}$ is 1 (total positive correlation when the prediction is perfect). The closer the value to 1, the better the results of the forecasting technique.

Table 2-2 summarizes the literature review on short-term solar generation forecasting methods. As the Table 2-2 shows, in most of the cases, the papers present either mean based errors or root mean square based errors to evaluate the performance of the techniques discussed. For normalization, rated capacity value is mostly used in these works. Because these works cited here focus on varied kinds of datasets and techniques, the error rates cannot be directly compared with each other to pick a superior method. However, the table depicts the range of forecasting errors for various short-term solar forecasting scenarios. Many of these works involve more than one forecasting technique and investigate their methods from different aspects. So to keep it concise, the table only includes notable results from these works. For detailed error comparison, each of these works can be consulted individually.

Table 2-2 Literature search on short-term solar generation forecasts

Method(s)	***System information***	***Dataset description***	***Errors reported***	
			Simple mean based	*RMS based*
Radial basis function neural network (RBFNN): This form of ANN's belong to the feed-forward class based on the function approximation theory. Hidden nodes which are located in between the input and output layers contain the radial basis function or the transfer function	PV system of 18 kWp capacity; located in Huazhong University of Science and Technology	SCADA registered 5-min averages of PV generation; ***input***: time series of solar power and NWP (meteorological	Average MAPE for sunny days= 9.45%; Minimum MAPE with inaccurate weather	

(non-linear transformation). Linear transformation or supervised learning takes place between hidden and output layer. This work forms the forecasting model based on weather types- sunny, cloudy and rainy.	in Wuhan, China	services of Wuhan) on irradiance, wind speed, air temperature and relative humidity; ***output***: 24 hour ahead hourly data of PV generation forecast	forecasting = 10.50% [93]	
▪ ***Seasonal ARIMA (Autoregressive integrated moving average)***: ARIMA is a time-series forecasting technique which predicts the future values based on the inertia of its own. Seasonal ARIMA is an extension applicable when cyclic components (in this case diurnal variations) are present. ▪ ***Radial basis function neural network (RBFNN)*** ▪ ***Least squares support vector machine (LS-SVM):*** SVM is a supervised learning algorithm to solve pattern recognition problems. This method deals with a quadratic programming problem instead of gradient based formulations as ANN's do [94]. LS-SVM can solve non-linear, high dimensional problem through a smaller training sample.	Hourly aggregate PV power production data from CAISO (California independent system operator). This net production varies within around 500-2000 MW	Past PV power data; ***input*** or training set: hourly aggregate data from Dec 1, 2012- Jun 18, 2013; ***output*** or target set: day-ahead hourly forecasts for Jun 18-Jul 8, 2013	[normalized with maximum PV output in the training period] nMAE= 3.97% (ARIMA); 5.09% (RBFNN); 4.53% (LS-SVM)	[normalized with maximum PV output in the training period] nRMSE= 5.21% (ARIMA); 6.61% (RBFNN); 5.85% (LS-SVM) [95]

Back propagation neural network (BPNN): BPNN is one of the most widely used NN structures due to its simplicity. It has a generic multi-layered feedforward topology. This technique has an underlying hypothesis that, the forward pass (input layer-hidden layer-output layer) is active all the time; but the backward pass is prompted when there is something to 'learn' or a mismatch is identified. [96]	PV system in Salem, OR; rated power: 1.12 kW	Classifies the weather and train the BPNN with data from similar days within three years; ***input***: hourly PV output power, temperature, humidity, wind speed and aerosol index; ***output:*** hourly PV power prediction for the day	Average MAPE for sunny days= 3.96%; for cloudy days= 6.57% [97]	
▪ ***Multilayer Perceptron Neural Network (MLPNN):*** Such NN's are found to be applicable to approximate extremely non-linear functions and also belong to the feedforward class like RBFNN. This NN learns in a supervised manner where the synaptic weights are adjusted so that the overall error is minimized [98] ▪ ***Recurrent Neural Network (RNN):*** RNN's have one or more feedback loops. Mathematically, an RNN can possess self-sustained dynamics along their recurrent paths making it a dynamical system whereas, a feedforward NN resemble a function [99] ▪ ***RBFNN***	20 kW system in Tokyo University of Agriculture and Technology	Four climactic seasons are considered- spring, summer, fall and winter; ***input***: hourly data for vapor pressure, humidity, cloud coverage and sunshine duration; ***output***: day-ahead hourly PV generation forecast	MAPE's in the order of RNN, RBFNN, MLPNN and NNE winter: 3.98%, 3.51%, 3.93%, 2.77%; spring: 6.27%, 5.18%, 5.25%, 4.13%; summer: 7.22%, 5.76%,	

▪ ***NN ensemble (NNE):*** NNE is a machine learning technique which combines the predictions of a set of NN's after training them with individual training sets. The NNE in this work forecasts PV generation based on the average of the MLPNN, RNN and RBFNN outputs.			6.63%, 4.68%; fall: 5.83%, 4.04%, 5.95%, 3.64% [65]	
▪ ***Seasonal ARIMA (Autoregressive integrated moving average)*** ▪ ***ANN's***	Four PV plants in Greece with 0.15, 1,0.15, and 5 MW of nominal capacity	Uses hourly PV generation and radiation measurement data from Jan 1 2011- Dec 31 2012; ***input***: hourly generation and radiation data and some derived parameters; ***output***: day-ahead hourly forecasts		[normalized with installed capacity]: yearly average nRMSE (for all of the 4 seasons): 11.12% (S-ARIMA), 11.42% & 11.26% (2 ANN's) [72]
Wavelet Neural Networks (WNN): This is a backpropagation NN and takes the wavelet basis function (Morlet wavelet basis function is used in this work) as the transfer function. The authors also implement weather clustering and train the NN's according to weather type.	Grid-connected PV system of Zhejiang Global Group gold sun engineering with installed capacity of 2.2 MW	Uses generation and environmental variables for days with same weather; ***input***: temperature, humidity, wind speed, wind direction and radiation intensity;	Average MAPE for four days= 7.24%	[normalized with rated capacity] Average nRMSE for four days= 9.75% [67]

		output: hourly generation forecast		
A ***hybrid approach*** is proposed here which combines ***self-organizing map*** (***SOM***: an unsupervised, competitive learning, clustering network which sorts out one neuron in a group which minimizes the defined error criterion) network, ***learning vector quantization*** (***LVQ***: simpler structure compared to ANN with only supervised learning network and classifies input vectors based on vector quantization) {for weather classification purpose} ***support vector regression (SVR)*** {to model the classified historical data} and ***fuzzy inference method*** {to select an appropriate model among the trained SVR models}.	PV system of total 5 kWp capacity	Uses hourly averages (for generation and irradiance) from measurements recorded every 5 minutes; ***input***: weather forecasts regarding maximum temperature, probability of precipitation, and solar irradiance; ***output***: day-ahead hourly PV power forecasts	Average or mean relative error or nMAE (normalized with capacity) for May 2012- Apr 2013: 3.295%	Average RMSE for a 5 kWp system: 350.2 W (nRMSE= 7%, if normalized with peak capacity) [76]
Neural networks based Nonlinear Autoregressive model with Exogenous inputs (NARX): NARX is a class of discrete time non-linear systems that mathematically models a time-series as a function of past values of the input and output vector(s). The mapping function is unknown and is approximated through a	Grid-connected PV system in Brædstrup city, Denmark with rated capacity 4080 Wp	Uses theoretical modeling and cloud cover index to calculate irradiance instead of direct measurement; ***input***: weather forecasts	MAPE for the test set (rest of the year 2006) = 16.47% [77]	

NN. In this case, the network weights are adaptively changed according to the forecast errors. This model was trained with data for Jan 1- Jun 30, 2006. The rest of the year was used as the test set.		regarding maximum and minimum temperature, and forecast day-type along with hourly radiation values; ***output***: day-ahead hourly generation forecasts		
▪ ***K-nearest neighbors prediction (KNN)***: Authors use KNN regression model which identifies similarity of the nearest patterns, as patterns close to the target are expected to contribute more to the prediction model than those located further away. ▪ ***Support vector regression (SVR)***: SVR is a regression technique which is realized through support vector machines by solving a quadratic problem with convex objective function. But instead of minimizing observed training error, SVR minimizes generalized error bound [100]	PV station with installed capacity of 70.37 MW near Erfurt, Germany	Uses combination of past solar power measurements and NWP's.1h ahead-hourly; ***input*** NWP data for temperature, irradiance and cloud cover; ***output***: hour-ahead generation forecast		RMSE for 1 station: 6.6323% (KNN), 6.2506% (SVR) [101]

A hybrid approach combining ***wavelet transform*** (***WT***: a mathematical tool with filtering effect which is used to parameterize time-series signals with complex time-frequency structures), ***fuzzy adaptive resonance theory mapping (ARTMAP) network*** (***FA:*** a supervised model of NN family which uses feedback mechanism to learn new information without eliminating previous knowledge), and ***firefly optimization algorithm (FF***: an optimization algorithm based on flashing behavior of fireflies. Here it is used to enhance the forecasting performance of the FA network through its vigilante parameter) for different seasons	15-kW PV system located at Ashland, Oregon	Uses hourly solar radiation data and power generation; ***input***: historical PV power time-series and solar radiation data; ***output***: 1 hour ahead generation forecast for next 12 hours	MAPE for sunny day: 9.81% (winter), 11.71% (spring), 11.83% (summer), 11.09% (fall); for rainy days: 3.38% (winter), 6.31% (spring), 5.76% (summer), 6.19% (fall)	[normalized with nameplate capacity] nRMSE for sunny days: 12.51% (winter), 13.13% (spring), 12.11% (summer), 12.82% (fall) [75]

The primary reason behind the analyses of different forecasting time horizon is that, the resource variability (in this case, solar irradiance) largely varies as the time interval changes from minutes-ahead to days-ahead. In [102], Hoff et al. discussed about the spatial and temporal variation of PV output and experimentally demonstrated that the variability (within the day) decreases when hourly averages are taken instead of minute-scale measurements. Yet it would be expected that the forecasting accuracy should not suffer for a given day if the timescale changes. A good number of works addressed this issue featuring solar power forecasting problem within different time horizons. In [103], a spatio-temporal solar forecast model is proposed based on AR model with exogenous inputs (ARX). They applied their technique for both hour-ahead and day-ahead timescales. In their model exogenous inputs are historical values of irradiance (from five locations in Colorado) and cloud cover percentage from neighboring sites. The authors concluded that, for their sample data sets, the persistence method provided better results than their proposed ARX based spatio-temporal method when the forecasting time horizon was 5-minute and 15-minute. But for hour ahead scenario, their proposed method showed improvement (measured with both

MAE and RMSE) over the persistence method. Chow et al. discussed about ANN based short-term forecast of energy generated by a 40 kWp building integrated PV system [104]. The authors use a Multi-Layer Perceptron network and train it with back-propagation technique for 90% of the sample dataset. For 10 or 20-minute ahead prediction the ANN inputs are real-time dry-bulb temperature and solar radiation together with 10 or 20-minute lapse solar angles. They evaluated their technique by measuring the correlation coefficient between the measured and predicted values. They used the measurement taken in 10 minute intervals during 28 Jun 2011 to 25 July 2011, and for this dataset carried out the network training and performance evaluation processes 10 times. For the 10-minute prediction, the correlation coefficient ranged from 0.8934 to 0.9862, and for 20-minute prediction, the minimum and maximum values were 0.8186 to 0.9509. As apparent from their study, for a given confidence interval, the prediction technique provides inferior performance when it is evaluated in case of 20-minute timescale compared to 10-minute timescale.

2.3 Knowledge gap analysis

This section summarizes the knowledge gaps established from the literature search as discussed in the previous sections. For the sake of organization, these ideas are put down under different segments, which are aligned with the scope and objective of this dissertation.

2.3.1 Prevention of distribution overvoltage from the inverter end

There have been a lot of discussions about how an inverter can be used to prevent overvoltage in the distribution grid. Smart inverter functionalities have been introduced which can implement variable reactive power injection within the inverter capability [105-106]. Individual voltage control modes like RPC, APC, and variable pf control have been investigated by researchers. Most research work usually discusses one such method. But there is still scope to analyze the superimposition of more than one or adaptively changing the operation mode. For example, distribution grid is more susceptible to real power components rather than reactive power. So, curtailing real power will provide better regulation than controlling reactive power in some scenarios. Also, the load or generation scenario does not remain the same from spatial or temporal perspective within a given day. Proper selection of control techniques or combining more than one technique can be studied to find out the efficacy of the adaptive strategy.

Most of the previous works cited here does not evaluate the performance of the proposed methods with respect to growing PV penetration. This creates space for studies to be conducted for analyzing local regulation methods keeping the PV penetration in mind. Impact studies have already been considered in details for different levels of PV penetration. Similar studies need to be done for voltage regulation scenario with hypothetical increase in PV penetration level. Such studies could benefit grid planners to screen new interconnection requests.

PV inverters can control voltage fluctuations on a faster timescale because of their internal power electronic circuitry. Very short-term flickers thus might be minimized by the inverters which in turn would most likely be overlooked by traditional controllers having motor-driven step switching techniques (tap-changing operation in VR, for example). These flickers would also get worse with high PV penetration. Studies have to be conducted on how to bring these spikes within acceptable limit very fast and maintain a smooth voltage profile.

2.3.2 Coordinating local regulation schemes with existing voltage control devices

Coordination of local schemes for network-wide optimization still needs to be discussed in great detail. There are many available options and thus finding an appropriate coordination technique might be difficult. Existing devices suffer from more frequent operation due to increasing PV penetration. There is a gap to direct the coordination schemes to relieve some stress off of these devices.

Previous work cited about optimizing system-wide voltage profile (or minimizing total losses) mentions that, the optimization problem becomes too cumbersome because of detailed network model and long list of constraints to follow. Many of such problems have to be reformulated with some form of relaxation to be executed on real-time basis. Also, if very short-term operation has to be optimized, stronger processing unit has to be installed for large amount of computation. These optimization methods (mostly realized with centralized approach) calculate each control variable and communicate the set-points to the respective devices via dedicated channels. Coordinated schemes have to be investigated which decentralizes this concept of decision making but still can aim for a common goal. For example, if the optimization problem determines the bandwidth or reference voltage instead of exact tap position for the VR's, then the computation is understandably less hectic. This supervisory control has not yet been addressed in the voltage regulation problem providing optimized solutions in presence of PV. Similar concept can be applied to inverter

operation where a range is considered rather than a particular point within its capability curve. This way, the operation will be sub-optimal but still be boosted with less computation cost.

If the coordinated scheme can be deployed to fulfil a central optimization function, then there can be a quite a number of cost function options to be incorporated. Researchers mostly target on minimizing the losses. Only a few talked about minimizing voltage deviation and even fewer discussed the likes of reducing tap change operation for VR's. There is a scope to build an optimization problem which has a cost function expressed as the weighted sum of these varied objectives. By controlling the weighing factors, the grid operator can set the ultimate purpose of the voltage control. Again, changing these weights can be automated for a particular level of penetration or local load/generation trend.

2.3.3 Augmentation of the voltage regulation with solar forecasting

Some of the previous work considers that PV generation forecasts are accessible (on 6/12/24 hour ahead basis), and formulates the voltage regulation problem around the available forecast. Shorter time-scale forecasts need to be investigated to aid the coordination scheme which includes traditional devices.

The PV inverter can control voltage on a fast timescale but other devices like VR need longer time to implement a tap change command. Variable time-scaled forecasting technique is thus needed for such a coordination scheme. Also, there is a need to study the effects of updating forecast values on a coordinated voltage regulation scheme. The extent of augmentation with forecasting can then be discussed against the basic coordinated scheme which does not have any available forecasts at hand.

If realistic applications are kept in mind, it also needs to be seen which techniques can be integrated to provide short-term forecasts within reasonable accuracy. Measurement based forecasting techniques (like KF theory based one) are suitable for augmenting the voltage regulation scheme, rather than neural network based methods which require handling of large datasets. Coordination approach can be dynamically updated with short-term forecasts and based on these forecasts device operation can be optimized.

2.3.4 Very short-term solar forecasting

Much has been discussed about short-term solar generation forecasting in the literature; but most of the previous work basically focuses upon techniques used and not so much about possible applications of the forecasts. With the arrival of advanced inverter functionalities, solar forecasting can be of great service to network operators and thus help mitigate the impacts of high PV penetration. Such applications, for example, voltage regulation (to be realized at the PV inverter), might require even shorter time-scale solar forecasts (<=1 minute). Such forecasting models are yet to be addressed in the literature. Also, research work found in the literature largely concerns 'average' generation (for example, hourly average), which cannot always be effective for online applications. Instantaneous forecasts would be more pertinent to such application-driven cases.

For very short-term forecasts, the sky imaging techniques may become cumbersome as these are computationally extensive. In this case, high resolution measurements can be used through dynamic system modeling techniques like KF method. KF based prediction models are being implemented in many other disciplines but its use in solar forecasting is yet scarce. KF algorithm adaptively learns and guides itself towards minimizing the forecasting error. Besides, it also can provide multiple time-rate forecasts. So, when high resolution measurements are available, KF based forecasting models can be benefitted from them. For example, when 1-minute interval data are available, KF can supposedly attain more accuracy for hour-ahead forecasting, compared to measurements sampled every 5 minutes.

Another aspect of the forecast studies carried out in the literature is that, many of the prediction models are based on the weather classification based on available insolation. This can be ambiguous at times because there is no absolute way to define the seasons or the weather type. Some researchers consider only two seasons, while others proceed with four. Similarly, there are studies which divide the weather into sunny, cloudy and rainy classes, whereas there can be more divisions like partly cloudy or partly sunny besides these major ones. It is thus necessary to identify what kind of weather and/or season classification provides best forecast results for the intended PV system given its geographical location. Those results can be further used to develop grid-integration applications particular to the PV system.

Machine learning techniques are useful in finding patterns but hybrid models which incorporate the physical characteristics of a PV system can provide better forecasting accuracy. Therefore, it

is necessary to investigate hybrid prediction models for very short-term solar generation forecasting. ANN based techniques can take other inputs like irradiance and temperature to provide solar forecasts, but again, these might not be computationally feasible for very short-term case as it would require the handling of a very large dataset at one time. Theoretically, ANN techniques need larger dataset to attain lower forecast errors. KF technique on the other hand can be hybridized with simplistic PV performance models which again can be evaluated and adjusted in online fashion with high resolution measurements.

PV generation is variable but the variability can entirely change depending on the time-horizon. Researchers thus have discussed short-term forecasting for different time intervals, like 1/2/3 hours ahead and demonstrated the changes in accuracy levels for these forecasting windows. Similar analyses can be done for very short-term scenarios, for instance, forecasting accuracy can be investigated for 1-minute, 5-minute or 15-minute windows. These studies should be helpful for developing local inverter controls.

Measurement based forecasting techniques can suffer from erroneous data recording. It is therefore important to make the model robust enough so that it can automatically identify whether any measurement is faulted and take appropriate action to weigh it down while calculating the forecast. For this, sensitivity analysis has to be done and outliers need to be characterized. As for example, if the generation measurement is non-zero while the irradiance measurement reads zero, it is evident that either of the measurements have some error. But the same thing cannot be said about wind velocity data, because the relationship between the wind velocity and PV generation is not that straightforward.

With this robust forecasting method, very-short term generation forecasts can be formulated which would be beneficial for pragmatic applications at the PV inverter end. These applications are intended to minimize the adverse footprint of growing PV penetration on the network operation and thus enable smooth integration of PV into the existing grid.

3. Local voltage regulation by PV inverter

This chapter looks into merging the droop-based inverter reactive power compensation (RPC) algorithm and active power curtailment (APC) techniques to keep the local voltage profile within pre-defined upper and lower limits, in case of large-scale PV integration in a particular location. When PV output is high and feeder load is low, distribution overvoltage situation emerges due to reverse power flow. In such case, only RPC might not provide desired regulation. So, APC is employed to further expand the range of inverter reactive (inductive) power capability, which will yield to better voltage regulation. As discussed in [107], APC is applied only to enhance the inductive VAR generation at peak PV generation time for this study. This way the real generation is curtailed simply to facilitate lowering of local voltage and therefore utilization of solar output (real) is ensured when the reactive injection cannot sufficiently maintain the voltage profile. The performance of this technique in terms of minimizing voltage regulator operations is also discussed later.

3.1 Reactive power compensation

As inverters can control their reactive current output, they can act like static VAR compensator operating in a fast timescale. Both inductive and capacitive VAR compensation can be delivered through PV inverter. The VAR compensation, however, depends on the inverter size (VA) and its Watt output. The following section describes the development of a reactive power compensation method for PV inverter, within its instantaneous capability constraints.

- **Reactive power compensation with capability constraint (RPC)**

Generic droop-based algorithm has been in vogue in power systems, for implementing power sharing and frequency control among traditional fossil-fueled generators. The droop-based RPC algorithm relies on the static Q-V relationship which can be assumed of linear type (example is given in case study section). In a radial network, if the loads at all other locations are kept fixed, Q-V contours can be derived to represent the relationship between the node voltage and reactive load/injection. These contours will again vary as the real load/generation changes at that node. These contours can be approximated as straight lines providing a linear relationship between the

estimated change in reactive load (ΔQ) at a given bus and the change in node voltage (ΔV); and can simply be written as:

$$\Delta Q = -Kp * \Delta V \quad \ldots \quad \text{Eqn. (3-1)}$$

The negative sign in Eqn. (3-1) implies the fact that to lower the local voltage by ΔV, reactive (inductive) load needs to be increased by ΔQ. This constant gain Kp is a function of local real load, as well as load variations throughout the system. Ideally, the value of the droop parameter Kp can be determined when the real and reactive consumptions throughout the network are fixed. But in a realistic scenario this is not possible. In turn, the droop parameter will change between two adjacent time steps. As time advances this gain can thus be updated from the following derived relationship (Eqn. (3-2)), which takes into consideration the actual voltage correction achieved by the change in reactive compensation (injection, in case of overvoltage prevention) in the previous time instance:

$$Kp(i) = \frac{|\Delta Q(i-1)|}{|Vm(i) - Vm(i-1)|} \quad \ldots \quad \text{Eqn. (3-2)}$$

Here,

$Vm(i)$= node voltage (mean of three-phases) at i^{th} time instance

$\Delta Q(i)$= change in reactive injection from i^{th} to $(i+1)^{th}$ instance

$Kp(i)$= RPC droop parameter at i^{th} time instance

This estimate $\Delta Q(i)$ gives the estimated amount of reactive injection at the next time instance:

$$Q_{inj}(i+1) = \Delta Q(i) + Q_{inj}(i) \quad \ldots \quad \text{Eqn. (3-3)}$$

Where,

$Q_{inj}(i)$= reactive injection at i^{th} time instance

Positive (/negative) $Q_{inj}(i)$ denotes that the inverter acts as an inductive (/capacitive) load to the grid or absorbs (/injects) VAR. $Q_{inj}(i)$ is initialized with zero, and for this study it is assumed that, no reactive power support is provided by the inverter at night. Reactive injection capability of an inverter is limited by its apparent power rating S and is described by the following relation in Eqn. (3-4).

$$|Q_{lim}(i)| = \left|\sqrt{S^2 - P_{PV}(i)^2}\right| \quad \ldots \quad \text{Eqn. (3-4)}$$

Here,

$P_{PV}(i)$= maximum real power generated by the PV module at ith time instance

$Q_{lim}(i)$= reactive injection limit from the inverter at ith time instance

S= inverter rating in kVA

When the inverter is expected to provide VAR support to the grid, the economically optimized inverter sizing increases, but a moderate kVA size of 110% of peak PV generation (in Watts) is deemed sufficient in the literature, to allow significant reductions in losses and voltage deviations [16]. So, for this work,

$$S = 1.1 * P_{max} \quad \ldots \quad \text{Eqn. (3-5)}$$

P_{max}= maximum possible real output from the PV arrays or its kWp specification

For RPC technique, when the required estimate $Q_{inj}(i)$ cannot be provided by the inverter, the injection has to be clamped at $Q_{lim}(i)$. Thus, RPC will enable the PV system to perform voltage

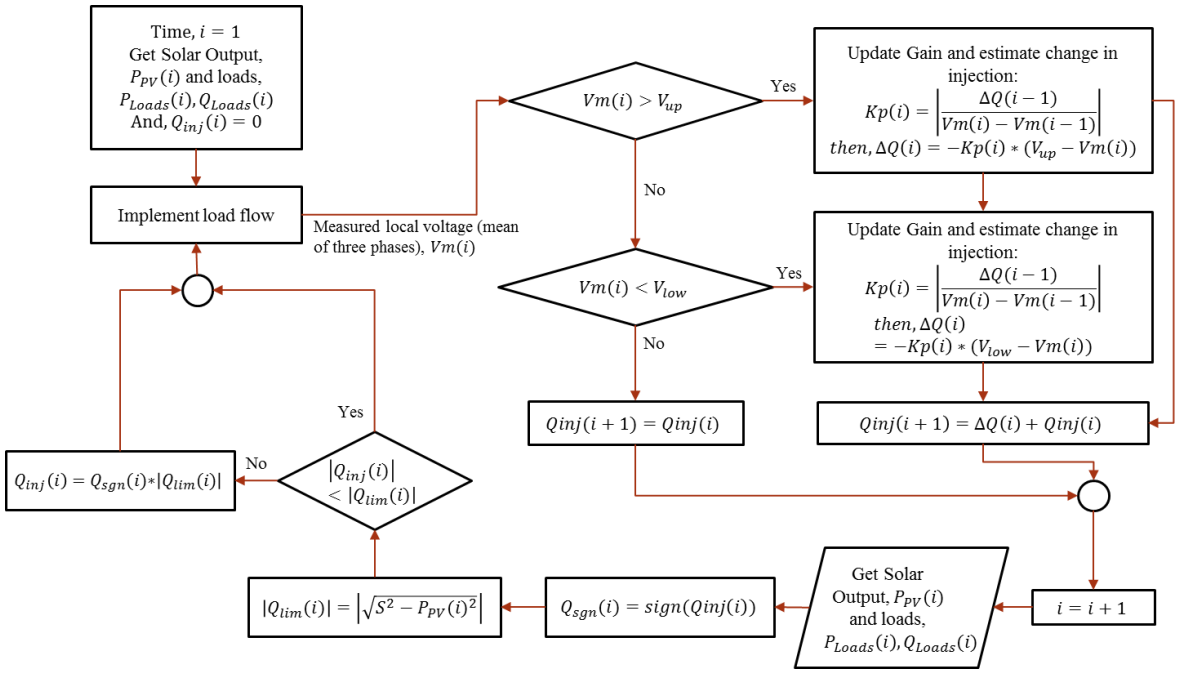

Fig. 3-1 Flow-chart of RPC technique

regulation but will not prevent local overvoltage all the times, particularly when PV output nears its peak. Time iteration for this technique is described in details in the flow chart seen in Fig. 3-1.

In this flow chart,

V_{up}= Upper threshold of prescribed voltage limit

V_{low}= Lower threshold of prescribed voltage limit

This algorithm updates the droop parameter or gain adaptively when it senses a voltage limit violation. Reactive power injection estimate is derived with this updated gain for the next time step. If this estimate is beyond the inverter capability (imposed by its kVA sizing and instantaneous real power output from PV arrays) then it injects only the available reactive power. This technique thus ensures that full real power output from the PV arrays is fed to the grid.

3.2 Active power curtailment

When the PV output is high, the local voltage would start to rise and more reactive support would be necessary to lower it. But the inverter fails to supply the adequate inductive VAR injection because of high real output. In such occasion, APC technique can be amalgamated with RPC. When APC is employed, the PV generation is not fully utilized and hence the amount of curtailment should be kept minimal.

- **Reactive power compensation enhanced with active power curtailment (RPC-APC)**

In this algorithm, the APC comes into play only when the voltage is out of the bound and the estimate required,

$$\left|Q_{inj}(i)\right| > \left|Q_{lim}(i)\right| \quad \ldots \quad \text{Eqn. (3-6)}$$

So, the lowering of local voltage is enabled by both reducing active power injection and increasing reactive power injection. The flow chart as seen in Fig. 3-2 depicts the RPC-APC algorithm implemented in this work.

As seen from Fig. 3-2, when reactive power estimate violates the reactive capability limit, a separate loop (with virtual index j) runs to determine the value of $P_{PV}(i)$ and $Q_{inj}(i)$ for which the target voltage, $Vm(i)$ would fall under the upper threshold V_{up}, while keeping the loads unchanged. To reduce the voltage, estimated curtailment of real injection is reduced gradually by:

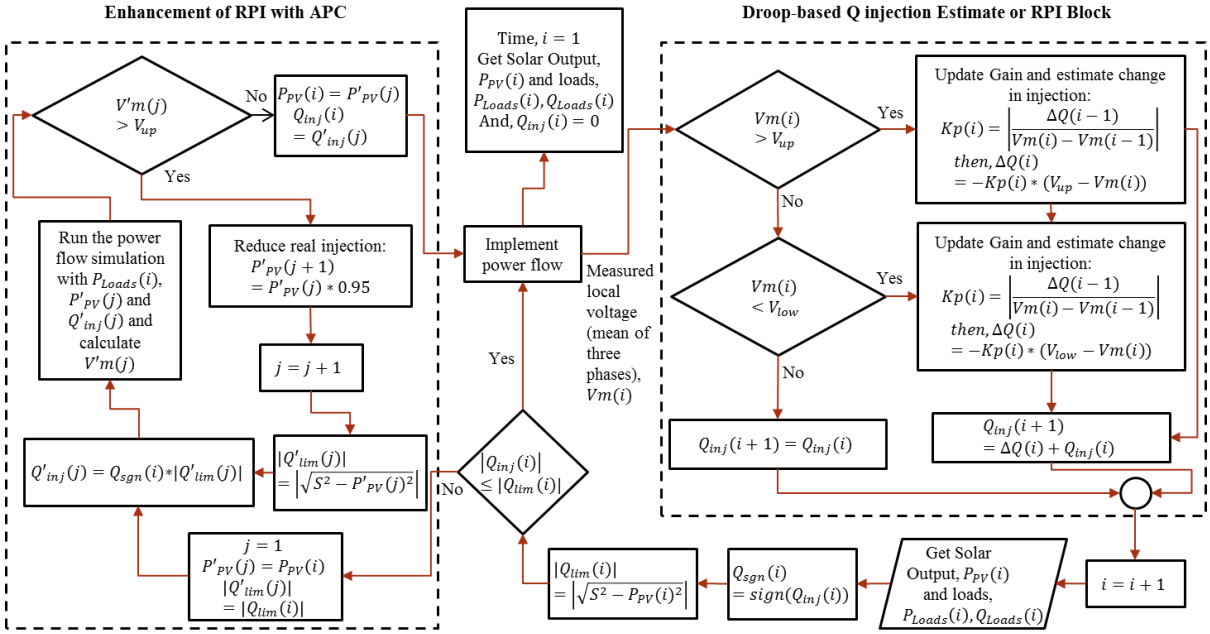

Fig. 3-2 Flow-chart of RPC-APC algorithm

$$P'_{PV}(j+1) = P'_{PV}(j) * 0.95$$

Where, $P'_{PV}(j)$ = reduced PV output at j[th] iteration of the APC loop

This reduction in real injection in turn increases the reactive injection capability of the inverter and thus the limit is pushed to,

$$|Q'_{lim}(j)| = \left|\sqrt{S^2 - P'_{PV}(j)^2}\right| = |Q'_{inj}(i)| \quad \ldots \quad \text{Eqn. (3-7)}$$

Here,

$|Q'_{lim}(j)| = |Q'_{inj}(i)|$ = increased magnitude of the reactive injection limit for i[th] time instance

Once the target voltage is within the upper voltage bound, the real and reactive injections are updated and used in the power flow implementation.

3.3 Case studies and discussions

The numerical analyses under this work are performed on modified IEEE 34 node test feeder system (Fig. 3-3). The substation transformer for this test feeder has a rating of 2500 kVA. Three different locations are considered for placing the PV plant for this study: close to the substation (will be denoted as L-ss) or at bus 812, midway in the feeder (will be denoted as L-mid) or at bus

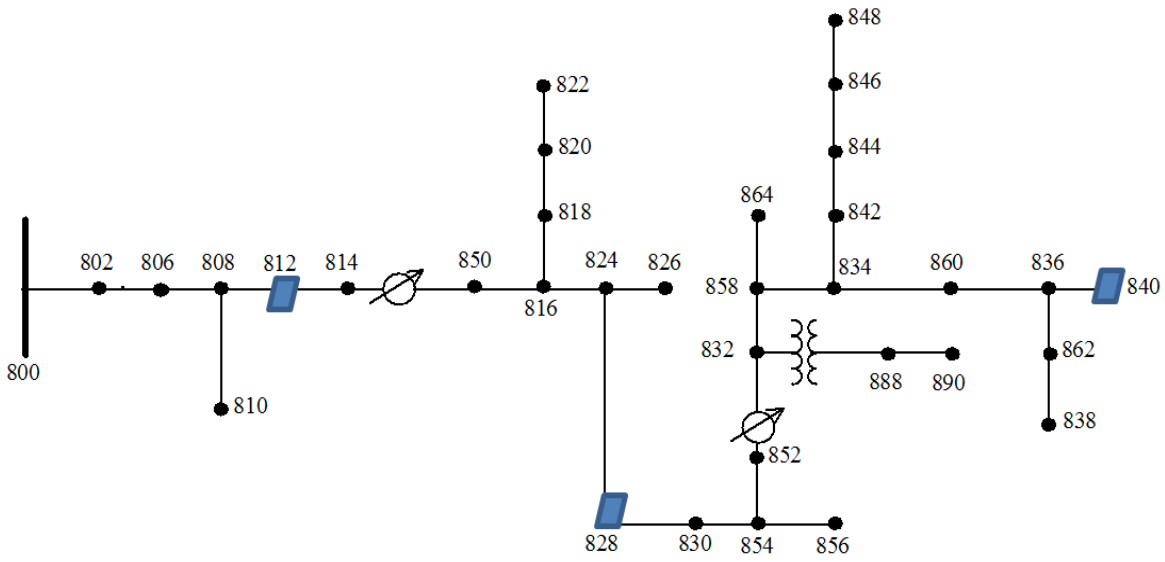

Fig. 3-3 Modified IEEE 34 node test feeder

(Blue boxes represent different locations for the PV system)

828, and at the end of the feeder (will be denoted as L-end) or at bus 840; as depicted by blue boxes in Fig. 3-3. Besides analyzing different locations, two different sizes of the PV system (750 kWp and 1000 kWp) are also considered here. Different kWp sizing of the PV system are studied here to analyze how the voltage regulation techniques perform with varying levels of PV penetration. The network is modeled in OpenDSS and the subsequent calculations about real/reactive injection are conducted in MATLAB.

The daily load profiles used here are based on data from a substation transformer which feeds mostly residential and commercial customers in the Northern Virginia area. 7049 residential, 316 small commercial and 133 large commercial buildings are fed by this distribution transformer. The PV output profile is generated based on 15-second interval data collected from the 6.4 kW rooftop PV system at VT-ARI. Individual spot loads at the test feeder are perturbed with Gaussian distribution with a mean resting at scaled base load (given by the test feeder configuration) and with a standard deviation of 5%, to synthesize a realistic net load profile of 1-minute resolution. The distributed loads are calculated from the scaled base values. Studying the prevention of overvoltage due to PV integration is most likely to obtain vivid results when the feeder load is low and PV generation is high. So, the days (Figs. 3-4 and 3-5) were chosen in the month of April when the residential load tends to be on the lower side.

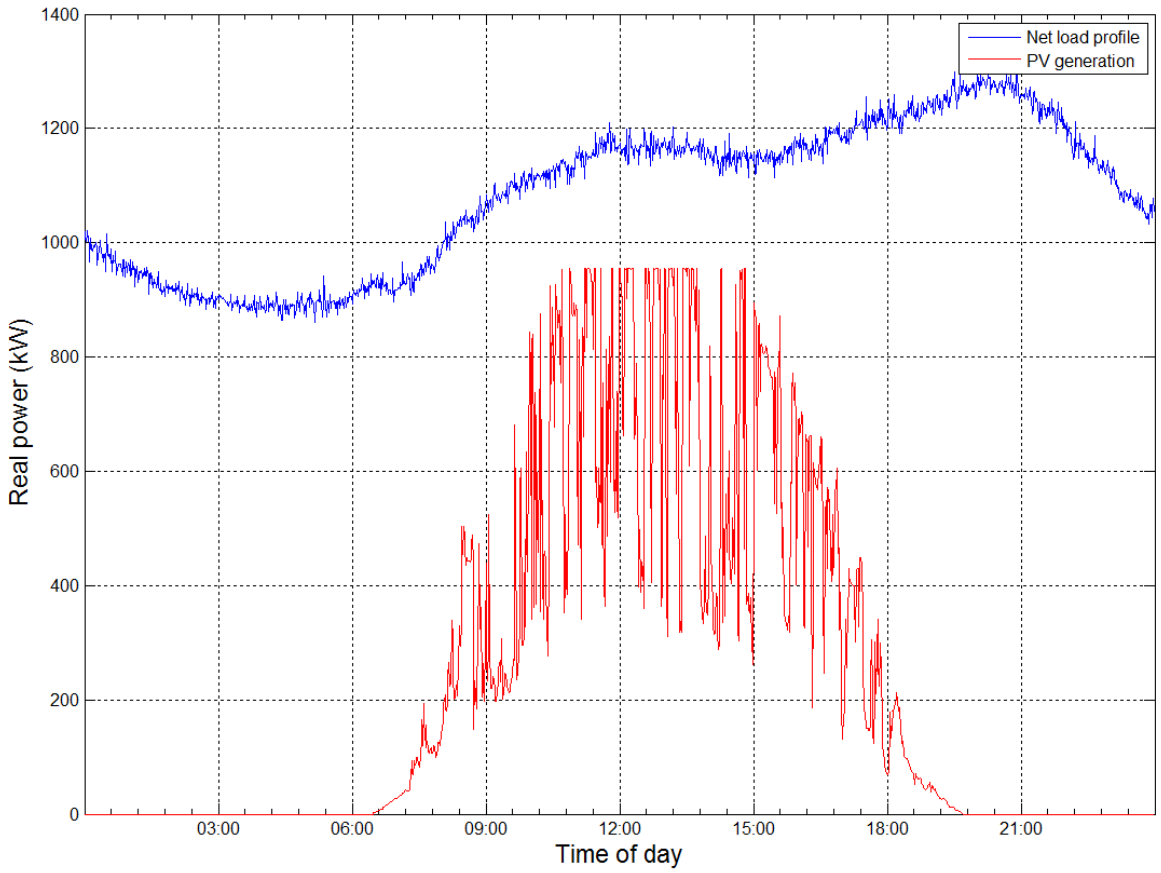

Fig. 3-4 Net Load and PV generation profile (1000 kWp) for April 22, 2013

As seen in Figs. 3-4 and 3-5, the peak PV generation are similar for both days but April 22 was a cloudy day with visible fluctuations in PV output; whereas April 26 was apparently sunny. These contrasting PV output profiles are taken to study the impact of PV integration on tap change operations of the VR's.

The RPC technique described in the previous section is based on the droop-based reactive injection from the inverter. Droop parameter which relates the change in reactive injection and node voltage can be derived from local Q-V contours (Fig. 3-6 – 3-8). As discussed in the previous section, the contours are almost linear within the specified range. All real and reactive loads throughout the network were constant for these contours except the dummy spot loads, i.e. real and reactive load at bus#812 for Fig. 3-6, and so on. As expected, the further the bus location from the substation, the wider the voltage range gets for the contours and the smaller the droop parameter becomes. So, if the PV plant is located at the end of the feeder it will be required to inject less reactive power to keep the local voltages within bounds compared to the case when it is located near the substation.

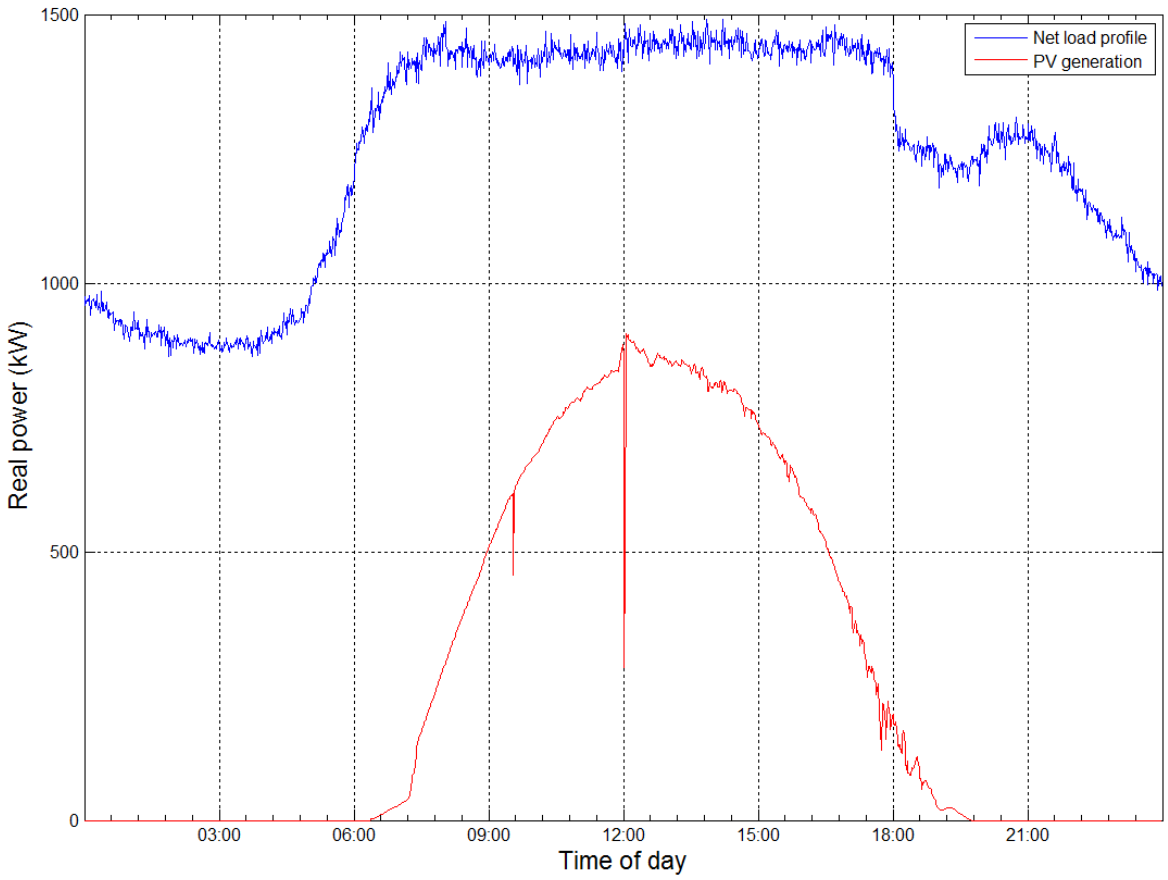

Fig. 3-5 Net Load and PV generation profile (1000 kWp) for April 26, 2013

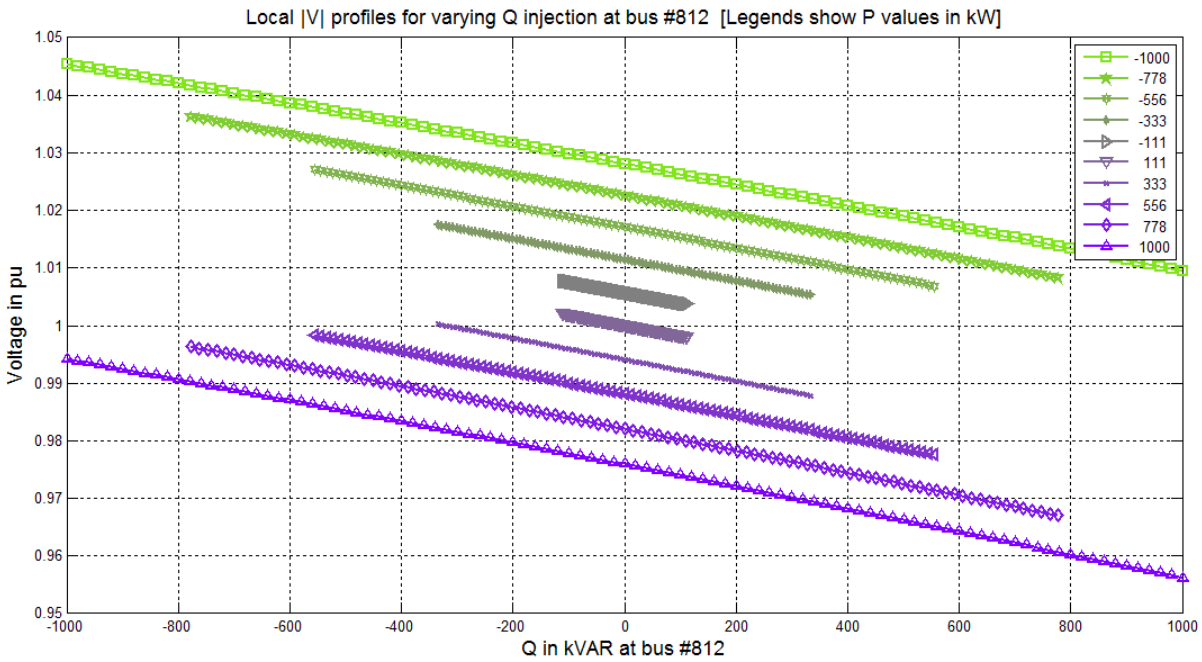

Fig. 3-6 Q-V contours at bus#812 with varying P (pf range: 0.707 leading to 0.707 lagging)

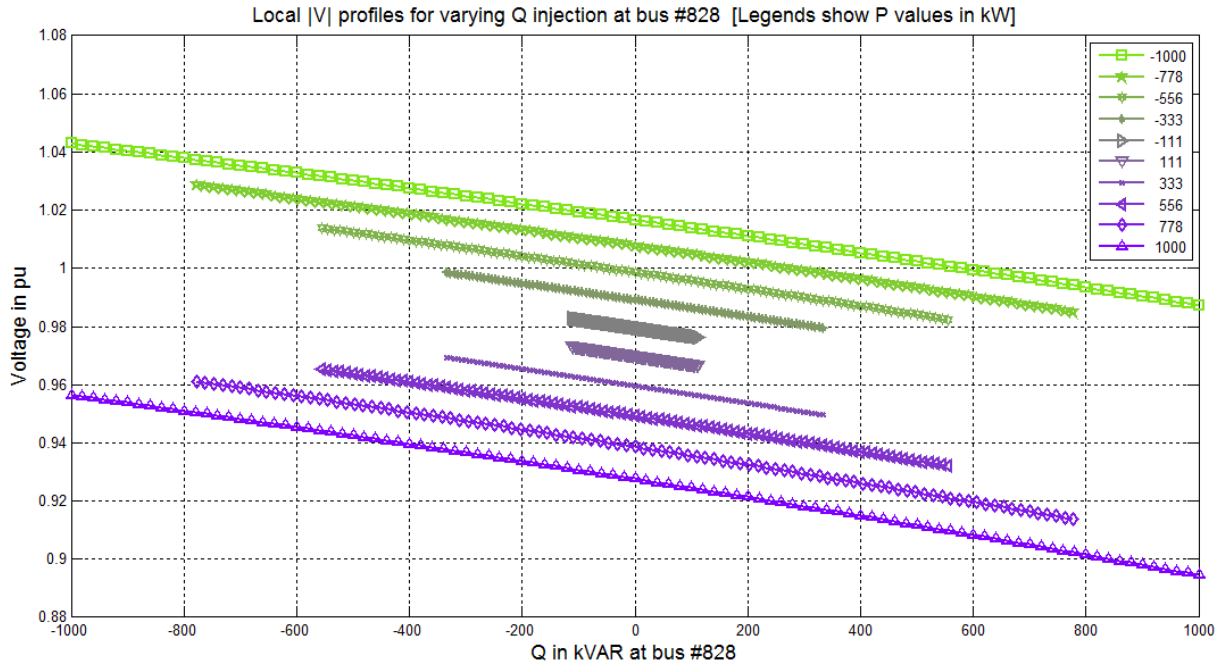

Fig. 3-7 Q-V contours at bus#828 with varying P (pf range: 0.707 leading to 0.707 lagging)

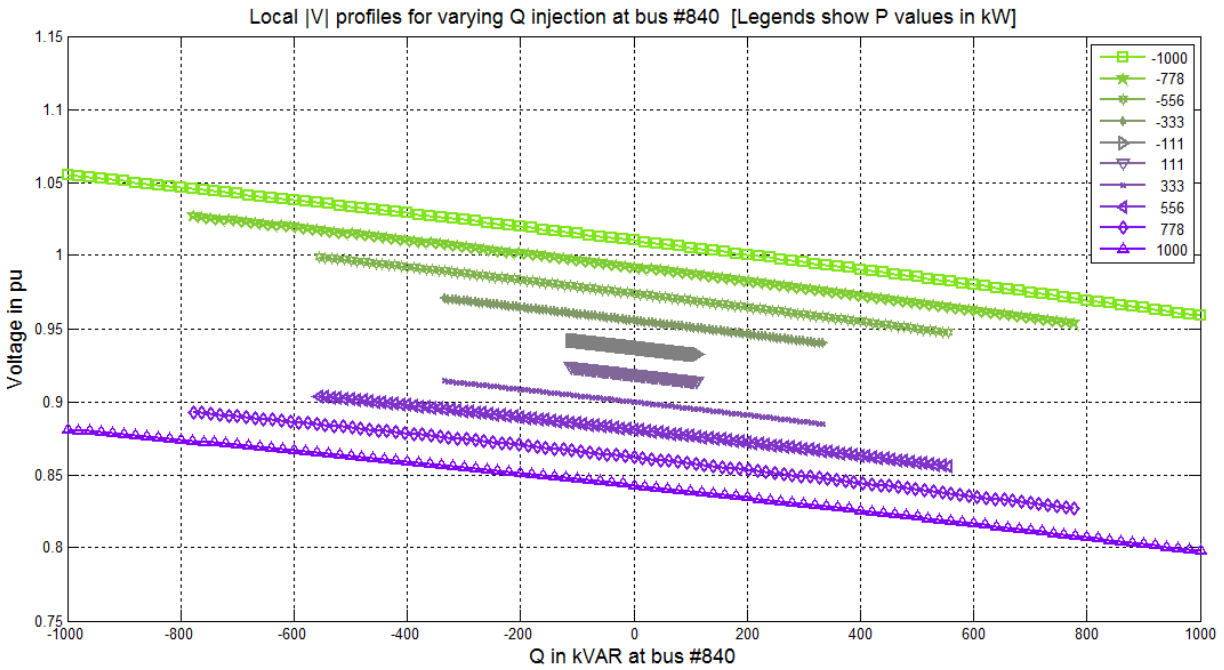

Fig. 3-8 Q-V contours at bus#840 with varying P (pf range: 0.707 leading to 0.707 lagging)

Simulation results

Traditional distribution network was built to deal with unidirectional power flow (from substation to consumers) and hence confront a gradually dropping voltage profile as the node distance from substation increases. Presence of high PV penetration alters the situation, as it can very well feed the major portion of total feeder load, yielding to reverse power flow at some parts of the feeder. Fig. 3-9a) – 3-9c) show the impact of growing PV penetration on local voltage profile or at the node where the PV system is connected. Overvoltage phenomenon is observed here, which even worsens as the PV location moves away towards the end of feeder. Typical overvoltage limit is usually set at 1.05 pu for distribution networks [108]. However, for this particular work a slightly narrower range is considered, i.e. upper threshold is set 1.04 pu and lower one is set at 0.96 pu. Like any other distribution circuit this test feeder is unbalanced too. So, the mean of all three-phase voltages is considered as the representative node voltage at any given bus. In presence of voltage control devices like line VR's, the overvoltage phenomenon can be counteracted. So, for the first part of the study, no VR control is imposed to evaluate the efficacy of the local voltage regulation techniques (RPC and RPC-APC).

The base cases designated for these discussions are the unity power factor or no Q injection cases. Two different parameters are studied here to analyze the performance of the RPC and RPC-APC

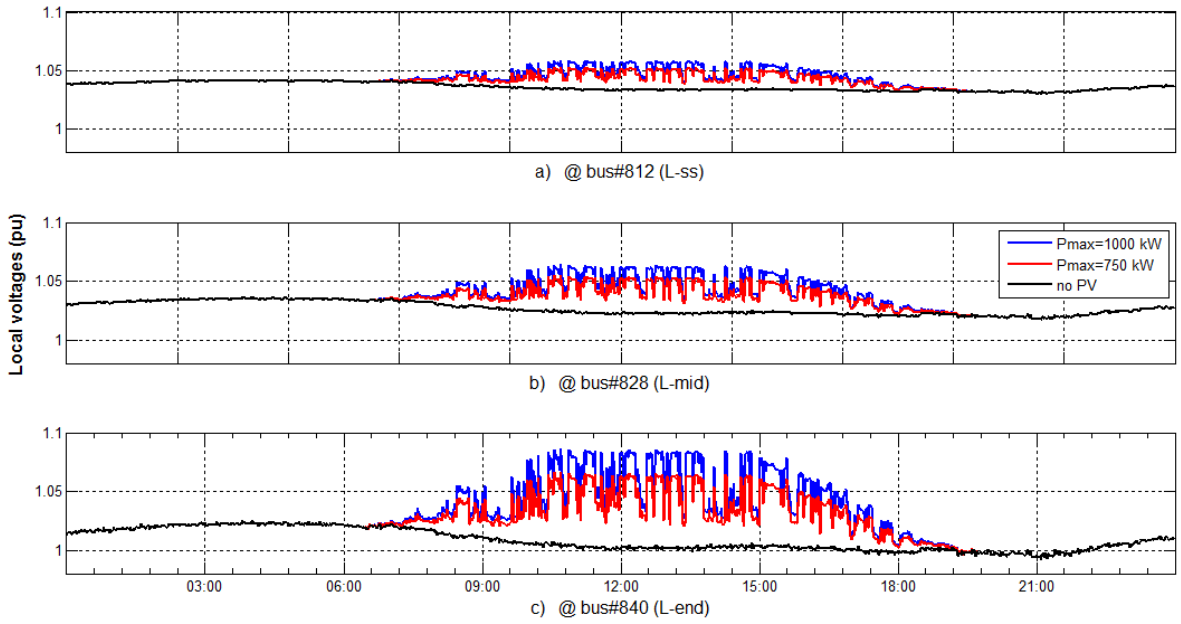

Fig. 3-9 Daily voltage profiles (at respective PV buses) for different PV locations and sizing

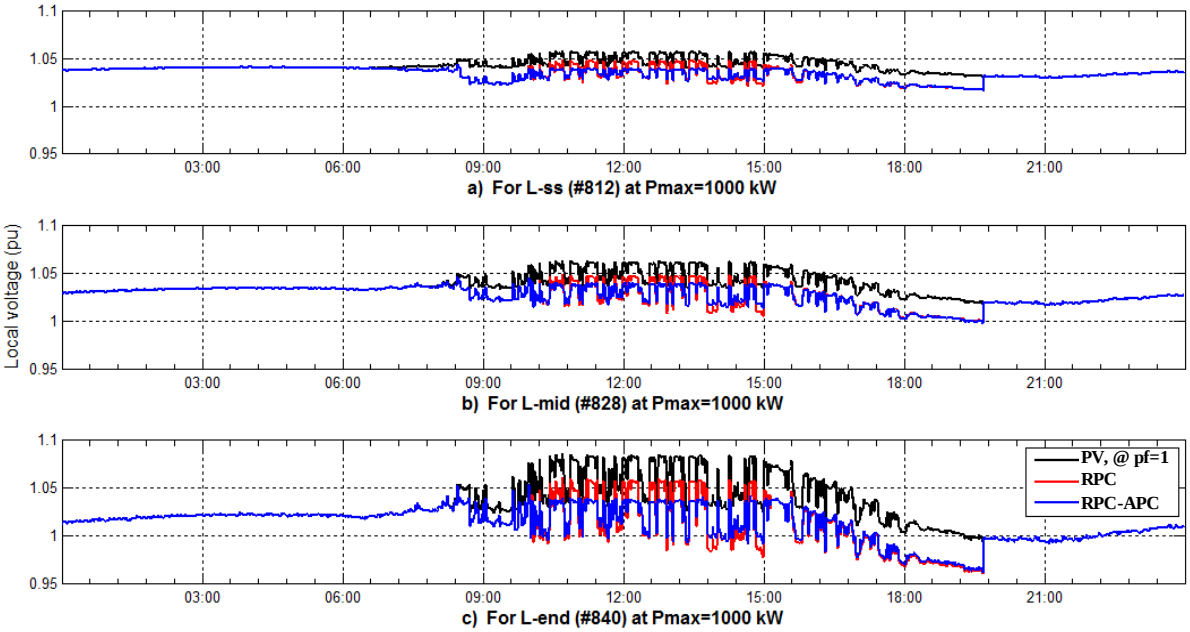

Fig. 3-10 Voltage profile improvement from base case with RPC and RPC-APC; a) L-ss position, b) L-mid, c) L-end for April 22, 2013

algorithms - voltage profile, and daily total number of tap-changing operations. The local voltage profiles after employing RPC and RPC-APC are given in Fig. 3-10. Cases with the higher level of penetration (i.e. Pmax=1000 kW) only are shown here. As already seen in Fig. 3-9, the local voltages were quite high for this level of penetration. Hence the prevention of overvoltage would be more discernible at PV size of 1000 kWp. Also, as seen in Fig. 3-4, the net load profile was quite low on April 22 compared to April 26 (Fig. 3-5) during peak PV generation hours. The voltage regulation techniques will thus be more effective for April 22. So, as shown in Fig. 3-10, RPC cannot always produce the required voltage regulation especially around noon time when the real output is at its peak. Consequently, for all the three locations the local voltages are out of bound, and the dimension of voltage rise worsens as the PV location nears the end of the feeder. Fig. 3-10 suggests that, RPC-APC provides the necessary reduction in voltage that RPC could not achieve alone. Almost all the times the voltages remained within the bounds when RPC-APC is employed. Even for the furthest location (L-end), the boundary limit violations are remedied within a minute or two. The abrupt voltage change at around 7 pm is due to the sudden discontinuation of reactive support from the PV inverter.

In the second part of this study the impact of the RPC and RPC-APC techniques on the required number of tap-changing operations for VR's is studied. For this simulation, the line VR's are controlled in 'Static' mode in OpenDSS, where the tap positions are calculated in each iteration for the varying 1-minute load and PV generation data. As seen in Fig. 3-10, regulator 1 is located at the line segment between bus 814 and 850, and regulator 2 is located at the line segment between bus 852 and 832. The voltage regulation set-points and bandwidths are kept the same as provided in the test feeder configuration. Table 4-1 shows the changes in tap-changing operations due to PV integration (real injection only); in comparison with base load only (i.e. no PV scenario) for Apr 22. Here, R1a denotes phase-a for regulator 1 and so on. As seen from table 4-1, the number of tap-changing operations increases as the PV plant size grows, irrespective of the location. And the further the PV plant is located from the substation, the more number of tap-changing is required, denoting the fact that the nodes closer to the substation face less local voltage variations.

Unlike voltage profiles, the numbers of tap-changing operations do not follow any definite trend with application of RPC and RPC-APC. When only RPC is implemented, it adds reactive power fluctuations on top of real fluctuations and hence the number of tap-changings goes higher compared to no Q injection or unity pf scenario, as seen in Table 3-2. As the RPC-APC limits real injection spikes for limiting the voltage, it can reduce the no. of tap-changing operations from RPC only case. Table 3-2 also shows that when the PV size gets larger (i.e., at 1000 kWp), in most cases, RPC-APC reduces the total number of tap-changings compared to unity pf PV integration case, as it gets to curtail higher amount of real injection which was responsible for voltage rise beyond the upper threshold. Table 3-2 also shows the contrast between the cases for April 22 and

Table 3-1 Tap-changing operations in line VR's due to PV integration

PV location	**kWp of PV**	**Total No of tap-changes required (daily) for:**					
		R1a	***R1b***	***R1c***	***R2a***	***R2b***	***R2c***
No PV	**0**	4	1	2	6	6	4
812 (L-ss)	750	26	3	14	43	12	28
	1000	46	19	38	70	41	59
828 (L-mid)	750	59	45	63	93	68	84
	1000	96	71	86	131	105	114
840 (L-end)	750	76	45	60	167	140	150
	1000	106	95	102	205	191	183

April 26. April 26 was a sunny day with less output fluctuations compared to April 22. This makes the required number of tap-changes vary on a lower range for April 26, compared to April 22 for all PV locations and size. But the net load was high for this day resulting in less reverse power flow from the PV system. So, the required number of tap-change operation did not change dramatically over the base case without any PV. Also, the similar numbers of tap-changes suggest that, APC was not necessary for that day over RPC to keep the voltages within bound.

Table 3-2 Required number of tap-changing for VR's throughout the day (Apr 22 and 26)

Day	PV location	kWp of PV	Technique	Total number of tap-changes required(daily) for:					
				R1a	R1b	R1c	R2a	R2b	R2c
22-Apr		0	n/a	4	1	2	6	6	4
	812 (L-ss)	750	Qinj=0	26	3	14	43	12	28
			RPC	37	19	42	58	46	55
			RPC-APC	20	11	6	28	13	15
		1000	Qinj=0	46	19	38	70	41	59
			RPC	71	61	58	101	90	88
			RPC-APC	38	9	20	52	17	35
	828 (L-mid)	750	Qinj=0	59	45	63	93	68	84
			RPC	89	54	75	104	85	93
			RPC-APC	65	49	62	82	65	79
		1000	Qinj=0	96	71	86	131	105	114
			RPC	128	100	118	158	133	144
			RPC-APC	96	75	83	126	101	113
	840 (L-end)	750	Qinj=0	76	45	60	167	140	150
			RPC	84	69	77	173	158	169
			RPC-APC	66	49	70	162	138	158
		1000	Qinj=0	106	95	102	205	191	183
			RPC	137	108	116	222	188	212
			RPC-APC	95	82	85	180	170	171
26-Apr		0	**n/a**	**10**	**4**	**6**	**13**	**13**	**14**
	812 (L-ss)	750	Qinj=0	10	2	8	15	9	16
			RPC	12	4	8	19	13	19
			RPC-APC	12	4	8	19	13	19
		1000	Qinj=0	14	4	10	15	13	15
			RPC	15	6	11	17	15	19
			RPC-APC	15	6	11	17	15	19
	828 (L-mid)	750	Qinj=0	16	8	13	15	12	14
			RPC	16	8	13	15	12	14
			RPC-APC	16	8	13	15	12	14
		1000	Qinj=0	19	10	14	21	13	16
			RPC	21	10	14	21	15	18
			RPC-APC	21	10	14	21	15	18
	840 (L-end)	750	Qinj=0	19	8	12	28	21	26
			RPC	19	8	12	28	21	26
			RPC-APC	19	8	12	28	21	26
		1000	Qinj=0	18	13	17	26	24	31
			RPC	21	14	17	32	26	28
			RPC-APC	21	14	17	32	26	28

4. Solar generation forecasts for local voltage regulation

Inverter-based voltage regulation applications can be further augmented by using PV generation forecasts. Solar forecasting is being used as a support tool to manage the intermittent nature of solar energy production which can lead to potential reliability concerns regarding network operation like voltage and frequency regulation [109]. Dispatching regulation reserves require short-term PV output forecasts for real-time market applications. For example, California Independent System Operator (CAISO) provides forecasts 105 minutes before the operating hour for its participating intermittent resource program [110]. As discussed in the literature review chapter (sub-section 2.2), the offline short-term solar generation forecasting problem using has been approached using two broad types of techniques – time-series based statistical methods and artificial neural network (ANN) based techniques. Statistical models rely on underlying stochastic properties of internal data structure in PV generation (direct forecasting) or solar irradiance (indirect forecasting) data [71-73, 92, 111]. ANN methods are mostly used for indirect PV generation forecasting using training dataset, which include different weather parameters [63, 65, 72-73]. Giorgi et al. presented the impact of different input variables for short-term PV power prediction in [58], where their analyses showed that the prediction accuracy improves when other measured weather parameters are taken into account, instead of only PV power and solar irradiance.

If PV generation forecasts are to be integrated with network operation applications, like local voltage regulation, it is useful to employ an online forecasting approach that does not handle a large dataset for very short-term forecasting scenario. In that case, measurement based dynamic prediction methods like Kalman Filter (KF) technique can help reduce processing time. KF theory provides a sequential learning method that considers hourly or sub-hourly measurements for short-term PV power forecasting applications [82, 84-85, 112].

This chapter describes the development of a local voltage regulation technique which merges a droop-based inverter reactive power compensation algorithm and active power curtailment method using very short-term PV power forecasts. This technique is based on the methodology presented in [113], which expands on the local voltage regulation scheme (discussed in chapter 3), and integrates the voltage regulation method with a hybrid forecasting algorithm that combines

physical PV modeling based on KF theory. This forecasting model provides very short-term PV generation forecasts (15-second) that are used by this voltage regulation technique to determine required reactive compensation from the PV inverter and active power curtailment threshold. The proposed voltage regulation method is designed to be realized as an online application that can run in a smart grid environment and reduce local overvoltage under a high PV penetration scenario.

4.1 Hybrid PV power forecasting model

The proposed hybrid forecasting model for very short-term PV generation forecasting combines two techniques - physical modeling of PV generation with weather parameters and application of recursive KF technique. For this problem, very short-term PV generation forecasting is represented with 15 seconds timescale. A high-level schematic depicting this forecasting model is given in Fig. 4-1. As seen in Fig. 4-1, the forecasting model requires a physical model for PV generation which uses weather parameters. The input to this block is the historical dataset (with weather classification) and past measurements (irradiance, temperature, and PV generation) for the day; while it outputs a numerical relationship (expressed as a gain matrix, developed in section 4.1.2) which would be used to transfer short-term prediction estimates of irradiance and temperature to PV output forecasts. The preceding block to this generation model conditions and classifies the historical dataset according to day types and seasons. The physical PV model, provided with coarse weather forecast for the day in question, is used as an initial seed to the recursive KF application

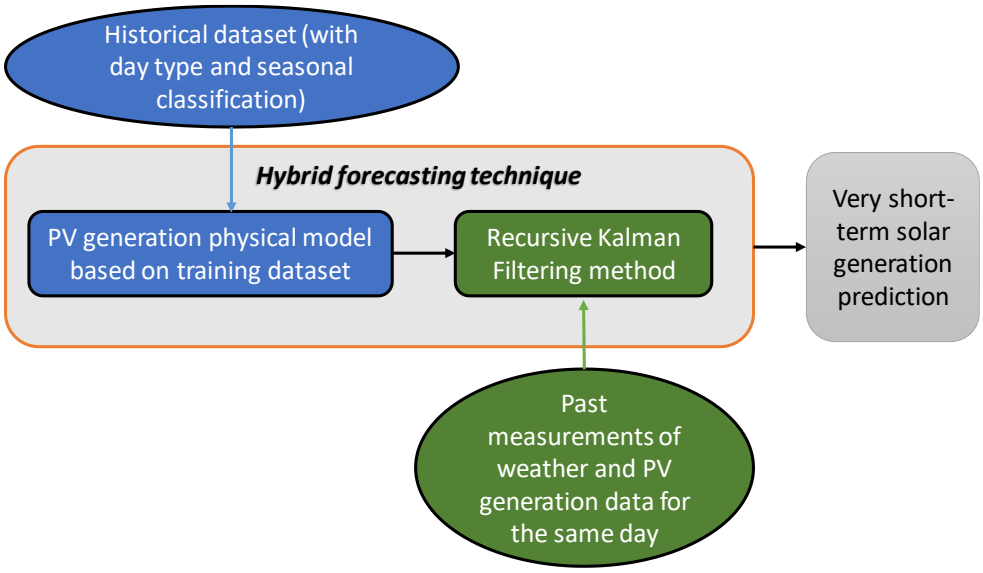

Fig. 4-1 High level schematic of the proposed hybrid forecasting model

block. Based on the measurements recorded for the day, this block recalibrates the initial PV lgeneration model to a steady-state condition once ample data is gathered. This way, the forecasting model reduces its dependence on the historical dataset and can lessen the impact of any bias present in the past dataset. Following sub-sections discuss these constituent processing blocks (as seen from Fig. 4-1) of the proposed hybrid technique.

4.1.1 Day type classification based clear sky radiation

Weather/day type and seasonal classification helps to cluster the historical dataset and thus has been featured in previous works [66, 76, 93]. These works mostly consider day types based on general weather conditions (sunny/cloudy/rainy). For the proposed hybrid forecasting model, a seven-group classification is assumed instead according to the incident solar energy or daily insolation (kWh/m^2). This classification provides more granularity to the clustering performed on the historical dataset. Eqn. (4-1) defines the day type by the ratio (R_{dt}) between the daily measured and theoretical clear sky insolation.

$$R_{dt} = \frac{measured\ insolation}{clear\ sky\ insolation} * 100\% \quad \ldots \quad \text{Eqn. (4-1)}$$

The day type classifications according to the range of R_{dt} are listed in Table 4-1. Seasonal classification is also considered in this model besides day type classification. For this work, two kinds of seasonal classifications are: a) long summer (from spring equinox to fall equinox) and long winter (from fall equinox to spring equinox), and b) usual four seasons- winter, spring,

Table 4-1 Day type classification according to available insolation

Day type	***Range of measured insolation to clear sky insolation***
Sunny	$R_{dt} > 95\%$
Mostly Sunny	$85\% < R_{dt} \leq 95\%$
Partly Sunny	$70\% < R_{dt} \leq 85\%$
Partly Cloudy	$55\% < R_{dt} \leq 70\%$
Cloudy	$40\% < R_{dt} \leq 55\%$
Overcast	$25\% < R_{dt} \leq 40\%$
Snowy/rainy	$R_{dt} \leq 25\%$

summer, and fall. Long summer/winter classification yields a larger cluster for each day type in a season, compared to four seasons classification.

The historical dataset used to develop and validate the hybrid forecasting model consists electrical and weather data measurements collected from a 6.44 kWp rooftop PV system located at Virginia Tech- Advanced Research Institute building in Arlington, Virginia. System configuration data are used to model the clear sky radiation for this PV site as described in the following section.

Clear sky radiation model:

Standard clear sky radiation models typically output the irradiance received on a horizontal or a tilted plane. As discussed in [77, 80, 114], the total incident radiation on a tilted PV array can be divided into three components according to their sources. The largest component is the beam or direct radiation (Gb) as received by the tilted plane. Other two components represent the diffused (Gd) and reflected (Gr) light (Eqn. 4-2 – 4-4).

$$G_b = G_0 \cos\theta \, \tau_b \quad \ldots \quad \text{Eqn. (4-2)}$$

$$G_r = \rho G_0 \cos\theta_z \tau_r \left(\frac{1+\cos\beta}{2}\right) \quad \ldots \quad \text{Eqn. (4-3)}$$

$$G_d = G_0 \cos\theta_z \tau_d \left(\frac{1+\cos\beta}{2}\right) \quad \ldots \quad \text{Eqn. (4-4)}$$

Where,

Daily radiation, $G_0 = G_{SC}(1 + 0.033\cos D)$;

$D = \frac{360N}{365}$; {N being the Julian date (1 for Jan 1)}

Solar Constant, $G_{SC} = 1353\ W/m^2$

For Solar zenith angle (the angle of incidence of the beam radiation on a horizontal surface), θ_z

$$\cos\theta_z = \cos\delta\cos\lambda\cos\omega + \sin\delta\sin\lambda \quad \ldots \quad \text{Eqn. (4-5)}$$

Declination angle or the angular position of the sun at the solar noon, $\delta = 23.45 * \sin\left[\frac{360(N+284)}{365}\right]$

For the PV unit, tilt or surface inclination angle, $\beta \approx 10^o$

Latitude, $\lambda = 38.8803^o N$ (for Arlington,VA)

$\omega =$ Hour angle or the angular displacement of the sun;

East or west of the local meridian due to earth's rotation on its axis at the rate of 15 degrees per hour, $\omega = (Solar\ hour * 15 - 180)^o$

$$Solar\ hour = Standard\ clock\ time\ (in\ hrs) + \left(\frac{EOT}{60}\right) - Longitudinal\ correction$$

Where standard clock time means the local time expressed in hours (for example, 2.15 pm would be 14.25^o). EOT stands for the equation of time (for the perturbations in the earth's rate of rotation which affects the time the sun crosses the observer's meridian) determined in minutes for the day as:

$$EOT = 229.2(0.000075 + 0.001868\cos D' - 0.032077\sin D' - 0.014615\cos 2D' - 0.04089\sin 2D') \quad \ldots \quad \text{Eqn. (4-6)}$$

$$D' = (N-1)\frac{360}{365}$$

The longitudinal correction part accounts for the constant difference between the meridians (standard and the local).

$$Longitudinal\ correction = \left(\frac{longitude}{15}\right) - lag\ from\ the\ GMT\ in\ hours$$

Angle of incidence (the angle between the beam radiation and the normal to the tilted surface), θ is described by:

$$\cos\theta = \cos\theta_z\cos\beta + \sin\theta_z\sin\beta\cos(\gamma_{sol} - \gamma) \quad \ldots \quad \text{Eqn. (4-7)}$$

Here,

γ_{sol} is the solar azimuth angle or the angular displacement from the south of the projection of the beam radiation on the horizontal plane. The calculation of this angle requires the knowledge about which quadrant the sun is at the time. It is related to the hour angle, latitude and zenith angle by:

$$\gamma_{sol} = C_1C_2{\gamma_{sol}}' + C_3(1 - C_1C_2)90 \quad \ldots \quad \text{Eqn. (4-8)}$$

$$\tan{\gamma_{sol}}' = \frac{\sin\omega}{\sin\lambda\cos\omega - \cos\lambda\tan\delta} \quad \ldots \quad \text{Eqn. (4-9)}$$

Constant terms C_{1-3} are determined with the boundary condition when the denominator in the above equation (Eqn. 4-9) turns zero:

$$\sin\lambda\cos\omega_{ew} - \cos\lambda\tan\delta = 0$$

$$\text{Or, } \cos\omega_{ew} = \frac{\tan\delta}{\tan\lambda}$$

This hour angle (ω_{ew}) represents when the sun is due east (or west).

$$C_1 = \begin{cases} 1 \; if \; |\omega| < \omega_{ew} \\ -1 \; otherwise \end{cases}$$

$$C_2 = \begin{cases} 1 \; if \; \lambda(\lambda - \delta) \geq 0 \\ -1 \; otherwise \end{cases}$$

$$C_3 = \begin{cases} 1 \; if \; \omega \geq 0 \\ -1 \; otherwise \end{cases}$$

γ is the surface azimuth angle which denotes the deviation of the projection on a horizontal plane of the normal to the surface from the local meridian. As per [114], it is zero due south, east negative and positive. The PV arrays in question are faced towards southeast direction; hence this angle was approximated to be -25^o.

The calculation of the solar azimuth angle is somewhat cumbersome, so another expression can be used to approximate the coefficient for beam radiation, which takes into account only surface azimuth angle, instead of both the azimuth angles:

$$\begin{aligned} \cos\theta = {} & \sin\delta\sin\lambda\cos\beta - \sin\delta\cos\lambda\sin\beta\cos\gamma \\ & + \cos\delta\cos\lambda\cos\beta\cos\omega + \cos\delta\sin\lambda\sin\beta\cos\gamma\cos\omega \\ & + \cos\delta\sin\beta\sin\gamma\sin\omega \end{aligned} \quad \ldots \quad \text{Eqn. (4-10)}$$

$\rho =$ average reflectance of the ground material

This reflectance index for the concrete rooftop is assumed to be ~0.3 which is approximately the average minimum value for this parameter as discussed in [115].

The multipliers in Eqn. (4-2 – 4-4) expressed with τ_b, τ_r, and τ_d are called atmospheric transmittances (AT) for beam, reflected and diffused solar radiation and are expressed with:

$$\tau_b = B_0 + B_1 * \exp(-\frac{B_2}{\cos\theta_z})$$

$$\tau_r = 0.271 + 0.706\tau_b \quad \ldots \text{ Eqn. (4-11)}$$

$$\tau_d = 0.271 - 0.294\tau_b$$

Here in Eqn. 4-11, the constants B_{0-2} are dependent on the altitude of the PV site in km (A):

$$B_0 = R_0[0.4237 - 0.00821(6 - A)^2]$$

$$B_1 = R_1[0.5055 - 0.00595(6.5 - A)^2] \quad \ldots \text{ Eqn. (4-12)}$$

$$B_2 = R_2[0.2711 + 0.01858(2.5 - A)^2]$$

$R_0, R_1, and\ R_2$ are correction factors which depend on the climate and given in Table 4-2:

Table 4-2 Correction parameters for atmospheric transmittance calculation

Climate type	R_0	R_1	R_2	**Range (in days/months)**
Mid-latitude summer (long summer)	0.97	0.99	1.02	Spring Equinox to fall equinox
Mid-latitude winter (long winter)	1.03	1.01	1.00	The rest of the year

The theoretical models discussed above are compared with measured irradiance values in the following section. From available irradiance data recordings (5-minute average), the days were selected which had maximum values in a month (2014) for daily mean irradiance (Table 4-3). So these days belong to sunny or mostly sunny type.

Table 4-3 Days with monthly maximum irradiance for 2014

Month (2014)	Jan	Feb	Mar	Apr	May	Jun	Jul	Aug	Sep	Oct	Nov	Dec
Day (monthly max)	30	28	31	27	31	6	25	15	12	5	10	7
Mean daily irradiance in W/m^2 (5 min average)	169	229	284	315	319	326	317	297	260	233	160	138

The theoretical models for clear sky radiation for these days (mentioned in Table 4-3) are plotted here against the measured data (Figs. 4-2 – 4-13). Both the models (with and without solar azimuth angle consideration) are includes in these figures for comparing them with the measured plane of array irradiance.

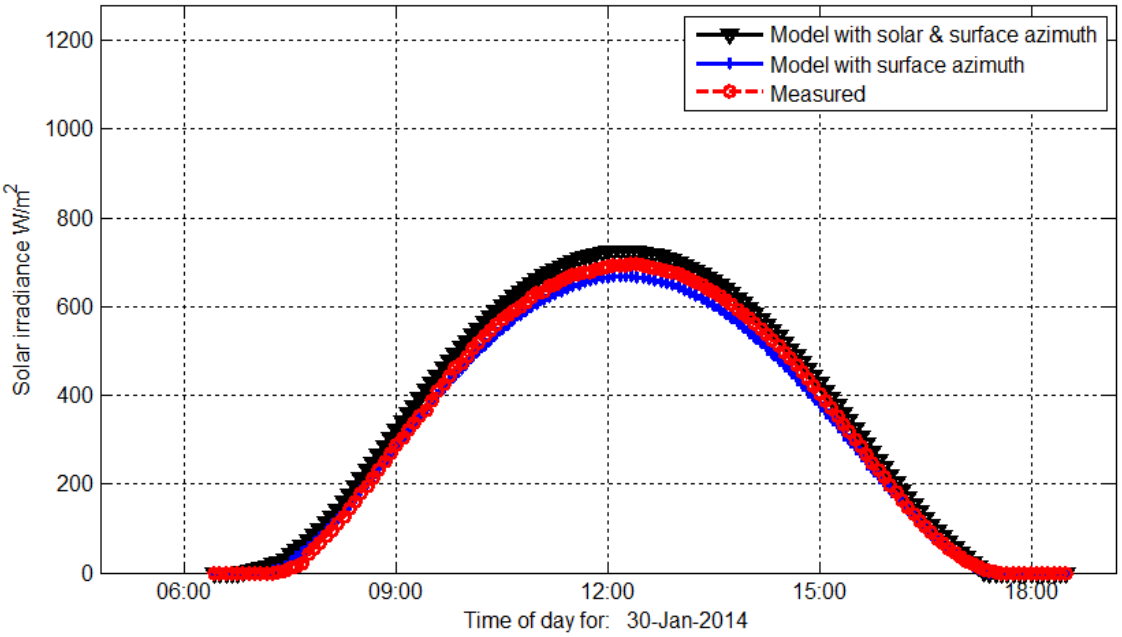

Fig. 4-2 Measured and calculated clear sky irradiance profile for Jan 30, 2014

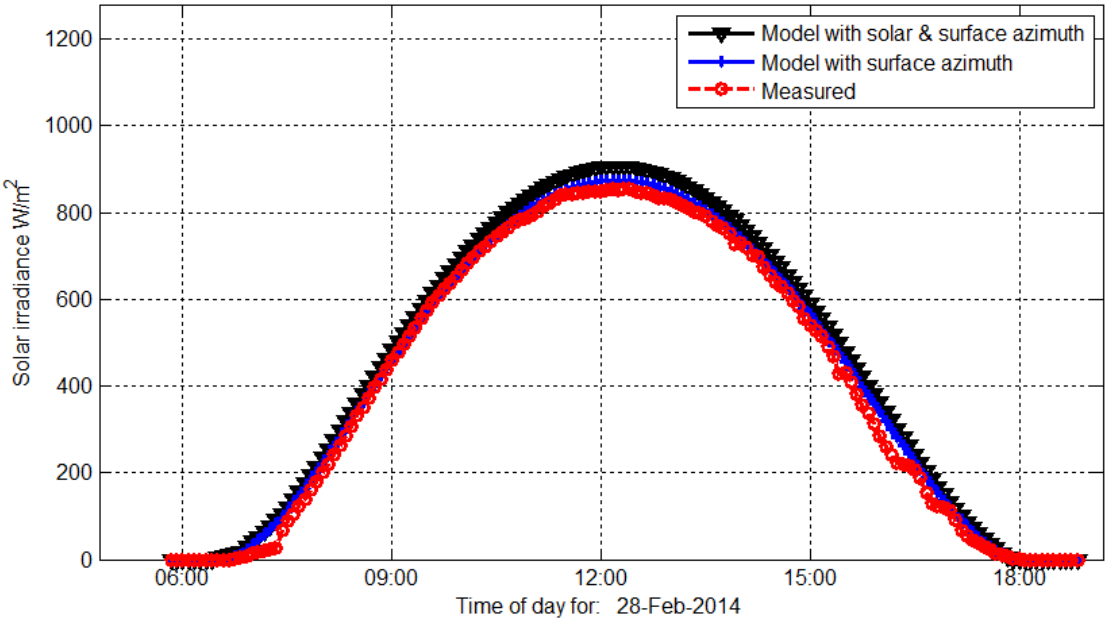

Fig. 4-3 Measured and calculated clear sky irradiance profile for Feb 28, 2014

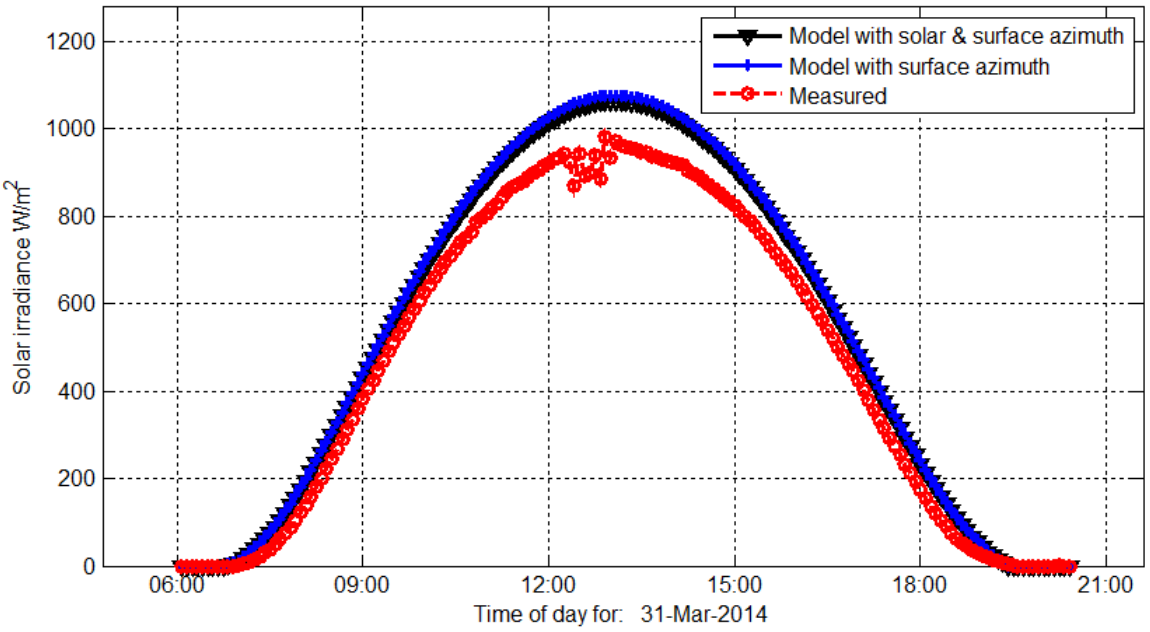

Fig. 4-4 Measured and calculated clear sky irradiance profile for Mar 31, 2014

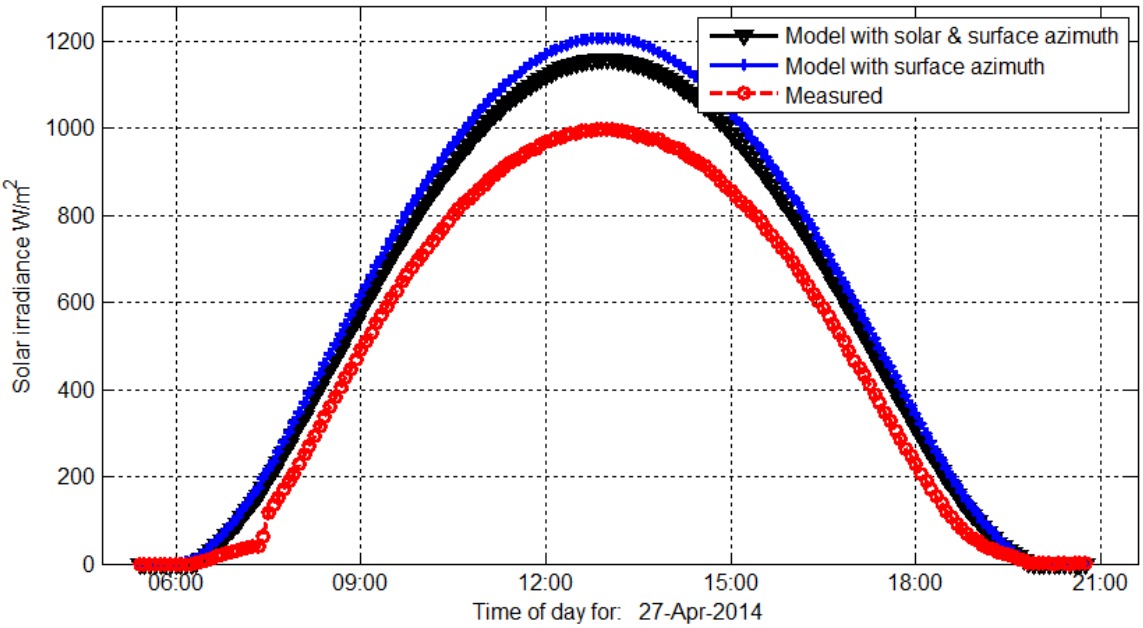

Fig. 4-5 Measured and calculated clear sky irradiance profile for Apr 27, 2014

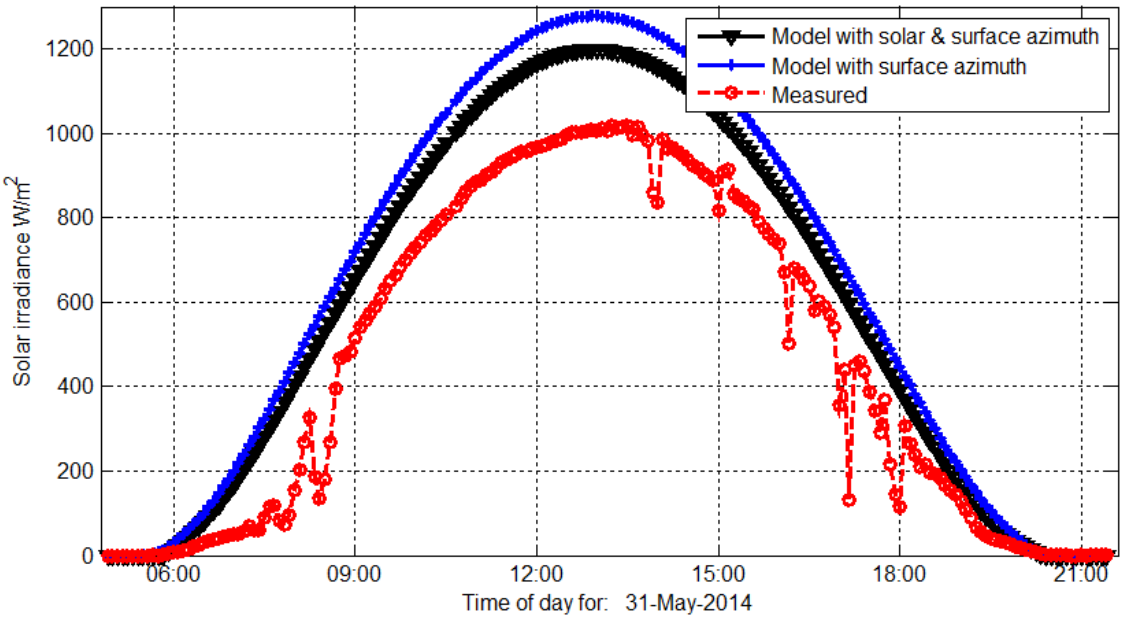

Fig. 4-6 Measured and calculated clear sky irradiance profile for May 31, 2014

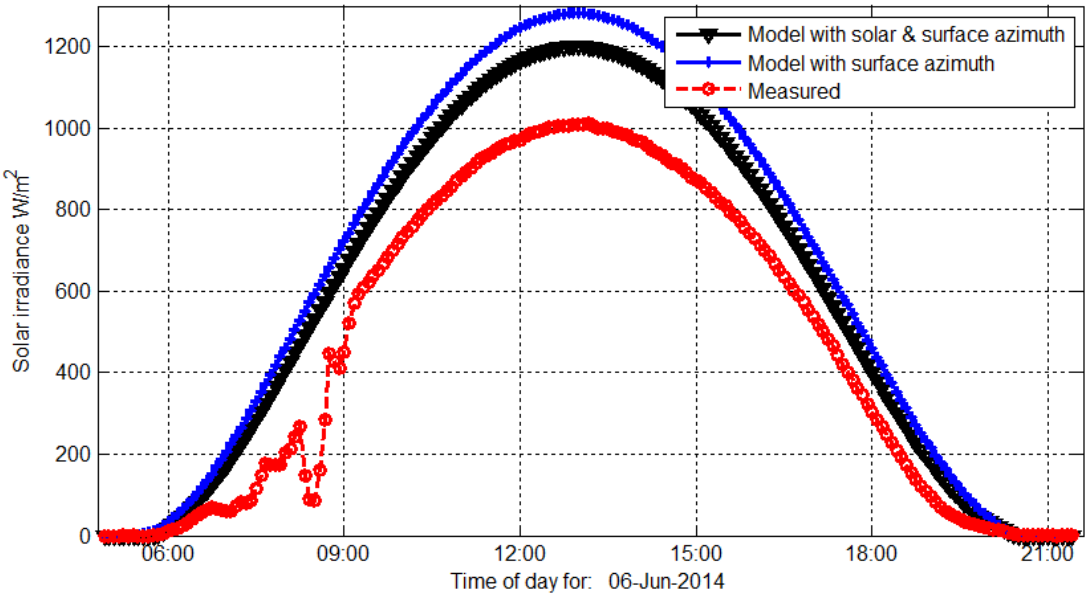

Fig. 4-7 Measured and calculated clear sky profile for Jun 6, 2014

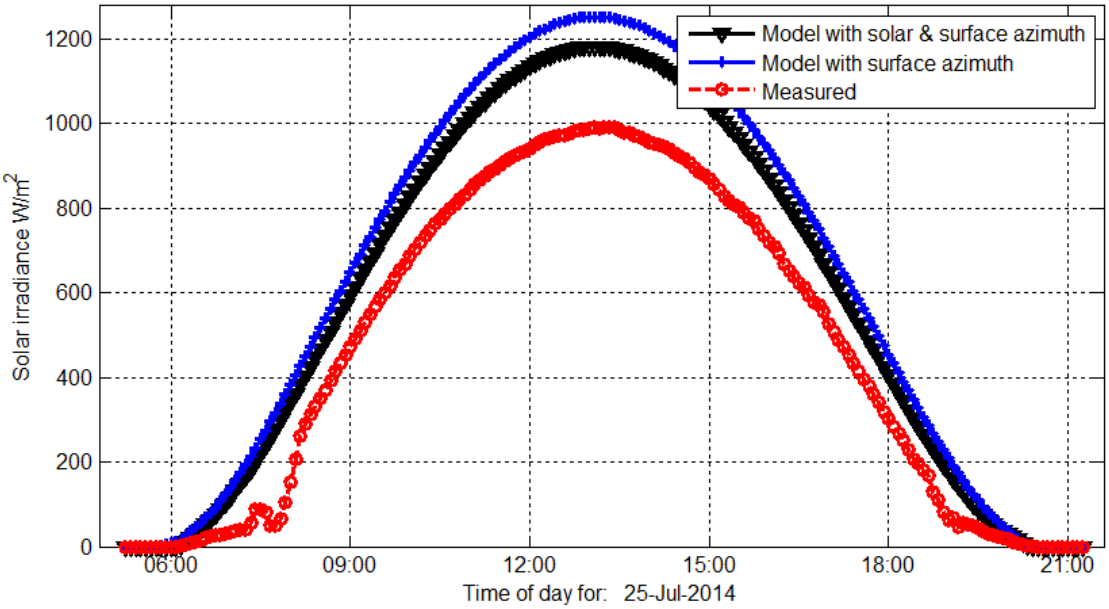

Fig. 4-8 Measured and calculated clear sky irradiance profile for Jul 25, 2014

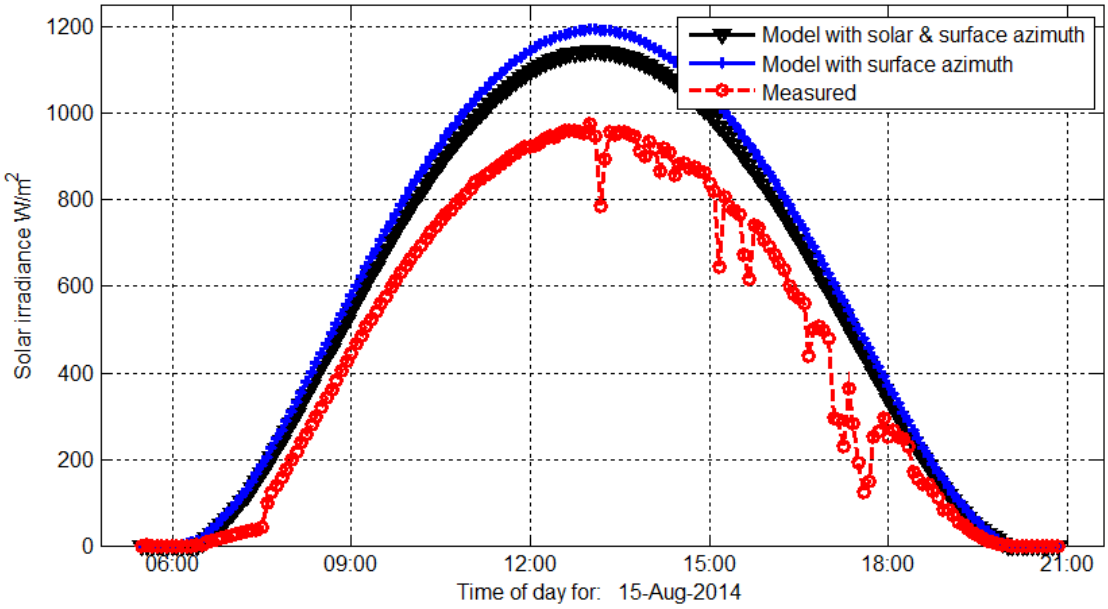

Fig. 4-9 Measured and calculated clear sky irradiance profile for Aug 15, 2014

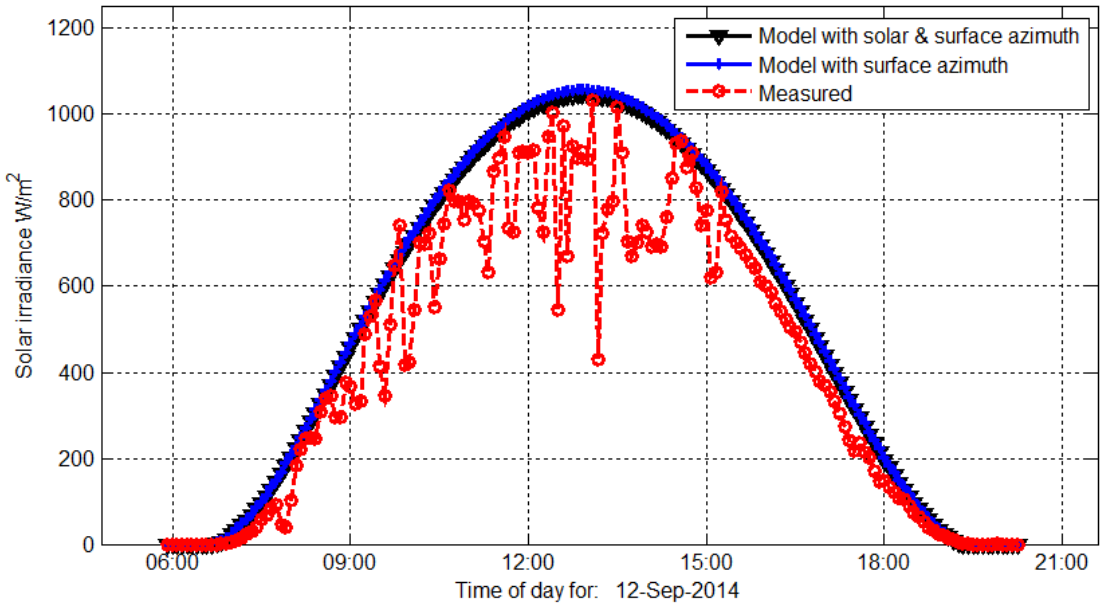

Fig. 4-10 Measured and calculated clear sky irradiance profile for Sep 12, 2014

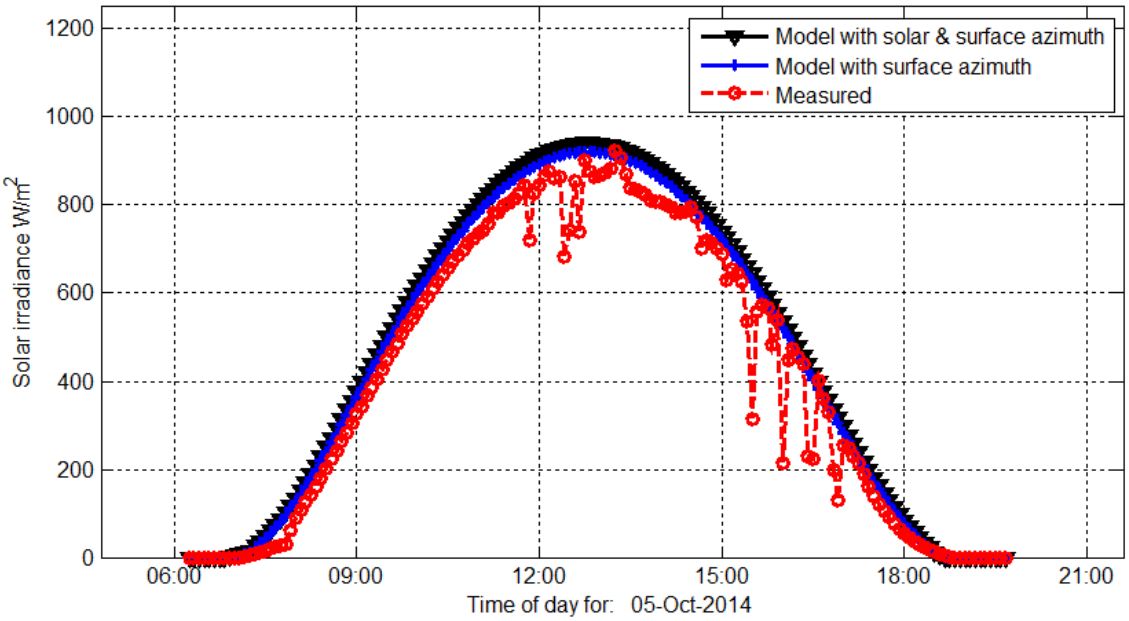

Fig. 4-11 Measured and calculated clear sky irradiance profile for Oct 5, 2014

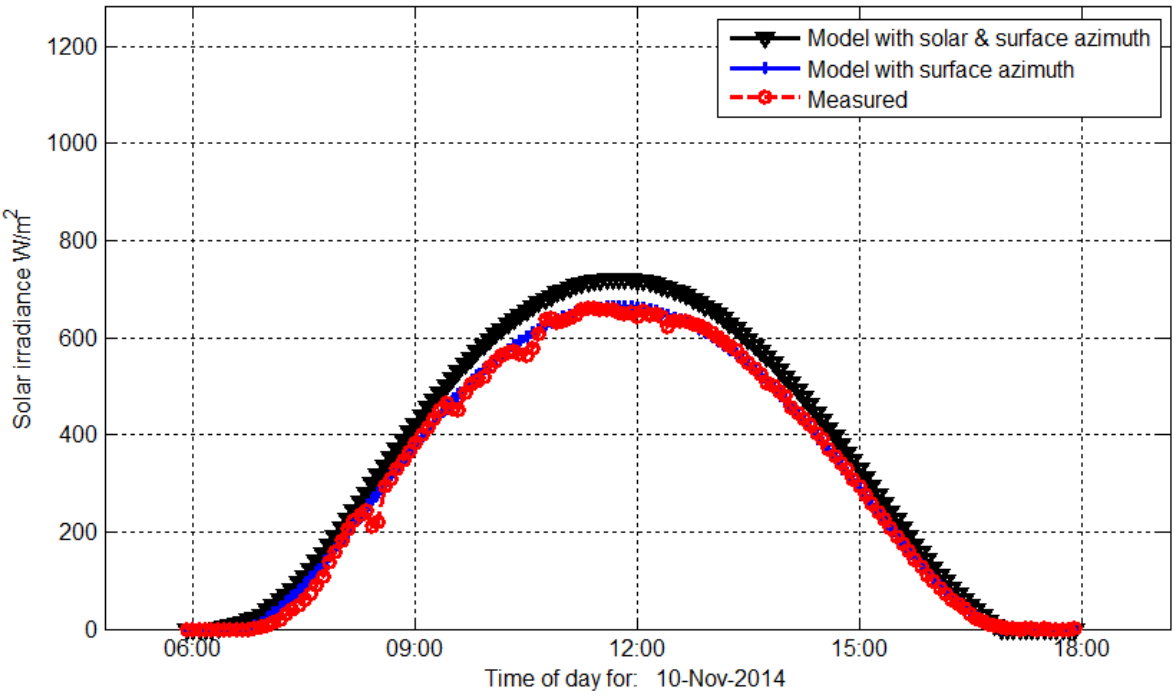

Fig. 4-12 Measured and calculated clear sky irradiance profile for Nov 10, 2014

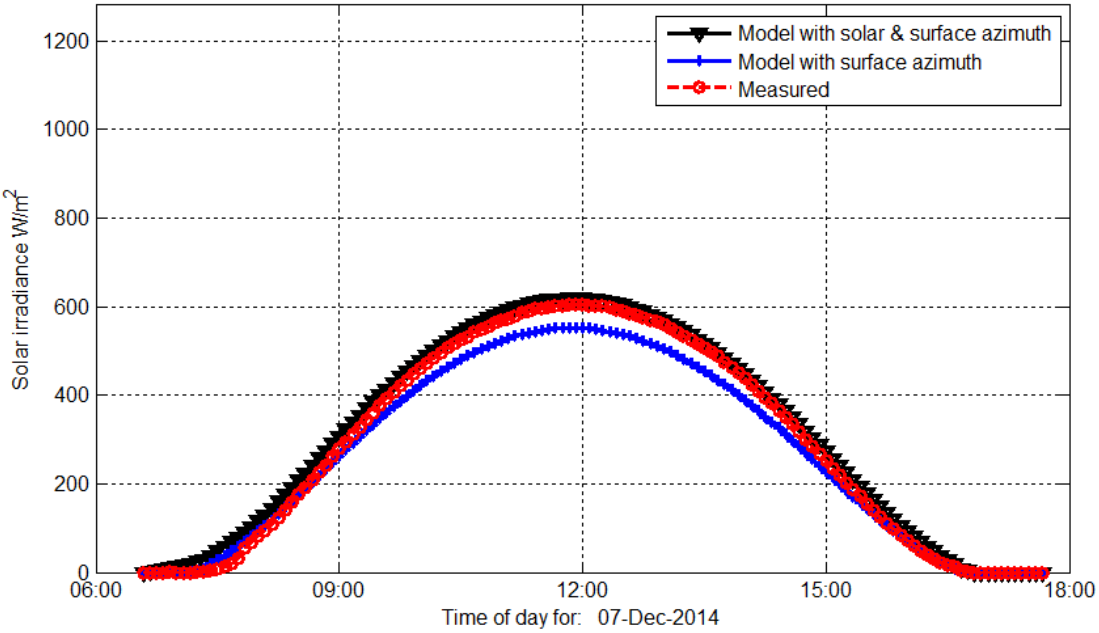

Fig. 4-13 Measured and calculated clear sky irradiance profile for Dec 7, 2014

Figs. 4-2 – 4-13 show the measured irradiance profiles for days in every month in 2014 when the recorded average irradiance was highest. Outputs from clear sky models with both solar and surface azimuth and only surface azimuth are plotted in these figures as well. For some of these days, there were slight cloud movements making the measured irradiance profiles fluctuate within narrow ranges. These figures show how expected clear sky radiation calculations (Eqns. (4-2) – 4-12) come across as compared to measured irradiance values. The comparison would be idealistic if these days were perfectly clear. However, as seen from these figures, for most parts the models' outputs are within close range, with small differences towards the noon hours. Also, when the model includes both solar and surface azimuth angles, the theoretical calculations are closer to the radiation measurements on apparently clear days. Although these figures show the averaged out irradiance values in every 5-minute window, but instantaneous values can be higher at times. Consequently, the hybrid forecasting model determines the clear sky radiation values when necessary using the model considering both solar and surface azimuth angles.

4.1.2 PV generation modeling using weather data

This section reports the regression analysis performed on solar PV output which expresses it as a function of environmental parameter inputs. For the analyses presented in this section, the rooftop PV data from the aforementioned 6.44 kWp system are used. The available data are of 15-second resolution, and for every day, data is collected for several electrical and meteorological parameters, for example, AC and DC current and voltage, ambient and module temperature, solar irradiance (internal/plane of array) and external/horizontal), wind velocity etc.

Various input parameters have been investigated in literature to build the model for PV power [73; 63; 65; and 84]. To ensure the accuracy of the multivariate regression based model discussed in this section, the basic physical model of PV array performance from [56] is used. The objective of this multivariate regression analysis is to develop a mathematical model of the closed form given by:

$$Pdc = Ipv * Vpv = f(weather\ data) \approx f(Irr, T_{amb}, wvel) \quad \ldots \text{ Eqn. (4-13)}$$

Where,

$Pdc =$ DC power from the PV module (W)

$Ipv =$ DC current from the PV module (A)

$Vpv =$ DC voltage across the PV module (V)

$Irr =$ Solar irradiance (W/m^2)

$T_{amb} =$ Ambient temperature (^{o}C)

$wvel =$ Wind velocity (m/s)

The thermal model relating the module temperature (T_{mdl}) with the three inputs in the Eqn. (4-13) is described as:

$$T_{mdl} = Irr\{e^{C_1 + C_2.wvel}\} + T_{amb} \quad \ldots \quad \text{Eqn. (4-14)}$$

Where, $C_i = Empirical\ Coefficients;\ i = 1,2, \ldots.$

Maclaurin series expansion of exponential function yields to,

$$e^x = 1 + x + \frac{x^2}{2!} + \frac{x^3}{3!} + \frac{x^4}{4!} + \cdots Higher\ Order\ Terms$$

Thus, elaborating the thermal model from Eqn. 4-14 gives:

$$T_{mdl} = \left\{1 + (C_1 + C_2.wvel) + \frac{(C_1 + C_2.wvel)^2}{2!} + \frac{(C_1 + C_2.wvel)^3}{3!} + \cdots H.O.T.\right\} Irr + T_{amb}$$

Ignoring the higher order terms (H.O.T.) beyond quadratic terms:

$$T_{mdl} \approx \left\{1 + (C_1 + C_2.wvel) + \frac{(C_1 + C_2.wvel)^2}{2!}\right\} Irr + T_{amb}$$

$$T_{mdl} = Irr + (C_1 + C_2.wvel)Irr + \left(\frac{(C_1 + C_2.wvel)^2}{2!}\right) Irr + T_{amb}$$

$$T_{mdl} = (1 + C_1)Irr + C_2.wvel.Irr + \left(\frac{{C_1}^2 + 2C_1C_2.wvel + {C_2}^2.wvel^2}{2}\right) Irr + T_{amb}$$

$$T_{mdl} = \left(1 + C_1 + \frac{{C_1}^2}{2}\right) Irr + (C_2 + C_1C_2)Irr.wvel + \left(\frac{{C_2}^2}{2}\right) Irr.wvel^2 + T_{amb}$$

The above equation can be used as the basis of the regression analysis to express the module temperature as a polynomial function of irradiance, ambient temperature and wind velocity. It can be rewritten as, without any loss of generality:

$$T_{mdl} = C_3 Irr + C_4 Irr.wvel + C_5 Irr.wvel^2 + C_6 T_{amb} \quad \ldots \quad \text{Eqn. (4-15)}$$

In Eqn. (4-15), C_6 is expected to be close to 1. All the coefficients here can be determined empirically based on robust regression analysis for the measured variables. This analysis was conducted separately on daily basis for different day types (as mentioned in Table 4-1). Fig. 4-14 shows median values of these regression coefficients for module temperature estimation in Eqn. (4-15) for different types of days over a year (Jul 1, 2014 - Jun 30, 2015).

As Fig. 4-14 suggests, numerically the coefficients C_4 and C_5 are smaller (in the order of 10^{-4}) than C_6 (~1) and C_3 (in the order of 10^{-2}) for all day types. It insinuates that irradiance and ambient temperature can be considered as dominant components, as compared to wind velocity, to estimate module temperature. This finding also reinstates the relatively weaker correlation between wind velocity and solar generation as identified in literature [62]. The thermal model can then be reconstructed as:

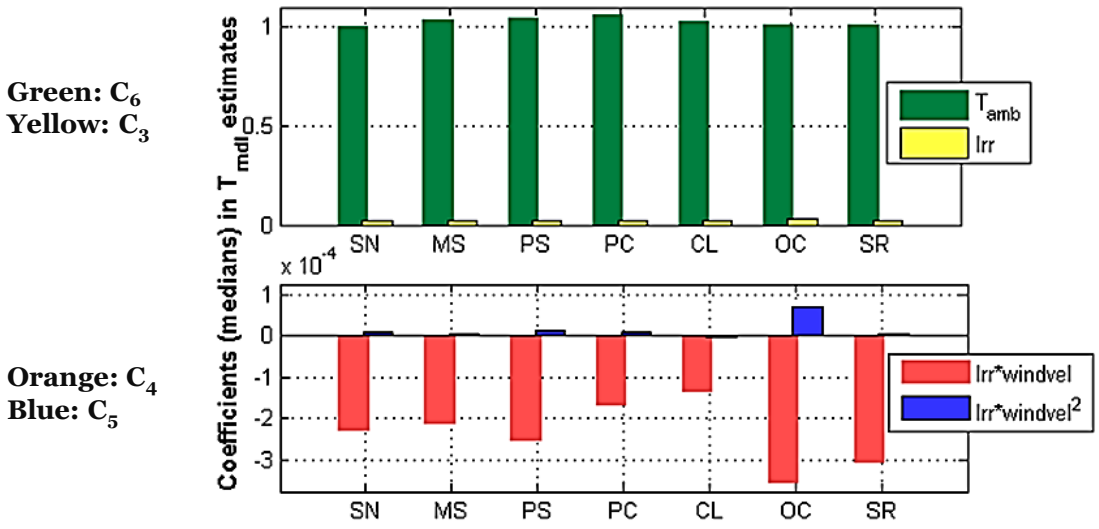

Fig. 4-14 Median coefficients (empirical) for constituent terms in module temperature estimates for different day types

[SN: Sunny, MS: Mostly Sunny, PS: Partly Sunny, PC: Partly Cloudy, CL: Cloudy, OC: Overcast, SR: Snowy/Rainy]

$$T_{mdl} = C_7 Irr + C_8 T_{amb} \quad \ldots \quad \text{Eqn. (4-16)}$$

The changes in module temperature estimates after dropping the wind velocity terms can be assessed with the errors for both models. Mean absolute percentage errors (MAPE) in module temperature estimation are shown in Fig. 4-15, for selected windy days (mean wind speed > 5m/s) within the one-year period (Jul 1, 2014 - Jun 30, 2015). As seen from this figure, including wind velocity in the model (Eqn. 4-15) provides marginal or no improvement in the module temperature estimation over the simplistic model which does not consider wind velocity (Eqn. 4-16). Also, module temperature estimation errors do not follow the same trend as the mean wind velocity for the given day. Hence, when necessary, Eqn. 4-16 is used to model the module temperature using irradiance and ambient temperature as independent variables.

Once module temperature is estimated, average cell temperature (T_C) in the PV array can be related to average back-surface module temperature by considering one-dimensional heat conduction through the module materials behind the cell. The cell temperature inside the module can then be calculated using a measured module temperature and a predetermined temperature difference between the back surface and the cell:

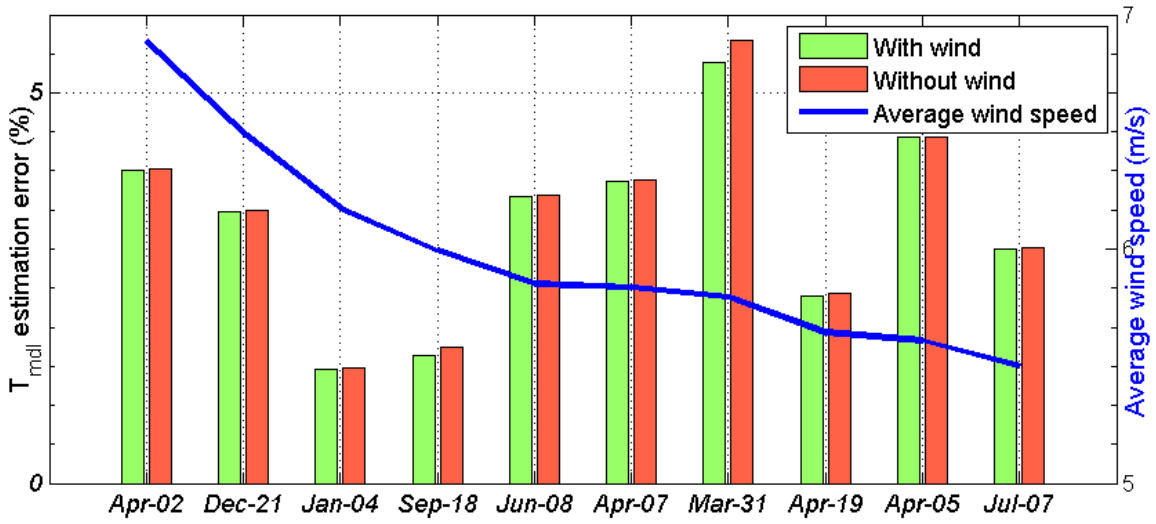

Fig. 4-15 Estimation errors for module temperature using models with and without wind velocity consideration, and corresponding average wind speed for the day

$$T_C = T_{mdl} + irr.T_{diff} \quad \ldots \quad \text{Eqn. (4-17)}$$

Where, normalized solar irradiance, $irr = \frac{Irr}{Irr_0}$

Here, Irr is the incident solar irradiance and Irr_0 is the reference irradiance ($= 1000\ \mathrm{W/m^2}$), and, T_{diff} denotes a predetermined temperature difference between the cell and the module temperature at the reference irradiance Irr_0 (T_{diff} is 3℃ for the PV module considered here). Because the PV system mostly operates in maximum power point tracking mode (MPPT), the current and voltage relations need to represent this mode of operation. At MPPT mode, the DC current (I_{mp}) and voltage (V_{mp}) for the PV module are given by:

$$\begin{aligned} I_{mp} &= I_{mp0}\{C_9 irr + C_{10} irr^2\}\{1 + C_{11}\Delta T\} \\ V_{mp} &= V_{mp0} + C_{12}\delta(T_C)\ln(irr) + C_{13}\{\delta(T_C)\ln(irr)\}^2 + C_{14} irr \Delta T \end{aligned} \quad \ldots \quad \text{Eqn. (4-18)}$$

In Eqn. (4-18), V_{mp0} and I_{mp0} are the voltage and current, respectively, in MPPT mode at standard reference condition (this reference condition is noted here with subscript '0', and refers to the operating condition of solar irradiance of $1000\ \mathrm{W/m^2}$ and solar cell temperature of 25℃). $\delta(T_C)$ in Eqn. (4-18) is the thermal voltage per solar cell at cell temperature T_C which can be considered negligible (mV range per cell) compared to V_{mp} which lies around 450 V . ΔT denotes the difference between the cell temperature (T_C) and reference condition temperature ($T_0 = 25$℃). Here,

$\delta(T_C) = \frac{nk(T_C + 273.15)}{q}$

$n = diode\ factor$

$k = Boltzmann's\ constant = 1.3\delta(T_C)8e - 23\ J/K$

$q = Elementary\ charge = 1.6e - 19\ C$

$$\Delta T = (T_C - T_0) \approx T_{mdl} + irr.T_{diff} - T_0 \quad \ldots \quad \text{Eqn. (4-19)}$$

Dropping the $\delta(T_C)$ terms, V_{mp} in Eqn. (4-18) can be rewritten as,

$$V_{mp} = V_{mp0} + C_{15} irr \Delta T$$

So, maximum dc power,

$$P_{mp} = I_{mp} * V_{mp} = \left[I_{mp0}\{C_9 irr + C_{10} irr^2\}\{1 + C_{11}\Delta T\}\right]\left[V_{mp0} + C_{15} irr \Delta T\right]$$

$$P_{mp} = \left[C_{16} irr + C_{17} irr^2 + C_{18} irr \Delta T + C_{19} irr^2 \Delta T\right]\left[V_{mp0} + C_{15} irr \Delta T\right]$$

$$P_{mp} = \left[C_{16} irr V_{mp0} + C_{17} irr^2 V_{mp0} + C_{18} irr \Delta T V_{mp0} + C_{19} irr^2 \Delta T V_{mp0} + \left(C_{16} irr V_{mp0} + C_{17} irr^2 V_{mp0} + C_{18} irr \Delta T V_{mp0} + C_{19} irr^2 \Delta T V_{mp0}\right) C_{15} irr \Delta T\right]$$

Or,

$$P_{mp} = C_{20} irr + C_{21} irr^2 + C_{22} irr \Delta T + C_{23} irr^2 \Delta T + C_{24} irr^3 \Delta T + C_{25} irr^2 \Delta T^2 \quad \ldots \text{ Eqn. (4-20)}$$

Eqn. (4-20) expresses P_{mp} as a function of intermediate variable irr and ΔT. The new set of empirical coefficients C_{20} to C_{25} merges the previous ones C_9 to C_{14} with V_{mp0} and I_{mp0}, since both of these parameters are constant for a specific PV unit. Ambient temperature and irradiance measurements can be used for this relationship through Eqn. (4-16), when measurements for module temperature are not available. However, the PV system considered here records temperature measurements using a sensor placed at the back of PV arrays along with other weather data. These measurements are used directly for T_{mdl} in Eqn. (4-19) for the model development. The coefficients C_{20} to C_{25} are determined through regression analysis performed on the measured dataset for each day using Eqn. (4.16) – (4-20). These coefficients represent the PV output model for the day which relates environmental variables to the solar generation. The final AC power output from the inverter is calculated from P_{mp} assuming 95.5% conversion efficiency.

While processing the raw measured dataset, data points which contain any erroneous measurements are discarded and data holes in the time-series are filled before the regression analysis. Examples of erroneous measurement can be- zero irradiance with non-zero power output, steep changes in temperature within a 15-second interval etc.

The output of this regression analysis are given in the following figures for several types of days in the month of January, 2014 (Figs. 4-16 – 4-20). These plots show the estimated MPPT dc power output using the irradiance and module temperature data. The plots are only shown for daytime (from sunrise to sunset). Both the mean and median of the percentage errors are reported with the plots.

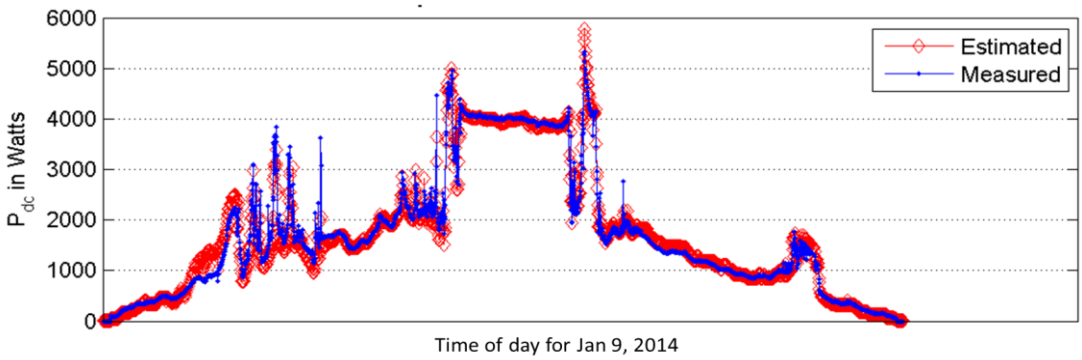

Fig. 4-16 PV dc power estimate for Jan 9, 2014

(Day type: Partly sunny; %error: mean=8.7, median=5.5)

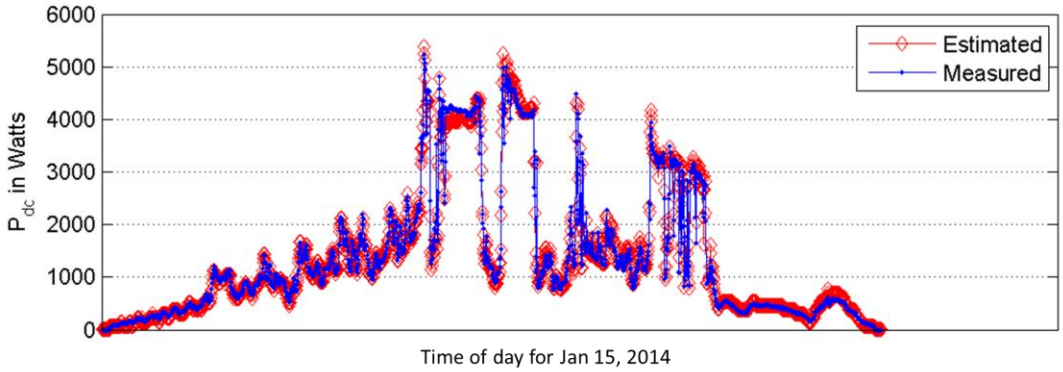

Fig. 4-17 PV dc power estimate for Jan 15, 2014

(Day type: Cloudy; %error: mean=7.1, median=4.2)

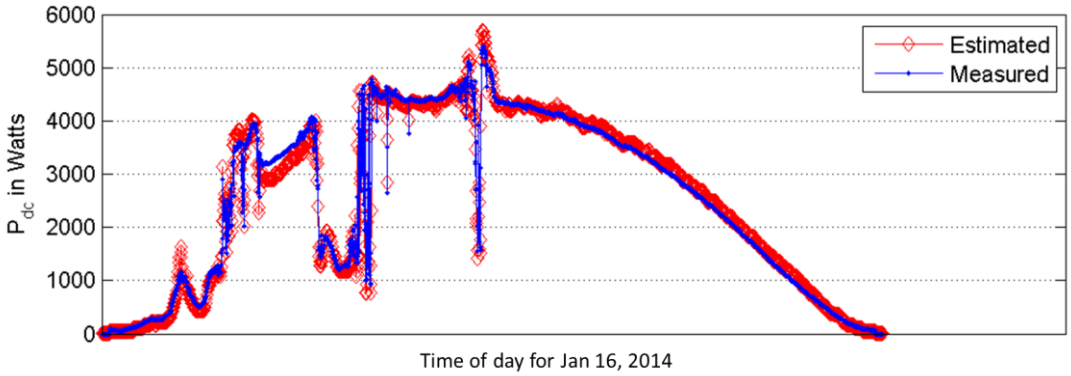

Fig. 4-18 PV dc power estimate for Jan 16, 2014

(Day type: Mostly sunny; %error: mean=7.9, median=4.2)

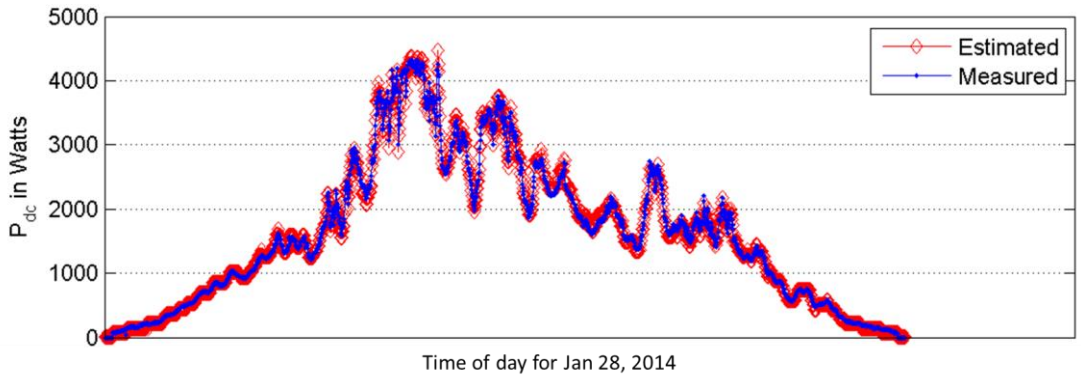

Fig. 4-19 PV dc power estimate for Jan 28, 2014

(Day type: Partly cloudy; %error: mean=4.6, median=2.5)

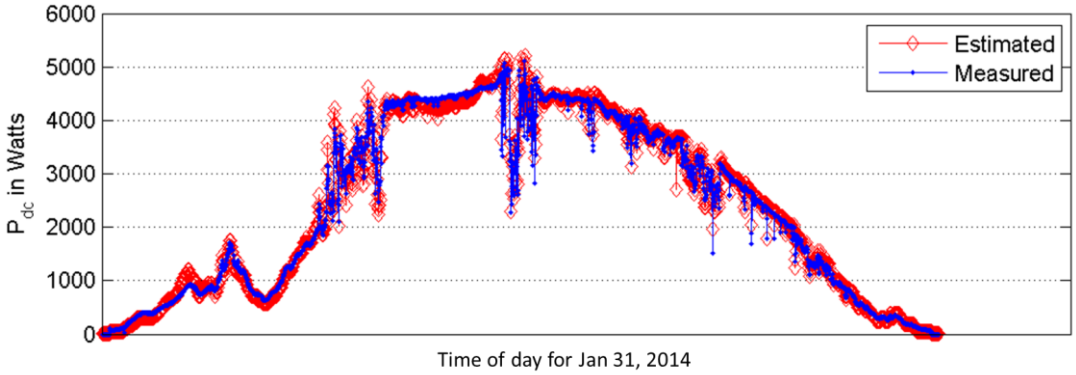

Fig. 4-20 PV dc power estimate for Jan 31, 2014

(Day type: Mostly sunny; %error: mean=6.2, median=2.8)

Following section presents PV dc power estimates through regression analysis for different day types with respect to seasonal differences.

Day type- Sunny:

Following are the regression results for sunny days for four different seasons: Mar-May (spring), Jun-Aug (summer), Sep-Nov (fall), and Dec-Feb (winter) in the year of 2013. Firstly, the PV output is estimated by the modified equation for a given day with irradiance and module temperature measurements. Then for the season, the median is calculated from all available daily data (of the sunny day type) and it is used to estimate daily output. Later, the seasonal coefficients from 2013 are also used to estimate PV output in 2014.

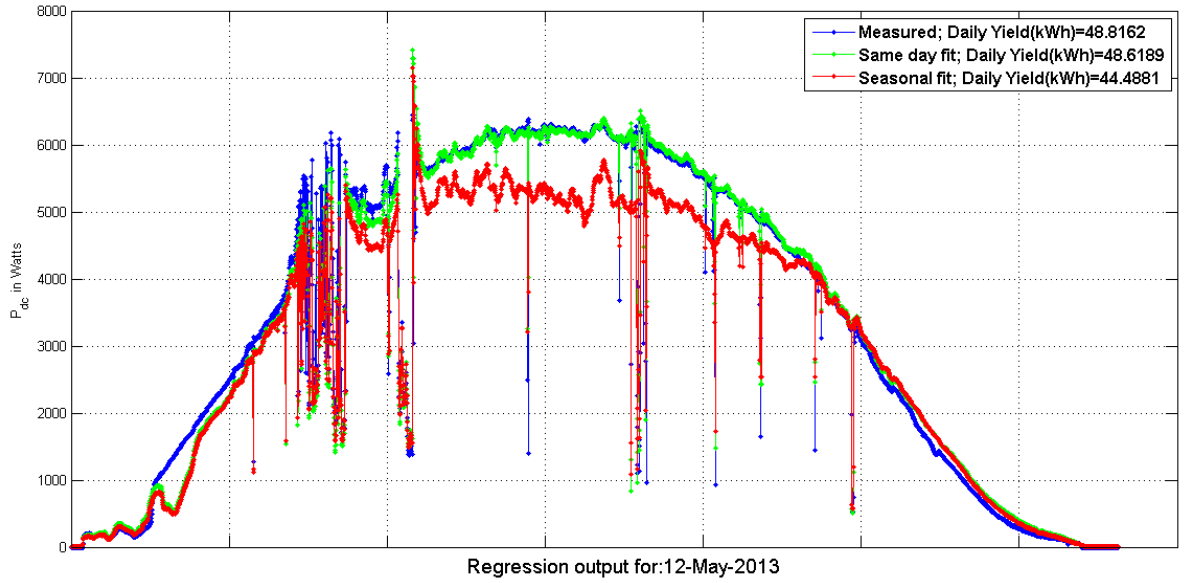

Fig. 4-22 Regression based estimation of PV power for May 12, 2013; considering regression coefficients from spring data

Fig. 4-21 shows the regression analysis for May 12, 2013 where the seasonal fit is estimated from the coefficients for the available sunny day data in spring (Mar-May). This regression estimate gets closer to the measured value, as depicted in Fig. 4-22, if the median set is used from Apr-Sep (long summer depicting the range from spring to fall equinox) instead of Mar-May. This happens

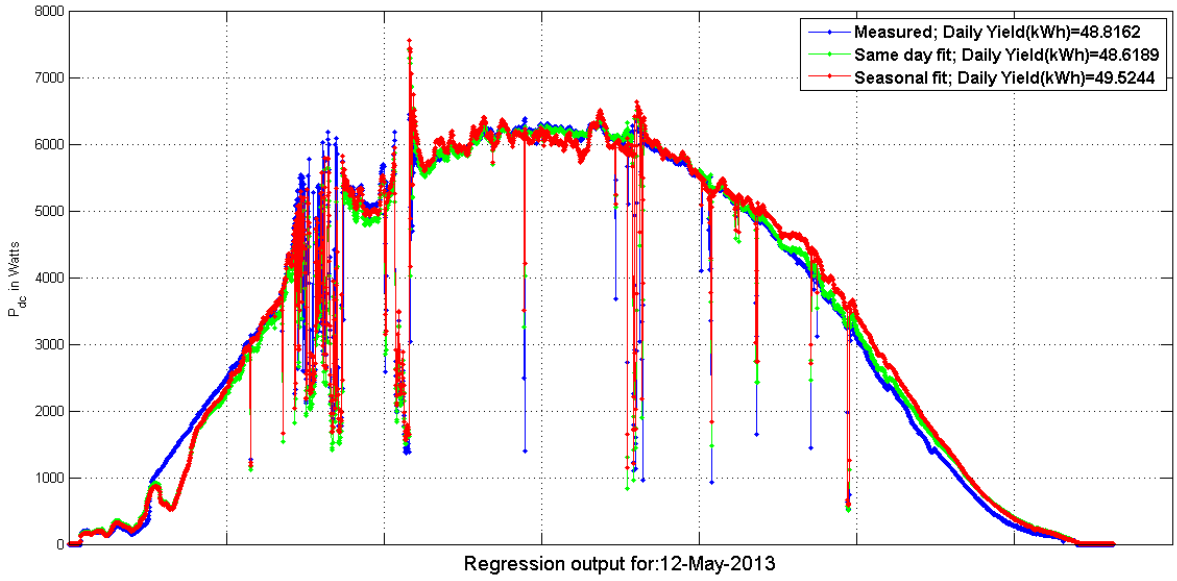

Fig. 4-21 Regression based estimation of PV power for May 12, 2013; considering regression coefficients from long summer data

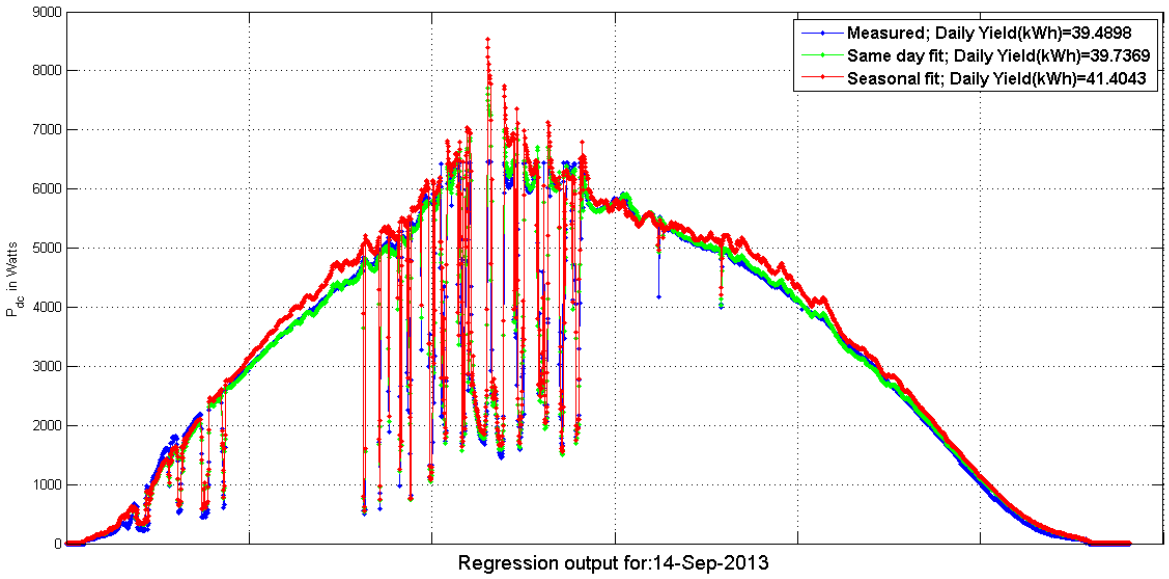

Fig. 4-23 Regression based estimation of PV power for Sep 14, 2013; considering regression coefficients from long summer data

because the insolation keeps getting higher in the summer time and that is better reflected in the extended summer range compared to the case when only spring is considered.

Similarly, for a day in September, the estimate based on long summer data is given in Fig. 4-23. When the coefficients are determined from fall data (Sep-Nov) instead of the long summer data the estimated daily yield becomes 41.0607 kWh, whereas with long summer model it is 41.4043 kWh. So, the error in the estimated PV power compared with the measured value is marginally reduced from 4.85% to 3.98% with long summer data. The following table (Table 4-4) summarizes regression estimates of daily yield (kWh) for some more sunny days in 2013.

Table 4-4 Regression estimates of daily solar generation for sunny days in 2013

Day	Measured *(kWh)*	Regression estimate from the same day *(kWh)*	Regression estimate based on sunny days in the same season (quarterly): spring (mar-may)/summer (jun-aug)/fall (sep-nov)/winter (dec-feb) *(kWh)*	Regression estimate based on sunny days in the same season(bi-yearly): long summer (apr-sep)/long winter (oct-mar) *(kWh)*
Apr 22	38.9433	39.0532	35.7224	39.8890
Jun 15	45.3637	43.8895	44.2036	41.2904
Sep 4	41.3725	41.5127	41.6590	40.5390
Nov 18	25.1022	25.1307	24.4830	24.4287
Dec 26	19.6743	19.7558	18.0918	18.9790
Jan 8	20.8140	20.8116	18.9935	19.9314
Feb 21	34.4199	34.8055	32.3481	34.1875

Table 4-5 Regression estimates of daily solar generation for cloudy days in 2013

Day	Measured *(kWh)*	Regression estimate from the same day *(kWh)*	Regression estimate based on sunny days in the same season (quarterly): spring (mar-may)/summer (jun-aug)/fall (sep-nov)/winter (dec-feb) *(kWh)*	Regression estimate based on sunny days in the same season(bi-yearly): long summer (apr-sep)/long winter (oct-mar) *(kWh)*	Regression estimate based on cloudy days throughout the whole year *(kWh)*
Feb 7	9.0957	9.0833	9.3996	8.7944	8.9584
Apr 28	22.7382	22.6648	24.3064	20.8156	20.9727
Jul 3	25.3564	25.4291	25.6982	23.2941	23.8869
Nov 1	11.5249	11.5392	11.0976	10.7434	11.2075

Day type-cloudy:

As seen in Figs. 4-24 and 4-25, the accuracy of the estimates with winter data (Dec-Feb) and long winter (Oct-Mar) data remains almost same for the cloudy days. In Table 4-5 regression estimates for some more cloudy days in 2013 are presented. Table 4-5 suggests that, for cloudy day type the seasonal variation does not alter the performance of this regression analysis. Coefficients derived for the whole year do not really degrade the performance of the regression either.

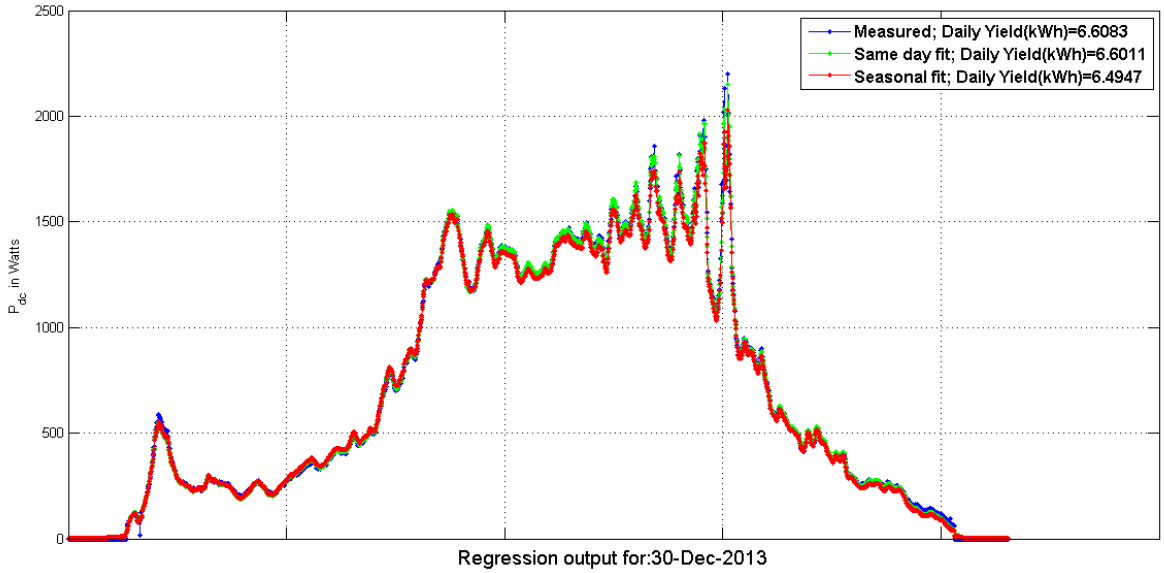

Fig. 4-24 Regression based estimation of PV power for Dec 30, 2013; considering regression coefficients from long winter data

Until now the analyses have been performed to reconstruct the daily solar generation profiles for 2013 based on the data from the same year. In the following part, the regression technique is applied on an uncorrelated data set, i.e. on some daily data from 2014; based on the corresponding seasonal coefficients derived from 2013 data. Table 4-6 and 4-7 summarize the estimated daily solar generations for different types of days in 2014 which are calculated with the representative coefficients from the same season as in 2013.

Table 4-6 Regression estimates of daily solar generation for snowy/rainy day type in 2014; based on coefficients derived from similar (season-wise) data in 2013

Day (mm/dd/ 2014)	Day type	Measured *(kWh)*	Regression estimate from the same day *(kWh)*	Regression estimate based on sunny days in the same season (quarterly): spring (mar-may)/summer (jun-aug)/fall (sep-nov)/winter (dec-feb) *(kWh)*	Regression estimate based on sunny days in the same season(bi-yearly): long summer (apr-sep)/long winter (oct-mar) *(kWh)*	Regression estimate based on cloudy days throughout the whole year *(kWh)*
Jan 10	Snowy/ rainy	3.537	3.5409	3.9988	3.1157	4.0354
Feb 5	Snowy/ rainy	5.61	5.6144	6.4898	4.4772	6.4249
Mar 19	Snowy/ rainy	8.8658	8.8649	8.9506	7.1905	10.3313

These tables show that the regression coefficients determined from 2013 data mostly give good estimates for days in 2014. Also, it can be observed that, the sunnier the day gets, the more visible the seasonal variation becomes, meaning for sunny and mostly sunny types of days, the estimate is likely to be more precise when coefficients are taken for a season, rather than lumped up for the whole year. For gloomy days, the lack of direct beam radiation is reflected in the fact that the solar generation would have less seasonal effects. Another thing to be noted is that, seasons defined in shorter duration (3 months) might not always provide better results than the ones defined in longer period (6 months). Especially, towards the end of spring (Mar-May) the regression technique tend to underestimate the solar generation as it is very close to ensuing summer. In such cases, coefficients from long winter/summer are seen to provide better results than spring-summer-fall-winter stratification.

Table 4-7 Regression estimates of daily solar generation for other day types in 2014; based on coefficients derived from similar (season-wise) data in 2013

Day (mm/dd/ 2014)	Day type	Measured *(kWh)*	Regression estimate from the same day *(kWh)*	Regression estimate based on sunny days in the same season (quarterly): spring (mar-may)/summer (jun-aug)/fall (sep-nov)/winter (dec-feb) *(kWh)*	Regression estimate based on sunny days in the same season(bi-yearly): long summer (apr-sep)/long winter (oct-mar) *(kWh)*	Regression estimate based on cloudy days throughout the whole year *(kWh)*
Apr 4	Overcast	13.4342	13.4217	13.7819	14.6603	14.835
Apr 3	Cloudy	19.5401	19.504	21.8335	19.096	19.1267
May 21	Partly Cloudy	26.2536	26.1918	26.4156	22.7572	24.9288
Apr 25	Partly Cloudy	30.4148	30.6876	29.9521	27.8197	29.3886
Jan 28	Partly Sunny	15.8184	15.7757	9.33172	17.4162	18.6136
Feb 4	Mostly Sunny	19.5298	19.4897	17.3279	25.2826	23.0883
Mar 6	Mostly Sunny	27.6642	27.7552	36.4355	27.4838	34.0517
Jan 30	Sunny	30.071	30.2578	27.6272	29.021	33.0657
Feb 6	Sunny	24.5309	24.5488	24.8343	25.8201	29.9071
Mar 9	Sunny	38.9703	38.8822	45.0284	38.4649	41.0527
Apr 17	Sunny	47.2857	47.54	45.2562	49.9794	41.897
May 19	Sunny	46.7687	46.4692	39.876	45.6894	38.3477

As seen from all these discussions, the best estimation for the empirical regression based model can be derived from the data for the given day. However, this modeling will not be applicable for its integration with the forecasting model. So, at the start of the day an initial model is derived based on the previous data, but the model is evaluated again (after couple of hours past sunrise) so that available measurements (for the same day till the time of recalculation) can enhance the model.

4.1.3 PV power forecasting model using Kalman Filtering technique

Direct solar generation forecasting methods rely on the inherent non-linear relationship between the PV output power and the weather data. Researchers have investigated various input parameters to build the model for PV power. As mentioned in the previous section (section 4.1.2), a basic physical model can be defined as [56]:

$$P_{PV}(t) = f(Irr(t), T_{amb}(t), wvel(t)) \quad \ldots \quad \text{Eqn. (4-21)}$$

Where,

$P_{PV}(t) = dc\ power\ generated\ by\ the\ PV\ array\ (W)\ at\ time\ 't'$

$Irr(t) =\ irradiance\ on\ plane\ (W/m^2)\ at\ time\ 't'$

$T_{amb}(t) = ambient\ temperature\ (℃)\ at\ time\ 't'$

$wvel(t) = wind\ velocity\ (m/s)\ at\ time\ 't'$

The function 'f' is understandably non-linear but can be expanded and linearized with respect to the derivative parameters from the weather data mentioned in the equation. After linearization, the coefficients of the weather parameters can be determined empirically. Instead of a fixed function, it can also be tailored to vary according to weather type of the day for providing better forecasting accuracy, as suggested by previous research works.

So, if time-series prediction for weather data or NWP data can be derived, the generation forecast can be expressed as a function of past weather data and power measurements. The weather data can be expressed mathematically as,

$$Irr(t+1) = f_i(Irr(t), X_{Irr}(t))$$

$$T_{amb}(t+1) = f_t\big(T_{amb}(t), X_{T_{amb}}(t)\big)$$

$$wvel(t+1) = f_w(wvel(t), X_{wvel}(t))$$

Where, the X's denote external inputs to the time transition functions f_i, f_t, and f_w and they can include any past data like weather data measurement or power measurement or any derivative available at time 't'. Here, the terms denoted with subscripted X stand for time-lagged variables, or,

$$X_{Irr}(t) = \begin{Bmatrix} Irr(t-1), Irr(t-2), \dots, Irr(t-\tau_i), T_{amb}(t), T_{amb}(t-1), \dots, \\ T_{amb}(t-\tau_t), wvel(t), wvel(t-1), \dots, wvel(t-\tau_w) \end{Bmatrix}$$

Where, τ_i, τ_t, τ_w are different integers which can take on similar or dissimilar values. To put it simply, these transition functions assume that irradiance at a time 't' can be modeled as a function of past irradiance values, and/or past and present values of temperature and wind velocity. Although preliminary analyses show that, the cross-correlation among these parameters are not too pronounced.

The nature of the transitional functions will again vary according to weather type and diurnal cycle. For a particular weather parameter, the correlation with other parameters would reveal how this prediction model would shape up. For example, in very short-term scenario (sub-minute interval), the ambient temperature would not change much. So, for ambient temperature, the transition function can only have previous ambient temperature measurements as its inputs; i.e. it can be expressed with an autoregressive model with no exogenous inputs. But, its autocorrelation function for the defined time interval has to be studied for determining how many past components need to be included in this function to accurately model the series for ambient temperature.

Physical model based on the historical dataset:

Regression analysis is done to derive this model which looks like,

$$P(n) = \boldsymbol{A}(n) * \boldsymbol{x}(n) \quad \ldots \quad \text{Eqn. (4-22)}$$

Or,

$$P(n) = A_1 x_1(n) + A_2 x_2(n) + \cdots + A_M x_M(n)$$

Here,

$P(n) = output\ or\ estimated\ PV\ generation\ at\ nth\ instance$

$x_1(n), x_2(n), \ldots\ x_M(n) = state\ variables\ derived\ from\ input\ measurements;$
$i.e.\ direct\ or\ derived\ parameters\ concerning\ Irr(n), T_{amb}(n), wvel(n)$

$\boldsymbol{A}(n) = coefficient\ matrix\ for\ state\ variables$

$And, the\ modeling\ error\ for\ P(n)\ is,$
$e(n) = P_{PV}(n) - P(n);\ when\ P_{PV}(n)\ is\ the\ true\ value\ or\ the\ measured\ PV\ generation$

The weights $A_1(n), A_2(n), \ldots\ A_M(n)$ are calculated from the regression analyses conducted on the training dataset. This dataset can include the measurements of a whole year, a particular season or just the day in question. Also, for more accurate modeling, these gains can again be changed as the time changes. Then, the PV model would become,

$$P(n) = A_1(n)x_1(n) + A_2(n)x_2(n) + \cdots + A_M(n)x_M(n)$$

For the sake of simplicity, the above equation can be rewritten as a linear form with the direct variables:

$$P(n) = A_1(n)Irr(n) + A_2(n)T_{amb}(n) + A_3(n)wvel(n) \quad \ldots \quad \text{Eqn. (4-23)}$$

As the physical model for PV power developed in section 4.1.2 includes irradiance and module temperature (T_{mdl}), Eqn.4-23 can be rewritten as:

$$P(n) = A_1(n)Irr(n) + A_2(n)T_{mdl}(n) \quad \ldots \quad \text{Eqn. (4-24)}$$

Or, $P(n) = \begin{bmatrix} A_1(n) & 0 \\ 0 & A_2(n) \end{bmatrix} \begin{bmatrix} Irr(n) \\ T_{amb}(n) \end{bmatrix}$

The development of the above model is discussed in details in the previous section of this chapter. As the above equation shows, this model calculates instantaneous values of $\boldsymbol{A}(n)$ based on the weather classification. Such classification is done beforehand to provide better accuracy to model the PV generation with input weather parameters. This analysis takes into account the weather type for a short-term scenario as well, i.e. the coefficient matrix or the gain values change when the weather is 'sunny' for a particular hour even though the day can be 'cloudy' as a whole.

Application of Kalman Filter (KF) theory

Once the regression based physical model is ready for assessing PV performance, it can be written as a discrete time linear system model, as described in [116]. In other words, the above equation can be rewritten in the form of:

$$\boldsymbol{z}(n) = \boldsymbol{H}(n)\boldsymbol{x}(n) + \boldsymbol{v}(n) \quad \ldots \quad \text{Eqn. (4-25)}$$

Where,

$\boldsymbol{z} = observation\ vector\ \{dimension\ (M \times 1)\} \approx measured\ PV\ generation\ or\ P_{PV}(n)$

$\boldsymbol{H} = observation\ matrix\ \{dimension\ (M \times N)\}$ or,

$$\boldsymbol{H}(n) = \begin{bmatrix} A_1(n) & 0 \\ 0 & A_2(n) \end{bmatrix} \quad \ldots \quad \text{Eqn. (4-26)}$$

$\boldsymbol{x} = state\ vector\ \{dimension\ (N \times 1)\} \approx \begin{bmatrix} Irr(n) \\ T_{mdl}(n) \end{bmatrix}$ or,

$$\boldsymbol{x}(n) = \begin{bmatrix} Irr(n) \\ T_{mdl}(n) \end{bmatrix} \quad \ldots \quad \text{Eqn. (4-27)}$$

$\boldsymbol{v} = observation\ uncertainty\ or\ measurement\ noise\ vector\ \{dimension\ (M \times 1)\} \approx e(n)$

$\boldsymbol{H}(n)\boldsymbol{x}(n) = \tilde{\boldsymbol{z}}(n) = measurement\ estimate\ from\ the\ state\ variables\ for\ \boldsymbol{z}(n)$

The dimensions M=1 (number of measurement parameters) here, while N=2 (number of state variables) for PV model based on irradiance and temperature.

For time increment between adjacent samples, the state space structure in this model can be described as:

$$\boldsymbol{x}(n+1) = \boldsymbol{\Phi}(n)\boldsymbol{x}(n) + \boldsymbol{G}(n)\boldsymbol{w}(n) \quad \ldots \quad \text{Eqn. (4-28)}$$

Here,

$\boldsymbol{\Phi}(n) = state\ transition\ matrix\ \{dimension\ (N \times N)\}$

$\boldsymbol{G}(n) = process\ noise\ gain\ matrix\ \{dimension\ (N \times N_w)\}$

$\boldsymbol{w}(n) = process\ noise\ or\ disturbance\ vector\ \{dimension\ (N_w \times 1)\}$

Here, the parameter N_w denotes the number of process noise elements modeled into the system. The noise vectors $\boldsymbol{v}$ and $\boldsymbol{w}$ are modeled stochastically, and are assumed to be white processes in Bayesian models. Also all the matrices, i.e. $\boldsymbol{H}, \boldsymbol{\Phi}, \boldsymbol{G}$ are known. But in the case of regression based PV model, as the inherent relationship among the irradiance, temperature and PV output are non-linear and is determined empirically, following assumptions are considered to make the KF theory applicable:

$N_w = N\ (number\ of\ states = 2)$

$\boldsymbol{G}(n) = I_N = \begin{bmatrix} 1 & 0 \\ 0 & 1 \end{bmatrix}$

So,

$\boldsymbol{x}(n+1) = \boldsymbol{\Phi}(n)\boldsymbol{x}(n) + \boldsymbol{w}(n)$

And,

$\boldsymbol{\Phi}(n)\boldsymbol{x}(n) = \tilde{\boldsymbol{x}}(n+1) = state\ estimate\ for\ \boldsymbol{x}(n+1)$

$\boldsymbol{w}(n-1) = numerically\ calculated\ from\ the\ measurements = \boldsymbol{x}(n) - \tilde{\boldsymbol{x}}(n)$

Theoretically, the best estimate of a state vector ($\boldsymbol{\Phi}(n)\boldsymbol{x}(n)$) is given by, $\boldsymbol{\Phi}(n)\hat{\boldsymbol{x}}(n|n)$

Where, the notation stands for,

$\hat{\boldsymbol{x}}(n_1|n_2) = best\ estimate\ of\ the\ state\ \boldsymbol{x}(n_1)\ using\ observations\ \ \boldsymbol{z}(1) \ldots \boldsymbol{z}(n_2)$

Where, $n_1 > n_2$

So, for one-step prediction, the best prediction for the next-step can be written as,

$$\hat{\boldsymbol{x}}(n+1|n) = \boldsymbol{\Phi}(n)\hat{\boldsymbol{x}}(n|n)$$

Or, in other words,

$$\boldsymbol{x_p}(n+1) = \boldsymbol{\Phi}(n)\boldsymbol{x_c}(n) \quad \ldots \quad \text{Eqn. (4-29)}$$

Where,

$$\hat{\boldsymbol{x}}(n+1|n) = \boldsymbol{x_p}(n+1) = predicted\ estimate\ of\ \boldsymbol{x}(n+1), calculated\ at\ nth\ time\ step$$

$$\hat{\boldsymbol{x}}(n|n) = \boldsymbol{x_c}(n) = corrected\ estimate\ of\ \boldsymbol{x}(n)\ based\ on\ measured\ \boldsymbol{z}(n)$$

This correction of the state variables is done over the predicted value from the previous time step.

$$\boldsymbol{x_c}(n) = \boldsymbol{x_p}(n) + \boldsymbol{K}(n)\{\boldsymbol{z}(n) - \boldsymbol{z_p}(n)\} \quad \ldots \quad \text{Eqn. (4-30)}$$

Where,

$$\boldsymbol{x_p}(n) = predicted\ estimate\ of\ \boldsymbol{x}(n), calculated\ at\ (n-1)th\ time\ step$$

$$\boldsymbol{K}(n) = Kalman\ Gain$$

This time-varying value of Kalman gain introduces differential correction to the predicted estimate based on the error as measured from the current instance or $\{\boldsymbol{z}(n) - \boldsymbol{z_p}(n)\}$. Here, $\boldsymbol{z_p}(n)$ denotes the predicted estimate of the output $\boldsymbol{z}(n)$ which was again calculated in the previous time-step.

Thus, the application of KF theory can be formulated as an iterative method. There are three major steps discussed below as seen in an arbitrary iteration 'k':

- *Correction*:

This part involves the correction of the prediction as estimated in the previous iteration, (k-1). For the correction, prediction error of the output variable is needed. This error term takes instantaneous Kalman gain as its weight, so the Kalman gain is updated in this step too.

$$\boldsymbol{x_c}(k) = \boldsymbol{x_p}(k) + \boldsymbol{K}(k)\boldsymbol{e}(k) \quad \ldots \quad \text{Eqn. (4-31)}$$

Where,

$$\boldsymbol{K}(k) = \boldsymbol{P_p}(k)\boldsymbol{H}'(k)\left[\boldsymbol{H}(k)\boldsymbol{P_p}(k)\boldsymbol{H}'(k) + \boldsymbol{R}(k)\right]^{-1} \quad \ldots \quad \text{Eqn. (4-32)}$$

$$\boldsymbol{e}(k) = \boldsymbol{z}(k) - \boldsymbol{z_p}(k)$$

Here,

$\boldsymbol{x_p}(k) = predicted\ estimate\ or\ the\ \boldsymbol{priori}\ estimate\ of\ \boldsymbol{x}(k), calculated\ previously\ at\ (k-1)^{th}\ iteration$

$\boldsymbol{x_c}(k) = corrected\ estimate\ or\ the\ \boldsymbol{posteriori}\ estimate\ for\ \boldsymbol{x}(k)\ based\ on\ measured\ values\ of\ \boldsymbol{z}(k)$

$\boldsymbol{K}(k) = Kalmain\ Gain\ for\ k^{th}\ iteration$

$\boldsymbol{e}(k) = prediction\ error\ for\ output$

$\boldsymbol{z}(k) = current\ measured\ output$

$\boldsymbol{z_p}(k) = prediction\ estimate\ of\ the\ output; as\ calculated\ in\ the\ (k-1)^{th}\ iteration$

$\boldsymbol{P_p}(k) = auto\ covariance\ matrix\ for\ predicted\ state\ estimate\ error;$

$derived\ in\ (k-1)^{th}\ iteration$

$\boldsymbol{H}(k) = observation\ matrix\ or\ measurement\ gain\ matrix\ evaluated\ at\ k^{th}\ iteration$

$\boldsymbol{R}(k) = auto\ covariance\ matrix\ for\ measurement\ noise\ recorded\ till\ k^{th}\ iteration;$

$calculated\ from\ \boldsymbol{v}(1), \ldots, \boldsymbol{v}(k)$

While, as mentioned previously,

$\boldsymbol{v}(k) = \boldsymbol{z}(k) - \tilde{\boldsymbol{z}}(k) = measurement\ noise$

$\tilde{\boldsymbol{z}}(k) = \boldsymbol{H}(k)\boldsymbol{x}(k)$

$\boldsymbol{x}(k) = current\ state\ measurements$

- *Prediction*:

This step calculates the prediction estimate(s) for the next time step. For that, all the information available till the current time step is used. The state estimate predictions are based on the recently corrected state estimate. Prediction for the output take these state estimate predictions as inputs:

$$\boldsymbol{x_p}(k+1) = \boldsymbol{\Phi}(k)\boldsymbol{x_c}(k)$$
$$\boldsymbol{z_p}(k+1) = \boldsymbol{H}(k)\boldsymbol{x_p}(k+1) = P_{PV,pred}(k+1) \quad \ldots \quad \text{Eqn. (4-33)}$$

Where similarly,

$\boldsymbol{x_p}(k+1) = predicted\ state\ estimate\ for\ (k+1)^{th}\ iteration\ or\ \boldsymbol{x}(k+1)$

$\boldsymbol{z_p}(k+1) = predicted\ observation\ estimate\ for\ (k+1)^{th}\ iteration\ or\ \boldsymbol{z}(k+1)$

$\boldsymbol{\Phi}(k) = state\ transition\ matrix\ evaluated\ at\ k^{th}\ iteration$

$\boldsymbol{H}(k) = measurement\ gain\ matrix\ evaluated\ at\ k^{th}\ iteration$

- *Parameter update*:

Here the error covariance matrices are updated for future use or to be used in the next iteration. Auto covariance matrix for predicted state estimate error is estimated by:

$$\boldsymbol{P_p}(k+1) = \boldsymbol{\Phi}(k)\boldsymbol{P_c}(k)\boldsymbol{\Phi}'(k) + \boldsymbol{G}(k)\boldsymbol{Q}(k)\boldsymbol{G}'(k) \quad \ldots \quad \text{Eqn. (4-34)}$$

Where,

$\boldsymbol{G}(k) = \boldsymbol{I_N}$

$$\boldsymbol{P_c}(k) = \boldsymbol{P_p}(k) - \boldsymbol{P_p}(k)\boldsymbol{H}'(k)\left[\boldsymbol{R}(k) + \boldsymbol{H}(k)\boldsymbol{P_p}(k)\boldsymbol{H}'(k)\right]^{-1}\boldsymbol{H}(k)\boldsymbol{P_p}(k) \quad \ldots \quad \text{Eqn. (4-35)}$$

As, from Eqn. 4-32,

$$\boldsymbol{K}(k) = \boldsymbol{P_p}(k)\boldsymbol{H}'(k)\left[\boldsymbol{H}(k)\boldsymbol{P_p}(k)\boldsymbol{H}'(k) + \boldsymbol{R}(k)\right]^{-1}$$

Eqn. 4-35 becomes:

$\boldsymbol{P_c}(k) = \boldsymbol{P_p}(k) - \boldsymbol{K}(k)\boldsymbol{H}(k)\boldsymbol{P_p}(k)$

Or,

$$\boldsymbol{P_c}(k) = [\boldsymbol{I} - \boldsymbol{K}(k)\boldsymbol{H}(k)]\boldsymbol{P_p}(k) \quad \ldots \quad \text{Eqn. (4-36)}$$

Here,

$\boldsymbol{P_c}(k) = auto\ covariance\ matrix\ for\ corrected\ state\ estimate\ error$

$\boldsymbol{Q}(k) = auto\ covariance\ matrix\ for\ process\ noise\ at\ k^{th}\ iteration$

To apply the formulae as discussed here, the matrices which define the system model needs to be known. When the model dynamics are not known deterministically these matrices can take assumed values, or, the model can be derived empirically. For example, when very short-term forecasting (15 seconds) is being done, a simplistic form of the state transition model can assume that the cloud cover is unchanged and the ambient temperature change is constant.

So, an example of the state transition matrix ($\boldsymbol{\Phi_{vs}}$) for very-short term forecast can be given by:

$$\boldsymbol{\Phi_{vs}}(n) = \begin{bmatrix} cloud\ cover\ index(n-1) * clear\ sky\ irradiance(n) & 0 \\ 0 & rate\ of\ temperature\ change(n-1) \end{bmatrix}$$

Here, the cloud cover index can be measured from the deterministic clear sky irradiance component and measured irradiance value from the previous time step. Similarly, the temperature change can be assumed to have a constant rate which can act as the weight for the current measured temperature to model the temperature value at the very next time step.

But when the forecasting horizon is longer, for example 15-minute, such assumptions might not simulate the scenario accurately in the model. For that case, multi-step KF technique can be used from 15 seconds time-series data recording or the problem can be formulated based on average values recorded every fifteen minutes only. In the latter case, weather forecast information or NWP data (from external online applications) can be used as the inputs to the model to provide the PV output forecast. This way, the temporal model is built on longer timescale which have different transitory propertied for the input parameters. For instance, weather prediction can provide numerical values for predicted ambient temperature and clearness parameter (like cloudy, sunny, rainy etc.). Using these values module temperature estimates can be built with Eqns. (4-16–4-20).

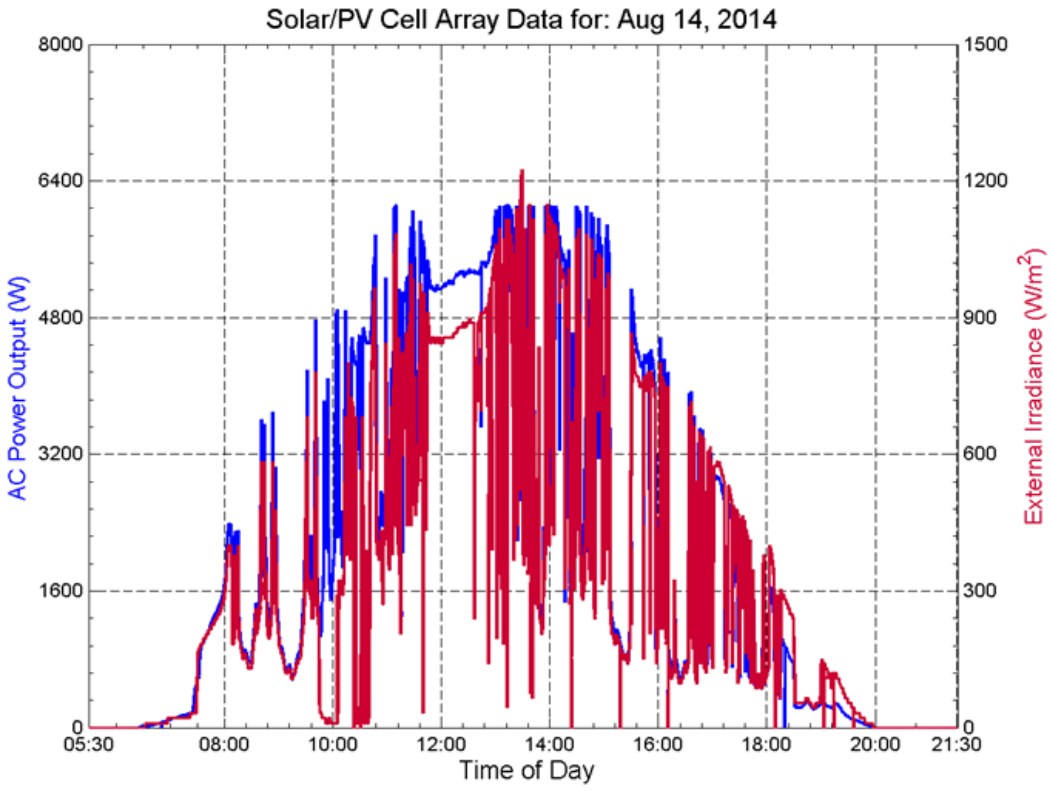

Fig. 4-26 PV AC output and horizontal irradiance measurements for Aug 14, 2014

These equations can then replace the predicted state estimates in Eqn. (4-29) and provide output prediction accordingly.

The required parameters for developing the KF theory based forecasting models are thus irradiance and module temperature. Module temperature, as discussed in the regression analysis section, is again a function of irradiance and ambient temperature. So, the dynamic characteristic of module temperature will be different than the ambient temperature. The range of the transitional properties of module temperature can be seen when the irradiance fluctuates within a very wide range and short duration. Such a sample day is shown in Fig. 4-26 for Aug 14, 2014, when fast cloud movements caused fluctuations in irradiance/power profile almost throughout the day.

For this day, the autocorrelation properties of the module temperature are shown in the following figures (Figs. 4-27 – 4-30).

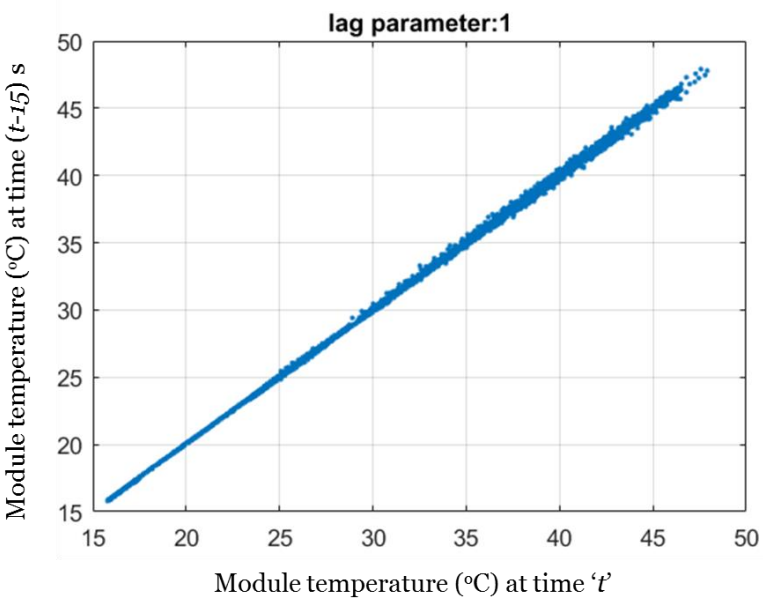

Fig. 4-27 Module temperature autocorrelation properties for lag=1 or 15s (Aug 14, 2014)

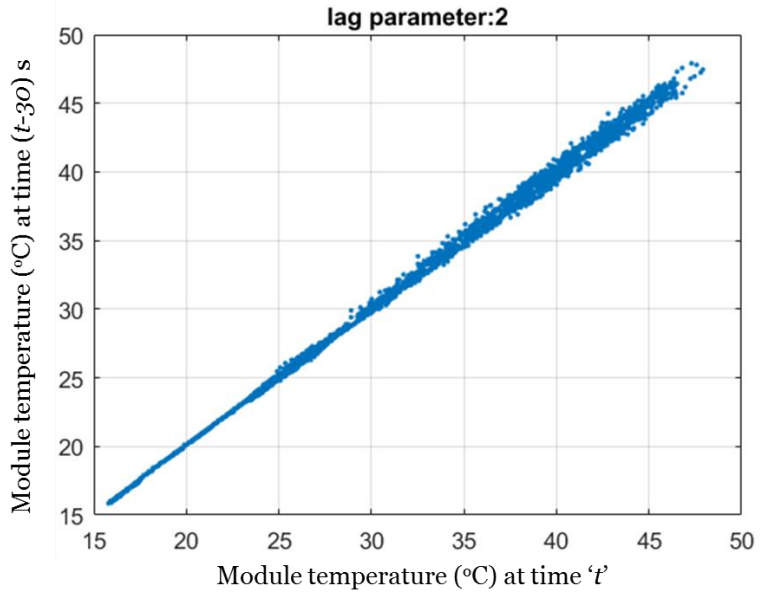

Fig. 4-28 Module temperature autocorrelation properties for lag=2 or 30s (Aug 14, 2014)

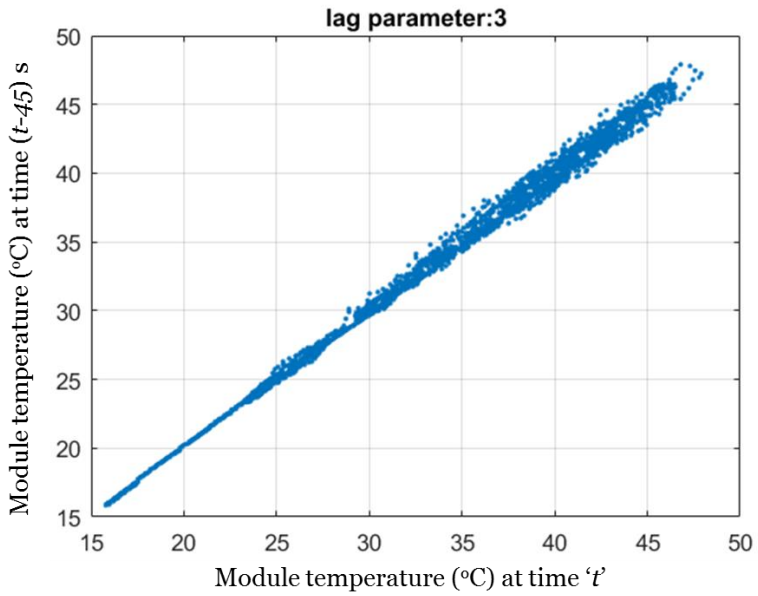

Fig. 4-29 Module temperature autocorrelation properties for lag=3 or 45s (Aug 14, 2014)

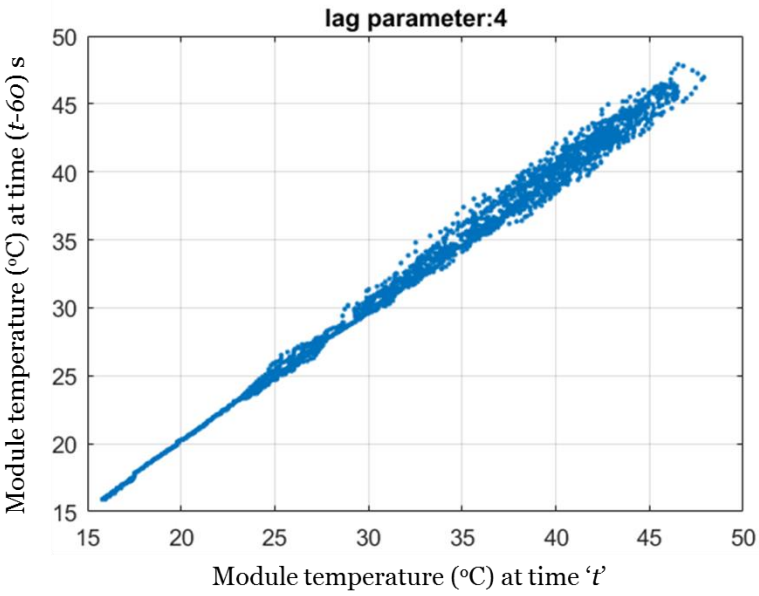

Fig. 4-30 Module temperature autocorrelation properties for lag=4 or 60s (Aug 14, 2014)

As seen from Figs. 4-27 – 4-30, nearly linear relationship between time lagged module temperature starts to get obscured when the time lag is 60-second. Hence, for this forecasting model module temperature is expressed as a function of its three previous measurements.

The output from the KF technique based forecasting models are now plotted in the Fig. 4-31– 4-35 for selected days of different day types in 2014. Corresponding forecasting errors, measured

both in MAPE and nRMSE (as defined in Eqn. 2-1 and 2-4) are also mentioned. The normalization constant is the rated PV power for nRMSE calculations.

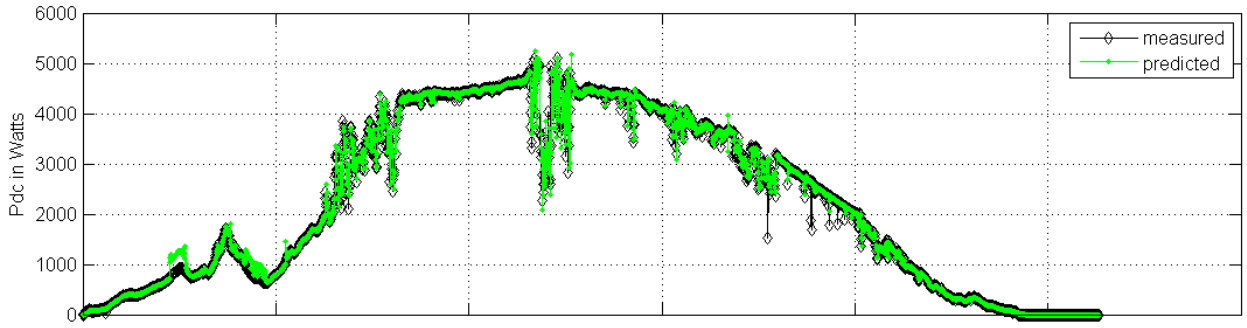

Fig. 4-31 Measured and forecast PV power (dc) for Jan 31, 2014 {mostly sunny}

(MAPE=4.5%, nRMSE=3.5%)

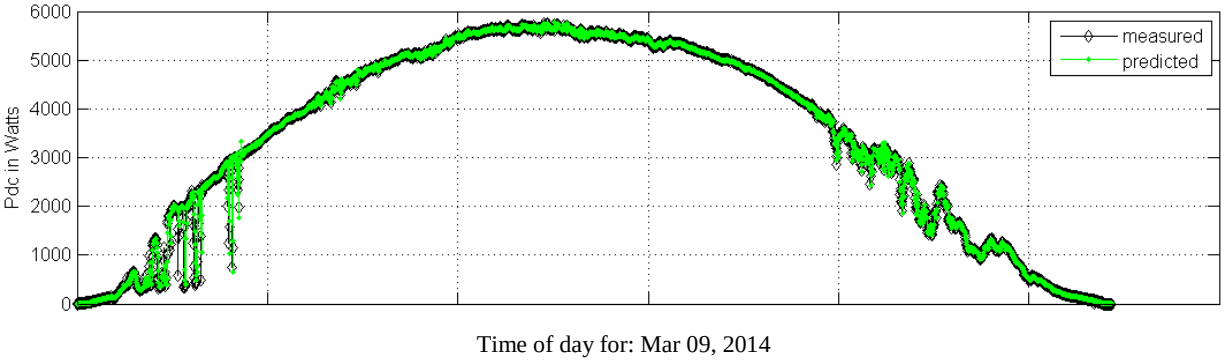

Fig. 4-32 Measured and forecast PV power (dc) for Mar 09, 2014 {sunny}

(MAPE=4.3%, nRMSE=2.2%)

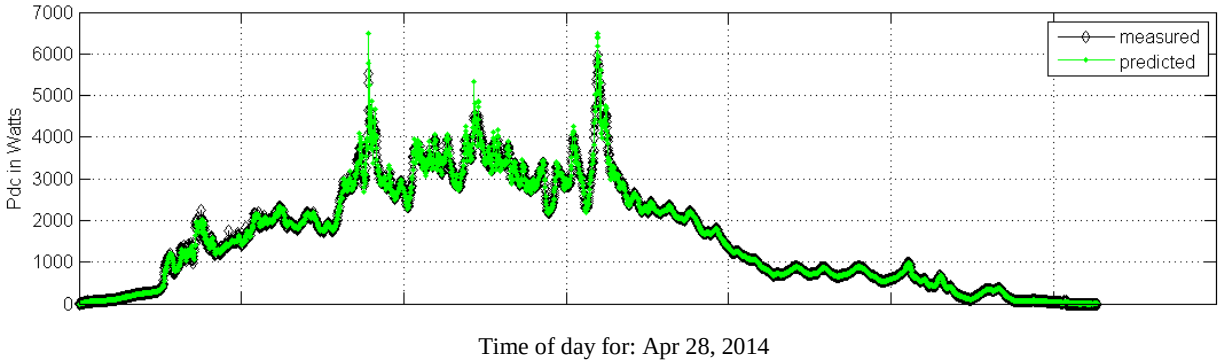

Fig. 4-33 Measured and forecast PV power (dc) for Apr 28, 2014 {cloudy}

(MAPE=2.4%, nRMSE=1.2%)

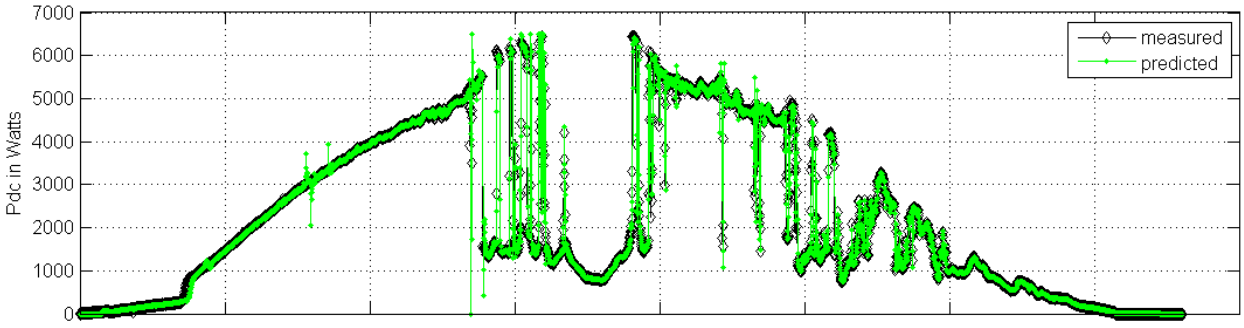

Fig. 4-34 Measured and forecast PV power (dc) for Jun 27, 2014 {partly cloudy}

(MAPE=6.6%, nRMSE=5.6%)

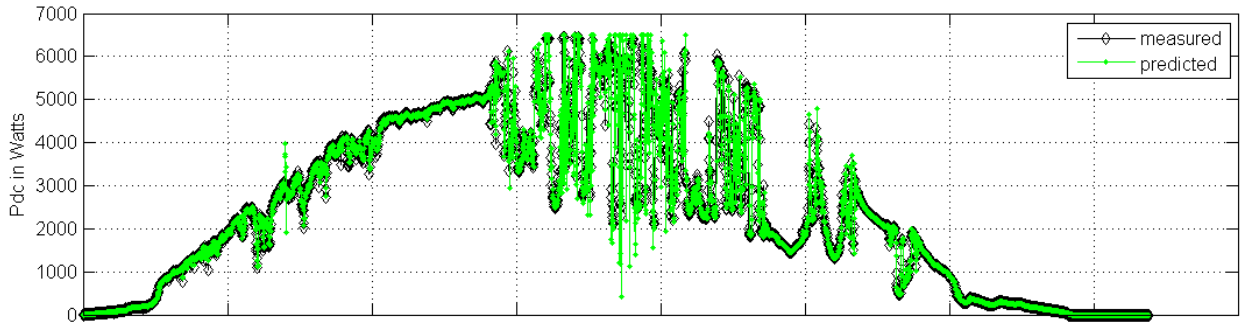

Fig. 4-35 Measured and forecast PV power (dc) for Jul 13, 2014 {partly sunny}

(MAPE=5.6%, nRMSE=6.1%)

As seen from these figures, the forecasting error is mostly dependent on the transitional changes rather than on the day types. Both MAPE and nRMSE increase when large and quick cloud transients are present. To improve the accuracy, the dynamic properties of the cloud cover index will be analyzed and incorporated with this forecasting model.

In this forecasting model, initial observation matrix elements or the regression coefficients are calculated from historical database when the day is starting. For sunny and mostly sunny days, the initial model is derived from regression analysis done over summer-fall-winter-spring classification. For the rest of the days, bi-yearly regression outputs are used, i.e. long summer and

long winter classification is taken. As discussed in section 4.1.2, the best performance is provided by the local fit for the same day. That's why this model re-calculates the gain matrix within the day when enough data are gathered (typically after 5-6 hours from sunrise).

Performance comparison with Naïve prediction method

To compare the performance of this proposed KF based method, a naïve predictor model is used here as benchmark. This predictor assumes that the PV power production for the next time step ($P_{PV,pred,Naive}(k+1)$) would be equal to the measurement for PV generation from the current time instance ($P_{PVg}(k)$), as mentioned in following equation:

$$P_{PV,pred,Naive}(k+1) = P_{PVg}(k)$$

Evidently, the performance of the proposed method will not be vividly different from the naïve predictor when the day is sunny or there is not much cloud movement. An example is shown in Fig. 4-36 where forecast outputs are compared with measured PV power.

As seen from errors mentioned with this figure, the nRMSE is marginally improved with the proposed method over the naïve predictor (by ~0.1%). However, the proposed method can outperform the naïve predictor when there is frequent cloud movement. Such improvements are visible in Table 4-8 which shows how much the hybrid method reduces errors over the naïve predictor when smaller dataset are considered with large ramps in PV power production.

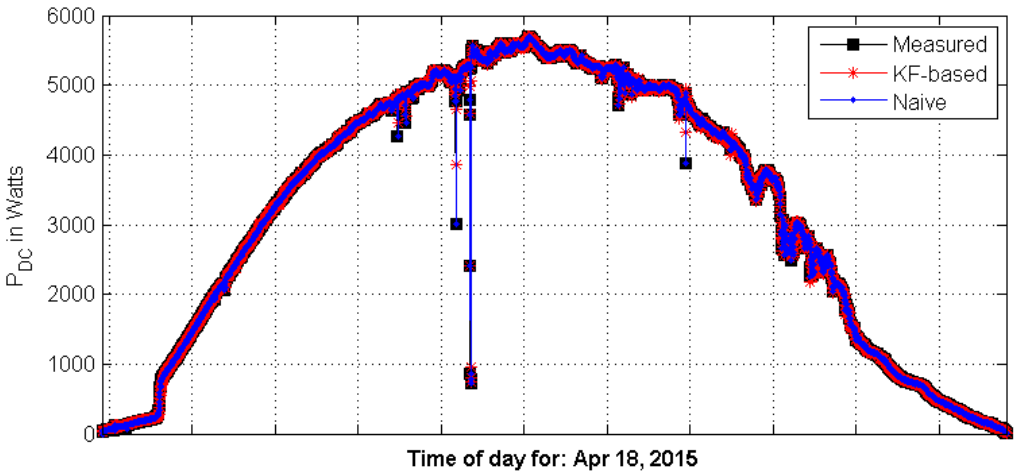

Fig. 4-36 Measured and forecast PV power (with KF-based and naïve predictor) for Apr 18, 2015 {sunny}

(nRMSE with proposed KF-based method=**1.7%**; with naïve predition method=**1.8%**)

In Table 4-8, nRMSE improvement (%) are recorded for several days when cloud-induced PV power fluctuations are high. This is represented in the third and fourth columns in Table 4-8. For example, on March 15, 2015, 2.58% of data samples among the whole day (dawn to dusk) had instantaneous PV power ramps which were higher than 50% of rated capacity (3370 DC Watts). Duration-wise, this dataset span is 18 minutes. For this particular dataset, proposed hybrid forecasting method improves the normalized RMS error by more than 4% over the aforementioned naïve prediction method. This reduction in error percentage decreases as the percentage of PV power ramps diminish. Similar observation can be made for all other days mentioned in Table 4-8. Findings presented in this table suggest that, the proposed method can offer superior performance compared to naïve predictor model if fast cloud movements cause high step changes in PV generation. This way, the proposed method can be of more help to the voltage regulation application (discussed in details in section 4.3), instead of a simplistic, naive approach.

Table 4-8 Error reduction by proposed hybrid forecasting model over naïve predictor model

Date	***Instantaneous ramp threshold, x (% of rated capacity)***	***% of daylight duration when instantaneous ramps are greater than x%***	***% of daylight duration when instantaneous ramps are greater than x% (in minutes span)***	***Improvement in error (=nRMSE with proposed KF-based method – nRMSE with naïve method) (%)***
March 15, 2015	50	2.58	18	4.62
	30	6.06	42	3.76
	15	9.72	68	2.79
April 23, 2015	50	1.77	14	2.7
	30	4.67	37	1.48
	15	9.52	75.5	0.96
May 27, 2015	50	1.32	11	1.98
	30	3.91	33	1.49
	15	7.17	61	0.6
May 23, 2014	50	1.67	14	3.7
	30	3.4	29	2.08
	15	6.13	52	1.19
August 17, 2014	50	1.11	9	3.23
	30	3.57	28	2.27
	15	7.08	56	1.36

4.2 Voltage regulation by PV inverters based on PV power forecasts

Active power curtailment technique (APC) combined with reactive power compensation (RPC) are employed here based on PV power forecasts. The proposed local voltage regulation scheme discussed here, is an augmentation on the RPC-APC method presented in chapter 3, and termed as 'Reactive power compensation enhanced with active power curtailment based on PV power forecasts' or APCf. This technique can be realized at the inverter end in a high PV penetration scenario where distribution overvoltage situation emerges due to reverse power flow for high PV output and low feeder load. In such case, only reactive power absorption cannot provide the desired regulation, because the R/X ratio in distribution network can be high (considering both overhead lines and cables, it can range from 0.5 to 7 for distribution network [117]), making it more sensitive to real power injection than to reactive power absorption. Therefore, curtailing active power can yield to better voltage regulation. In this algorithm, APC is applied based on PV generation forecasts when reactive power absorption alone cannot prevent overvoltage within the predefined power factor (pf) limit.

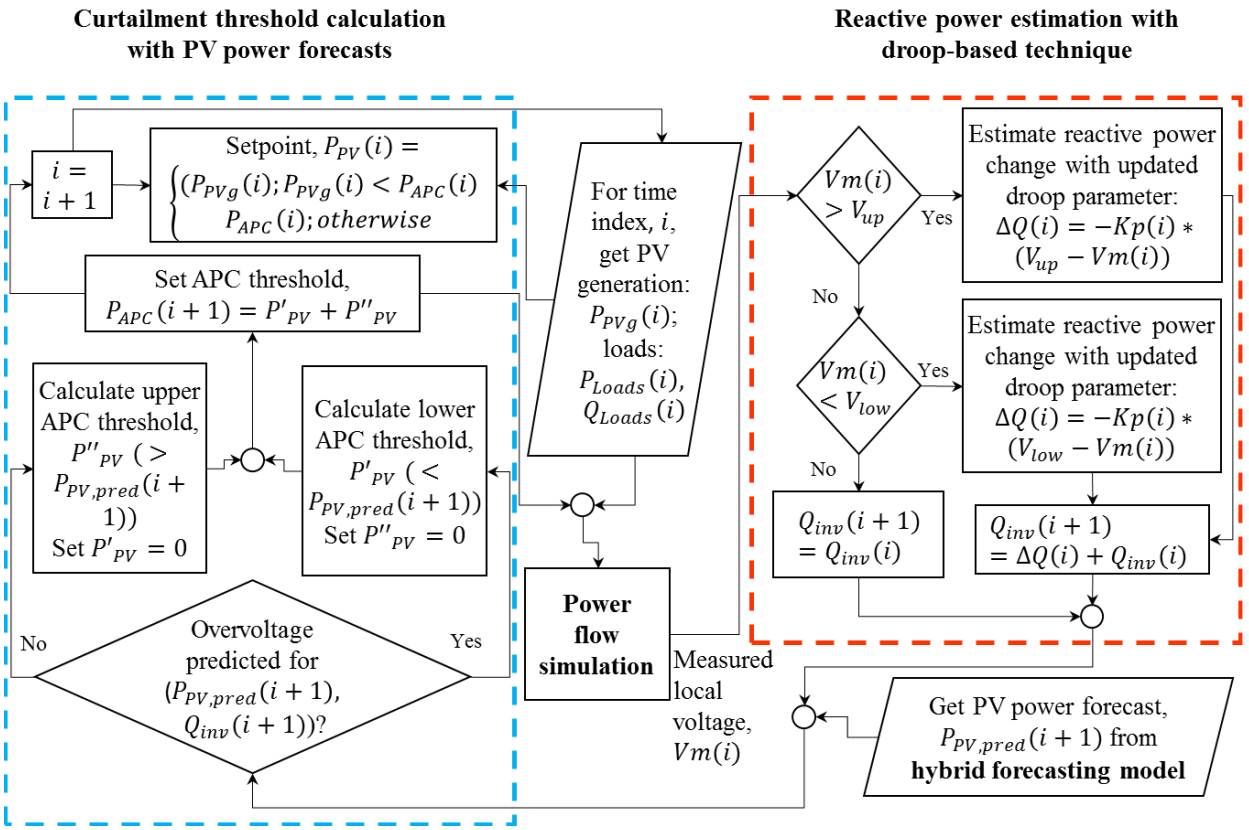

Fig. 4-37 Flow chart of the proposed APCf algorithm

A flow-chart for the combined APCf technique is shown in Fig. 4-37. In this schematic, the droop-based reactive power compensation (RPC) block processes the estimated incremental change in reactive compensation ($\Delta Q(i)$) using updated droop parameter $Kp(i)$. This updated droop parameter helps the RPC technique to follow the changes in PV output (active) and other spot load variations. The range of Kp (corresponding maximum and minimum values) is set using the slope of Q-V contours for each bus derived from steady-state power flow analyses. Some of these contours are shown in chapter 3, Fig. 3-6 – 3-8. With the updated droop parameter, the estimated incremental change in inverter reactive power for the next time step ($\Delta Q(i)$) is calculated by:

$$\Delta Q(i) = \begin{cases} -Kp(i) * \left(V_{up} - Vm(i)\right); if\ Vm(i) > V_{up} \\ -Kp(i) * \left(V_{low} - Vm(i)\right); if\ Vm(i) < V_{low} \end{cases} \quad \dots \quad \text{Eqn. (4-37)}$$

Here, as mentioned earlier in chapter 3,

$V_{up/low} =$ Upper/lower threshold of prescribed voltage limit

$Vm(i) =$ Measured voltage at i-th instant

The reactive compensation (positive denotes inductive VAR) $Q_{inv}(i+1)$ needs to increase, or, inverter needs to absorb reactive power, when the voltage is violating the upper limit. So, as seen in Eqn. 4-37, $\Delta Q(i)$ takes on positive value in such case, as $Kp(i)$ defined to be positive all throughout. On the other hand, if the voltage is too low and violating the lower limit ($V_{low} - Vm(i) > 0$), inverter has to produce VAR (acting as a capacitive element), or reactive compensation needs to decrease which is given by negative $\Delta Q(i)$. The inverter can only provide this estimated reactive power support within its reactive power capability limit, $Q_{lim}(i)$. Although this limit is primarily defined by the apparent power rating of the inverter, S (in kVA and taken to be $1.1 * P_{max}$ as per the discussions in section 3.1.1), it can be further redefined using the power factor criterion. To consider both the active injection and power factor requirement, this limit is employed only after the curtailment threshold is derived. At any given time, the proposed voltage regulation technique clamps the inverter reactive power, $Q_{inv}(i)$ at $\pm Q_{lim}(i)$ if $|Q_{inv}(i)| > |Q_{lim}(i)|$.

When adequate inductive VAR absorption cannot be provided by RPC, PV output can be curtailed to prevent possible overvoltage. Although curtailing solar energy can cost the PV system owner(s), it can help avoid excess injection to the grid and thus reduce the need for grid strengthening [1,

118]. The APCf algorithm proposed here, as shown in the flow chart in Fig. 4-37, combines APC method with RPC based on PV generation forecasts and enhances the voltage regulation performance. In practice, APCf can be implemented with constant power generation control realized at the inverter terminal which ensures a stable output power level [119]. For this algorithm, active power curtailment only comes into play when an imminent overvoltage situation is being projected with the PV power forecast and estimated reactive power, or,

Target local voltage, $Vm\big(P_{PV,pred}(i+1), Q_{inv}(i+1)\big) > V_{up}$

Here, $Q_{inv}(i+1)$ represents the required reactive power given by the RPC block, and $P_{PV,pred}(i+1)$ gives the PV power forecast for the next time step as discussed in section II. This voltage is derived with the assumption that each PV system can access the load and generation data till the previous time step and does not have any forecast information for other PV units. This way, the local decision variables are determined independently by each PV system. Reducing active power injection decreases the target voltage and thus yield to a curtailment threshold that is lower than the predicted PV generation. Fig. 4-38a) depicts the schematic for this lower threshold calculation. First, the pf limit is imposed on the estimated $Q_{inv}(i+1)$ if $pf < pf_{min}$. The relationship between the limiting reactive power and pf limit is:

$$|Q_{lim}(i+1)| = W^{pf_{min}} * P_{PV,pred}(i+1)$$
$$W^{pf_{min}} = \tan(\cos^{-1}(pf_{min})) \quad \ldots \quad \text{Eqn. (4-38)}$$

Eqn. 4-38 expresses the proportional relationship between the PV output and the reactive power limit. Here, $W^{pf_{min}}$ acts as a proportional constant which depends on the minimum power factor criterion specified by the grid codes.

Expectedly, the voltage would be still outside the upper voltage boundary after the reassessment of the reactive compensation, as imposing the limit would rather reduce the value of Q_{inv}. So to prevent predicted overvoltage scenario, the active power injection has to be curtailed. This APC curtailment threshold is determined in a dynamic fashion for the proposed APCf technique. This way, the curatilment is not fixed by a set portion for a given period of time, and it can be tuned to curtail the minimum amount needed in each time step. For this APC threshold calculation, as seen in Fig. 4-38a), predicted real injection is reduced until it reaches an operating point (P'_{PV} and corresponding Q'_{inv}) for which the target voltage would be right under the upper voltage limit

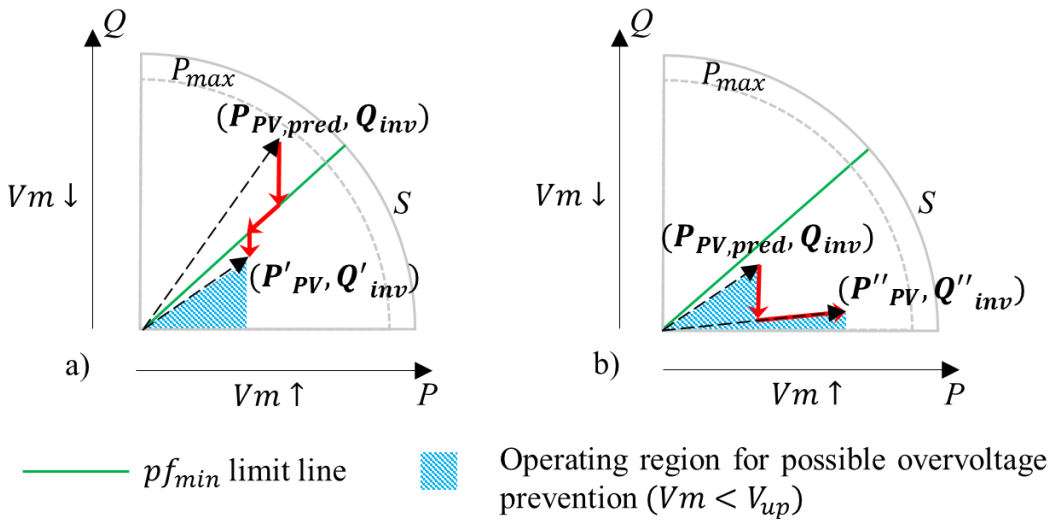

Fig. 4-38 a) Lower and b) upper threshold calculation for APCf

(V_{up}). These updated estimates of real and reactive power denote the lower APC threshold parameters, as P'_{PV} is lower than the predicted PV output:

$$P'_{PV} \leq P_{PV,pred}(i+1);\ Q'_{inv} \leq W^{pf_{min}} * P'_{PV} \quad \ldots \quad \text{Eqn. (4-39)}$$

To make this method robust against forecasting errors, a virtual upper threshold (P''_{PV}) is calculated even when no overvoltage scenario is predicted with $P_{PV,pred}(i+1)$ and $Q_{inv}(i+1)$. This upper APC threshold calculation is thematically explained in Fig. 4-38b). P''_{PV} is derived by gradually increasing the real injection from the forecast value (keeping the pf fixed near unity) until the target voltage barely touches the upper limit. As seen in Fig. 4-38b), the voltage can be increased if reactive absorption is lowered or pf is improved. So:

$$P''_{PV} > P_{PV,pred}(i+1);\ Q''_{inv} = 0.1 * P''_{PV} \quad \ldots \quad \text{Eqn. (4-40)}$$

As the depiction presented in Fig. 4-38, both P'_{PV} and P''_{PV} are calculated considering the predicted PV output for the next time instance. Due to forecast errors, $P_{PV,pred}(i+1)$ can either underestimate or overestimate the actual PV generation, $P_{PVg}(i)$, leading to erroneous prediction of possible overvoltage scenario. If the overvoltage scenario is predicted properly, the lower APC threshold calculation can help to prevent it. On the contrary, the upper APC threshold calculation acts as a preventive measure when an overvoltage condition is not being predicted because of the

error in the PV forecast. At any instance, either upper or lower APC threshold is calculated for the next step; and the other one is set to be zero. So, net APC threshold can be written as:

$$P_{APC}(i+1) = P'_{PV} + P''_{PV}$$
$$Q_{APC}(i+1) = Q'_{inv} + Q''_{inv} \quad \ldots \quad \text{Eqn. (4-41)}$$

The APCf technique calculates this net curtailment threshold ($P_{APC}(i+1)$) and corresponding reactive compensation ($Q_{APC}(i+1)$) adaptively based on PV power forecasts to keep the voltage within V_{up}. At any time step, 'i', $P_{APC}(i)$ acts as the curtailment threshold and if the measured PV generation, $P_{PVg}(i)$ is higher than this threshold then active power curtailment takes place. Otherwise, the instantaneous PV generation is injected without any curtailment. The PV inverter set-point ($P_{PV}(i), Q_{PV}(i)$) is thus given by:

$$P_{PV}(i) = \min\left(P_{PVg}(i), P_{APC}(i)\right)$$
$$Q_{PV}(i) = \max(Q_{APC}(i), Q_{inv}(i)) \quad \ldots \quad \text{Eqn. (4-42)}$$

Here, $Q_{PV}(i)$ is set as the maximum between $Q_{APC}(i)$ and $Q_{inv}(i)$ so that the reactive compensation from the inverter can be maximized within the reactive capability limit ($Q_{inv}(i) \leq Q_{lim}(i)$), as given by Eqn. 4-38.

4.3 Case studies and simulation results

The proposed APCf technique is evaluated for two kinds of case studies here- PV system at the end of feeder location (section 4.3.1), and multiple PV systems at other locations (section 4.3.2). For the multiple PV scenario, the performance of this technique is also compared with other realistic voltage control practices. Both of these case studies are built around modified IEEE 34 node test feeder. The modified test feeder is modeled with OpenDSS. Numerical calculations regarding the hybrid forecasting model, RPC and APCf algorithms are executed in MATLAB.

These case studies use load profile data which are derived from measurements of 1-minute resolution from a substation transformer that feeds mostly residential and commercial customers in the Northern Virginia area. The modified IEEE 34-node test feeder system is simulated here to represent a usual radial distribution network with a smaller substation transformer (2500 kVA). Scaling of loads in the test feeder is done using per unit values of actual load profile. Per unit loads are derived with the actual substation transformer rating (= 50,400 kVA). Individual spot loads at

the test feeder are perturbed with Gaussian distribution (mean= scaled down base loads given by the test feeder configuration; standard deviation= 5%), to synthesize a realistic net load profile of 15-second resolution. Scaled base values are used for distributed loads.

The daily PV generation profiles used in these case studies are derived based on real-time data collected from the 6.44 kW rooftop PV array located at Virginia Tech- Advanced Research Institute building in Arlington, Virginia (coordinates: 38.8803° N, 77.1083° W). Weather data and electrical data collected by this system are used to formulate and validate the hybrid forecasting model, as discussed section 4.1.3. System configuration data are used to model the clear sky radiation for this PV site (section 4.1.1). High penetration PV scenario are assumed for these case studies, which would give rise to distribution overvoltage. The efficacy of the APCf method is assessed in this section with different PV sizing and location.

4.3.1 PV integration at the end of the feeder

For this case study, the PV placement is assumed to be at the end of the feeder where the overvoltage phenomenon is most prominent [107]. Fig. 4-39 shows the system setup for this case, where the PV system is integrated at bus#840 at the modified IEEE 34 node test feeder. To simulate high PV penetration scenario, a 1000 kWp PV system is considered for this modified 34-node test feeder ($P_{max} = 1000\ kW$). Generation profiles are accordingly scaled up from the 6.44 kW PV array data. Because the study presented here analyzes the proposed voltage regulation technique for preventing overvoltage on a very short timescale (15-second), the voltage regulators are operated with fixed tap positions. Thus, the effectiveness of the regulation technique can be

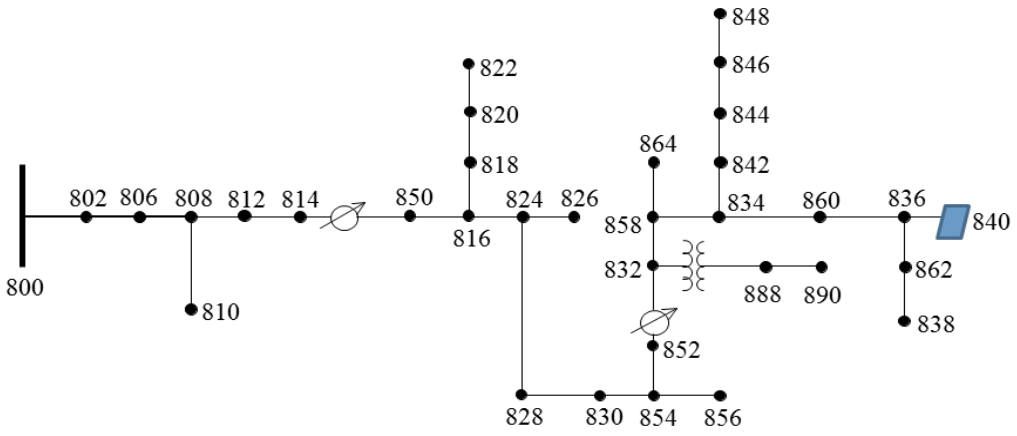

Fig. 4-39 Modified IEEE 34 node test feeder (PV location: end of feeder)

assessed in absence of any voltage control device located on the feeder. For this case study, the proposed technique is evaluated with a narrower voltage regulation band ($V_{up} = 1.03\ p.u.$ and $V_{low} = 0.97\ p.u.$) compared to the standard $\pm 5\%$ range. The power factor limit (pf_{min}) is taken to be 0.9 for the oversized inverters and large-scale PV integration [21, 118]. This value of pf_{min} leads the proportional constant in Eqn. 4-38 to be:

$$W^{pf_{min}} = \tan(\cos^{-1}(pf_{min})) = 0.4843$$

It means that, at any time, the inverter is capable of providing reactive compensation of nearly 50% of its instantaneous real output.

Simulation results

The application of the proposed APCf technique focuses on the prevention of overvoltage and thus improves the local voltage profile. This improvement shows vivid results when the feeder load is low and PV generation is high. As the feeder is located in Northern Virginia area, the net load tends to be on the lower side during spring or March-May timeframe. The overvoltage phenomenon also depends on the load profile of a particular day. This work uses two indices for selecting the days when the local overvoltage scenario is prominent- mean overvoltage index, $\overline{V_{ov}}$ and relative frequency of overvoltage, RF_{ov}. These are defined in Eqn. 4-43.

$$\begin{aligned} &\overline{V_{ov}} = mean\big(\boldsymbol{V_m} - V_{up}\big); when\ \boldsymbol{V_m} > V_{up} \\ &RF_{ov} = \%\ of\ data\ samples\ when\ \boldsymbol{V_m} > V_{up} \end{aligned} \quad \ldots \quad \text{Eqn. (4-43)}$$

Here, $\boldsymbol{V_m}$ represents the vector containing measured voltage profile, and V_{up} is the predefined upper voltage limit. The numeric values of $\overline{V_{ov}}$ (p.u. or percent) quantify the degree of the overvoltage scenario. Ideally, $\overline{V_{ov}}$ should be zero when no overvoltage is observed for the given day. RF_{ov} (%) gives a measure of the number of times overvoltage occurs among all the data samples collected for that day. To evaluate the performance of the APCf method, the days are taken from March- May, 2013-15, for which $\overline{V_{ov}} > 0.01\ p.u.$ or 1%, and $RF_{ov} > 15\%$. Fig. 4-40a) – c) display the load profile, PV generation and output profiles (with APCf) along with the PV power forecasts for such a day (May 20, 2015) and the improvement in the voltage profile against the base case. The base case considers the original PV generation profile when no active

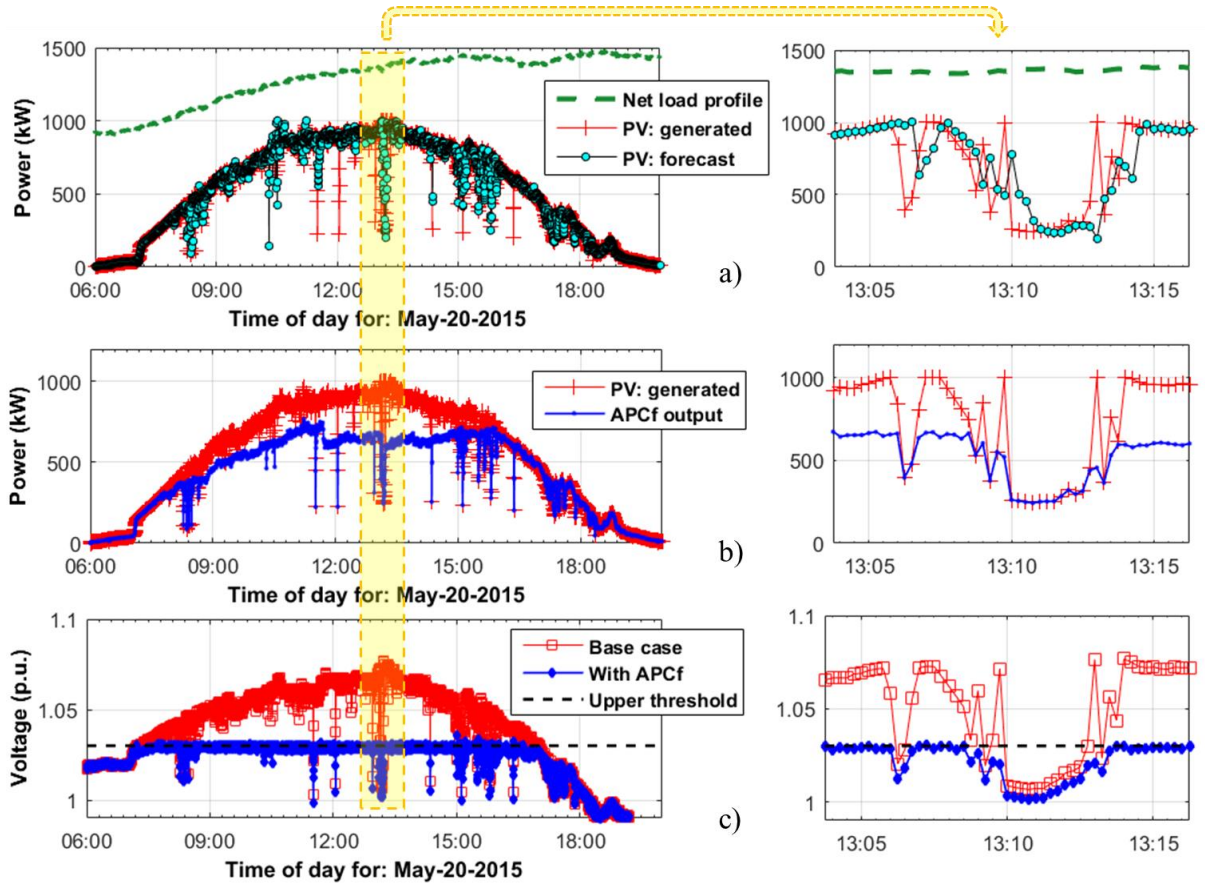

Fig. 4-40 a) Net load, PV generation, and forecast; b) base case PV generation and PV output profiles (after APCf); and c) voltage profile improvement with APCf over base case (unity pf, no curtailment) for May 20, 2015

power curtailment takes place and the inverter operates at unity pf. As discussed in section 4.2, the APCf technique curtails a portion of the generated PV power to keep the voltage within the upper limit and reduces the $\overline{V_{ov}}$ from 2.27% to 0.0343%; while reducing the RF_{ov} from 39.39% to 2.76%. Fig. 4-40c) demonstrates that the APCf technique keeps the voltage within the arbitrary upper bound 1.03 p.u. almost all the times, even when the PV forecast values are not close to the measured values. Similar improvement regarding overvoltage scenario can be seen in Table 4-9 which compares $\overline{V_{ov}}$ and RF_{ov} indices between base case and cases with APCf application. Corresponding curtailed PV energy (%) and normalized root mean square errors (nRMSE) for PV forecasts are also given in this table. As suggested by Eqn. 4-43, these indices are dependent on the specified value of V_{up} (=1.03 p.u. in this case) and will decrease when V_{up} is set at higher level. Table 4-9 only presents the results for ten sample days when base case $\overline{V_{ov}}$ and RF_{ov} are the highest

Table 4-9 Mean overvoltage indices, relative frequencies of overvoltage, curtailed energy and corresponding forecasting errors for different types of days in Mar-May, 2016

Date	*Day Type*	$\overline{V_{ov}}$ *Base case (%)*	$\overline{V_{ov}}$ *with APCf (%)*	RF_{ov} *Base case (%)*	RF_{ov} *with APCf (%)*	*Curtailed energy (%)*	*nRMSE %*
05/12/2013	Sunny	2.54	0.0308	36.11	1.89	19.61	5.86
05/14/2013	Mostly Sunny	2.83	0.0256	27.50	1.63	22.67	2.72
03/31/2014	Sunny	3.25	0.0228	36.77	3.14	36.76	1.68
04/01/2014	Mostly Sunny	2.60	0.0237	38.77	3.85	39.05	3.46
04/10/2014	Sunny	2.47	0.0300	31.11	2.12	17.23	1.37
04/27/2014	Sunny	2.83	0.0249	33.65	2.17	22.80	0.89
03/18/2015	Sunny	2.41	0.0377	29.76	1.63	15.60	1.46
04/22/2015	Partly Sunny	2.91	0.0372	26.75	2.05	34.15	5.51
04/29/2015	Sunny	3.27	0.0256	41.02	4.10	44.76	2.76
05/20/2015	Sunny	2.27	0.0343	39.39	2.76	18.45	4.27

and therefore the proposed APCf technique is proved to be effective for given voltage and pf bounds.

Because this technique depends upon the hybrid forecasting model, the forecasting accuracy can affect the performance of this technique. The relationship between forecasting accuracy and improvement in overvoltage index is shown in Fig. 4-41. This figure plots the improvement in $\overline{V_{ov}}$ for a larger set of days that qualify within the selected criteria for this case study (base case $\overline{V_{ov}} > 1\%$ and $RF_{ov} > 15\%$). The days are organized in descending order of forecasting accuracy in this figure. The nRMSE between the PV power forecasts and generated PV power is used here as a performance evaluation criterion for the forecasting model (normalization constant= $P_{max} = 1000\ kW$). As seen from Fig. 4-41, application of the proposed APCf technique reduces the $\overline{V_{ov}}$ indices to <0.1% for all days, regardless of the levels of nRMSE's in PV power forecasts, or the base case $\overline{V_{ov}}$ values. This range of $\overline{V_{ov}}$ values (with APCf) indicates that the target voltage remains within 0.001 p.u beyond the upper threshold (V_{up}), on average, throughout the whole day.

Also the $\overline{V_{ov}}$'s with APCf do not follow the pattern of increasing nRMSE's, proving that the technique is robust against increasing forecasting errors.

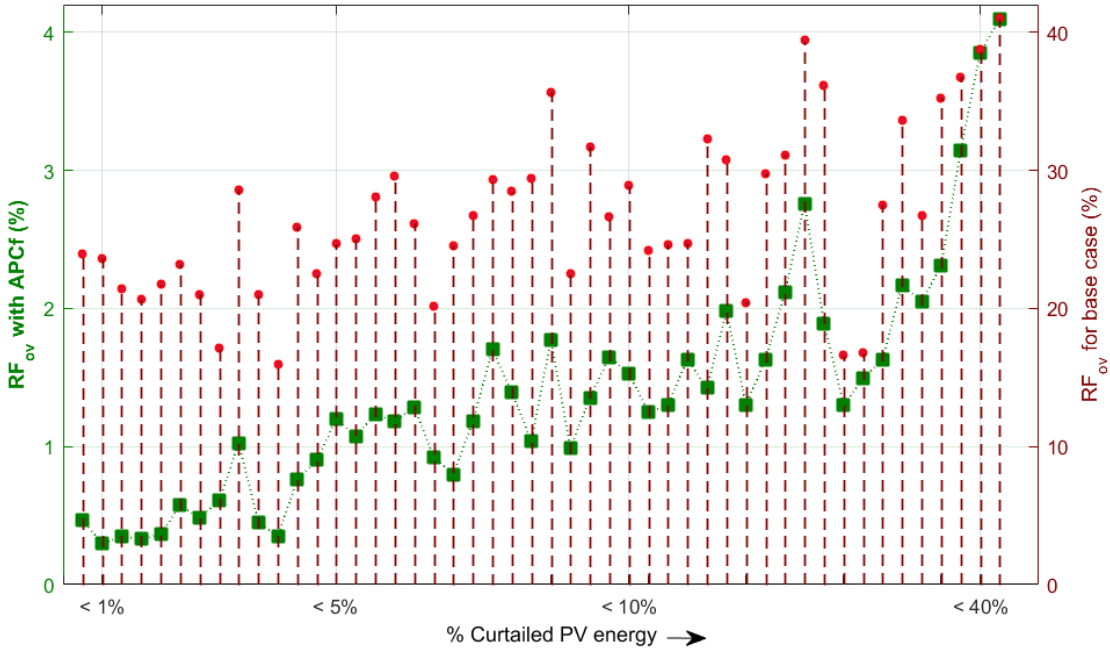

Fig. 4-41 Relative frequency of overvoltage vs percentage of curtailed PV energy for different days: base case and after APCf application

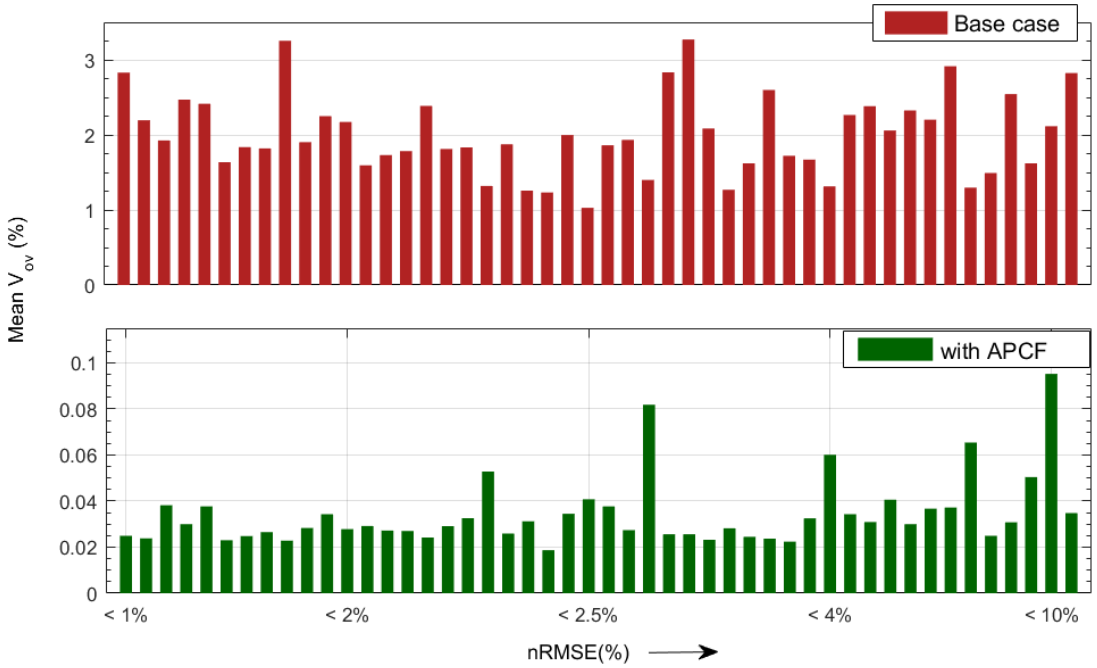

Fig. 4-42 Mean overvoltage indices for different days: base case and after APCf application

The improvement in relative frequency of overvoltage (RF_{ov}) for the days shown in Fig. 4-41 is depicted in Fig. 4-42 against resultant range of variation in curtailed PV energy (percentage). Fig. 4-42 implies that higher RF_{ov} yields to higher curtailment of PV energy with APCf. Higher levels of RF_{ov} for base case suggest that the PV generation profiles are high for those days compared to the respective daily load profiles, leading to frequent overvoltage occurrences. Consequently, higher curtailment is required to reduce the RF_{ov} indices for such days. Similar to the improvement seen with $\overline{V_{ov}}$'s, the APCf technique reduces the RF_{ov} indices from the base cases, and keeps them under a moderate level of 5% for all these days irrespective of the initial RF_{ov} values in the base cases.

4.3.2 Multiple PV locations

As shown in Fig. 4-43, the PV systems are integrated at two different locations for this case study- bus#848 (PV1) and bus#860 (PV2). Bus#848 represents another end of the feeder location, like bus#840 in the previous case study. A 700 kWp PV system is considered for PV1 and for PV2 a 300 kWp system, as a representation of high PV penetration. The PV sizing are selected in a way so that they pose similar local overvoltage scenario at the two locations. For PV1, generation profiles are scaled up from the 6.44 kW PV array data, For PV2, data from another day in the month (with similar day type and irradiance/temperature profiles) is chosen and accordingly scaled up, to signify spatial variability. Similar to the case study discussed in section 4.3.1, the voltage regulators are operated with fixed tap positions in the 34 node test feeder. The power factor limit

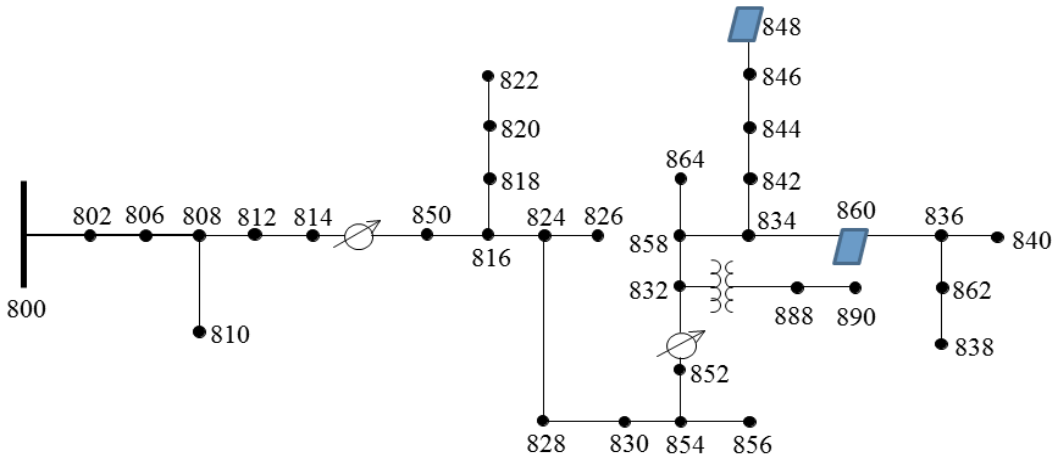

Fig. 4-43 Modified IEEE 34 node test feeder (PV locations at bus#848 & #860)

is also 0.9 here, however, lower values of pf_{min} are also considered here to analyze the performance of APCf under different power factor criteria.

The APCf technique is independently applied to each PV system which calculates the necessary reactive power compensation and the APC threshold based on the local voltage measurements and the individual forecast data. However, it is assumed here that the PV system has access to the past load/generation data for the day through a communication infrastructure. These data are used to predict any impending local overvoltage scenario. This architecture can be visualized in a centralized fashion where each inverter sends its query to a control/data center for available load/generation data. Once these data are dispatched to the PV units, they can calculate their threshold parameters considering local injections as variables. In reality, a PV unit in one location can impact the local voltage seen by another unit, and thus the voltage can fluctuate even with locally optimized real/reactive injection. This masking effect, however, depends on the network topology, as well as the size of the PV systems, and variations in spot loads.

Simulation results

As described in previous case study, overvoltage prevention through APCf technique needs to be investigated with an underlying assumption that, the feeder load is low and PV generation is high. So, in a similar fashion, the performance of the APCf technique is evaluated here during Spring or March-May timeframe when the feeder load in Northern Virginia area tends to be low. To keep the case studies consistent, same day is picked for this case study as in section 4.3.1. Fig. 4-44

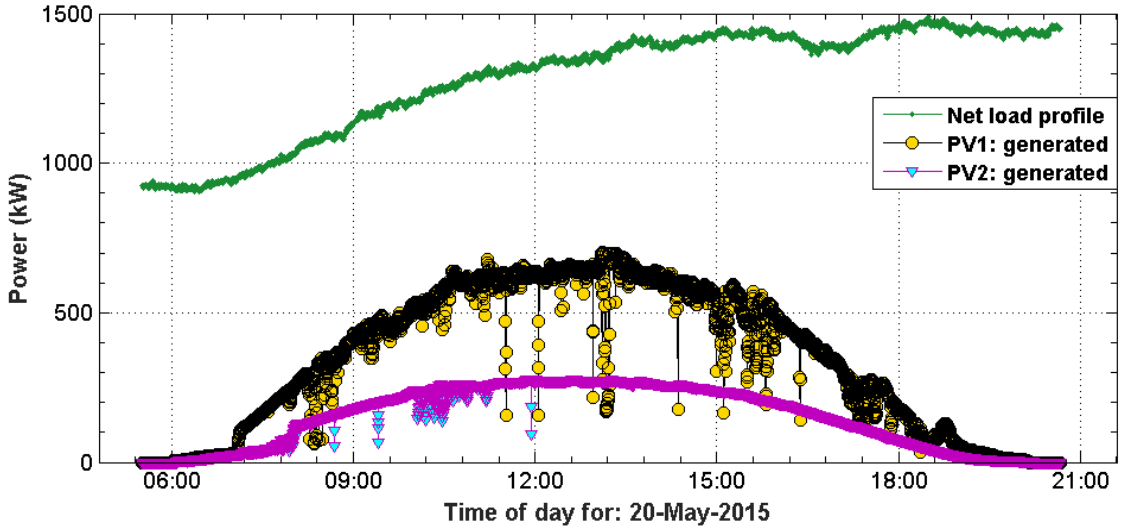

Fig. 4-44 Net load (daytime) and PV generation profiles (PV1 & PV2) for May 20, 2015

displays the daytime load and PV generation profiles for this day (May 20, 2015). For PV2, the PV generation profile is taken for May 23, 2015 to mimic spatial variability. This is also a 'sunny' type day, but with fairly different cloud movement, as seen from Fig. 4-44.

Unlike the previous case study, the voltage profile improvement with APCf technique is compared here against two cases:

i) *Base case:* Same as section 4.3.1, considers the actual PV generation profile without any active power curtailment or reactive power compensation (unity pf).

ii) *Modified base case:* Assumes constant pf operation without any curtailment. To keep it consistent with the case study presented in section IV, the pf is fixed at 0.9 for the modified base case.

Fig. 4-45a) and 4-46a) show improved voltage profiles with APCf application for PV1 and PV2 against these two cases.

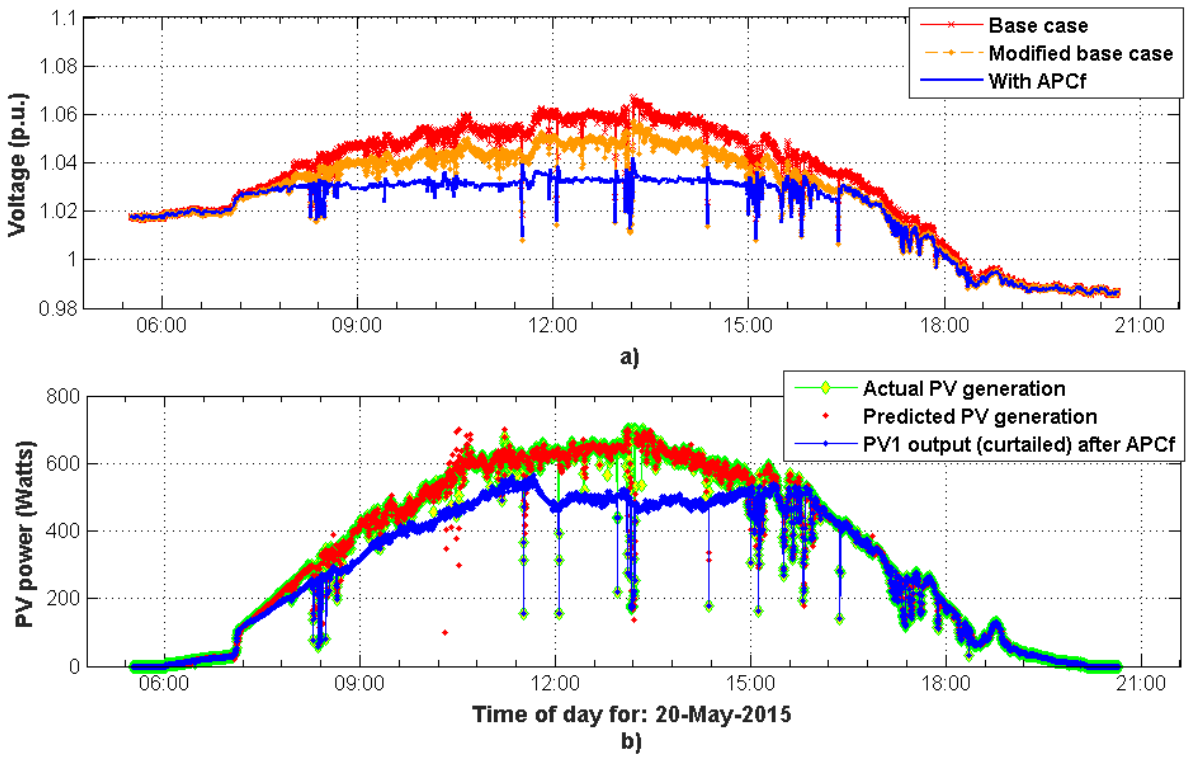

Fig. 4-45 a) Voltage profile improvement with APCf over base case and modified base case, b) PV generation, prediction and output profiles (after APCf) for May 20, 2015 (for PV1)

PV1 and PV2 voltage profiles for the base case show overvoltage situations in these figures, as they violate the upper threshold (1.03 p.u.) during peak generation hours. For the modified base case, because the reactive power compensation is limited by the pf constraint and no active power curtailment takes place, sufficient voltage regulation cannot be provided. Thus, even though the degree of overvoltage is reduced from the base case (Fig. 4-45a) and 4-46a)), the corresponding voltage profiles remain beyond 1.03 p.u. most of the times. In contrast, the APCf technique dynamically curtails a portion of the generated PV power, as shown in Fig. 4-45b) and 4-46b), and keeps the voltage steady near about the upper limit even when the PV forecast values are not very close to the measured ones. It can be seen from Fig. 4-45a) and 4-46a) that, the voltage profiles for PV2 are mostly shaped by the larger PV system at the end of the feeder, PV1. Thus it needs to curtail less active power compared to PV1 (seen in Fig. 4-45b) and 4-46b)) even though the base case voltage profiles were showing similar overvoltage scenario. Also, both PV1 and PV2 attempt to keep their local voltages within the upper threshold independently based on their own measurements and calculations. Therefore, the actual voltage is different from their independent estimation, when both the PV systems are operating simultaneously.

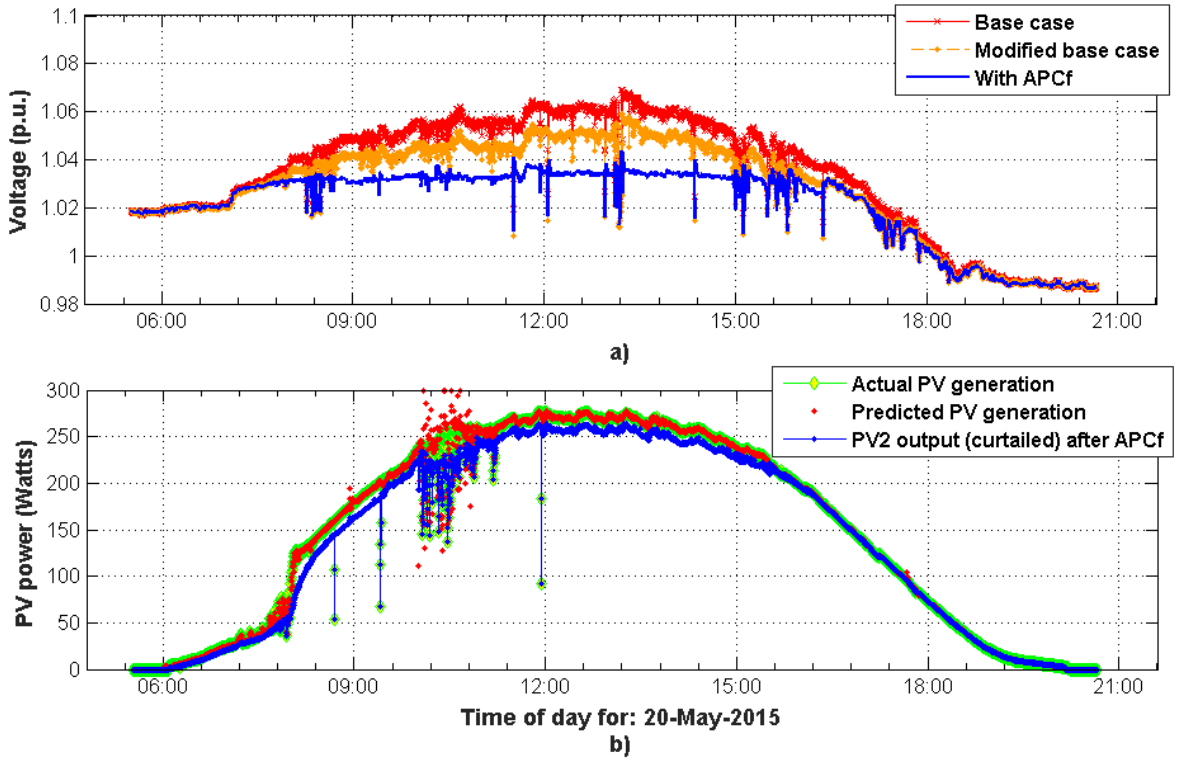

Fig. 4-46 a) Voltage profile improvement with APCf over base case and modified base case, b) PV generation, prediction and output profiles (after APCf) for May 20, 2015 (for PV2)

Mean overvoltage index, $\overline{V_{ov}}$ (%) (given by Eqn. 4-43) for other Spring days along with the corresponding curtailed energy (%) and forecast errors are mentioned in Table 4-10. For the forecast errors, normalized root mean square error (nRMSE in %) between the PV power forecasts and generated PV power is used in this case study too, as a performance evaluation criterion (normalization constant= P_{max}). As seen from this table, the $\overline{V_{ov}}$'s for modified base case are less than their base case counterparts due to the reactive power compensation under a constant pf condition for all these sample days. Compared to the modified base case, the APCf technique reduces the $\overline{V_{ov}}$ indices significantly through adaptive active power curtailment and variable reactive power compensation. Also the application of the proposed APCf technique provides nearly similar improvement of the $\overline{V_{ov}}$ indices for all these days for both the PV locations. This again implies that the improvement in PV2 voltage profile is influenced by the APCf technique applied for both PV1 and PV2. The range of $\overline{V_{ov}}$ values (with APCf) indicates that the local voltage

Table 4-10 Mean overvoltage indices, curtailed energy and forecasting errors for different types of days in Mar-May, 2016

Date (Day Type)	***Base case*** $\overline{V_{ov}}$	***Modified base case*** $\overline{V_{ov}}$	***APCf*** $\overline{V_{ov}}$	***Base case*** $\overline{V_{ov}}$	***Modified base case*** $\overline{V_{ov}}$	***APCf*** $\overline{V_{ov}}$	***Curtailed energy with APCf***	***Curtailed energy with APCf***	***nRMSE***	***nRMSE***
	PV1 (%)	***PV1 (%)***	***PV1 (%)***	***PV2 (%)***	***PV2 (%)***	***PV2 (%)***	***PV1 (%)***	***PV2 (%)***	***PV1 (%)***	***PV2 (%)***
05/12/2013 (Sunny)	1.94	1.35	0.14	2.06	1.49	0.22	15.02	6.28	5.86	2.34
04/01/2014 (Mostly sunny)	2.38	1.74	0.43	2.51	1.84	0.49	36.68	6.75	3.46	1.76
03/17/2015 (Partly sunny)	1.92	1.39	0.29	2.04	1.50	0.36	19.59	9.27	4.85	6.09
04/29/2015 (Sunny)	2.78	1.17	0.43	2.92	2.30	0.49	42.12	7.13	2.80	2.39
05/20/2015 (Sunny)	1.91	1.25	0.21	2.04	1.35	0.31	13.91	5.28	4.27	2.34

profiles remain within a moderate level of 0.5%. beyond the upper threshold (V_{up}), on average, throughout the whole day. Also the $\overline{V_{ov}}$'s with APCf do not show any direct correlation with corresponding nRMSE's, proving that the technique is robust against forecasting errors. Similar observation was also made for the previous case study where no direct relationship was found between forecasting accuracy and improvement in overvoltage index (shown in Fig. 4-42).

Unlike $\overline{V_{ov}}$ with APCf, the curtailed energy is directly related to the $\overline{V_{ov}}$ for base case. High base case $\overline{V_{ov}}$ suggests that the PV generation profile is high for these days compared to the respective daily load profiles (for example: 04/01/2014, 04/29/2015). As a result, corresponding $\overline{V_{ov}}$'s for the modified base case also remain on the higher end, as no energy is curtailed under its assumptions (Table II). Higher curtailment is mandated by the APCf technique subsequently, to reduce the extent of overvoltage for such days, for both the PV systems. However, the active power curtailment was much less for PV2, compared to PV1 (situated at the end of the feeder) even for such days. In general, PV2 does not need to curtail as much energy as PV1 because it is closer to the substation (as seen in Table 4-9). Similar findings were reported in [19] which demonstrated that the amount of curtailed energy depends on the location of the PV system (with respect to the substation or transformer) for their droop-based active power curtailment scheme. This work modeled a residential suburban feeder with 12 houses, each having a PV system of 8.4 kWp. Their results show that the farthest houses (from the transformer) produced 15-16 kWh less than the nearest ones to the transformer, which is ~50% of the expected daily electricity generation for these houses.

The curtailed active power is also related to the power factor requirement. The closer pf_{min} is to 1 the lower the reactive power absorption/injection capability limit should be. Here, all the case studies conform to the 0.9 pf criterion. However, the proposed APCf technique is also evaluated against other hypothetical power factor criteria. Table 4-11 shows the results regarding the PV output (real and reactive) with these values of pf_{min} for PV1 (700 kWp) for May 20, 2015. The daily average curtailed power (kW) is derived by taking the mean difference between the generated (PV_{gen}) and output (PV_{out}) PV power when APC takes place ($PV_{gen} > PV_{out}$). Daily average reactive absorption (kVAR) is calculated as the mean of reactive compensation Q_{inv} when $Q_{inv} > 0$. As seen from this table, the average curtailed power increases from 10.23 kW to 24.18 kW when pf_{min} goes up from 0.8 to 0.9. The increase in active power curtailment is commensurate with the

Table 4-11 Active power curtailment and reactive power compensation for different power factor requirements (PV1 for May 20, 2016)

pf_{min}	***Average curtailed power*** $(= mean(PV_{gen} - PV_{out})$; *when* $PV_{gen} > PV_{out})$ **(kW)**	***Average reactive compensation*** $(= mean(Q_{inv})$; *when* $Q_{inv} > 0)$ **(kVAR)**
0.9	24.18	137.42
0.85	18.46	177.91
0.8	10.23	215.63

decrease in reactive compensation as it is falls from 215.63 kVAR to 137.42 kVAR. This analysis infers that if the pf requirement is relaxed, the proposed APCf technique can utilize the inverter reactive compensation capability and further reduce the necessity of active power curtailment.

4.3.3 Discussions

Case studies presented in section 4.3.1 and 4.3.2 use load profiles from the same day (May 20, 2015) and similar PV generation patterns. The net amount of PV on the feeder is also same but the selected PV locations are different. First case study has 1000 kW (1100 kVA inverter) at the end of feeder whereas for the second one 1000 kW (700 kW at bus#848 and 300 kW at bus#860) of PV is dispersed in two separate locations. With $pf_{min} = 0.9$, the amount of curtailed energy is 18.45% for the first case. The same pf criterion yields to total of 19.19% energy curtailment with PV1 and PV2 in the second case study (from Table 4-10) which is a little bit higher than the first case. This is also applicable for other days, as seen from Tables 4-8 and 4-9. Higher curtailment for multiple PV scenario appears because individual PV systems are unaware of the forecasts for other systems. Also, the control actions are only applicable for itself. For very short-term forecasting, it would also require high data transfer rate to pass on PV power forecasts to other controllers. So, from the perspective of an individual APCf controller, the overvoltage occurring due to neighboring PV systems can only be compensated for by curtailing its own output. This yields in lower curtailment threshold values and therefore higher percentage of curtailed energy. To work around this issue, as mentioned in section 4.3.2, it is assumed that each PV system can access past load/generation data. Therefore, while determining local inverter set-point for next time step, this technique assumes that other PV systems' set-points are going to remain unchanged. Due to this assumption, PV2 curtails less amount of energy compared to PV1, and overvoltages at the both these nodes (#848 and #860) are reduced.

4.3.4 Modeling variability for distributed PV fleet

Variability in PV power can be addressed from two different aspects- temporal variability and spatial variability. Temporal variability reflects on how the solar power profile changes when the averaging time window is changed. The shorter the time interval, the higher the variation in PV power in a temporal sense. This masking effect of longer averaging window can be clearly seen on a partly cloudy day in Fig. 4-47 As seen from this figure, variations in 5-minute average is partially captured here in the 30-minute average data; but almost neutralized in hourly average values. For a sunny day though, these variations might oscillate within close range, as can be seen in Fig. 4-48. The temporal variability can be of interest to other devices present in the circuit which work on varying timescales. For example, as discussed in details later in section 5.3, voltage regulators work with different time-delay parameters depending on their location in the feeder (from the substation). Consequently, if the time-delay of a regulator is set as 1-minute, its required number of tap-changing operation would be less due to the temporal variation in sub-minute interval than that for 30 seconds time-delay.

Spatial variability in PV power aggregate has been studies in literature due to the rise of distributed PV applications [102; 120-122]. Physical dispersion can yield to geographic smoothing when the net fleet power (for an ensemble of PV installations), or average irradiance is being considered [102]. The relationship between PV fleet or large-scale PV plant variability and collective irradiance sensor data is a function of many interrelated factors and thus difficult to model universally [120]. Wiemken et al. analyzed 10 years of hourly irradiance data from 6 stations in

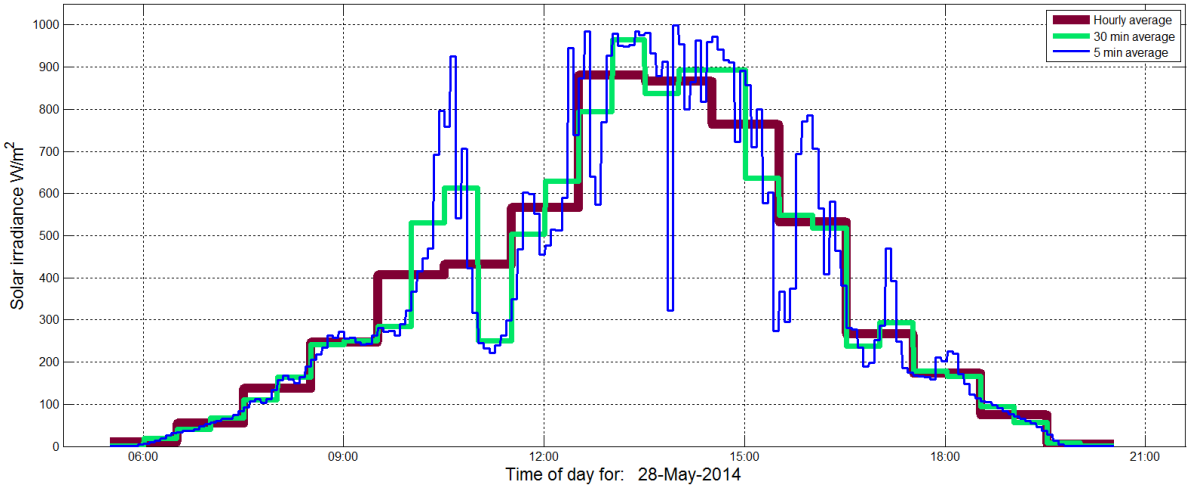

Fig. 4-47 Average irradiance in different timescales for a partly cloudy day (May 28, 2014)

Germany with interstation distance range of 200-680 km [121]. In their model, cross-correlation coefficients for station pairs plotted as a function of the interstation distance were approximated with an exponential function. It signifies that, the spatial cross-correlation decays almost exponentially as the distance between two sites increases. Higher resolution (1-minute horizontal irradiance and AC power data for 52 PV systems located nationwide in Japan) dataset were studied by Murata et al. and their analyses showed that output fluctuations for 1-minute data are poorly correlated even when the distance between the locations is short (50-100 km). However, for longer time-interval (20-minute) the correlations between output fluctuations decreases almost exponentially but do not diminish to zero when the distance between two sites is increasing to ~1000 km [123]. Similar observation was reported by Lave et al. who presented studies on 1-second data collected from a 2.1 MWp Ota City plant in Japan consisting 553 houses (PV systems range: 3-5 kWp) and a 19MWp central power plant in Alamosa, Colorado [122]. These studies revealed that maximum relative ramp rate also follow exponential decay pattern. This decay rate differs in different timescales but the shorter the timescale the more pronounced the geographic smoothing gets. They also found out that for a residential cluster like Ota city plant, maximum ramp rates decrease fast when capacity is added to a small existing fleet (~10 kW) but change slowly in case of additional units to large existing capacity (~1000 kW).

Case studies discussed in previous sections assumed scaled up data from a single site. Including the effects of geographic smoothing can be applied to model aggregate PV fleet power in such cases. Following numerical analyses form a basis to estimate variability in PV fleet power using

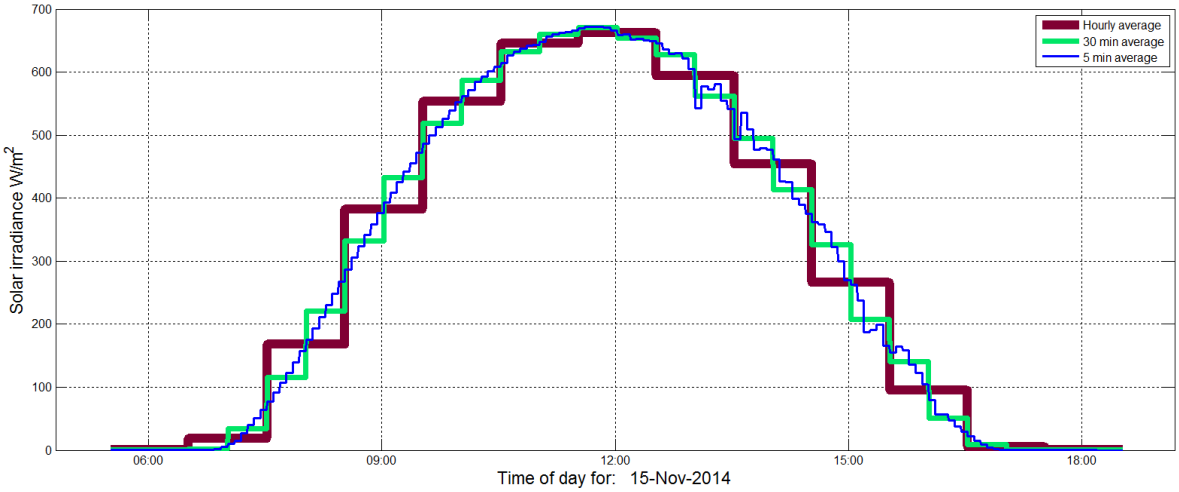

Fig. 4-48 Average irradiance in different timescales for a sunny day (Nov 15, 2014)

point measurements. The outcome from these analyses are later applied to the 6.44 kW ARI PV data for simulating feasible PV fleet output of larger capacity (~1000 kW).

Output variability due to geographic dispersion: PV fleet aggregate vs single PV site power

The data used in this section to analyze geographic dispersion are taken for the St. Lucia campus of The University of Queensland (UQ), Australia. UQ St Lucia Campus hosts one of the largest integrated PV installation in Australia with nearly 2 MW of rooftop PV units. This campus is located in Brisbane on a 114-hectare (~0.45 sq. miles) suburban site. UQ solar PV portal provides live feed and public access to the archive hosting 1-minute resolution data for combined PV generations as well as separate PV sites [124]. For the analyses performed in this section, measurements for Mar-May, 2016 were used. Table 4-12 lists individual PV arrays placed throughout the St Lucia campus and their nominal ratings. As seen from this table, UQ Centre (UQC) has the largest PV system (433.44 kWp DC) which makes up nearly 22% of the net PV capacity. On the other hand, the smallest installation is placed on the Prentice Building (PRB) with a nominal DC rating of 13.5 kWp. Fig. 4-49 shows the normalized PV output for all sites combined along with its largest (UQC) and smallest components (PRB) for a mostly sunny day (May 5, 2016). As normalization constants, corresponding daily maximum values are used here. From Fig.

Table 4-12 PV sites in UQ St Lucia campus

PV site	**Nominal DC output (kWp)**
University of Queensland Centre (UQC)	433.44
Multi-Level Carpark 1 (MLCP1)	338.9
Multi-Level Carpark 2 (MLCP2)	338.9
Warehouse Building (WRB)	164
Global Change Institute Building (GCI)	138
Advanced Engineering Building (AEB)	95.75
Sir Llew Edwards Building (LEB)	89.76
General Purpose South Building (GPSB)	72.56
General Purpose North 3 Building (GPN3)	66.5
Joyce Ackroyd Building (JAB)	54.3
Colin Clark Building (CCB)	51.5
Learning and Innovation Building (LIB)	45.25
Queensland Bioscience Precinct (QBP)	34.66
Axon Building (AXB)	34.32
Pedestrian Link Bridge (PLINK)	15.25
Prentice Building (PRB)	13.5

4-49 it can be seen that for most of the day when the sky is clear, the net output and point outputs are largely similar. But, as revealed by the closer look in this figure, the cloud movements captured in the net PV output profile are different from that in UQC or PRB outputs. This effect of geographic dispersion is also evident in Fig. 4-50 which plots the normalized step changes for this day. As this figure suggests, instantaneous changes in the largest and smallest component are not too correlated temporally. As a result, steep fluctuations present either in UQC data or PRB data are considerably diminished for the combined PV output.

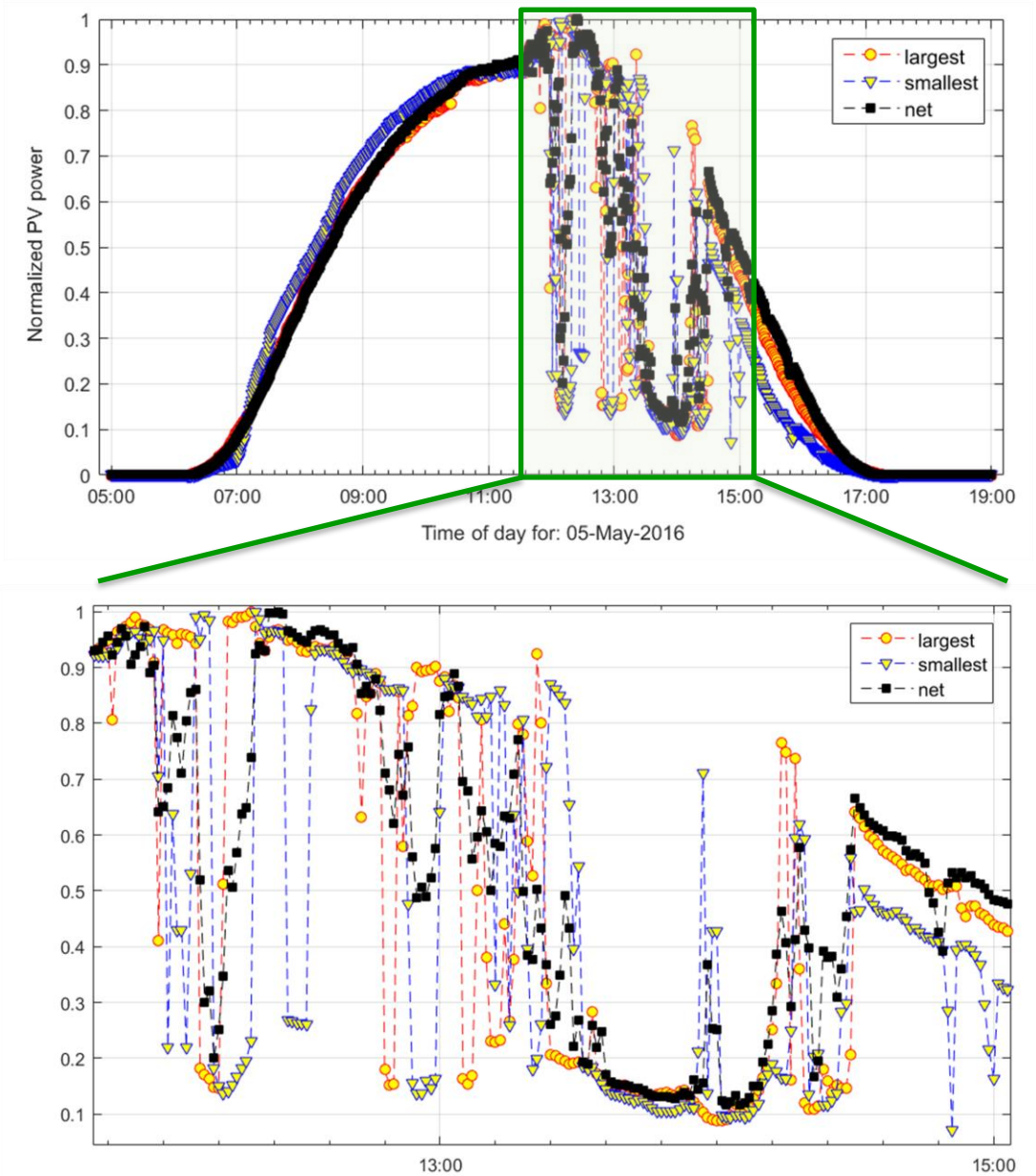

Fig. 4-49 Normalized net PV power from St. Lucia campus, and normalized power from two sites (largest: UQC, smallest: PRB) for May 5, 2016 in 1-minute interval

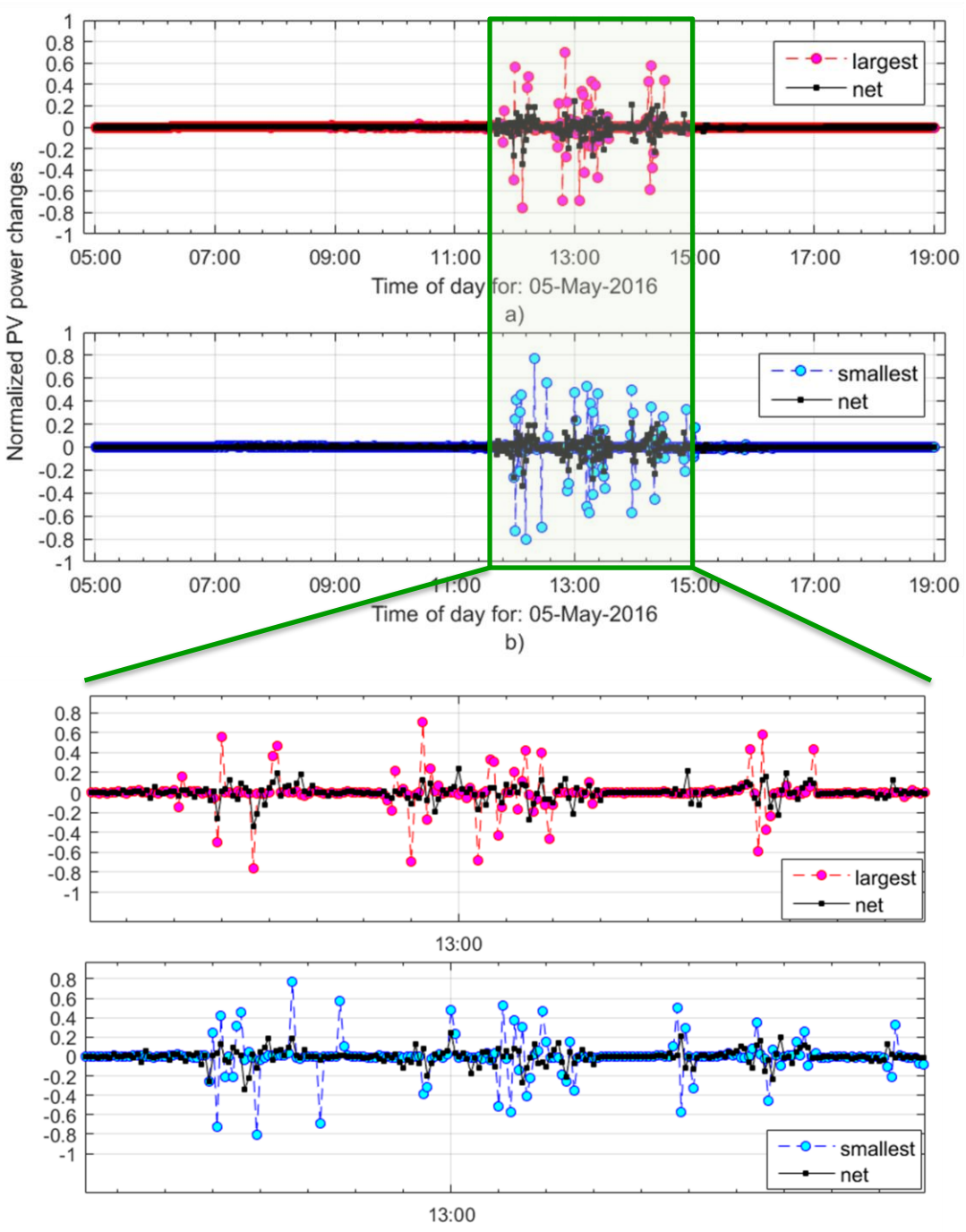

Fig. 4-50 Normalized step changes in net PV power from St. Lucia campus, and normalized step changes in PV power from two sites (largest: UQC, smallest: PRB) for May 5, 2016

To understand how the net PV ramp fluctuates with respect to a local or point PV ramp (the largest system, UQC, is considered here), conditional probability distributions are derived for the whole dataset. This conditional probability is defined as:

$$P\left(y_1 < \Delta PV_{fleet} \leq y_2 \middle| x_1 < \Delta PV_{local} \leq x_2\right)$$
$$\approx \frac{No.\,of\ samples, n, among\ N\ samples\ when\ \Delta PV_{fleet}\ lies\ between\ y_1\ and\ y_2}{Total\ no.\,of\ samples, N, when\ \Delta PV_{local}\ lies\ between\ x_1\ and\ x_2} \quad \cdots \quad \text{Eqn. (4-44)}$$

As explained in Eqn. 5-1, for determining this conditional probability, first, 'N' number of samples are identified where local ramps (ΔPV_{local}) remain within a certain range ($[x_1, x_2]$). Among these samples, a subset can be identified with 'n' samples for which fleet ramps (ΔPV_{fleet}) are found within a given range ($[y_1, y_2]$). Fig. 4-51 shows these empirical conditional probability distributions for several values of $[x_1, x_2]$. Negative values of ramps mean power output falls from the previous value and positive values mean power output is on the rise.

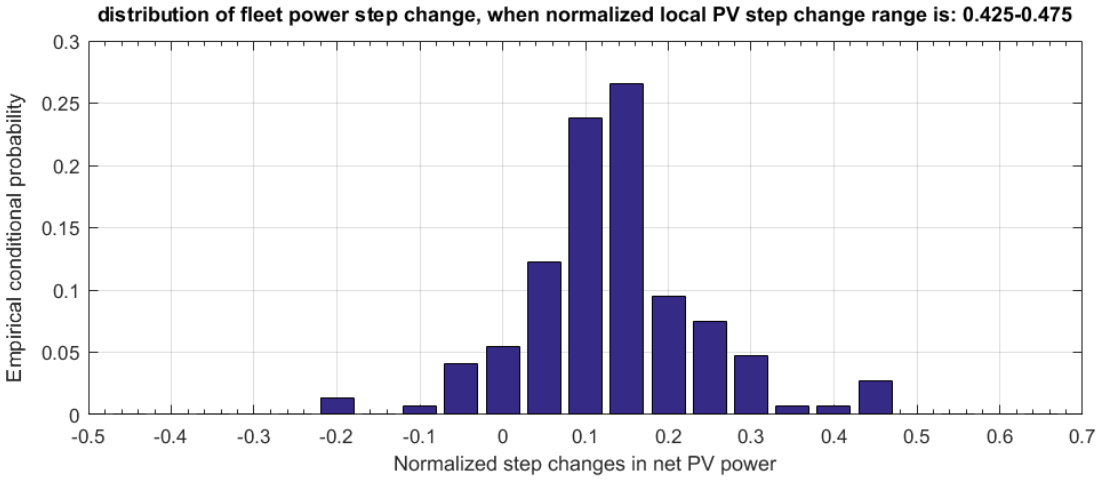

a)

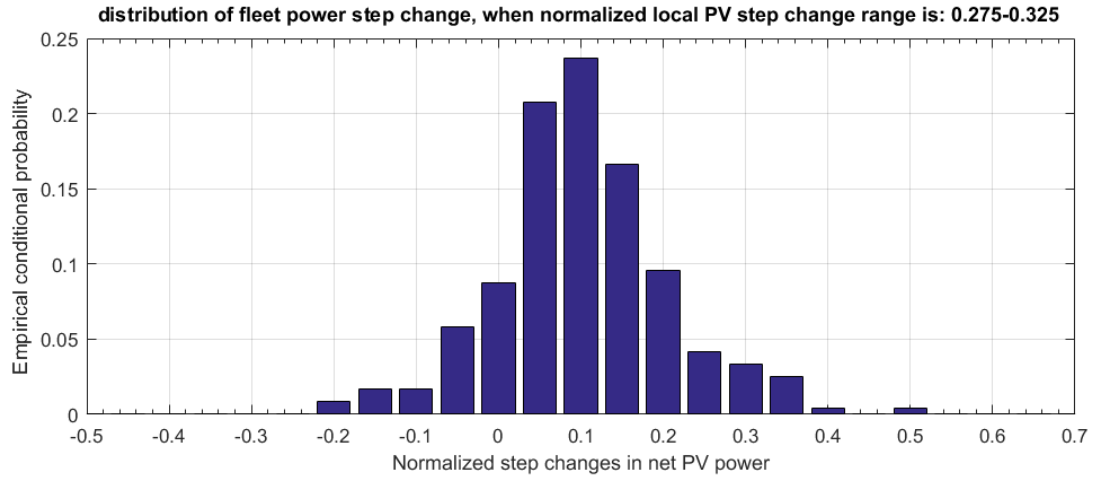

b)

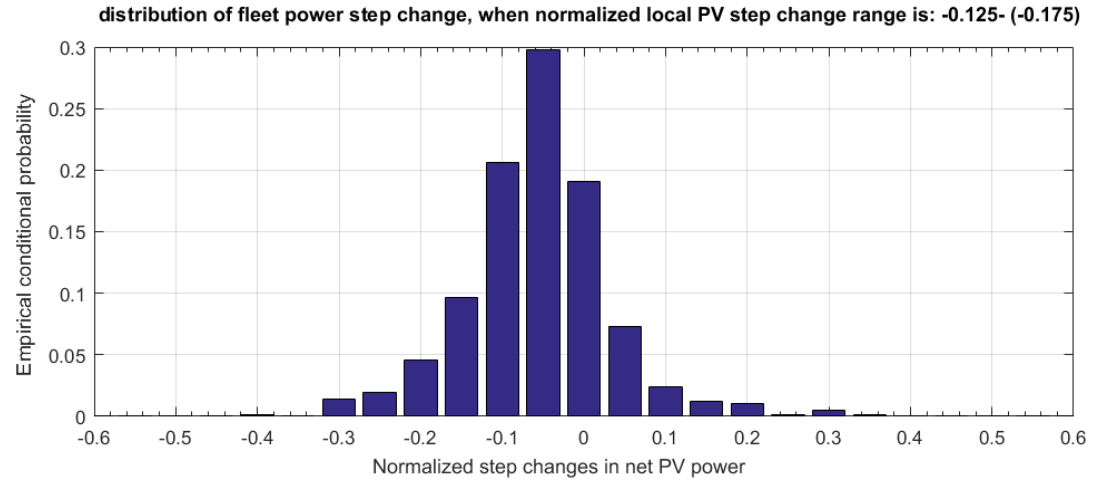

c)

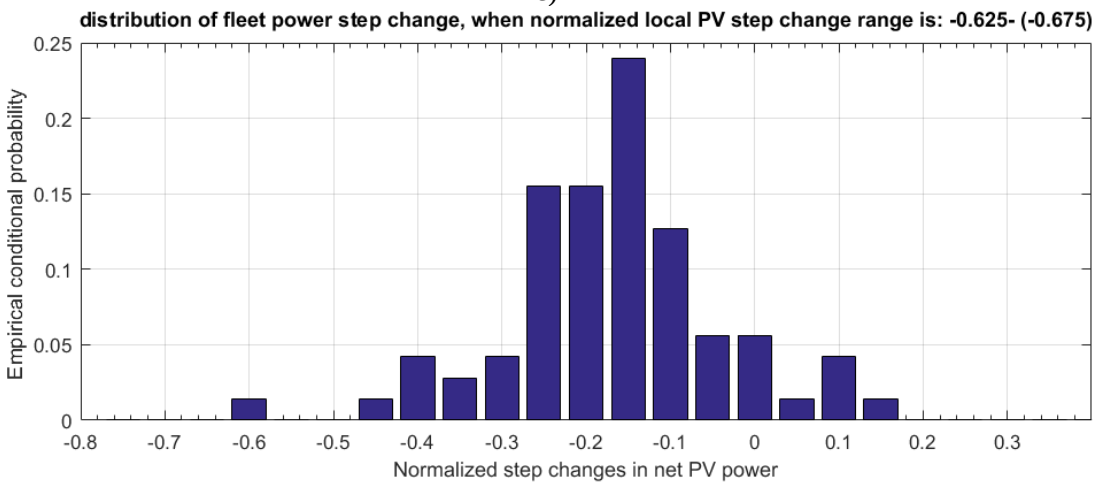

d)

Fig. 4-51 Empirical conditional probability for fleet power ramps when local PV ramps are within ranges: a) 0.425-0.475; b) 0.275-0.325; c) -0.125 – (-0.175); and d) -0.625 – (-0.675)

As seen from Fig. 4-51, these distributions can be represented with Gaussian distribution with varying mean and variance parameters for different $[x_1, x_2]$. In Fig. 4-51, the bar heights express the ratio between 'n' and 'N" as defined in Eqn. (5-1). For example, in Fig. 4-51c), the distribution infers that, when $-0.125 < \Delta PV_{local} \leq -0.175$, the mean lies near -0.05 for ΔPV_{fleet}, and nearly 70% of the data are contained within [-0.1,0], or the standard deviation is 0.05. This is derived from the fact that for a Gaussian distribution, 68.27% of the values drawn randomly, remain within one standard deviation range around the mean. Also, the mean values of these distributions are apparently positively correlated with local PV ramps, while the variance increases as the range of local ramp is increased. For the whole dataset, these conditional probability distributions are showed with contours in Fig. 4-52. As seen in this figure, the fleet or net power ramps remain

within a narrow range around zero when local PV ramps are also close to zero. These ramps represent clear day conditions when local PV outputs are steady and thus net PV output does not fluctuate too much. From these contours it can be assumed that, mean values of representative Gaussian distributions can be expressed as a sigmoid function of local PV ramps. Sigmoid functions represent 'S' shaped curves showing linear growth with saturated ends. Standard deviation parameters, on the contrary, increase almost linearly as local PV ramps get higher. Such a relationship indicates that, when local PV power fluctuates due to cloud movements, the probability is high that these fluctuations would be visible into the fleet power profile as well. Though, as previous works suggest, this probability is dependent on the topology of the PV fleet. In essence, geographic smoothing effect would shrink the amplitude of the ramps seen by a single PV/measurement unit in aggregate PV power for a fleet or a large plant.

These insights can now be used to simulate PV fleet power from a smaller PV system. An example is shown in Fig. 4-53a) plotting ramps in local PV measurements and simulated PV fleet for a cloudy day. Measurements are taken from aforementioned 6.44 kW PV unit data for April 17, 2015. As inferred from the numerical analyses, the PV fleet ramps are simulated to be varying

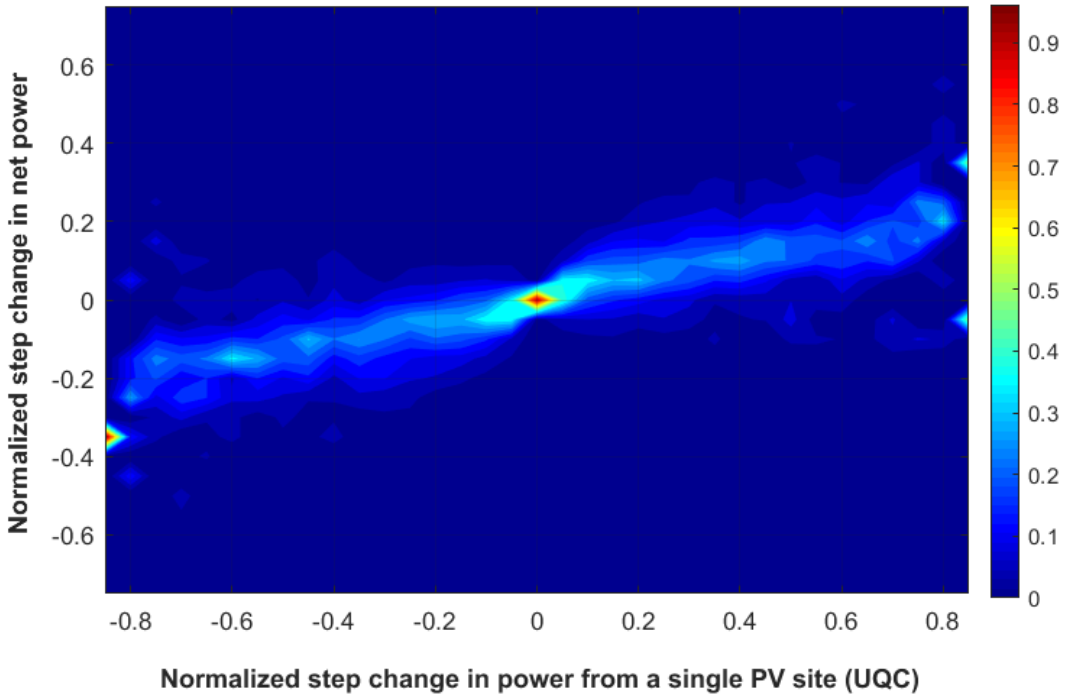

Fig. 4-52 Empirical probability contours for net PV power step changes with respect to local PV power step changes in UQC (derived for Mar-May, 2016)

within smaller range (50%) when local PV ramps are going as high as 80%. This translates in normalized power profiles, as seen in Fig. 4-53b). These simulated profiles can be further tuned by mapping accurate topology of the PV fleet being considered.

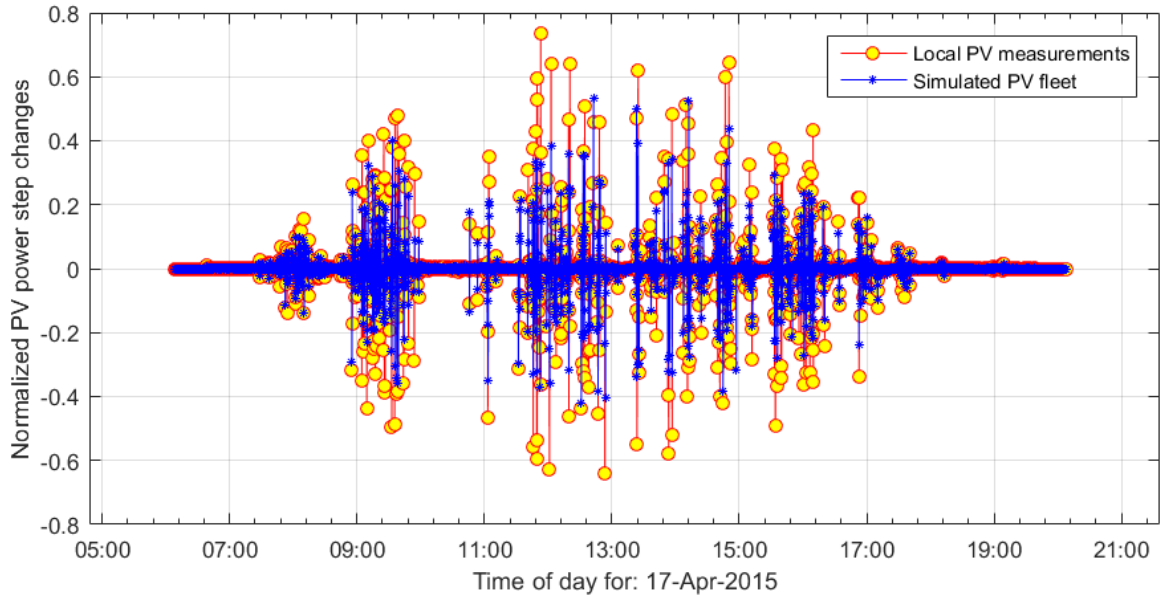

a)

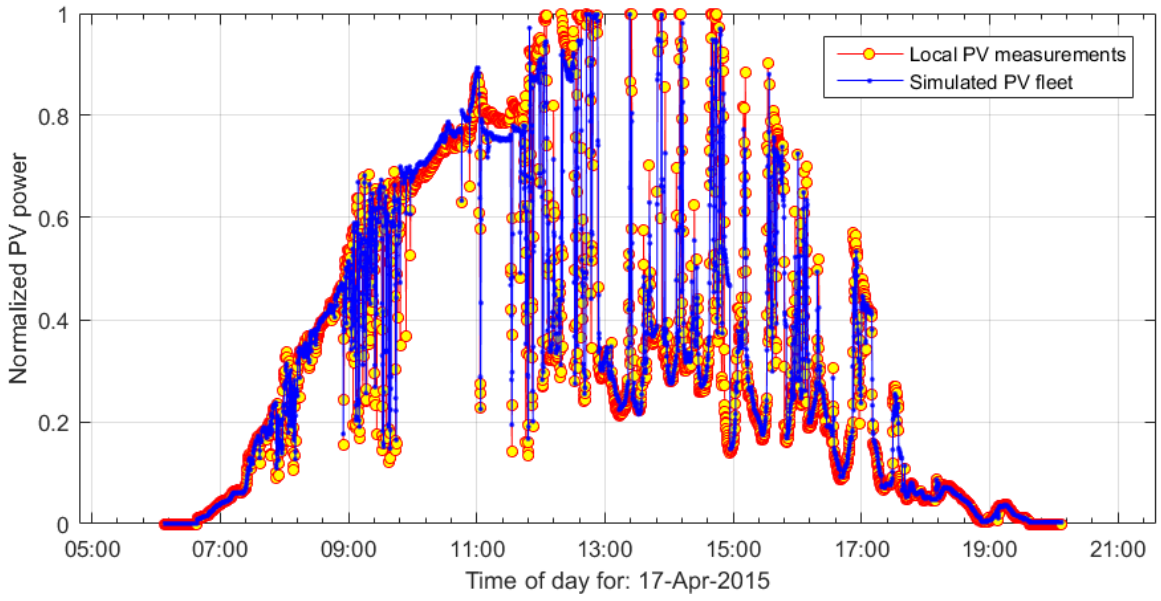

b)

Fig. 4-53 a) Simulated PV fleet power ramps derived using measured local PV; b) normalized power profiles for local PV unit and simulated PV fleet aggregate

5. Forecast-based approach for a coordinated voltage regulation scheme

Solar generation forecasts can not only aid the local voltage regulation at the inverter end, it can also be used to coordinate inverter operation with other voltage control devices, like voltage regulators (VR's), present in the circuit. This section discusses a coordinated scheme realizable with multi-timescale solar forecasting method which reduces tap-changing operations for VR's.

5.1 Autonomous control of step voltage regulators

The proposed method utilizes autonomous control of step VR's based on specific control set-points. This way, optimal tap positions need not be found at every time step, which could be computationally burdensome. Also, VR operation can then be coordinated with inverter voltage regulation by only tuning these control parameters. Besides, this method demonstrates a more realistic scenario, since a voltage regulator typically operates in an autonomous fashion, where operators specify regulation voltage level and bandwidth for the control mechanism. To understand how these VR control parameters should be adjusted to achieve desired voltage regulation, it is needed to know how these devices are modeled. Next section briefly visits the basics of VR's [125] for modeling purposes.

VR modeling

A VR is an autotransformer with an online tap changing mechanism on the series winding. It can be located at the load center in which case it can control a particular bus voltage directly. Or it can control the voltage at the load center by compensating for the voltage drop along the lines. By changing the taps of the series winding, VR changes the voltage at the target bus. The setting variables are:

- *Regulation voltage level*: desired voltage level to be maintained at the target bus. This is expressed on a 120V base.
- *Voltage bandwidth*: the range of variation allowed for the target voltage from the set voltage level. For example, if the voltage level is 121V and bandwidth is 2V, the VR will change its tap positions until the target voltage is within the range of 120-122V.

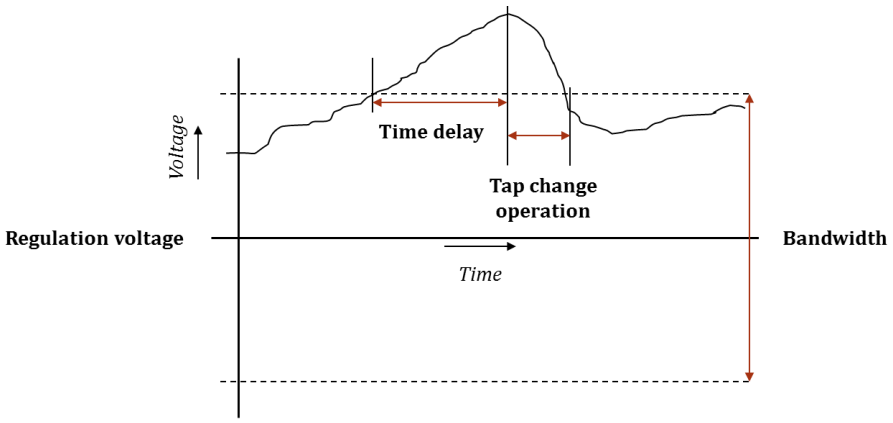

Fig. 5-1 Step voltage regulator control actions [126]

- *Time delay*: Time delay is the length of time for which the regulator waits before the actual execution of a tap change command. This delay prevents the regulator from accidentally tapping for voltage fluctuations of very short life span.

These control parameters are explained in Fig. 5-1 [126]. As seen in the figure, the VR waits for the 'time delay' duration after the voltage limit violation is sensed. The target voltage gets back within the band after the tap change operation is complete.

- *Line drop compensator settings (R/X)*: line drop compensator (LDC) circuit determines tap position for VR in such a way so that the voltage drop along the line (between the VR and the load center) is compensated for. Fig. 5-2 depicts a schematic of the LDC circuit and following tap change operation. The LDC circuit estimates the line drop with the help of the current transformer (CT) and adds it in potential transformer (PT) loop. The settings of resistance (R') and reactance (X') are expressed as voltage drop across these elements (in Volts). These

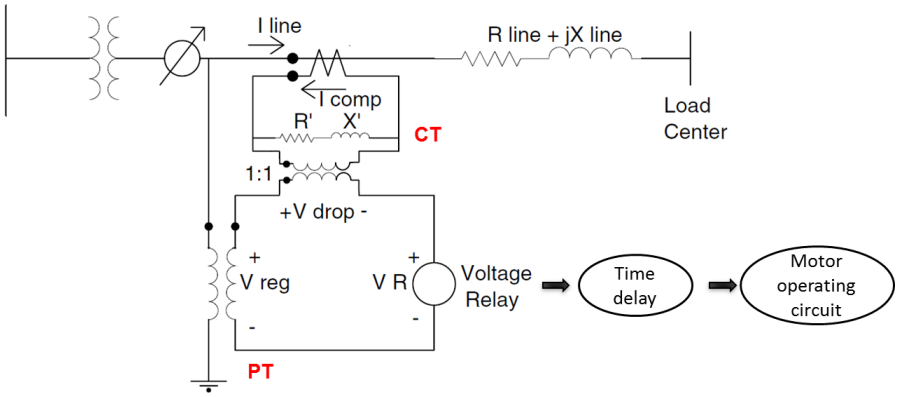

Fig. 5-2 Line drop compensator circuit in VR and its operational schematic [125]

elements act as the equivalent impedance between the regulator and the load center. So it requires the per-unit line impedance to be equal to the per-unit compensator impedance to accurately model the line drop. The voltage across the voltage relay represents the voltage at the load center, and thus initiates necessary motor operation (which conducts the tap position change in the series winding) after the specified time delay.

For standard VR's ±10% voltage regulation is achieved with 32 discrete steps. On a 120V base, each tap change provides 0.625% or 0.00625 pu or 0.75V change. For sensing the current tap position, the tap changers mostly have an output shaft on the rotary mechanism whose angular position is a mechanical analog of the tap position [9]. So, additional taps can be considered which will reduce this voltage change per step to smaller value, making the VR to control the voltage with finer resolution. This will also quicken the tap change as shifting to adjacent tap position will take less time. This tap changing operation time is also coming down as new gears are being innovated. For example, Eaton's quik-drive tap changer can rotate through all 33 (32 steps and 1 neutral) positions within less than 10 seconds [127]. These new technologies will extend the solution set for the intended optimization problem proposed here. For example, when additional steps in VR are considered, it can prevent the voltage violations of smaller magnitudes. Also faster switching mechanism will respond to voltage excursions quickly. In that case, the time delay of the VR can be set to higher value so that when inverter is regulating the voltage, the VR is not attempting to overcorrect the target bus voltage.

In OpenDSS, a control object (RegControl) is designed which emulates a standard utility voltage regulator or LTC control. As described in [128], some of the key properties are:

- **Transformer:** Name of Transformer to which the RegControl is connected
- **Winding:** Number of the winding (1 or 2) of the transformer element that the RegControl is monitoring.
- **Vreg:** Voltage regulator setting, in V, for the winding being controlled. Vreg times the Ptratio should give the voltage across the winding of the controlled transformer. (Default= 120.0V)
- **Band:** Bandwidth in V. (Default= 3.0)
- **Delay:** Time delay, in seconds. This is used to determine which regulator control will act first among the ones present at the circuit.

- **Ptratio:** Ratio of the PT that converts the controlled winding voltage to the regulator voltage.
- **CTprim:** Rating, in Amperes, of the primary CT rating for converting the line amps to control amps.
- **R:** R setting on the line drop compensator in the regulator, expressed in V.
- **X:** X setting on the line drop compensator in the regulator, expressed in V.

Based on input values for these properties, OpenDSS outputs tap positions for a static load flow simulation. If the VR has three phase connection and 'regcontrol' objects are defined for each phase, there are three resultant tap positions, given that the feeder is represented with an unbalanced circuit.

5.2 Minimizing tap-changing operations in voltage regulators

The presence of power electronic circuitry allows inverters to react within short time-scale but conventional VR's require longer time to control the voltage. In this case, a multi-timescale forecasting model can be applied. Using this model, very short-term (15-second) forecasts can be employed by PV inverters to manage the local voltage. On the other hand, short-term (1-6 hours) forecasts can be applied to approximate required regulation voltage level and/or bandwidth for the VR's based on previous analyses. These analyses are performed in an offline manner to determine VR control parameters which would minimize tap-changing operations for the forecasting horizon. Thus the proposed method will provide supervisory control for the VR's to minimize their tap-change operations over the day (or a specific time window).

Because this minimization problem does not decide on exact tap position, prediction error in the short-term case can be accommodated within the autonomous operation of the VR's. While average generation forecast will be used to determine the regulation voltage level for the VR's, a variance parameter will be guiding the bandwidth change of the VR. This variance parameter will be estimated from the past measurements and NWP data which provide forecast about weather type.

The objective function for an optimization problem considering voltage deviation and tap-changing counts can be written as,

Minimize:

$$J = w_v \sum_{i=1}^{N} V_{dev_i} + w_t \sum_{j=1}^{Nt} TC_j \quad \ldots \quad \text{Eqn. (5-1)}$$

Here,

w_v= weighing parameter for the voltage deviation component of the objective function

w_t= weighing parameter for the tap-changing count component of the objective function

V_{dev_i}= voltage deviation at i-th node (from previous time step)

N= number of nodes (this can represent all of the nodes in the circuit or a reduced set of selected critical nodes)

TC_j= tap-changing count for j-th VR within the time window

Nt= number of VR's

The constraints are:

Inverter capacity constraint: $P_{inv} \leq P_{MPPT}$; and $\sqrt{{P_{inv}}^2 + {Q_{inv}}^2} \leq S$

Power factor criterion: $|Q_{inv}| \leq \tan(\cos^{-1}(pf_{min})) * P_{inv}$

Regulation voltage limit: $V_{reg,up} \leq V_{Reg_j} \leq V_{reg,low}$

Bandwidth limit: $V_{bw,up} \leq V_{BW_j} \leq V_{bw,low}$

Where,

P_{inv}= instantaneous real injection from PV inverter (after APCf)

Q_{inv}= instantaneous reactive injection from PV inverter (after APCf considering RPC)

V_{Reg}= regulation voltage level for the VR

V_{BW}= voltage bandwidth for the VR

$V_{reg,up}$= Upper threshold to set regulation voltage level for the VR

$V_{reg,low}$= Lower threshold to set regulation voltage level for the VR

$V_{bw,up}$= Upper threshold to set bandwidth for the VR

$V_{bw,low}$= Lower threshold to set bandwidth for the VR

As described in chapter 4, section 4.3.2, the voltages at the inverter end are taken care by applying APCf (N only represents the nodes where PV systems are connected). So, for the problem at hand, which minimizes tap-changing counts, the weight terms are defined as:

$$w_v = 0;\ w_t = 1$$

The voltage deviations terms will be directly coming from the measurements, while the tap-changing count will be expressed as a function given by,

$$TC = f(V_{reg}, V_{BW}) \quad \ldots \quad \text{Eqn. (5-2)}$$

This function will be derived offline by numerically sweeping the decision variables, i.e. regulation voltage and voltage bandwidth of the VR. Load and PV generation profiles are kept same in this case.

As the tap change process depends on instantaneous variations in target voltage profile, TC in Eqn. (5-2) cannot be expressed in a closed form. So the minimization problem is solved here in MATLAB by finding the valley(s) in the search space.

The underlying assumption for realizing this coordinated scheme is that, it works in a smart grid environment i.e. a reliable communication infrastructure already exists and connecting the inverter and VR's to the decision center. For this particular application, the data/control center can be coordinate with the smart inverter, and VR's. In that case, VR's have to be equipped with controllers which ensure remote control functionalities for setting up the control parameters. Uncertainties in load profile are not addressed for this work as it is out of the scope. However, a load forecasting block can be easily integrated with PV forecasting method and thus the overall system modeling can be further improved.

The proposed coordinated voltage regulation scheme will derive the VR set-points based on the optimal solutions for similar load/generation (from short-term PV generation forecasts) scenario. Thus, for online application, the decision time will be reduced as the set-points will have to be updated on a short-term basis.

5.3 Case study design

To evaluate the performance of the proposed technique, a modified version of IEEE 34 node test feeder is taken for the case study. As the case study presented in section 4.3.2, multiple PV locations are considered here. This test feeder has been modeled in OpenDSS while the algorithms are implemented in MATLAB code blocks. Data exchange between OpenDSS and MATLAB takes place through the built-in component object model (COM) interface in OpenDSS. In general, grid measurements like node voltages or branch flows are sent to MATLAB from OpenDSS and MATLAB sends back operational set-point data, to OpenDSS based on numerical calculations, like real/reactive power to be provided by PV inverters. Fig. 5-3 shows a sample case study design for multiple PV scenario where local voltage regulation methods are employed through RPC-APCf from inverter-end based on very short-term PV generation forecasts. VR control is implemented after the APCf layer with known inverter set-points to find out appropriate regulation voltage level and bandwidth value to minimize number of tap-change counts over APCf application.

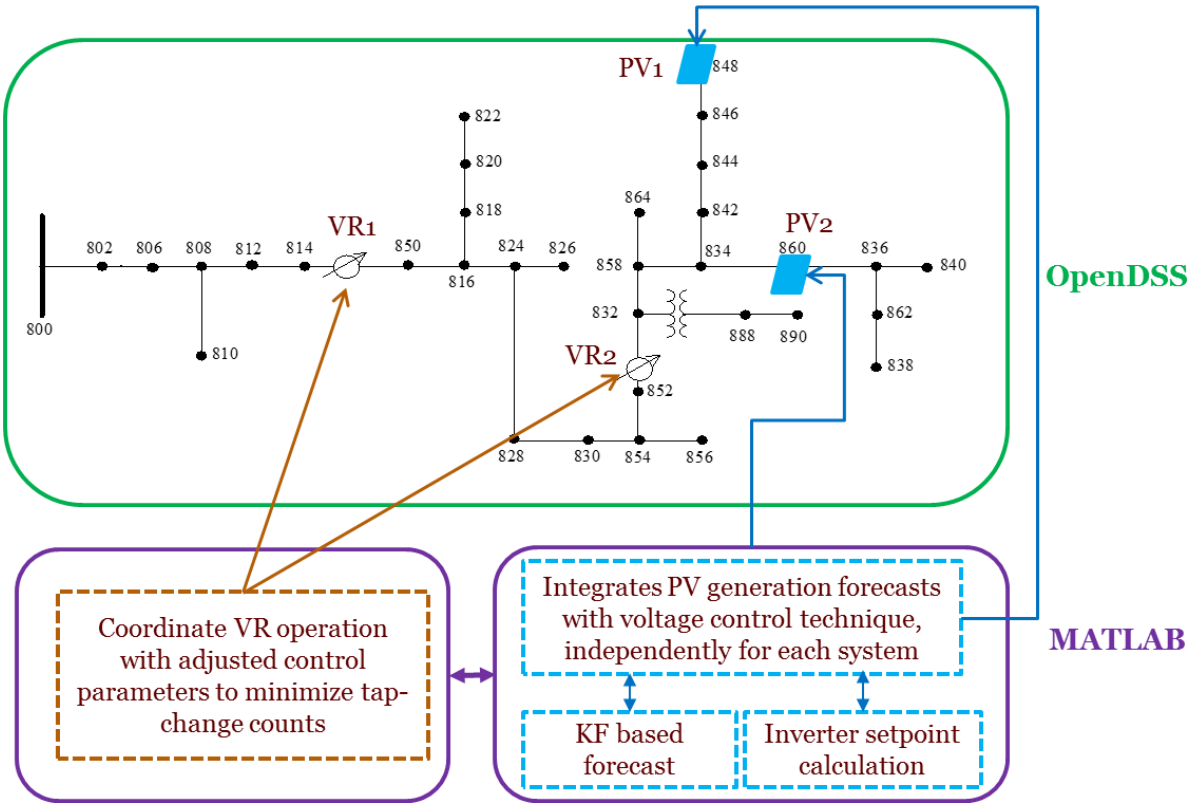

Fig. 5-3 Case study design schematic to minimize tap-change counts over APCf application

For the test feeder, the regulation voltage level, V_{Reg}, is defined on a 120 V base. On a 120 V base, the allowable voltage excursion is $\pm 5\%$, or within 114-126V. So, while changing the regulation voltage (V_{Reg}) and bandwidth (V_{BW}) it has to be kept in mind that:

$$V_{Reg} + V_{BW} \leq 126V \; and \; V_{Reg} - V_{BW} \geq 114V \qquad \cdots \quad \text{Eqn. (5-3)}$$

If the band center is set at the middle of this range, the maximum bandwidth can be achieved. The minimum is defined by the range of voltage change allowed by a 32-step VR, that is 0.75 V. So, the minimum voltage regulation bandwidth these VR's can provide would be 0.75 V on each side of the band center, or 1.5 V.

$$V_{bw,up} = 6\ V \; and \; V_{bw,low} = 1.5\ V$$

This gives the range of V_{Reg} to be:

$$V_{reg,low} = 115.5\ V \; and \; V_{reg,up} = 124.5\ V \; for \; V_{BW} = 1.5\ V$$

V_{Reg} and V_{BW} are selected based on Eqn. (5-3). For any V_{Reg}, 2-2.5 V bandwidth is commonly used, whereas 3 V and higher values can be used if tight regulation is not desired [129]. According to these considerations, the combinations of V_{Reg} and V_{BW} are showed in Table 5-1. In this table, the color code works as: green colored cells are deemed okay, orange is not preferred but can be taken into consideration, yellow is okay but not preferred and red means these combinations will violate Eqn. (5-3) or voltage would fall outside the 114-126V bound.

So, the simulation search space is limited between 1.5-4 V for V_{BW} and corresponding V_{Reg} values according to Table 5-1. If the tap-change count minimization is not being addressed, the preset values, given by the test feeder configuration are used.

Table 5-1 Combination of allowable sets of control parameters for VR's

V_{Reg} \ V_{BW}	1.5	2	2.5	3	3.5	4	4.5	5	6
115.5									
116									
117									
118									
119									
120									
121									
122									
123									
124									
124.5									

The test feeder configurations are specified as:

$$\text{For VR1: } V_{Reg} = 122\,V;\ V_{BW} = 2\,V$$
$$\text{For VR2: } V_{Reg} = 124\,V;\ V_{BW} = 2\,V \qquad \cdots \quad \text{Eqn. (5-4)}$$

Time delay parameters are defined according to the distance of the VR from the substation. Commonly, the closer the VR, the faster it should work or the less the time delay. So, for VR2 (As seen from Fig. 5-3) time delay is more than that for VR1. Usual value for time delay is set within 30-60 seconds range [129]. As the case studies are simulated with 15-second data, the time delay for VR1 is set to be 2 data samples or 30-second. This accounts for the fastest tap-changing mechanism to be placed at the substation transformer with least delay (15 seconds). For VR2, time delay is set as 45-second. For these case studies, static load flow simulation is performed with OpenDSS, that is, steady-state values are derived for every 15 seconds. If the voltage fluctuation happens on a faster timescale than the time delays defined for VR's, tap positions are kept fixed as the previous time step. In other words, the 'regcontrol' object in OpenDSS is activated at every 30-second interval for VR1, and at 45-second interval for VR2. In between these intervals, the tap positions do not change. This method models realistic operation of the VR control which do not

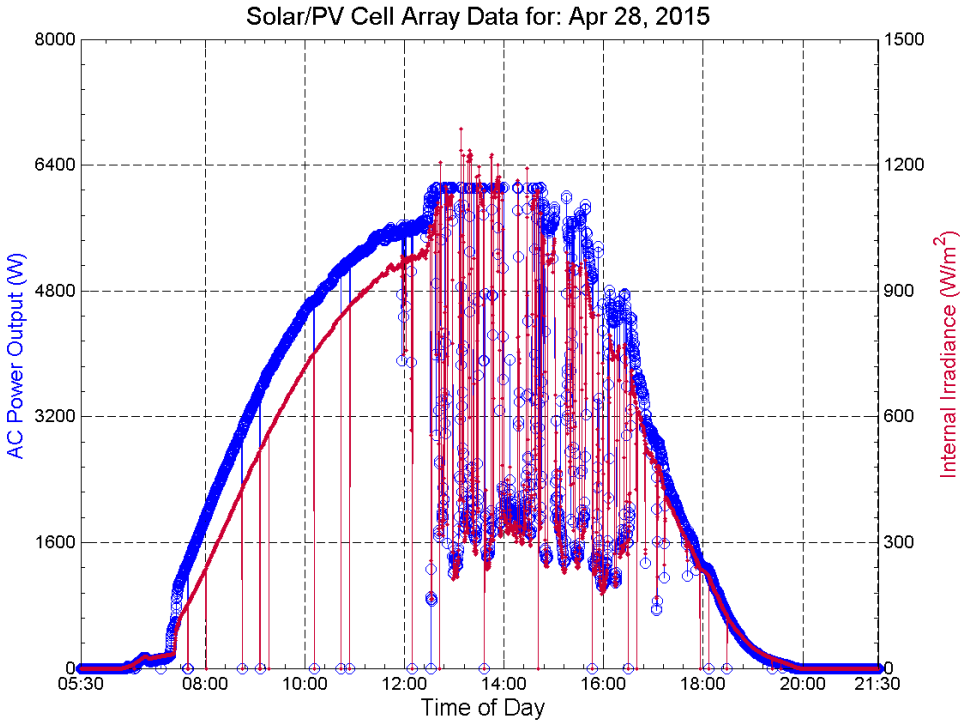

Fig. 5-4 PV AC output and plane of array irradiance measurements for Apr 28, 2015

issue a tap raise/lower command if the voltage fluctuation is too fast or occurs within its 'time delay' duration.

To effectively study the reduction in tap-change operation, days with high irradiance fluctuations need to be chosen for this case study (for example, Apr 28, 2015, as seen in Fig. 5-4).

5.4 Results and discussions

Tap position for VR's throughout the day of Apr 28, 2015 are showed in Figs. 5-5 – 5-6. Base case and modified base case data, as discussed in section 4.3.2 are also included for comparison. The base case refers to PV integration without any control, modified base case refers to fixed pf control and APCf technique uses dynamic active power curtailment and reactive power compensation based on PV forecasts (details in section 4.2).

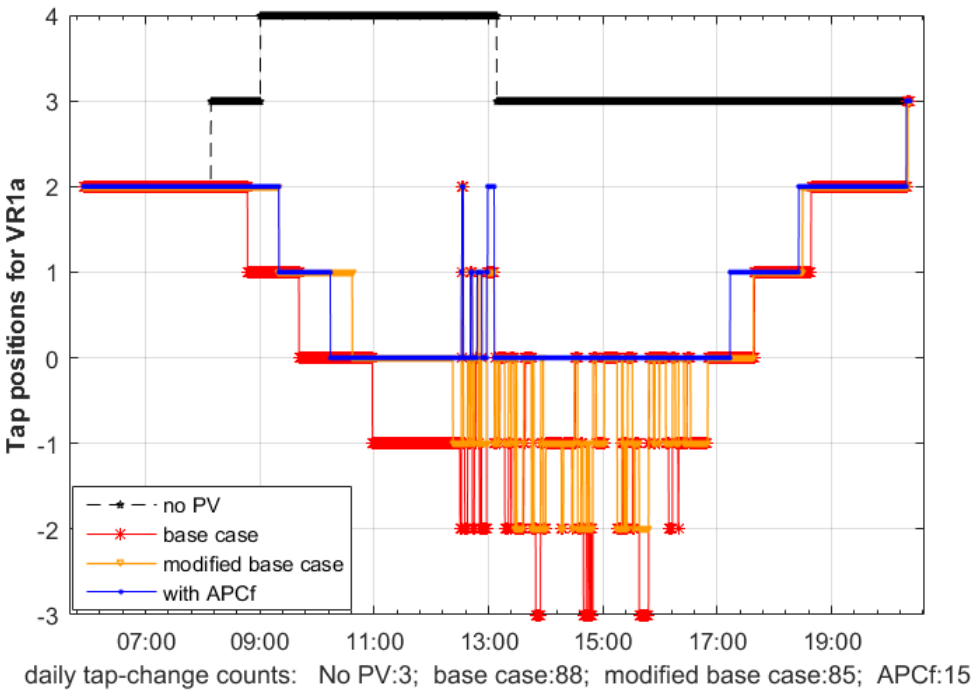

a)

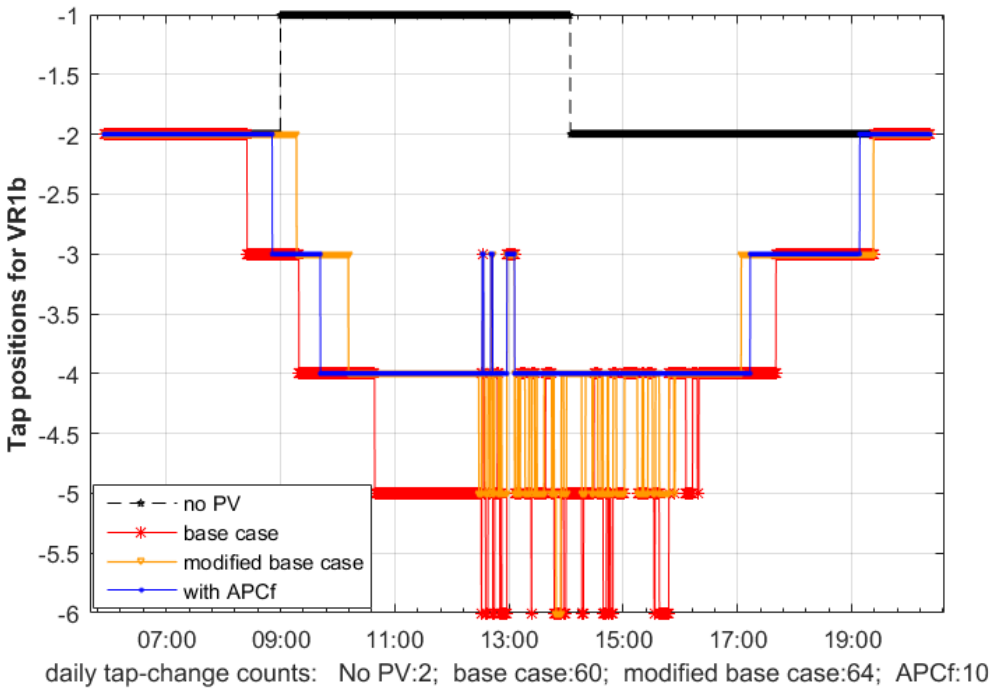

b)

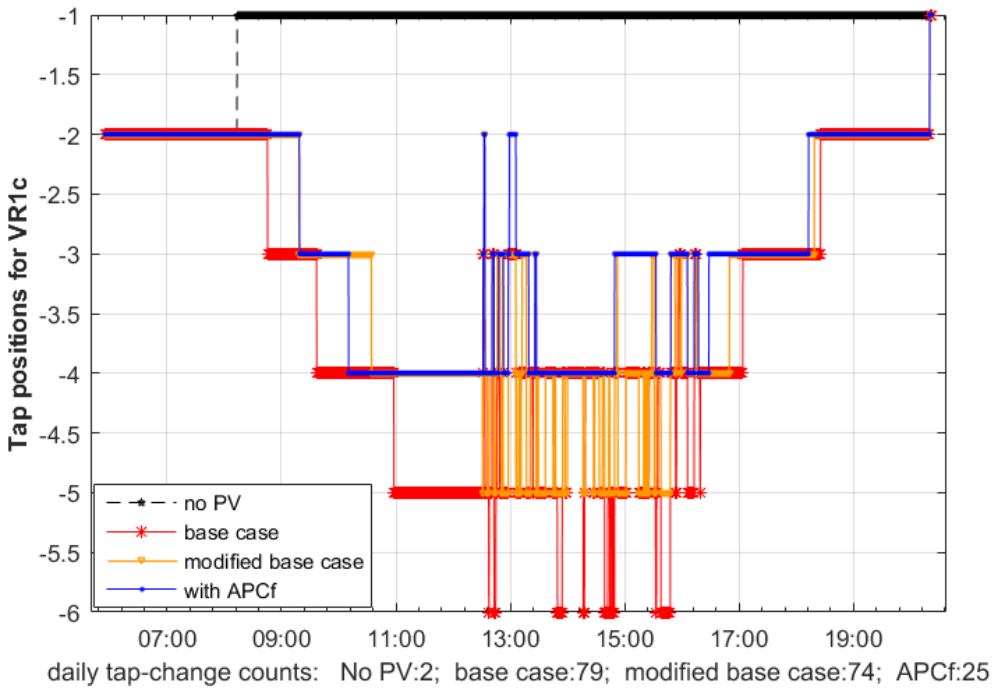

c)

Fig. 5-5 Tap positions for 3 phases of VR1 for Apr 28, 2015, and tap-change counts

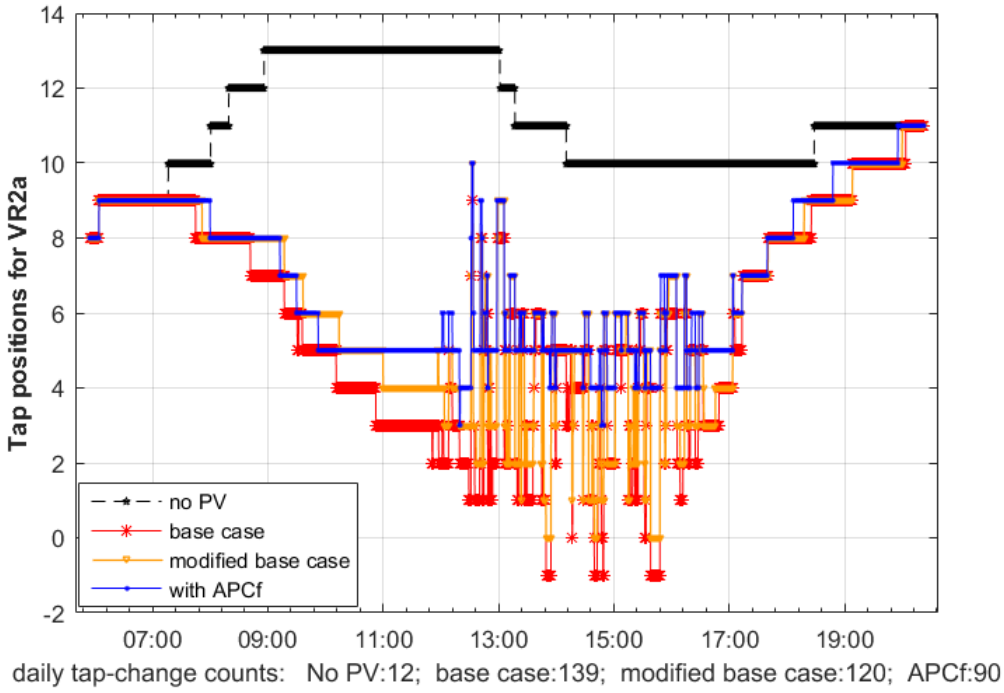

daily tap-change counts: No PV:12; base case:139; modified base case:120; APCf:90

a)

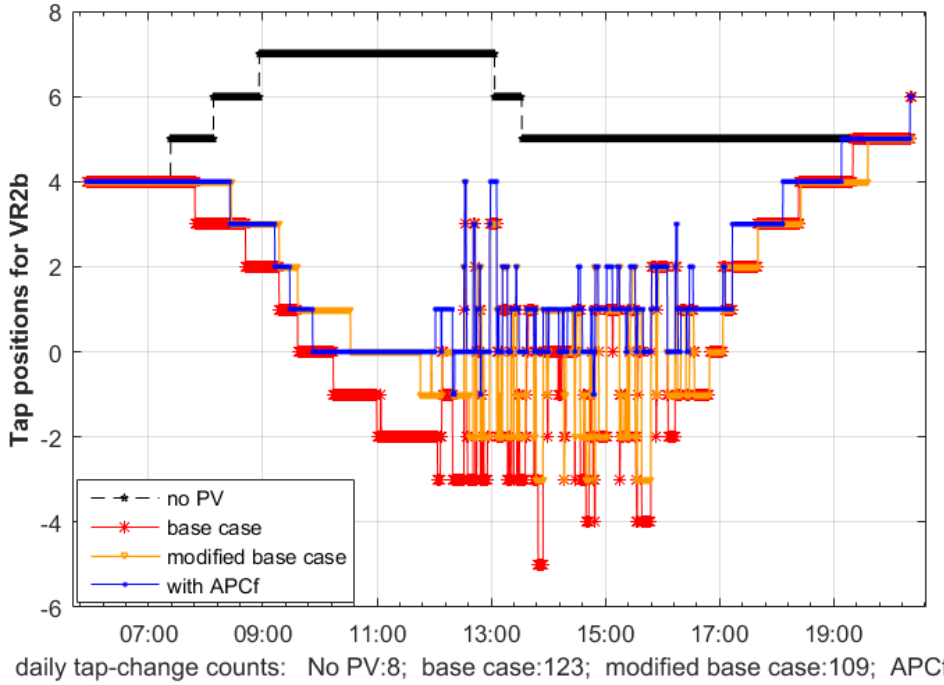

daily tap-change counts: No PV:8; base case:123; modified base case:109; APCf:85

b)

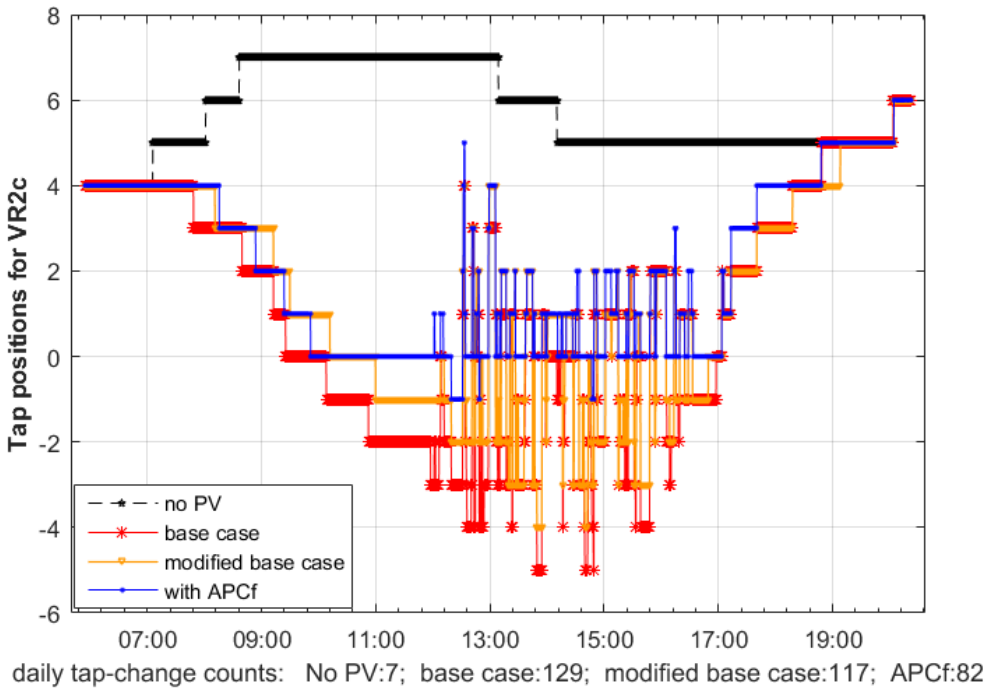

c)

Fig. 5-6 Tap positions for 3 phases of VR2 for Apr 28, 2015 and tap-change counts

All these cases include preset VR settings defined by the test feeder configuration. Because of the relative location, VR2 does not show significant improvement over base case or modified base case after the application of APCf. To reduce tap-change count further, VR2 control parameters can be tuned accordingly. As seen from Fig. 5-6, there is scope to minimize tap-change operations in the daytime, specifically during12-6 pm. The minimization problem is solved in two segments- each for a 3-hour interval. Outcome considering the whole search space are put together in Tables 5-2 and 5-3. Numbers in this table represent total tap count for all three phases in the given period of time.

In these tables the minimum in the ‘green’ range and the minimum right at the starting edge of the ‘orange’ range are highlighted. For both these cases (Tables 5-2 and 5-3), the tap change counts are minimal in the vicinity of 3-3.25 V of bandwidth with regulation levels lying near 118-118.5 V. So, for this whole 6 hours (12-6 pm) 118.5 V (closer to 120 V) and 3 V are selected as a conservative choice, and the tap-position profiles are re-evaluated for the whole day.

Table 5-2 Number of total tap-change counts for VR2 (Apr 28, 2015: 12-3 pm)

V_{Reg} \ V_{BW}	1.5	1.75	2	2.25	2.5	2.75	3	3.25	3.5	3.75	4
115.5	149										
116	138	111	97								
116.5	152	131	101	85	71						
117	146	123	106	83	49	44	33				
117.5	141	115	97	82	65	47	33	31	21		
118	150	133	100	90	70	51	38	26	19	21	17
118.5	146	126	109	88	54	43	30	27	14	28	16
119	145	122	97	84	63	51	38	32	26	17	9
119.5	150	136	108	91	71	57	37	29	20	16	15
120	145	126	105	91	61	43	33	27	16	19	15
120.5	147	121	102	85	66	54	38	32	25	17	9
121	151	137	111	89	73	52	39	31	19	15	9
121.5	147	122	104	92	62	44	37	27	23	21	8
122	150	128	107	87	70	56	35	32	23	18	13
122.5	160	143	114	98	77	54	41	30	21		
123	146	124	108	93	72	50	38				
123.5	149	134	108	90	77						
124	157	134	117								
124.5	149										

With the adjusted settings, the daily total tap-change counts for three phases are shown in Table 5-4 along with those from previously discussed methods. As seen in Table 5-4, modified base case reduces the tap change count by 13.7%, 11.4% and 9.3% over base case for VR2a, 2b and 2c, respectively. APCf application further improves the VR operation by reducing these counts to 33.9% (on average) over base case. Lastly, coordinated VR operation, i.e. redefined V_{Reg}, V_{BW} values yield to much higher degree of reduction in daily tap change counts for all three phases. In general, this process can be applied with lower time duration to fine tune control parameters of VR's and attain even greater reduction in tap changing operation throughout the day.

Table 5-3 Number of total tap-change counts for VR2 (Apr 28, 2015: 3-6 pm)

V_{Reg} \ V_{BW}	1.5	1.75	2	2.25	2.5	2.75	3	3.25	3.5	3.75	4
115.5	117										
116	102	92	80								
116.5	111	98	79	64	59						
117	115	91	81	63	37	33	24				
117.5	105	92	79	68	50	33	28	26	18		
118	110	100	76	67	57	40	29	20	13	10	10
118.5	114	95	79	69	42	31	22	17	7	25	17
119	111	96	79	69	48	35	31	27	20	19	10
119.5	107	103	81	69	58	45	30	24	17	13	11
120	113	96	78	73	47	33	25	19	9	18	14
120.5	109	94	82	70	52	38	30	24	23	11	3
121	111	104	82	67	60	42	32	23	18	17	13
121.5	110	94	82	71	51	34	27	19	17	18	14
122	111	99	86	71	54	36	28	24	20	11	7
122.5	120	107	85	71	62	42	35	24	16		
123	110	96	84	74	59	36	26				
123.5	113	100	86	72	59						
124	124	100	87								
124.5	111										

Table 5-4 Daily tap-change counts for Apr 28, 2015; for VR2 with different methods

	Base case tap change count	**Modified base case** {% reduction from base case}	**APCf** {% reduction from base case }	**VR coordination** {% reduction from base case }
VR2a	139	120 {13.7%}	90 {35.3%}	31 {77.7%}
VR2b	123	109 {11.4%}	85 {30.1%}	21 {82.9%}
VR2c	129	117 {9.3%}	82 {36.4%}	27 {79.1%}

5.5 Integration of storage

Energy storage systems have been discussed in literature with regard to their growing applications in smart grid environment. Rapid growth in battery technologies has enabled multiple applications of battery storage systems in frequency regulation, grid stabilization, transmission loss reduction, diminished congestion, wind and solar energy smoothing, peak-shaving, load-leveling etc. [130]. Being an inverter connected device, energy storage or battery systems can provide local active and/or reactive compensation which can improve voltage stability and thus assist in preventing possible voltage collapse [131]. For example, NaS based grid-scale batteries are suitable for renewable resource integration due to their long discharge cycles and fast response characteristics [132]. Similar to large-scale energy storage systems, load-side batteries can be used for voltage smoothing applications, given that communication infrastructure is accessible to these smart devices. The following section briefly talks about how efficient charging/discharging operation of battery storage can aid the PV system to regulate network voltage in a distribution feeder.

5.5.1 System setup and simulation scenario

The numerical analyses presented in this section are performed on modified IEEE 34 node test feeder system. End of feeder location or bus#840 (Fig. 4-39) is chosen for PV placement, as in the case study presented in section 4.3.1.

Battery charging scenario is simulated under the assumption that the charging takes place when real injection is reduced from the Maximum power point tracking (MPPT) operating condition by employing reactive power compensation enhanced with active power curtailment (RPC-APC) technique (discussed in chapter 3). This technique curtails real injection from PV system when the inverter cannot supply required reactive power to prevent overvoltage situation. The load-side battery systems are charged using this curtailed PV power.

When sudden drop in PV generation is observed, corresponding node voltage will also follow the trend leading to steep voltage fluctuation. In this developed scenario, battery will be discharged to prevent such voltage fluctuations. This discharged power compensates for any sudden change (drop in this case) in real power injected from the inverter while the reactive compensation remains unaffected. Here, only the requisite values for battery charging/discharging power are calculated

which keep the voltage within predefined regulation bandwidth. The algorithm is briefly discussed below in relevant steps:

Battery- charging:

i. Estimates required reactive compensation to prevent voltage limit (upper) violation.

ii. Proceeds when required reactive compensation cannot be supplied due to high real power output.

iii. Curtails the real output (and thus increases the available reactive compensation) till the voltage gets within the bound.

iv. The curtailed power is fed to charge the battery.

Battery- discharging:

i. Determines the average value of the node voltage within a predefined time-window (smoothing window).

ii. Checks if the deviation between the measured voltage due to PV generation drop and the average voltage (calculated in previous step) is outside a predefined fluctuation deadband. This deviation represents instantaneous value of voltage fluctuation.

iii. Draws power from the battery until the voltage fluctuation is within acceptable threshold value. The battery unit is assumed to be connected at the same bus as the PV system.

Battery- idle:

i. Battery is not charged when there is no PV power curtailment, i.e. required reactive compensation can be supplied by the inverter for MPPT generation, keeping node voltage within upper bound.

ii. Battery does not need to discharge when instantaneous voltage fluctuation falls within the predefined deadband.

5.5.2 Results from case studies and discussions

Numerical analyses are presented here for several days with varying PV generation and load profiles. As the primary objective of this algorithm is to provide voltage regulation, voltage profiles (mean of three-phase values) are compared for two cases: 1) with original MPPT output

of PV system (RPC) and 2) after battery compensation (with RPC-APC). For the first case, reactive power compensation is limited by the instantaneous active PV generation, and thus often the voltage violates the prescribed threshold for end of feeder PV location [107]. In the second case, either i) PV active power is curtailed to increase in reactive compensation capability of the inverter (battery charging operation) for preventing overvoltage, or ii) battery is discharged to provide active power in order to prevent sudden and rapid voltage drop (as described in the previous section).

To show the efficacy of the proposed technique, a narrower voltage regulation bandwidth is considered compared to typical ±5% range. So, for the example presented here,

Upper voltage limit, V_{up}= 1.01 p.u.

Lower voltage limit, V_{low}= 0.99 p.u.

Fluctuation deadband=1/4 of regulation bandwidth= 0.005 p.u.

Smoothing window= 10 min

Here, the voltage fluctuation parameter is,

$$\Delta V(i) = V(i) - V(i-1) \quad \cdots \quad \text{Eqn. (5-5)}$$

And power fluctuation parameters are defined as,

$$\Delta P_{PV}(i) = P_{PV}(i) - P_{PV}(i-1)$$
$$\Delta P_{batt}(i) = P_{batt}(i) - P_{batt}(i-1) \quad \cdots \quad \text{Eqn. (5-6)}$$

For the battery, +ve sign of P_{batt} denotes charging and -ve sign represents discharging operation.

Line voltage regulators (VR's) are operated with fixed taps here to evaluate the performance of the voltage regulation technique. Results from this analysis are summarized in the following graphs (Figs. 5-7 –5-11).

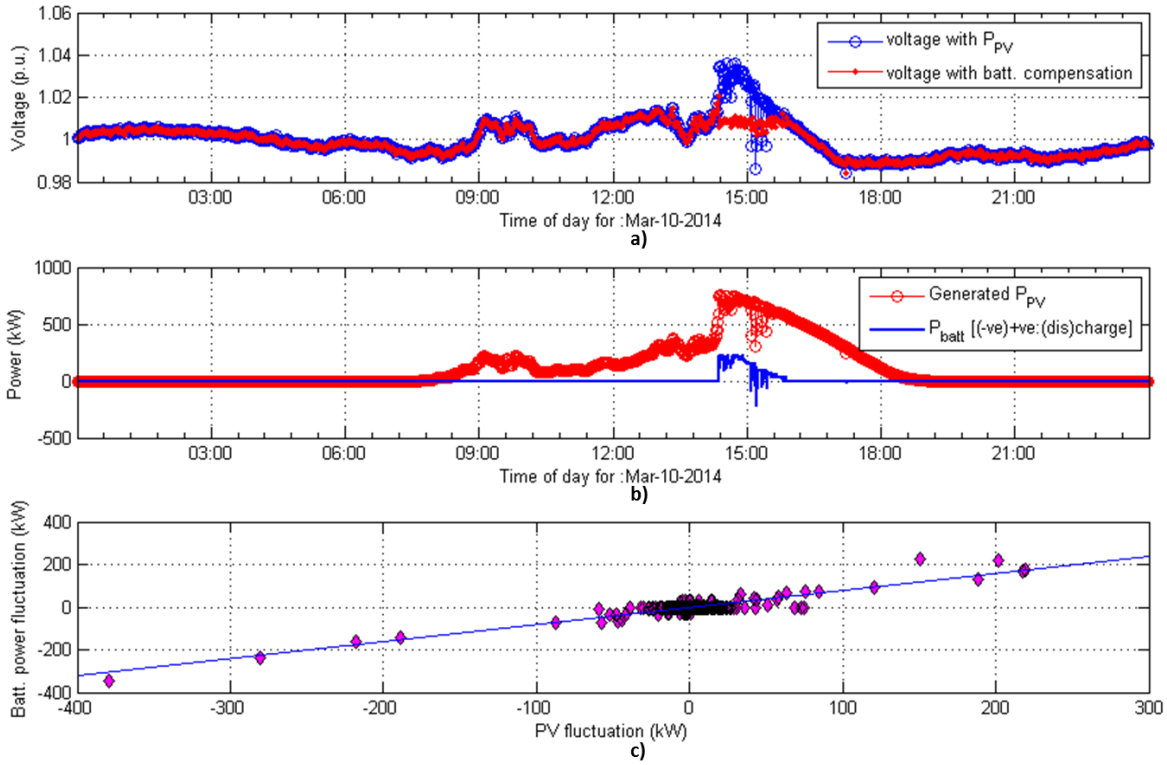

Fig. 5-7 a) voltage profile improvement, b) required PV and battery power, and c) battery and PV power fluctuations for Mar 10, 2014

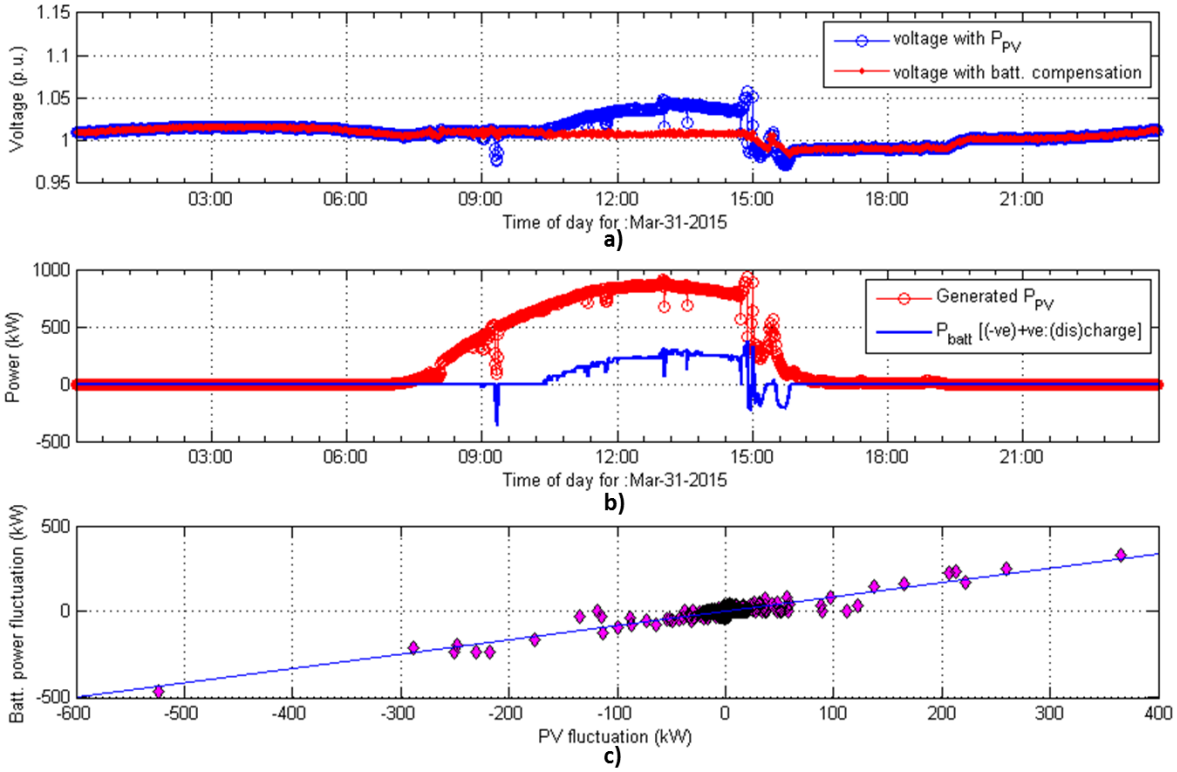

Fig. 5-8 a) voltage profile improvement, b) required PV and battery power, and c) battery and PV power fluctuations for Mar 31, 2015

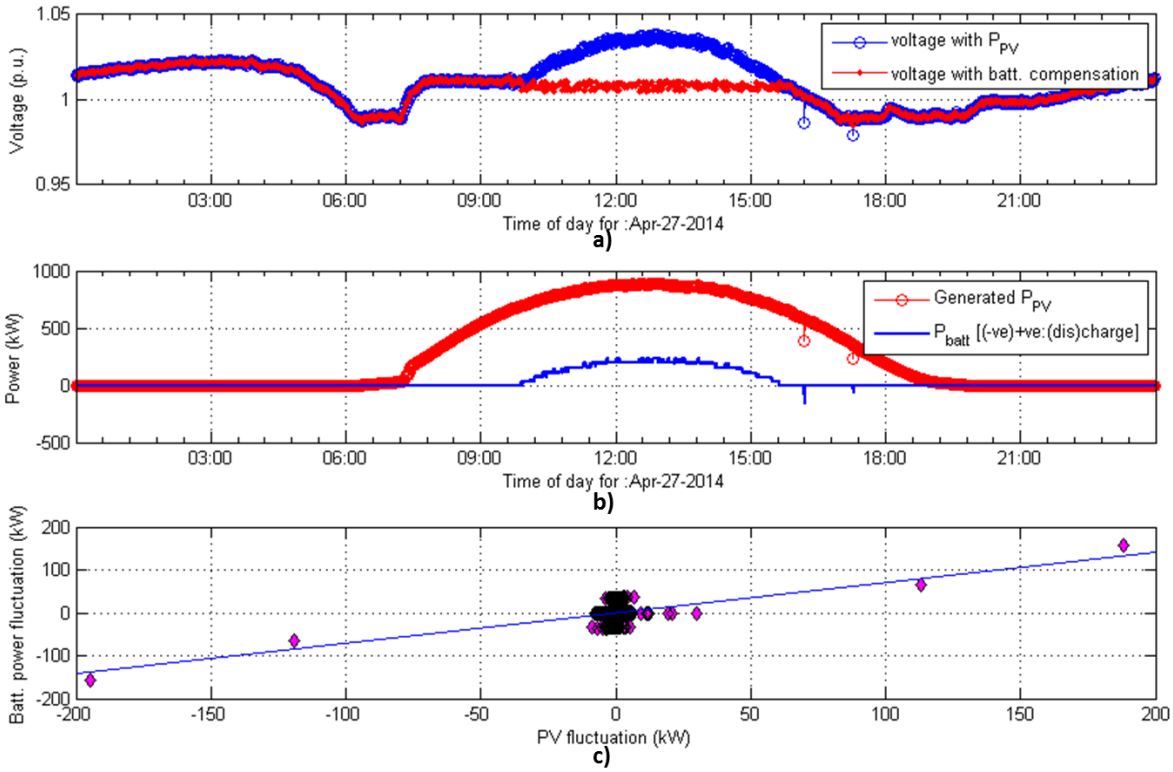

Fig. 5-9 a) voltage profile improvement, b) required PV and battery power, and c) battery and PV power fluctuations for Apr 27, 2014

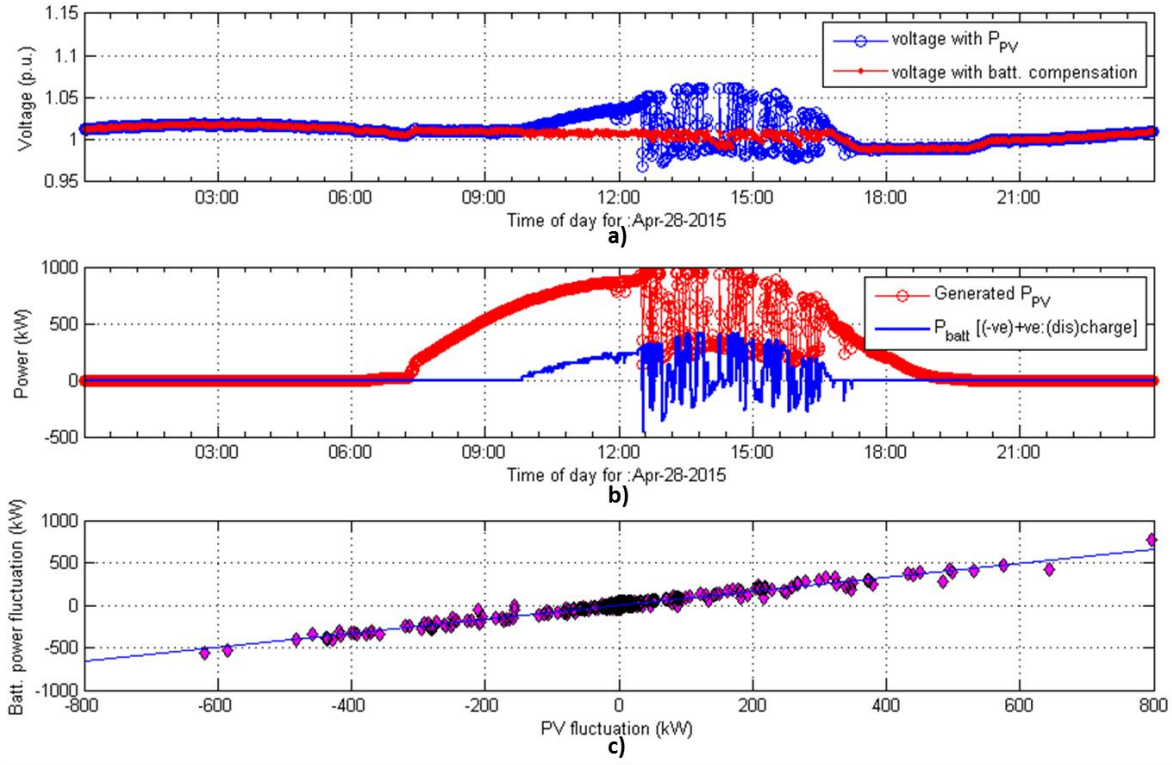

Fig. 5-10 a) voltage profile improvement, b) required PV and battery power, and c) battery and PV power fluctuations for Apr 28, 2015

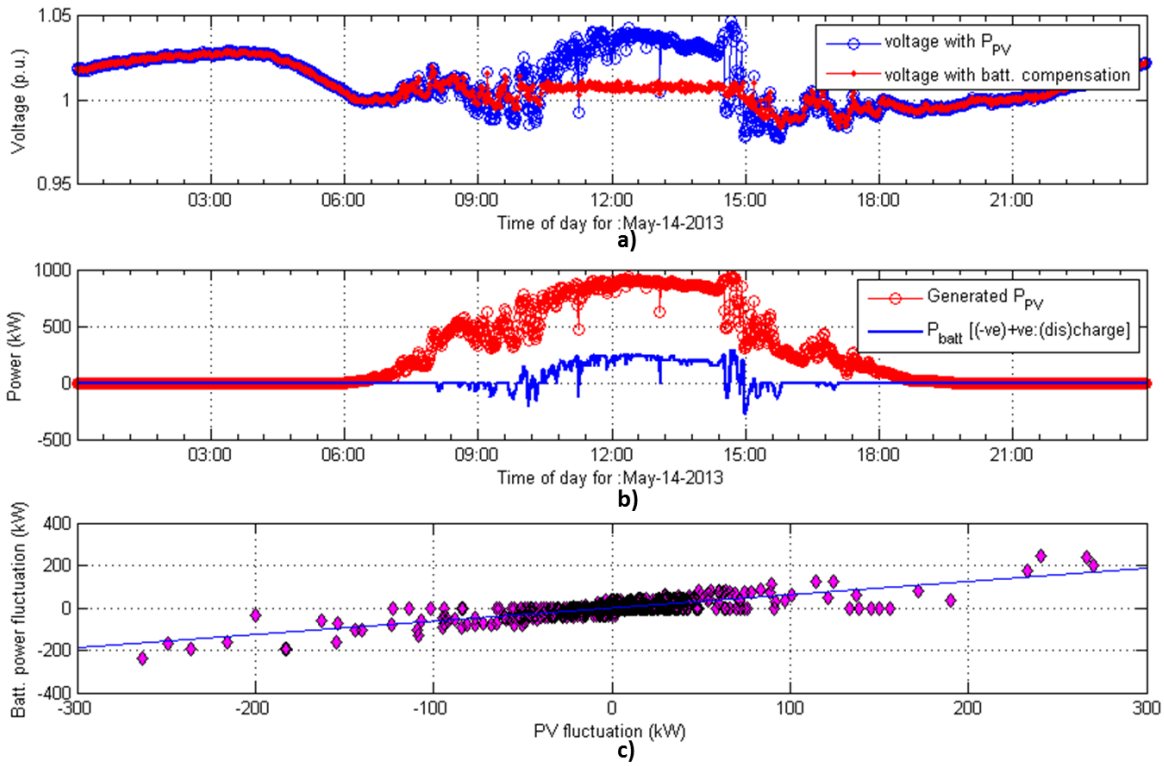

Fig. 5-11 a) voltage profile improvement, b) required PV and battery power, and c) battery and PV power fluctuations for May 14, 2013

As seen in the graphs (Figs. 5-7 –5-11), the overvoltage is prevented with RPC-APC technique and the instantaneous fluctuations (drop) are prevented by discharging the battery. The improvement of the voltage profiles is vivid during noon hours when PV generation nears its peak but the loads are not that high. Second parts of these graphs (Figs. 5-7b) –5-11b)) show PV generation (MPPT) along with necessary power from the battery. In cases of fast PV output fluctuations, battery has to charge/discharge frequently. Figs. 5-7c) –5-11c) show how the battery power (charging/discharging) changes with respect to PV output fluctuations. These scatter plots show actual values of the fluctuations whereas the blue lines show the linear fit. The battery is used as a smoothing device for PV in this scenario, but it does not directly smoothen P_{PV}. Rather this algorithm tries to keep the voltage profile smooth over the day. That is why the battery charging/discharging power does not reflect the rise/drop in PV output precisely. For example, when there is a sudden rise in PV generation by 200 kW, the system voltage might fall within the upper bound after curtailing only 170 kW. Thus the battery charging power will then be 170 kW. The dots along the blue lines show the extent of PV output (and corresponding P_{batt}) fluctuations

throughout the day. For a clear day (like Apr 27, 2014 in Fig. 5-9), the dots are gathered near the origin. On the other hand, for Apr 28, 2015, the dots are all over the fitted line, as the PV output fluctuates within large range due to fast cloud movements.

The maximum values of these fluctuations can give an insight about the required battery characteristics suitable for this particular scenario. Table 5-5 shows maximum levels of fluctuations in PV generation for these days and required changes in battery charging/discharging power. The fluctuation data presented in this table are taken for 1 min interval.

Table 5-5 PV generation fluctuation vs required battery charging/discharging rates

Day	**Max PV fluctuation (+ve: rise) (kW)**	**Required battery power change (+ve: charging) (kW)**	**Max PV fluctuation (-ve: fall) (kW)**	**Required battery power change (-ve: discharging) (kW)**
Mar 10, 2014	219.1382	174.9520	-379.6924	-344.4013
Mar 31, 2015	365.1009	329.9766	-523.5248	-465.0871
Apr 27, 2014	188.3734	156.1790	-194.7787	-156.1790
Apr 28, 2015	797.9037	768.9064	-619.4099	-560.6599
May 14, 2013	270.2252	200.8316	-263.4705	-239.8159

As seen in the table, 2nd and 3rd column represent the overvoltage scenario where active power curtailment takes place and battery is charged. The negative values shown in the 4th and 5th column denote the discharging of battery which compensates for the sudden fall in PV output. This table also reinstates that the required battery charging/discharging rate will be high when the PV is fluctuating within a wide range (for example, about 80% of the peak value for Apr 28, 2015).

Limitations

This numerical example primarily focusses on regulating the node voltage rather than smoothing the PV output directly. If power transactions are considered (between PV and battery), capacity optimization needs to be discussed to avoid excessive capital cost for battery establishment. This optimization study will also consider battery parameters like charging/discharging rate and their limiting values [133].

The usage of battery for voltage regulation in presence of PV is a power application of energy storage which employs short periods of discharge (seconds to minutes), short recharging periods

and often require many cycles per day; as opposed to energy applications requiring long discharge hours and a single cycle [134]. This is also evident in the result of the aforementioned numerical example. So, the operational costs of batteries might increase for such applications where very fast response and high charging/discharging rate is required.

Choosing the parameters can significantly affect the outcome of this numerical example. For example, if the smoothing window is very large the voltage will tend to stay at a steady value for that long period and thus battery will charge/discharge at a faster rate to smoothen fast transients in PV output. This will require even more number of cycles for the battery and will reduce its life. The voltage thresholds dictate how much energy will be transferred from/to the battery. Due to high PV penetration the network voltage profile is expected to remain at higher values. So, the lower the threshold values are, the larger is the active power curtailment (from PV). Consequently, the battery will get to charge more and discharge less. But then, once the battery's state of charge (SOC) hits its upper limit, the battery cannot charge anymore. Similarly, if the threshold values are higher, there will be less curtailment and the battery will charge less. In that case, it will deplete quickly and cannot provide required regulation for the rest of the day.

6. Conclusion and future work

6.1 Conclusion

This dissertation presents the development of a framework which helps to mitigate impacts of high PV penetrations on the distribution voltage profile. Growing presence of PV in distribution grid causes overvoltage and voltage fluctuations. Intermittency in solar irradiance reflects into feeder voltage fluctuations with a life-span ranging from few cycles (transient overvoltage) to few minutes. Commonly used voltage regulating devices, like line voltage regulators and switched capacitor banks cannot typically act in such short timescale because of their control mechanism which includes motor-driven switching operations. But even if they do, they need to switch more frequently, which increases the wear and tear and can lead to higher maintenance and replacement costs. As a possible remedy, the smart PV inverter is being considered as a viable option to participate in feeder voltage regulation in a faster timescale. A PV inverter, which is capable to operate as a four-quadrant converter, can control its real and reactive power outputs and maintain the voltage at its terminals. The proposed local voltage regulation method builds upon this variable real/reactive injection/absorption capability of an inverter.

In this dissertation, solar forecasting is applied to augment the local voltage regulation scheme. If PV generation forecasts are to be integrated with network operation applications, like local voltage regulation, it is useful to employ an online forecasting approach that does not handle a large dataset for a very short-term forecasting scenario. In that case, measurement based dynamic prediction methods like the Kalman Filtering (KF) technique, can help reduce processing time. A hybrid method which combines physical PV modeling with the KF method is developed in this work. This hybrid forecasting technique can provide better accuracy compared to a naïve approach, when the PV output fluctuates due to fast cloud movements. To address the distributed PV scenario, modeling spatial variability or geographic dispersion are also discussed here using real data. The findings are applied to simulate large-scale PV generation profiles or PV fleet power profiles.

Based on the PV generation forecasts provided by the hybrid forecasting model, active power curtailment threshold values are determined in a dynamic manner. These threshold values along with estimated reactive compensation helps prevent predicted overvoltage scenarios. Power factor limits are also explored with this regulation technique. Case studies have been presented here with

varying PV locations, which show that this method can effectively prevent local overvoltage situations.

Voltage regulator operation is coordinated with this proposed method to reduce the number of tap-changing operations. This coordination method assumes that these devices can access communication infrastructure and receive control parameters from a remote data/control center. Properly tuned control settings can reduce the required number of tap-changing operations for voltage regulators. Case studies discussed here demonstrate the efficacy of this coordinated scheme.

Finally, the integration of storage has been studied to manage voltage fluctuations. This way, the otherwise curtailed energy can be utilized to charge the storage device to prevent overvoltages. Sudden voltage drops can be compensated for by discharging the storage/battery.

6.2 Future work

In essence, the proposed techniques in this dissertation outline a methodology to utilize inverter functions for providing grid-support and thus accommodate more and more PV systems into the grid. Following are some research topics which can be explored using the work presented in this dissertation as a point of departure:

- The distributed PV model discussed here can be modeled considering greater details on the topology of the PV units. Such a study can be done for a large-scale PV plant using measurement data from point irradiance sensors. As large-scale PV applications are gaining grounds throughout the globe, such analyses would be beneficial to both utilities and investors.

- A central optimization algorithm can be addressed including all the control devices at once. These studies, however, may not be too suitable for practical implementation. But these would still provide important theoretical insight about how the future grid should operate. Based on such studies, a unified voltage control technique can be developed.

- Integrating storage elements to the grid in presence of growing PV penetration poses a multi-objective optimization problem. Storage capacity needs to be modeled with both capital and depreciation costs along with the inverter costs. Optimal battery characteristics for this particular application, i.e. voltage regulation, can be derived through such planning studies. These studies can investigate which kind of battery technology or chemistry, storage capacity and control strategy would be the most beneficial for high PV penetration scenario.

- Because the inverter is capable of providing both capacitive/inductive VAR compensations, solving undervoltage problem using PV inverter can provide an interesting field to study. This way, other grid-support functions can be developed using smart inverter capabilities.

- Demand response (DR) provides a method to shift and structure load shapes. DR programs often employ load forecasting models. Integrating load and PV generation forecasting can lead to formation of advanced algorithms. Such algorithms would combine smart inverter techniques with DR opportunities. For example, the overvoltage problems identified in this work would not occur if the loads were comparatively higher. If DR applications can shift some load according to PV forecasts, curtailment can be minimized at that point of time. Solar energy can then be fully utilized by serving some temporary or transitory loads.

References

[1] International Energy Agency, “Technology Roadmap: Solar Photovoltaic Energy,” September, 2014. Available: https://www.iea.org/publications/freepublications/publication/TechnologyRoadmapSolarPhotovoltaicEnergy_2014edition.pdf

[2] Global Market Outlook 2016-2020, SolarPower Europe, 2016. Available: http://www.solarpowereurope.org/insights/global-market-outllook/

[3] Solar Market Insight Report: 2014 Year in Review (Exec. Summary), GTM research and Solar Energy Industries Association, March 2016. Available: http://www.seia.org/research-resources/solar-market-insight-2015-q4; and News: http://www.seia.org/news/us-solar-market-sets-new-record-installing-73-gw-solar-pv-2015

[4] M. J. R. Perez, V. Fthenakis, “Impacts of long-timescale variability in solar resources at high PV penetrations: Quantification,” *38th IEEE Photovoltaic Specialists Conference (PVSC)*, pp. 2481-2486, Austin, TX, June 2012.

[5] J. Kleissl, M. Lave, M. Jamaly, J. Bosch, “Aggregate Solar Variability,” *IEEE Power and Energy Society General Meeting*, pp. 1-3, San Diego, CA, July 2012.

[6] F. Katiraei, J.R. Agüero, “Solar PV Integration Challenges,” *IEEE Power and Energy Magazine*, vol. 9, no. 3, pp. 62-71, May-June 2011.

[7] J. Bank, B. Mather, J. Keller, and M. Coddington, “High Penetration Photovoltaic Case Study Report,” NREL, 2013. Available: http://www.nrel.gov/docs /fy13osti/54742.pdf

[8] Digital Tapchanger Control M-2001C, M-2001D for Transformers and Regulators [Online]. Available: http://www.beckwithelectric.com/docs/specs/M-2001C-SP.pdf & http://www.beckwithelectric.com/docs/specs/M-2001D-SP.pdf

[9] Digital Voltage Regulator Control M-6200A [Online]. Available: http://www.beckwithelectric.com/docs/specs/M-6200A-SP.pdf

[10] M. F. McGranaghan, R. M. Zavadil, G. Hensley, T. Singh and M. Samotyj, “Impact of utility switched capacitors on customer systems-magnification at low voltage capacitors,” *1991 IEEE Power Engineering Society Transmission and Distribution Conference*, pp. 908-914, Dallas, TX, 1991.

[11] T. E. Grebe, “Application of Distribution System Capacitor Banks and Their Impact on Power Quality,” *IEEE Transactions on Industry Applications*, vol. 32, no. 3, pp. 714-719, May/June 1996.

[12] Abraham Ellis, Robert Nelson, Edi Von Engeln, Reigh Walling, Jason McDowell, Leo Casey, Eric Seymour, William Peter, Chris Barker, and Brendan Kirby, “Reactive power interconnection requirements for PV and wind plants- recommendations to

NERC," Sandia report, Sandia National Laboratories, February 2012. Available: http://energy.sandia.gov/wp-content/gallery/uploads/Reactive-Power-Requirements-for-PV-and-Wind-SAND2012-1098.pdf

[13] "IEEE Standard for Interconnecting Distributed Resources with Electric Power Systems - Amendment 1," in *IEEE Std 1547a-2014 (Amendment to IEEE Std 1547-2003)*, pp.1-16, May 2014.

[14] "Common Functions for Smart Inverters, Version 3," EPRI, February 2014. Available: http://www.epri.com/abstracts/Pages/ProductAbstract.aspx?ProductId=000000003002002233

[15] Pacific Gas and Electric Company, "Electric Rule No. 21: Generating Facility Interconnections," July 2016. Available: https://www.pge.com/tariffs/tm2/pdf/ELEC_RULES_21.pdf

[16] K. Turitsyn, S. Backhaus, and M. Chertkov, "Options for Control of Reactive Power by Distributed Photovoltaic Generators," in *Proceedings of the IEEE*, vol. 99, no. 6, pp. 1063-1073, June 2011.

[17] Reno, M.J.; Broderick, R.J.; Grijalva, S., "Smart inverter capabilities for mitigating over-voltage on distribution systems with high penetrations of PV," *2013 IEEE 39th Photovoltaic Specialists Conference (PVSC)*, pp. 3153-3158, Tampa, FL, June 2013.

[18] Y. Wang; P. Zhang; W. Li; W. Xiao; Abdollahi, A., "Online Overvoltage Prevention Control of Photovoltaic Generators in Microgrids," *IEEE Transactions on Smart Grid*, vol. 3, no. 4, pp. 2071-2078, December 2012.

[19] R. Tonkoski, L.A.C. Lopes, and T.H.M El-Fouly, "Coordinated Active Power Curtailment of Grid Connected PV Inverters for Overvoltage Prevention," *IEEE Transactions on Sustainable Energy*, vol. 2, no. 2 pp. 139-147, April 2011.

[20] D. Reeves, G. Nourbakhsh, G. Mokhtari, and A. Ghosh, "A distributed control based coordination scheme of household PV systems for overvoltage prevention," *IEEE Power and Energy Society General Meeting (PES*), Vancouver, BC, pp. 1-5, July 2013.

[21] Demirok, E.; Casado González, P.; Frederiksen, K.H.B.; Sera, D.; Rodriguez, P.; Teodorescu, R., "Local Reactive Power Control Methods for Overvoltage Prevention of Distributed Solar Inverters in Low-Voltage Grids," *IEEE Journal of Photovoltaics*, vol. 1, no. 2, pp. 174-182, October 2011.

[22] Fila, M.; Reid, D.; Taylor, G.A.; Lang, P.; Irving, M.R., "Coordinated voltage control for active network management of distributed generation," *Power & Energy Society General Meeting*, pp. 1-8, Calgary, AB, July 2009.

[23] Richardot, O.; Viciu, A.; Besanger, Y.; HadjSaid, N.; Kieny, C., "Coordinated Voltage Control in Distribution Networks Using Distributed Generation," *2005/2006 IEEE PES*

Transmission and Distribution Conference and Exhibition, pp. 1196-1201, Dallas, TX, May 2006.

[24] Polymeneas, E.; Benosman, M., "Multi-agent coordination of DG inverters for improving the voltage profile of the distribution grid," *2014 IEEE PES General Meeting | Conference & Exposition*, pp. 1-5, National Harbor, MD, July 2014.

[25] Rizy, D.T.; Yan Xu; Huijuan Li; Fangxing Li; Irminger, P., "Volt/Var control using inverter-based distributed energy resources," *2011 IEEE Power and Energy Society General Meeting*, pp. 1-8, San Diego, CA, July 2011.

[26] L. Liu; Y. Zhou; H. Li, "Coordinated active and reactive power management implementation based on dual-stage PLL method for grid-connected PV system with battery," *2010 IEEE Energy Conversion Congress and Exposition (ECCE)*, pp. 328-335, Atlanta, GA, September 2010.

[27] Kabir, M.N.; Mishra, Y.; Ledwich, G.; Dong, Z.Y.; Wong, K.P., "Coordinated Control of Grid-Connected Photovoltaic Reactive Power and Battery Energy Storage Systems to Improve the Voltage Profile of a Residential Distribution Feeder," *IEEE Transactions on Industrial Informatics*, vol. 10, no. 2, pp. 967-977, May 2014.

[28] X. Liu; A. Aichhorn, L. Liu, and H. Li, "Coordinated Control of Distributed Energy Storage System With Tap Changer Transformers for Voltage Rise Mitigation Under High Photovoltaic Penetration," *IEEE Transactions on Smart Grid*, vol. 3, no. 2, pp. 897-906, June 2012.

[29] H. Zheng; S. Li; C. Zang; W. Zheng, "Coordinated control for grid integration of PV array, battery storage, and supercapacitor," *2013 IEEE Power and Energy Society General Meeting (PES)*, pp.1-5, Vancouver, BC, July 2013.

[30] X. Su, M. Masoum, and P. Wolfs, "Optimal PV inverter reactive power control and real power curtailment to improve performance of unbalanced four-wire LV distribution networks," *IEEE Transactions on Sustainable Energy*, vol. 5, no. 3, pp. 967-977, July 2014.

[31] E. Dall'Anese, S. V. Dhople, and G. B. Giannakis, "Optimal Dispatch of Photovoltaic Inverters in Residential Distribution Systems," *IEEE Transactions on Sustainable Energy*, vol. 5, no. 2, pp. 487-497, April 2014.

[32] E. Dall'Anese, G. B. Giannakis, and B. F. Wollenberg, "Optimization of unbalanced power distribution networks via semidefinite relaxation," *North American Power Symposium (NAPS)*, pp. 1-6, Champaign, IL, September 2012.

[33] M. Farivar, R. Neal, C. Clarke, S. Low, "Optimal inverter VAR control in distribution systems with high PV penetration," *IEEE Power and Energy Society General Meeting*, pp.1-7, San Diego, CA, July 2012.

[34] B.W. Kennedy, R. H. Fletcher, "Conservation voltage reduction (CVR) at Snohomish County PUD," *IEEE Transactions on Power Systems*, vol. 6, no. 3, pp. 986-998, August 1991.

[35] H. J. Liu, T. J. Overbye, "Smart-grid-enabled distributed reactive power support with Conservation Voltage Reduction," *Power and Energy Conference at Illinois (PECI)*, pp.1-5, Champaign, IL, February 2014.

[36] T. Senjyu, Y. Miyazato, A. Yona, N. Urasaki, T. Funabashi, "Optimal Distribution Voltage Control and Coordination With Distributed Generation," *IEEE Transactions on Power Delivery*, vol. 23, no. 2, pp. 1236-1242, April 2008.

[37] T. Senjyu, Y. Miyazato, S. Toma, A. Yona, T. Funabashi, C. Kim, "Optimal control of distribution voltage profile by considering the number of operation of the distribution installations," *IEEE Power and Energy Society General Meeting*, pp. 1-8, Pittsburgh, PA, July 2008.

[38] M. Oshiro, K. Tanaka, T. Senjyu, S. Toma, A. Yona, A. Y. Saber, T. Funabashi, C. Kim, "Optimal voltage control in distribution systems using PV generators," *International Journal of Electrical Power & Energy Systems*, vol. 33, no. 3, pp. 485-492, March 2011.

[39] E. Dall'Anese, S. V. Dhople, B.B. Johnson, and G. B. Giannakis, "Optimal Dispatch of Residential Photovoltaic Inverters Under Forecasting Uncertainties," *IEEE Journal of Photovoltaics*, vol. 5, no. 1, pp. 350-359, January 2015.

[40] Z. Ziadi, M. Oshiro, T. Senjyu, A. Yona, N. Urasaki, T. Funabashi, and C. Kim, "Optimal Voltage Control Using Inverters Interfaced With PV Systems Considering Forecast Error in a Distribution System," *IEEE Transactions on Sustainable Energy*, vol. 5, no. 2, pp. 682-690, April 2014.

[41] M. Oshiro, K. Uchida, T. Senjyu, A. Yona, "Voltage control in distribution systems considered reactive power output sharing in smart grid," International *Conference on Electrical Machines and Systems (ICEMS)*, pp. 458-463, Incheon, October 2010.

[42] Tanaka, K.; Oshiro, M.; Toma, S.; Yona, A.; Senjyu, T.; Funabashi, T.; Kim, C.-H., "Decentralised control of voltage in distribution systems by distributed generators," *IET Generation, Transmission & Distribution*, vol. 4, no. 11, pp. 1251-1260, November 2010.

[43] Di Fazio, A.R.; Fusco, G.; Russo, M., "Decentralized Control of Distributed Generation for Voltage Profile Optimization in Smart Feeders," *IEEE Transactions on Smart Grid*, vol. 4, no. 3, pp. 1586-1596, September 2013.

[44] Goodwin, S.E.; Krause, O., "Mitigation of voltage band violations through distributed active and reactive power control of inverter based PV generation on LV networks,"

IEEE Power and Energy Society General Meeting (PES), pp.1-5, Vancouver, BC, July 2013.

[45] Kundu, S.; Backhaus, S.; Hiskens, I.A., "Distributed control of reactive power from photovoltaic inverters," *IEEE International Symposium on Circuits and Systems (ISCAS)*, pp. 249-252, Beijing, May 2013.

[46] P. Jahangiri, and D. C. Aliprantis, "Distributed Volt/VAR Control by PV Inverters," *IEEE Transactions on Power Systems*, vol. 28, no. 3, pp. 3429-3439, August 2013.

[47] N. Daratha, B. Das, and J. Sharma, "Coordination Between OLTC and SVC for Voltage Regulation in Unbalanced Distribution System Distributed Generation," *IEEE Transactions on Power Systems*, vol. 29, no. 1, pp. 289-299, January 2014.

[48] K. M. Muttaqi, A. D. T. Le, M. Negnevitsky, and G. Ledwich, "A Coordinated Voltage Control Approach for Coordination of OLTC, Voltage Regulator, and DG to Regulate Voltage in a Distribution Feeder," *IEEE Transactions on Industry Applications*, vol. 51, no. 2, pp. 1239-1248, March/April 2015.

[49] A. Samadi, R. Eriksson, L. Söder, B. G. Rawn, and J. C. Boemer, "Coordinated Active Power-Dependent Voltage Regulation in Distribution Grids With PV Systems," *IEEE Transactions on Power Delivery*, vol. 29, no. 3, pp. 1454-1464, June 2014.

[50] J. Jung, A. Onen, R. Arghandeh, and R. P. Broadwater, "Coordinated control of automated devices and photovoltaic generators for voltage rise mitigation in power distribution circuits," *Renewable Energy*, vol. 66, pp. 532-540, June 2014.

[51] F. Bignucolo, R. Caldon, and V. Prandoni, "Radial MV networks voltage regulation with distribution management system coordinated controller," *Electric Power Systems Research*, vol. 78, no. 4, pp. 634-645, April 2008.

[52] J. Barr and R. Majumder, "Integration of Distributed Generation in the Volt/VAR Management System for Active Distribution Networks," *IEEE Transactions on Smart Grid*, vol. 6, no. 2, pp. 576-586, March 2015.

[53] M. Watanabe, K. Matsuda, T. Futakami, K. Yamane, and R. Egashira, "Control method for voltage regulator based on estimated amount of photovoltaic generation power," *China International Conference on Electricity Distribution (CICED)*, pp.1-4, Shanghai, September 2012.

[54] M. Chamana, and B. H. Chowdhury, "Impact of smart inverter control with PV systems on voltage regulators in active distribution networks," *11th Annual High-capacity Optical Networks and Emerging/Enabling Technologies (HONET)*, pp. 115-119, Charlotte, NC, December 2014.

[55] Y. P. Agalgaonkar, B. C. Pal, and R. A. Jabr, "Distribution Voltage Control Considering the Impact of PV Generation on Tap Changers and Autonomous

Regulators," *IEEE Transactions on Power Systems*, vol. 29, no. 1, pp. 182-192, January 2014.

[56] D.L. King, W.E. Boyson, J.A. Kratochvill, "Photovoltaic Array Performance Model," Sandia Report, Available: http://prod.sandia.gov/techlib/access-control.cgi/2004/043535.pdf

[57] Sophie Pelland, Jan Remund, Jan Kleissl, Takashi Oozeki, Karel De Brabandere, "Photovoltaic and Solar Forecasting: State of the Art," October 2013, International Energy Agency. Available: www.iea-pvps.org/index.php?id=3&eID=dam_frontend_push&docID=1690

[58] M. G. D. Giorgi, P. M. Congedo, and M. Malvoni, "Photovoltaic power forecasting using statistical methods: impact of weather data," *IET Science, Measurement & Technology*, vol. 8, no. 3; pp 90-97, May 2014.

[59] L. Mora-L´opez, I. Mart´ınez-Marchena, M. Piliougine, and M. Sidrach-de-Cardona, "Binding Statistical and Machine Learning Models for Short-Term Forecasting of Global Solar Radiation," *10th International Symposium on Advances in Intelligent Data Analysis*, vol: 7014, pp. 294-305, Porto, Portugal, October 2011.

[60] A. Mellita, and S. A. Kalogirou, "Artificial intelligence techniques for photovoltaic applications: A review," Progress in Energy and Combustion Sciences, vol. 34, no. 5, pp. 574-632, October 2008.

[61] Hernandez-Travieso, J.G.; Travieso, C.M.; Alonso, J.B.; and Dutta, M.K., "Solar radiation modelling for the estimation of the solar energy generation," *2014 Seventh International Conference on Contemporary Computing (IC3)*, pp. 536-541, August 2014.

[62] N. Sharma, P. Sharma, D. Irwin, and P. Shenoy, "Predicting Solar Generation from Weather Forecasts Using Machine Learning," *IEEE Conference on Smart Grid Communications (SmartGridComm)*, pp. 528-533, Brussels, October 2011.

[63] J. Zeng, and W. Qiao, "Short-Term Solar Power Prediction Using an RBF Neural Network," *IEEE Power and Energy Society General Meeting*, pp. 1-8, San Diego, CA, July 2011.

[64] T. Hiyama, and K. Kitabayashi "Neural Network Based Estimation of Maximum Power Generation from PV Module Using Environmental Information," *IEEE Transactions on Energy Conversion*, vol. 12, no. 3, pp. 241-247, September 1997.

[65] A. Chaouachi, R.M. Kamel, R. Ichikawa, H. Hayashi, and K. Nagasaka, "Neural Network Ensemble-based Solar Power Generation Short-Term Forecasting," *World Academy of Science, Engineering and Technology*, vol. 3, 2009.

[66] J. Shi, W. Lee, Y. Liu, Y. Yang, and P. Wang, "Forecasting Power Output of Photovoltaic Systems Based on Weather Classification and Support Vector Machines,"

IEEE Transactions on Industry Applications, vol. 48, no. 3, pp. 1064-1069, May-June 2012.

[67] Y. Yang, and L. Dong, "Short-term PV Generation System Direct Power Prediction Model on Wavelet Neural Network and Weather Type Clustering," *5th International Conference on Intelligent Human-Machine Systems and Cybernetics (IHMSC*), pp. 207-211, Hangzhou, August 2013.

[68] M. Cococcioni, E. D'Andrea and B. Lazzerini, "24-hour-ahead forecasting of energy production in solar PV systems," *Intelligent Systems Design and Applications (ISDA)*, pp. 1276-1281, Cordoba, November 2011.

[69] C. S. Ioakimidis, S. Lopez, K. N. Genikomsakis, P. Rycerski, and D. Simic, "Solar Production Forecasting Based on Irradiance Forecasting Using Artificial Neural Networks," *Industrial Electronics Society- 39th Annual Conference of the IEEE*, pp. 8121-8126, Vienna, November 2013.

[70] M. Lei, L. Shiyan, J. Chuanwen, L. Hongling, and Z. Yan, "A review on the forecasting of wind speed and generated power," *Renewable and Sustainable Energy Reviews*, vol.13, no. 4, pp. 915–920, May 2009.

[71] R. Huang, T. Huang, R. Gadh, and N. Li, "Solar Generation Prediction using the ARMA Model in a Laboratory-level Micro-grid," *2012 IEEE Conference on Smart Grid Communications (SmartGridComm)*, pp. 528-533, Tainan, November 2012.

[72] E. G. Kardakos, M. C. Alexiadis, S. I. Vagropoulos, C. K. Simoglou, P. N. Biskas, and A. G. Bakirtzis, "Application of Time Series and Artificial Neural Network Models in Short-term Forecasting of PV Power Generation," *48th International Universities' Power Engineering Conference (UPEC)*, pp. 1-6, Dublin, September 2013.

[73] P. Bacher, H. Madsen, and H. A. Nielsen, "Online short-term solar power forecasting," *Solar Energy*, vol. 83, no. 10, pp. 1772–1783, October 2009.

[74] Hossain, M.R.; Rockhampton; Oo, A.M.T.; Ali, A.B.M.S., "Hybrid Prediction Method of Solar Power using Different Computational Intelligence Algorithms," *Universities Power Engineering Conference (AUPEC)*, pp. 1-6, Bali, September 2012.

[75] A. U. Haque, M. H. Nehrir, and P. Mandal, "Solar PV Power Generation Forecast Using a Hybrid Intelligent Approach," *IEEE Power and Energy Society General Meeting (PES*), pp. 1-5, Vancouver, BC, July 2013.

[76] H. T. Yang, C. M. Huang, Y. C. Huang, and Y. S. Pai, "A Weather-Based Hybrid Method for 1-Day Ahead Hourly Forecasting of PV Power Output," *IEEE Transactions on Sustainable Energy*, vol. 5, no. 3, pp. 917-926, July 2014.

[77] Cai Tao, Duan Shanxu, and Chen Changsong, "Forecasting Power Output for Grid-connected Photovoltaic Power System without using Solar Radiation Measurement,"

2nd IEEE International Symposium on Power Electronics for Distributed Generation Systems, pp. 773-777, Hefei, China, June 2010.

[78] H. C. Hottel, "A simple model for estimating the transmittance of direct solar radiation through clear atmospheres," *Solar Energy*, vol. 18, pp. 129-134, 1976.

[79] Y. Huang, J. Lu, C. Liu, X. Xu, W. Wang, and X. Zhou, "Comparative Study of Power Forecasting Methods for PV Stations," *International Conference on Power System Technology*, pp. 1-6, Hangzhou, China, October 2010.

[80] M. G. De Giorgi, P. M. Congedo, M. Malvoni, and M. Tarantino, "Short-Term Power Forecasting by Statistical Methods for Photovoltaic Plants in South Italy," *4th Imeko TC19 Symposium on Environmental Instrumentation and Measurements*, pp. 171-175, Lecce, Italy, June 2013.

[81] R. G. Brown, "Introduction to Random Signal Analysis and Kalman filtering," John Wiley and Sons, 1983.

[82] M. Hassanzadeh, M. Etezadi-Amoli and M.S.Fadali, "Practical Approach for Sub-Hourly and Hourly Prediction of PV Power Output," *North American Power Symposium (NAPS)*, pp. 1-5, Arlington, TX, September 2010.

[83] M. Chaabene and M. B. Ammar, "Neuro-fuzzy dynamic model with Kalman filter to forecast irradiance and temperature for solar energy systems," *Renewable Energy*, vol. 33, pp. 1435–1443, July 2008.

[84] M. Chaabene, "Measurements based dynamic climate observer," *Solar Energy*, vol. 82, no. 9, pp. 763-771, September 2008.

[85] B. Tuyishimire, R. McCann, and J. Bute, "Evaluation of a Kalman Predictor Approach in Forecasting PV Solar Power Generation," *4th IEEE International Symposium on Power Electronics for Distributed Generation Systems (PEDG*), pp. 1-6, Rogers, AR, July 2013.

[86] C. W. Chow, B. Urquhart, M. Lave, A. Dominguez, J. Kleissl, J. Shields, and B. Washom, "Intra-hour forecasting with a total sky imager at the UC San Diego solar energy testbed," *Solar Energy*, vol. 85, no. 11, pp. 2881-2893, November 2011.

[87] R. Perez, S. Kivalov, J. Schlemmer, K. H. Jr., D. Renne´, and T. E. Hoff, "Validation of short and medium term operational solar radiation forecasts in the US," *Solar Energy*, vol. 84, no. 12 pp. 2161-2172, December 2010.

[88] R. Marquez, H. T.C. Pedro, and C. F.M. Coimbra, "Hybrid solar forecasting method uses satellite imaging and ground telemetry as inputs to ANNs," *Solar Energy*, vol. 92, pp. 176-188, June 2013.

[89] European Photovoltaic Industry Association, "Connecting the Sun: Solar Photovoltaics on the Road to Large-Scale Grid Integration," Brussels, Belgium, 2012. Available:

http://www.epia.org/fileadmin/user_upload/Publications/Connecting_the_Sun_Full_Report_converted.pdf

[90] Jan Kleissl, "Solar Energy Forecasting and Resource Assessment," 1st edition, Academic Press, 2013.

[91] Lorenzo, A.T.; Holmgren, W. F.; Leuthold, M.; Chang Ki Kim; Cronin, A. D.; Betterton, E.A., "Short-term PV power forecasts based on a real-time irradiance monitoring network," *40th Photovoltaic Specialist Conference (PVSC)*, pp. 75-79, Denver, CO, June 2014.

[92] Moreno-Munoz, A., De la Rosa, J. J. G., Posadillo, R.; Bellido, F., "Very short term forecasting of solar radiation," *33rd IEEE Photovoltaic Specialists Conference (PVSC '08)*, pp. 1-5, San Diego, CA, May 2008.

[93] C. Chen, S. Duan, T. Cai, and B. Liu, "Online 24-h solar power forecasting based on weather type classification using artificial neural network," *Solar Energy*, vol. 85, no. 11, pp. 2856-2870, November 2011.

[94] J. A. Suykens and J. Vandewalle, "Least squares support vector machine classifiers," Neural processing letters, vol. 9, no. 3, pp. 293–300, June 1999.

[95] Y. Zhang, M. Beaudin, H. Zareipour and D. Wood, "Forecasting Solar Photovoltaic power production at the aggregated system level," North American Power Symposium (NAPS), pp.1-6, Pullman, WA, September 2014.

[96] Hecht-Nielsen, R., "Theory of the backpropagation neural network," International Joint Conference on Neural Networks, vol. 1, pp.593-605, 1989.

[97] J. Kou, J. Liu, Q. Li, W. Fang, Z. Chen, L. Liu and T. Guan, "Photovoltaic power forecasting based on artificial neural network and meteorological data," *IEEE Region 10 Conference (31194)- TENCON 2013*, pp.1-4, Xi'an, China, October 2013.

[98] M.W. Gardner and S.R. Dorling, "Artificial neural networks (the multilayer perceptron)—a review of applications in the atmospheric sciences," *Atmospheric Environment*, vol. 32, no. 14–15, pp. 2627-2636, August 1998.

[99] M. Lukoševičius and H. Jaeger, "Reservoir computing approaches to recurrent neural network training," *Computer Science Review*, vol. 3, no. 3, pp. 127-149, August 2009.

[100] D. Basak, S. Pal, and D. C. Patranabis, "Support vector regression," Neural Information Processing-Letters and Reviews, vol. 11, no.10, pp. 203-224, October 2007.

[101] B. Wolff, E. Lorenz, O. Kramer, "Statistical Learning for Short-Term Photovoltaic Power Predictions," *Computational Sustainability*, Springer International Publishing, vol. 645, pp. 31-45, April 2016.

[102] T. E. Hoff and R. Perez, "Quantifying PV power Output Variability," *Solar Energy*, vol. 84, no. 10, pp. 1782-1793, October 2010.

[103] C. Yang and L. Xie, "A novel ARX-based multi-scale spatio-temporal solar power forecast model," *North American Power Symposium (NAPS),* pp.1-6, Champaign, IL, September 2012.

[104] S. K. H. Chow, E. W. M. Lee, and D. H. W. Li, "Short-term prediction of photovoltaic energy generation by intelligent approach," *Energy and Buildings*," vol. 55, pp. 660-667, December 2012.

[105] Smith, J.W.; Sunderman, W.; Dugan, R.; Seal, B., "Smart inverter volt/var control functions for high penetration of PV on distribution systems," *2011 IEEE/PES Power Systems Conference and Exposition (PSCE),* pp.1-6, Phoenix, AZ, March 2011

[106] B. Mather, "Analysis of High-Penetration Levels of PV into the Distribution Grid in California," Presented in DOE/CPUC High Penetration Solar Forum, March 2011. Available (June, 2015): http://www1.eere.energy.gov/solar/pdfs/highpen forum2-01_mather_nrel.pdf

[107] Ghosh, S.; Rahman, S.; Pipattanasomporn, M., "Local distribution voltage control by reactive power injection from PV inverters enhanced with active power curtailment," *2014 IEEE PES General Meeting,* pp. 1-5, National Harbor, MD, July 2014.

[108] J. Smith, "Solar PV: Addressing Integration 'Now' and the 'Future'," presented at TVPPA Engineering and Operations Conference, August, 2013. Available: http://www.tvppa.com/SiteAssets/Pages/conferences/ Conf_EO/EPRI%20-%20Solar%20PV.pdf [Online]

[109] Sioshansi, Fereidoon P., "Prospects for Renewable Energy: Meeting the Challenges of Integration with Storage," in *Smart Grid: Integrating Renewable, Distributed and Efficient Energy,* Elsevier, 2012.

[110] North American Electric Reliability Corporation (NERC), "2013 Special Reliability Assessment: Accommodating an Increased Dependence on Natural Gas for Electric Power," May 2013. Available: http://www.nerc.com/pa/RAPA/ra/Reliability%20Assessments%20DL/NERC_PhaseII_FINAL.pdf [Online]

[111] C. Voyant, C. Paoli, M. Muselli, M. Nivet, "Multi-horizon solar radiation forecasting for Mediterranean locations using time series models," *Renewable and Sustainable Energy Reviews,* vol. 28, pp. 44-52, December 2013.

[112] Ciabattoni, L., Grisostomi, M., Ippoliti, G., Longhi, S., and Mainardi, E., "On line solar irradiation forecasting by minimal resource allocating networks," *20th Mediterranean Conference on Control & Automation (MED),* pp. 1506-1511, Barcelona, July 2012.

[113] S. Ghosh; S. Rahman; M. Pipattanasomporn, "Distribution Voltage Regulation through Active Power Curtailment with PV Inverters and Solar Generation Forecasts," *IEEE Transactions on Sustainable Energy,* in Press.

[114] John A. Duffie, William A. Beckman, “Solar Engineering of Thermal Processes,” Second edition, John Wiley & Sons Inc., June 1980.

[115] Medgar L. Marceau and Martha G. VanGeem, “Solar Reflectance of Concretes for LEED Sustainable Sites Credit: Heat Island Effect,” Portland Cement Association, 2007.

[116] F. C. Schweppe, “Uncertain dynamic systems,” Prentice-Hall Inc, New Jersey, 1973.

[117] Blazic, B.; Papic, I., “Voltage profile support in distribution networks — influence of the network R/X ratio,” in *13th Power Electronics and Motion Control Conference 2008 EPE-PEMC*, pp. 2510-2515, Poznan, September 2008.

[118] Stetz, T., Marten, F., Braun, M., “Improved Low Voltage Grid-Integration of Photovoltaic Systems in Germany,” *IEEE Transactions on Sustainable Energy*, vol. 4, no. 2, pp. 534-542, April 2013.

[119] Sangwongwanich, A.; Yang, Y.; Blaabjerg, F., “High-Performance Constant Power Generation in Grid-Connected PV Systems,” *IEEE Transactions on Power Electronics*, vol. 31, no. 3, pp. 1822-1825, March 2016.

[120] van Haaren, R., Morjaria, M. and Fthenakis, V., “Empirical assessment of short-term variability from utility-scale solar PV plants,” *Progress in Photovoltaics*, vol. 22, no. 5, pp. 548-559, November 2012.

[121] E. Wiemken, H.G. Beyer, W. Heydenreich, K. Kiefer, “Power characteristics of PV ensembles: experiences from the combined power production of 100 grid connected PV systems distributed over the area of Germany,” *Solar Energy*, vol. 70, no. 6, pp. 513-518, 2001.

[122] M. Lave, J. S. Stein and A. Ellis, “Analyzing and simulating the reduction in PV powerplant variability due to geographic smoothing in Ota City, Japan and Alamosa, CO,” *2012 IEEE 38th Photovoltaic Specialists Conference (PVSC), Volume 2*, pp. 1-6, Austin, TX, June 2012.

[123] Murata, A., Yamaguchi, H. and Otani, K. “A method of estimating the output fluctuation of many photovoltaic power generation systems dispersed in a wide area,” *Electrical Engineering in Japan 166 (4)*, pp. 9-19, 2009.

[124] The University of Queensland solar PV data. Available: http://solar.uq.edu.au/user/reportEnergy.php

[125] William H. Kersting, “Distribution System Modeling and Analysis,” CRC Press, Boca Raton, 2002.

[126] Jim Cross, “Voltage Regulator Placement & Settings,” Presented at Milsoft Users Conferece, 2013, Available: http://www.milsoft.com/sites/www.milsoft.com/files/presentation-files/2013%20UC%20Voltage%20Regulator%20Placement%20&%20Settings%20-%20Jim%20Cross,%20PE.pdf

[127] "Smart Grid solution: Smarter voltage regulation," Cooper Power Systems by Eaton, 2013. Available: http://www.cooperindustries.com/content/ dam/public/powersystems/resources/library/ 225_VoltageRegulators/B22514036.pdf

[128] Reference Guide: The Open Distribution System Simulator (OpenDSS), Program revision 7.6, June 2013.

[129] Load Tap Changing Control, J. H. Harlow, Beckwith Electric Company, Presented to National Rural Electric Cooperative Association (NRECA), March, 1996. Available: https://www.beckwithelectric.com/docs/tech-papers/loadcntl.pdf

[130] X. Li, D. Hui, and X. Lai, "Battery Energy Storage Station (BESS)-Based Smoothing Control of Photovoltaic (PV) and Wind Power Generation Fluctuations," *IEEE Transactions on Sustainable Energy*, vol. 4, no. 2, pp. 464-473, April 2013.

[131] M. Sagara, M. Furukakoi, H. Matayoshi, T. Senjyu, M. S. Shah, and T. Funabashi, "Voltage Stability Improvement to Power Systems with Energy Storage Systems," *17th International conference on Harmonics and Quality of Power*, Brazil, October 2016. Available: http://www.ichqp2016.org/ichqp/public/files/PID4387481.pdf

[132] "Grid Energy Storage," U.S. Department of Energy, December 2013. [Online] Available: http://energy.gov/sites/prod/files/2014/09/f18/Grid%20Energy%20Storage%20 December%202013.pdf

[133] T. Senjyu, M. Datta, A. Yona, T. Funabashi, C.H. Kim, "PV output power fluctuations smoothing and optimum capacity of energy storage system for PV power generator," *International Conference on Renewable Energies and Power Quality*, Santander, Spain, 2008.

[134] A. Poullikkas, "A comparative overview of large-scale battery systems for electricity storage," *Renewable and Sustainable Energy Reviews*, vol. 27, pp. 778-788, November 2013.